Ministry of Education and Science of the Russian Federation
Saint Petersburg National Research University of Information Technologies, Mechanics, and Optics

NANOSYSTEMS:

PHYSICS, CHEMISTRY, MATHEMATICS

2014, volume 5(5)

Наносистемы: физика, химия, математика
2014, том 5, № 5

NANO
Ф&Х&М

NANOSYSTEMS:

PHYSICS, CHEMISTRY, MATHEMATICS

Address: University ITMO, Kronverkskiy pr., 49, St. Petersburg 197101, Russia.
Phone: +7(812)232-67-65, **Journal site:** http://nanojournal.ifmo.ru/,
E-mail: popov1955@gmail.com

AIM AND SCOPE

The scope of the journal includes all areas of nano-sciences. Papers devoted to basic problems of physics, chemistry, material science and mathematics inspired by nanosystems investigations are welcomed. Both theoretical and experimental works concerning the properties and behavior of nanosystems, problems of its creation and application, mathematical methods of nanosystem studies are considered.

The journal publishes scientific reviews (up to 30 journal pages), research papers (up to 15 pages) and letters (up to 5 pages). All manuscripts are peer-reviewed. Authors are informed about the referee opinion and the Editorial decision.

Content

MATHEMATICS

M.I. Muminov, T.H. Rasulov
On the number of eigenvalues of the family of operator matrices **619**

K.V. Pravdin, I.Yu. Popov
Photonic crystal with negative index material layers **626**

PHYSICS

M.B. Belonenko, Ju.V. Nevzorova, E.N. Galkina
Few cycle pulses in the Bragg medium containing carbon nanotubes **644**

R. Drampyan, T. Vartanyan
Optical micro-structuring of metal films on the surface of dielectric materials: prospects of shaping by non-diffracting optical beams **650**

E.F. Sheka, N.N. Rozhkova, K. Hołderna-Natkaniec, I. Natkaniec
Nanoscale reduced-graphene-oxide origin of shungite in light of neutron scattering **659**

M. Zohrabi
Electric field enhancement of gold tip optical antenna with special geometry **677**

A.A. Zvekov, M.V. Ananyeva, A.V. Kalenskii, A.P. Nikitin
Regularities of light diffusion in the composite material pentaerythriol tetranirate - nickel **685**

CHEMISTRY AND MATERIAL SCIENCE

A.T. Nguyen, M.V. Knurova, T.M. Nguyen, V.O. Mittova, I.Ya. Mittova
Synthesis and the study of magnetic characteristics of nano $La_{1-x}Sr_xFeO_3$ by co-precipitation method **692**

V.I. Popkov, O.V. Almjasheva
Formation mechanism of $YFeO_3$ nanoparticles under the hydrothermal conditions **703**

K.N. Semenov, N.A. Charykov, A.S. Kritchenkov, I.A. Cherepkova, O.S. Manyakina, D.P. Tyurin, A.A. Shestopalova, V.A. Keskinov, E.A. Kulenova, K.V. Ivanova, N.M. Ivanova, D.G. Letenko, V.A. Nikitin, E.L. Fokina
Concentration dependence of electric conductivity and pH for aqueous solutions of water-soluble light fullerene - $C_{60}[=C(COOH)_2]_3$ tris-malonate **709**

V.V. Shelkovnikov, G.A. Lyubas, S.V. Korotaev
Controlled interference color of the metal surface by combination of the chemical and electrochemical aluminum surface treatment **718**

NANOSYSTEMS: PHYSICS, CHEMISTRY, MATHEMATICS, 2014, 5 (5), P. 619–625

ON THE NUMBER OF EIGENVALUES OF THE FAMILY OF OPERATOR MATRICES

M. I. Muminov[1], T. H. Rasulov[2]

[1]Universiti Teknologi Malaysia, Faculty of Science, Department of Mathematical Sciences, 81310 UTM Johor Bahru, Malaysia
[2]Bukhara State University, Faculty of Physics and Mathematics, 11 M. Ikbol str., Bukhara, 200100, Uzbekistan

[1]mmuminov@mail.ru, [2]rth@mail.ru

PACS 02.30.Tb

We consider the family of operator matrices $H(K)$, $K \in \mathbb{T}^3 := (-\pi;\pi]^3$ acting in the direct sum of zero-, one- and two-particle subspaces of the bosonic Fock space. We find a finite set $\Lambda \subset \mathbb{T}^3$ to establish the existence of infinitely many eigenvalues of $H(K)$ for all $K \in \Lambda$ when the associated Friedrichs model has a zero energy resonance. It is found that for every $K \in \Lambda$, the number $N(K,z)$ of eigenvalues of $H(K)$ lying on the left of z, $z < 0$, satisfies the asymptotic relation $\lim\limits_{z\to-0} N(K,z)|\log|z||^{-1} = \mathcal{U}_0$ with $0 < \mathcal{U}_0 < \infty$, independently on the cardinality of Λ. Moreover, we show that for any $K \in \Lambda$ the operator $H(K)$ has a finite number of negative eigenvalues if the associated Friedrichs model has a zero eigenvalue or a zero is the regular type point for positive definite Friedrichs model.

Keywords: operator matrix, bosonic Fock space, annihilation and creation operators, Friedrichs model, essential spectrum, asymptotics.

Received: 3 June 2014

1. Introduction

One of the important problems in the spectral theory of Schrödinger operators and operator matrices in Fock space is to study the finiteness or infiniteness (Efimov's effect) of the number of eigenvalues located outside the essential spectrum. The Efimov effect for the three-particle continuous Schrödinger operator has been discussed in [5]. A rigorous mathematical proof of the existence of this effect was originally carried out by Yafaev [14] and then many works devoted to this subject, see for example [12, 13].

It was shown in [1,2,7] that for the three-particle discrete Schrödinger operator $H_\mu(K)$, the Efimov effect exists only for the zero value of the three-particle quasi-momentum ($K = 0$) and for some value $\mu = \mu_0 > 0$ of the interaction energy of two particles. Moreover, the operator $H_\mu(K)$ has only a finite number of eigenvalues for all sufficiently small nonzero values of K and $\mu > 0$. An asymptote analogous to [12, 13] was obtained in [1, 2] for the number of eigenvalues of $H_\mu(K)$.

In all above mentioned papers devoted to the Efimov effect, the systems where the number of quasi-particles is fixed have been considered. In solid-state physics theory [10], quantum field theory [6] and statistical physics [9] some important problems arise where the number of quasi-particles is finite, but not fixed.

In the present note, we consider the family of 3×3 operator matrices $H(K)$, $K \in \mathbb{T}^3$, associated with the lattice systems describing two identical bosons and one particle, another nature in interactions, without conservation of the number of particles. We find a finite set

$\Lambda \subset \mathbb{T}^3$ and under some smoothness assumptions on the parameters of a family of Friedrichs models $h(k)$, $k \in \mathbb{T}^3$, we obtain the following results: if $h(0)$ has a zero energy resonance, then for the number $N(K,z)$ of eigenvalues of $H(K)$ lying on the left of z, $z<0$, we establish the asymptotics $N(K,z) \sim \mathcal{U}_0|\log|z||$ with $0<\mathcal{U}_0<\infty$ for all $K \in \Lambda$.

We show the finiteness of negative eigenvalues of $H(K)$ for $K \in \Lambda$, if the operator $h(0)$ has a zero eigenvalue or a zero is the regular type point for $h(0)$ with $h(0) \geq 0$.

We point out that the operator $H(K)$ has been considered before in [3,4,8] for $K=0$ and $n=1$, where the existence of Efimov's effect has been proven. Moreover, similar asymptotics for the number of eigenvalues was obtained in [3].

2. Family of 3×3 operator matrices and main results

We denote by $\mathbb{T}^3$ the three-dimensional torus, the cube $(-\pi,\pi]^3$ with appropriately identified sides equipped with its Haar measure. Let $\mathcal{H}_0 := \mathbb{C}$ be the field of complex numbers, $\mathcal{H}_1 := L_2(\mathbb{T}^3)$ be the Hilbert space of square integrable (complex) functions defined on $\mathbb{T}^3$ and $\mathcal{H}_2 := L_2^{\rm s}((\mathbb{T}^3)^2)$ be the Hilbert space of square integrable (complex) symmetric functions defined on $(\mathbb{T}^3)^2$. The spaces $\mathcal{H}_0$, $\mathcal{H}_1$ and $\mathcal{H}_2$ are called zero-, one- and two-particle subspaces of a bosonic Fock space $\mathcal{F}_{\rm s}(L_2(\mathbb{T}^3))$ over $L_2(\mathbb{T}^3)$, respectively.

Let us consider the following family of 3×3 operator matrices $H(K)$, $K \in \mathbb{T}^3$ acting in the Hilbert space $\mathcal{H} := \mathcal{H}_0 \oplus \mathcal{H}_1 \oplus \mathcal{H}_2$ as :

$$H(K) := \begin{pmatrix} H_{00}(K) & H_{01} & 0 \\ H_{01}^* & H_{11}(K) & H_{12} \\ 0 & H_{12}^* & H_{22}(K) \end{pmatrix},$$

with the entries:

$$H_{00}(K)f_0 = w_0(K)f_0, \quad H_{01}f_1 = \int\limits_{\mathbb{T}^3} v_0(s)f_1(s)ds, \quad (H_{11}(K)f_1)(p) = w_1(K;p)f_1(p),$$

$$(H_{12}f_2)(p) = \int\limits_{\mathbb{T}^3} v_1(s)f_2(p,s)ds, \quad (H_{22}(K)f_2)(p,q) = w_2(K;p,q)f_2(p,q),$$

where $f_i \in \mathcal{H}_i$, $i=0,1,2$; $w_0(\cdot)$ and $v_i(\cdot)$, $i=0,1$ are real-valued bounded functions on $\mathbb{T}^3$, the functions $w_1(\cdot;\cdot)$ and $w_2(\cdot;\cdot,\cdot)$ are defined by the equalities:

$$w_1(K;p) := l_1\varepsilon(p) + l_2\varepsilon(K-p) + 1, \quad w_2(K;p,q) := l_1\varepsilon(p) + l_1\varepsilon(q) + l_2\varepsilon(K-p-q),$$

respectively, with $l_1, l_2 > 0$ and

$$\varepsilon(q) := \sum_{i=1}^{3}(1-\cos(nq^{(i)})), \quad q=(q^{(1)},q^{(2)},q^{(3)}) \in \mathbb{T}^3, \quad n \in \mathbb{N}.$$

Here, H_{ij}^* $(i<j)$ denotes the adjoint operator to H_{ij} and

$$(H_{01}^*f_0)(p) = v_0(p)f_0, \ (H_{12}^*f_1)(p,q) = \frac{1}{2}(v_1(p)f_1(q) + v_1(q)f_1(p)), \ f_i \in \mathcal{H}_i, \ i=0,1.$$

Under these assumptions, the operator $H(K)$ is bounded and self-adjoint.

We remark that the operators H_{01} and H_{12} resp. H_{01}^* and H_{12}^* are called annihilation resp. creation operators [6], respectively. In this note, we consider the case where the number of annihilations and creations of the particles of the considering system is equal to 1. It means that $H_{ij} \equiv 0$ for all $|i-j|>1$.

We denote by $\sigma_{\rm ess}(\cdot)$ and $\sigma_{\rm disc}(\cdot)$, respectively, the essential spectrum, and the discrete spectrum of a bounded self-adjoint operator.

To study the spectral properties of the operator $H(K)$, we introduce a family of bounded self-adjoint operators (Friedrichs models) $h(k)$, $k \in \mathbb{T}^3$, which acts in $\mathcal{H}_0 \oplus \mathcal{H}_1$ as follows:

$$h(k) := \begin{pmatrix} h_{00}(k) & h_{01} \\ h_{01}^* & h_{11}(k) \end{pmatrix},$$

where

$$h_{00}(k)f_0 = (l_2\varepsilon(k)+1)f_0, \quad h_{01}f_1 = \frac{1}{\sqrt{2}}\int\limits_{\mathbb{T}^3} v_1(s)f_1(s)ds,$$

$$(h_{11}(k)f_1)(q) = E_k(q)f_1(q), \quad E_k(q) := l_1\varepsilon(q) + l_2\varepsilon(k-q).$$

It is easily to seen that $\sigma_{\rm ess}(h(0)) = [0; 6(l_1+l_2)]$.

The following theorem describes the location of the essential spectrum of operator $H(K)$ by the spectrum of the family $h(k)$ of Friedrichs models.

Theorem 2.1. *For the essential spectrum of $H(K)$, the equality*

$$\sigma_{\rm ess}(H(K)) = \bigcup_{p\in\mathbb{T}^3} \{\sigma_{\rm disc}(h(K-p)) + l_1\varepsilon(p)\} \cup [m_K; M_K]$$

holds, where the numbers m_K and M_K are defined by:

$$m_K := \min_{p,q\in\mathbb{T}^3} w_2(K;p,q) \quad \textit{and} \quad M_K := \max_{p,q\in\mathbb{T}^3} w_2(K;p,q).$$

Let us consider the following subset of $\mathbb{T}^3$:

$$\Lambda := \left\{(p^{(1)},p^{(2)},p^{(3)}) : p^{(i)} \in \left\{0, \pm\frac{2}{n}\pi; \pm\frac{4}{n}\pi; \ldots; \pm\frac{n'}{n}\pi\right\} \cup \Pi_n,\ i=1,2,3\right\},$$

where

$$n' := \begin{cases} n-2, & \text{if } n \text{ is even} \\ n-1, & \text{if } n \text{ is odd} \end{cases} \quad \text{and} \quad \Pi_n := \begin{cases} \{\pi\}, & \text{if } n \text{ is even} \\ \emptyset, & \text{if } n \text{ is odd} \end{cases}$$

Direct calculation shows that the cardinality of Λ is equal to n^3. It is easy to check that for any $K \in \Lambda$, the function $w_2(K;\cdot,\cdot)$ has non-degenerate zero minimum at the points of $\Lambda \times \Lambda$, that is, $m_K = 0$ for $K \in \Lambda$.

The following assumption we needed throughout the note: the function $v_1(\cdot)$ is either even or odd function on each variable and there exists all second order continuous partial derivatives of $v_1(\cdot)$ on $\mathbb{T}^3$.

Let us denote by $C(\mathbb{T}^3)$ and $L_1(\mathbb{T}^3)$ the Banach spaces of continuous and integrable functions on $\mathbb{T}^3$, respectively.

Definition 2.2. *The operator $h(0)$ is said to have a zero energy resonance if the number 1 is an eigenvalue of the integral operator given by:*

$$(G\psi)(q) = \frac{v_1(q)}{2(l_1+l_2)}\int\limits_{\mathbb{T}^3} \frac{v_1(s)\psi(s)}{\varepsilon(s)}ds, \quad \psi \in C(\mathbb{T}^3)$$

and at least one (up to a normalization constant) of the associated eigenfunction ψ satisfies the condition $\psi(p') \neq 0$ for some $p' \in \Lambda$. If the number 1 is not an eigenvalue of the operator G, then we say that $z = 0$ is a regular type point for the operator $h(0)$.

We note that in Definition 2.2, the requirement for the existence of an eigenvalue 1 of G corresponds to the existence of a solution of $h(0)f = 0$ and the condition $\psi(p') \neq 0$ for some $p' \in \Lambda$ implies that the solution f of this equation does not belong to $\mathcal{H}_0 \oplus \mathcal{H}_1$. More precisely, if the operator $h(0)$ has a zero energy resonance, then the solution $\psi(\cdot)$ of $G\psi = \psi$ is equal to $v_1(\cdot)$ (up to constant factor) and the vector $f = (f_0, f_1)$, where

$$f_0 = \text{const} \neq 0, \quad f_1(q) = -\frac{v_1(q)f_0}{\sqrt{2}(l_1 + l_2)\varepsilon(q)}, \tag{2.1}$$

obeys the equation $h(0)f = 0$ with $f_1 \in L_1(\mathbb{T}^3) \setminus L_2(\mathbb{T}^3)$. If the operator $h(0)$ has a zero eigenvalue, then the vector $f = (f_0, f_1)$, where f_0 and f_1 are defined by (2.1), again obeys the equation $h(0)f = 0$ and $f_1 \in L_2(\mathbb{T}^3)$.

Denote by $\tau_{\text{ess}}(K)$ the bottom of the essential spectrum of $H(K)$ and by $N(K, z)$ the number of eigenvalues of $H(K)$ on the left of z, $z \leq \tau_{\text{ess}}(K)$.

Note that if the operator $h(0)$ has either a zero energy resonance or a zero eigenvalue, then for any $K \in \Lambda$ and $p \in \mathbb{T}^3$ the operator $h(K - p) + l_1\varepsilon(p)I$ is non-negative, where I is the identity operator in $\mathcal{H}_0 \oplus \mathcal{H}_1$. Hence Theorem 2.1 and equality $m_K = 0$, $K \in \Lambda$ imply that $\tau_{\text{ess}}(K) = 0$ for all $K \in \Lambda$.

The main results of the present note are as follows.

Theorem 2.3. *Let $K \in \Lambda$ and one of the following assumptions hold:*
(i) *the operator $h(0)$ has a zero eigenvalue;*
(ii) *$h(0) \geq 0$ and a zero is the regular type point for $h(0)$.*

Then the operator $H(K)$ has a finite number of negative eigenvalues.

Theorem 2.4. *Let $K \in \Lambda$. If the operator $h(0)$ has a zero energy resonance, then the operator $H(K)$ has infinitely many negative eigenvalues accumulating at zero and the function $N(K, \cdot)$ obeys the relation:*

$$\lim_{z \to -0} \frac{N(K, z)}{|\log |z||} = \mathcal{U}_0, \quad 0 < \mathcal{U}_0 < \infty. \tag{2.2}$$

Remark 2.5. *The constant $\mathcal{U}_0$ does not depend on the functions $v_0(\cdot)$, $v_1(\cdot)$ and the cardinality of the set Λ. It is positive and depends only on the ratio l_2/l_1.*

Remark 2.6. *Clearly, by equality* (2.2)*, the infinite cardinality of the negative discrete spectrum of $H(K)$ follows automatically from the positivity of $\mathcal{U}_0$.*

3. Sketch of proof of the main results

For any $k \in \mathbb{T}^3$, we define an analytic function $\Delta(k\,; \cdot)$ (the Fredholm determinant associated with the operator $h(k)$) in $\mathbb{C} \setminus [E_{\min}(k); E_{\max}(k)]$ by:

$$\Delta(k\,; z) := l_2\varepsilon(k) + 1 - z - \frac{1}{2}\int\limits_{\mathbb{T}^3} \frac{v_1^2(s)ds}{E_k(s) - z},$$

where the numbers $E_{\min}(k)$ and $E_{\max}(k)$ are defined by

$$E_{\min}(k) := \min_{q \in \mathbb{T}^3} E_k(q) \quad \text{and} \quad E_{\max}(k) := \max_{q \in \mathbb{T}^3} E_k(q).$$

Set

$$\Sigma(K) := \bigcup_{p \in \mathbb{T}^3} \{\sigma_{\text{disc}}(h(K - p)) + l_1\varepsilon(p)\} \cup [m_K; M_K].$$

Let us consider 2×2 block operator matrix $\widehat{T}(K,z)$, $z\in\mathbb{C}\setminus\Sigma(K)$ acting on $\mathcal{H}_0\oplus\mathcal{H}_1$ as

$$\widehat{T}(K,z):=\begin{pmatrix}\widehat{T}_{00}(K,z) & \widehat{T}_{01}(K,z)\\ \widehat{T}_{10}(K,z) & \widehat{T}_{11}(K,z)\end{pmatrix},$$

with the entries $\widehat{T}_{ij}(K,z):\mathcal{H}_j\to\mathcal{H}_i$, $i,j=0,1$:

$$\widehat{T}_{00}(K,z)g_0=(1+z-w_0(K))g_0,\quad \widehat{T}_{01}(K,z)=-H_{01};$$

$$(\widehat{T}_{10}(K,z)g_0)(p)=-\frac{v_0(p)g_0}{\Delta(K-p\,;z-l_1\varepsilon(p))};$$

$$(\widehat{T}_{11}(K,z)g_1)(p)=\frac{v_1(p)}{2\Delta(K-p\,;z-l_1\varepsilon(p))}\int\limits_{\mathbb{T}^3}\frac{v_1(s)g_1(s)ds}{w_2(K;p,s)-z},$$

$g_i\in\mathcal{H}_i$, $i=0,1$.

The following lemma is an analog of the well-known Faddeev's result for the operator $H(K)$ and establishes a connection between eigenvalues of $H(K)$ and $\widehat{T}(K,z)$.

Lemma 3.1. *The number $z\in\mathbb{C}\setminus\Sigma(K)$ is an eigenvalue of the operator $H(K)$ if and only if the number $\lambda=1$ is an eigenvalue of the operator $\widehat{T}(K,z)$. Moreover, the eigenvalues z and 1 have the same multiplicities.*

The inclusion $\Sigma(K)\subset\sigma_{\rm ess}(H(K))$ in the proof of Theorem 2.1 is established with the use of a well-known Weyl criterion. An application of Lemma 3.1 and analytic Fredholm theorem (see, e.g., Theorem VI.14 in [11]) proves inclusion $\sigma_{\rm ess}(H(K))\subset\Sigma(K)$.

To find conditions which guarantee for the finiteness or infiniteness of the number of eigenvalues of $H(K)$, $K\in\Lambda$, we establish in which cases the bottom of the essential spectrum of $h(0)$ is a threshold energy resonance or eigenvalue.

Lemma 3.2. (i) *The operator $h(0)$ has a zero eigenvalue if and only if $\Delta(0\,;0)=0$ and $v_1(q')=0$ for all $q'\in\Lambda$;*

(ii) *The operator $h(0)$ has a zero energy resonance if and only if $\Delta(0\,;0)=0$ and $v_1(q')\neq 0$ for some $q'\in\Lambda$.*

Since $\Delta(K-p\,;z-l_1\varepsilon(p))>0$ for any $K,p\in\mathbb{T}^3$ and $z<\tau_{\rm ess}(K)$, one can define a symmetric version of the operator $\widehat{T}(K,z)$ for $z<\tau_{\rm ess}(K)$, which is important in our analysis of the discrete spectrum of $H(K)$, $K\in\mathbb{T}^3$. So, we consider the self-adjoint compact 2×2 block operator matrix $T(K,z)$, $z<\tau_{\rm ess}(K)$ acting on $\mathcal{H}_0\oplus\mathcal{H}_1$ as follows:

$$T(K,z):=\begin{pmatrix}T_{00}(K,z) & T_{01}(K,z)\\ T_{01}^*(K,z) & T_{11}(K,z)\end{pmatrix},$$

with the entries $T_{ij}(K,z):\mathcal{H}_j\to\mathcal{H}_i$, $i,j=0,1$:

$$T_{00}(K,z)g_0=(1+z-w_0(K))g_0,\quad T_{01}(K,z)g_1=-\int\limits_{\mathbb{T}^3}\frac{v_0(s)g_1(s)ds}{\sqrt{\Delta(K-s\,;z-l_1\varepsilon(s))}};$$

$$(T_{11}(K,z)g_1)(p)=\frac{v_1(p)}{2\sqrt{\Delta(K-p\,;z-l_1\varepsilon(p))}}\int\limits_{\mathbb{T}^3}\frac{v_1(s)g_1(s)ds}{\sqrt{\Delta(K-s\,;z-l_1\varepsilon(s))}(w_2(K;p,s)-z)},$$

$g_i\in\mathcal{H}_i$, $i=0,1$.

To prove Theorem 2.3, first we show $N(K,z)=n(1,T(K,z))$ (so-called Birman-Schwinger principle for the operator $H(K)$), where $n(1,A)$ is the number of the eigenvalues

(counted multiplicities) of the compact operator A bigger than 1. Then, under the conditions of Theorem 2.3, we prove that the operator $T(K,z)$ is continuous from the left up to $z=0$ and $T(K,0)$ is a compact operator. Using the Weyl inequality,

$$n(\lambda_1+\lambda_2, A_1+A_2) \le n(\lambda_1, A_1) + n(\lambda_2, A_2)$$

for the sum of compact operators A_1 and A_2, and for any positive numbers λ_1 and λ_2, we have

$$n(1, T(K,z)) \le n(1/2, T(K,0)) + n(1/2, T(K,z) - T(K,0))$$

for all $z<0$. Hence, $\lim\limits_{z\to-0} N(K,z) = N(K,0) \le n(1/2, T(K,0)) < \infty$.

The study of the behavior of $T(K,z)$, $K\in\Lambda$, that is, proof of Theorem 2.4, is based on the analysis of the behavior of $\Delta(K-p\,; z-l_1\varepsilon(p))$ as $z\to-0$ and $|p-p'|\to 0$ for $K,p'\in\Lambda$.

Set

$$\Lambda_0 := \{q'\in\Lambda : v_1(q')\neq 0\}.$$

Lemma 3.3. *Let the operator $h(0)$ have a zero energy resonance and $K,p'\in\Lambda$. Then, the following decomposition:*

$$\Delta(K-p\,; z-l_1\varepsilon(p)) = \frac{2\pi^2}{n^2(l_1+l_2)^{3/2}}\Big(\sum_{q'\in\Lambda_0} v_1^2(q')\Big)\sqrt{\frac{l_1^2+2l_1l_2}{l_1+l_2}|p-p'|^2 - \frac{2z}{n^2}} + O(|p-p'|^2) + O(|z|),$$

holds for $|p-p'|\to 0$ and $z\to-0$.

By applying Lemma 3.3, we single out the principal part of the operator $T(K,z)$ $K\in\Lambda$ as $z\to-0$, which is unitarily equivalent to the compact integral operator S_R, $R=1/2|\log|z||$ in $L_2((0,R), L_2(\mathbb{S}^2))$ with the kernel

$$S(y,t) := \frac{1}{4\pi^2}\frac{(l_1+l_2)^2}{\sqrt{l_1^2+2l_1l_2}}\frac{1}{(l_1+l_2)\cosh y + l_2 t},$$

where $\mathbb{S}^2$ be the unit sphere in $\mathbb{R}^3$; $y=x-x'$, $x,x'\in(0,R)$ and $t=\langle\xi,\eta\rangle$ is the inner product of the arguments $\xi,\eta\in\mathbb{S}^2$.

The eigenvalue asymptotics for the operator S_R have been studied in detail by Sobolev [12], by employing an argument used in the calculation of the canonical distribution of Toeplitz operators.

Acknowledgments

This work was supported by the IMU Einstein Foundation Program. T. H. Rasulov wishes to thank the Berlin Mathematical School and Weierstrass Institute for Applied Analysis and Stochastics for the invitation and hospitality.

References

[1] Zh.I. Abdullaev, S.N. Lakaev. Asymptotics of the discrete spectrum of the three-particle Schrödinger difference operator on a lattice. *Theor. Math. Phys.*, **136** (2), P. 1096–1109 (2003).

[2] S. Albeverio, S.N. Lakaev, Z.I. Muminov. Schrödinger operators on lattices. The Efimov effect and discrete spectrum asymptotics. *Ann. Henri Poincaré*, **5**, P. 743–772 (2004).

[3] S. Albeverio, S.N. Lakaev, T.H. Rasulov. On the spectrum of an Hamiltonian in Fock space. Discrete spectrum asymptotics. *J. Stat. Phys.*, **127** (2), P. 191–220 (2007).

[4] S. Albeverio, S.N. Lakaev, T.H. Rasulov. The Efimov effect for a model operator associated with the Hamiltonian of a non conserved number of particles. *Methods Funct. Anal. Topology*, **13** (1), P. 1–16 (2007).

[5] V. Efimov. Energy levels arising from resonant two-body forces in a three-body system. *Phys. Lett. B.*, **33** (8), P. 563–564 (1970).
[6] K.O. Friedrichs. *Perturbation of spectra in Hilbert space*. Amer. Math. Soc. Providence, Rhole Island, 1965.
[7] S.N. Lakaev, M.É. Muminov. Essential and discrete spectra of the three-particle Schrödinger operator on a lattices. *Theor. Math. Phys.*, **135** (3), P. 849–871 (2003).
[8] S.N. Lakaev, T.Kh. Rasulov. Efimov's effect in a model of perturbation theory of the essential spectrum. *Funct. Anal. Appl.*, **37** (1), P. 69–71 (2003).
[9] R.A. Minlos, H. Spohn. The three-body problem in radioactive decay: the case of one atom and at most two photons. Topics in Statistical and Theoretical Physics. *Amer. Math. Soc. Transl.*, Ser. 2, **177**, P. 159–193 (1996).
[10] A.I. Mogilner. Hamiltonians in solid state physics as multiparticle discrete Schrödinger operators: problems and results. *Advances in Sov. Math.*, **5**, P. 139–194 (1991).
[11] M. Reed, B. Simon. Methods of modern mathematical physics. IV: Analysis of Operators. Academic Press, New York, 396 P. (1979).
[12] A.V. Sobolev. The Efimov effect. Discrete spectrum asymptotics. *Commun. Math. Phys.*, **156** (1), P. 101–126 (1993).
[13] H. Tamura. The Efimov effect of three-body Schrödinger operators: asymptotics for the number of negative eigenvalues. *Nagoya Math. J.*, **130**, P. 55–83 (1993).
[14] D.R. Yafaev. On the theory of the discrete spectrum of the three-particle Schrödinger operator. *Math. USSR-Sb.*, **23**, P. 535–559 (1974).

NANOSYSTEMS: PHYSICS, CHEMISTRY, MATHEMATICS, 2014, 5 (5), P. 626–643

PHOTONIC CRYSTAL WITH NEGATIVE INDEX MATERIAL LAYERS

K. V. Pravdin, I. Yu. Popov

ITMO University, Saint Petersburg, Russia

construeman@gmail.com, popov1955@gmail.com

PACS 42.70.Qs, 78.67.Pt

We consider the one-dimensional photonic crystal composed of an infinite number of parallel alternating layers filled with a metamaterial and vacuum. We assume the metamaterial is an isotropic, homogeneous, dispersive and non-absorptive medium. We use a single Lorentz contribution and assume the permittivity and permeability are equal. Using the time and coordinate Fourier transforms and the Floquet-Bloch theorem, we obtain systems of equations for TE and TM modes, which ones are identical. We consider radiative and evanescent regimes for the metamaterial and vacuum layers and find sets of frequencies, where the metamaterial has the positive or negative refractive index. We use a numerical approach. As a result, we obtained the photonic band gap structure for different frequency intervals and ascertain how it changes with modification of the system parameters. We observe the non-reflection effect for any directions for a certain frequency but this fails with the layer width modification.

Keywords: phonic crystals, photonic band gap, negative index materials, metamaterial.

Received: 10 June 2014
Revised: 08 July 2014

1. Introduction

Materials with a periodically modulated refractive index function of spatial coordinates are known as photonic crystals (PCs). Photonic crystals occur in nature over millions years. Biological systems were using nanometer-scale architectures, which are the natural photonic structures, to produce striking optical effects [1].

Extensive studies on PCs began with these pioneering works [2, 3]. The propagation of electromagnetic (EM) wave in the PC depends on its frequency and can be forbidden. The forbidden frequencies make up the forbidden bands or so-called photonic band gaps (PBGs). Analogously, the permitted frequencies make up the permitted bands [4, 5]. Forbidden and permitted bands comprise the so-called PBG structure. The PBGs lead to various applications of PCs such as perfect dielectric mirror [6], nonlinear effects [7], resonant cavities [8], PC fibers [9], waveguides [10], and PC devices, e.g., ultra-fast, efficient and high power nanocavity lasers, optical buffer and storage components [11].

The simplest model of a PC is the one-dimensional PC (1DPC). The 1DPC is a system of alternating layers with different refractive indices. Using negative index materials (NIMs) [12, 13] in 1DPCs can lead to unusual phenomena, such as spurious modes with complex frequencies, discrete modes and photon tunneling modes [14]. Therefore, numerous investigations of 1DPC composed of layers filled with positive index materials (PIMs) and NIMs, have been performed recently [15-21]. But, most of these investigations consider nondisperdive systems, i.e., the permittivity and permeability (and therefore, the refractive index) are the same for all frequencies of EM waves.

The goal of our work is to obtain the PBG structure for a system of alternating layers filled with a metamaterial and vacuum. We assume the metamaterial is an isotropic, homogeneous, dispersive and non-absorptive medium. We also assume the permittivity and permeability have the identical expression. We use a single Lorentz contribution to describe them [22, 23]. Therefore, for a certain frequency interval, the metamaterial has a negative refractive index and behaves like a NIM (NIM case). For other frequencies, it has a positive refractive index and behaves like a PIM (PIM case). We have a chance to compare the NIM case with the PIM case. Also, we are interested in the dependence of the PBG structure upon the system's parameters.

2. Model

2.1. Maxwell's equations

We consider the Maxwell's equations in a differential form:

$$\frac{d\mathbf{D}}{dt}(\mathbf{x},t) = \nabla \times \mathbf{H}(\mathbf{x},t), \tag{1}$$

$$\frac{d\mathbf{B}}{dt}(\mathbf{x},t) = -\nabla \times \mathbf{E}(\mathbf{x},t), \tag{2}$$

$$\nabla \cdot \mathbf{D}(\mathbf{x},t) = 0, \tag{3}$$

$$\nabla \cdot \mathbf{B}(\mathbf{x},t) = 0, \tag{4}$$

where $\mathbf{x}$ is the vector located in the $\{\mathbf{e}_i\}_{i=1}^3$ Cartesian basis, ∇ is the Hamilton operator, $\times$ is a cross product symbol, $\cdot$ is an inner product symbol as well as a symbol for the matrix product. Also, we consider the auxiliary field equations:

$$\mathbf{D}(\mathbf{x},t) = \varepsilon_0 \mathbf{E}(\mathbf{x},t) + \mathbf{P}(\mathbf{x},t), \tag{5}$$

$$\mathbf{B}(\mathbf{x},t) = \mu_0 \left[\mathbf{H}(\mathbf{x},t) + \mathbf{M}(\mathbf{x},t)\right], \tag{6}$$

where

$$\mathbf{P}(\mathbf{x},t) = \varepsilon_0 \int_{t_0}^{t} \boldsymbol{\chi}_e(\mathbf{x},t-s) \cdot \mathbf{E}(\mathbf{x},s)\, ds,$$

$$\mathbf{M}(\mathbf{x},t) = \int_{t_0}^{t} \boldsymbol{\chi}_m(\mathbf{x},t-s) \cdot \mathbf{H}(\mathbf{x},s)\, ds,$$

and ε_0 and μ_0 are the electric and magnetic constants ($\varepsilon_0\mu_0 = 1/c^2$, where c is the speed of light in vacuum), $\boldsymbol{\chi}_e(\mathbf{x},t)$ and $\boldsymbol{\chi}_m(\mathbf{x},t)$ are the electric and magnetic susceptibility tensors. We use the causality condition $\boldsymbol{\chi}_e(\mathbf{x},t) = \boldsymbol{\chi}_m(\mathbf{x},t) = 0$ for $t < t_0$ and assume $t_0 = 0$. We also use the passivity condition [23]. Then, the electromagnetic energy,

$$U_{em}(t) = \frac{1}{2} \int \left[\mathbf{E}^2(\mathbf{x},t) + \mathbf{H}^2(\mathbf{x},t)\right] d\mathbf{x},$$

is a non-increasing function of time. With the causality and passivity conditions and the auxiliary field formalism (AFF), the system has a proper time evolution [23]. In case the initial fields are square integrable they remain so for all later times.

We use the Fourier transform with t time,

$$\hat{f}(\omega) = \int_{-\infty}^{+\infty} f(t)\, e^{-i\omega t} dt, \quad f(t) = \frac{1}{2\pi} \int_{-\infty}^{+\infty} \hat{f}(\omega)\, e^{i\omega t} d\omega, \tag{7}$$

to obtain the Maxwell's equations (1)–(4) in relation on ω frequency

$$i\omega \hat{\mathbf{D}}(\mathbf{x},\omega) = \nabla \times \hat{\mathbf{H}}(\mathbf{x},\omega), \tag{8}$$

$$i\omega\hat{\mathbf{B}}(\mathbf{x},\omega) = -\nabla \times \hat{\mathbf{E}}(\mathbf{x},\omega), \tag{9}$$

$$\nabla \cdot \hat{\mathbf{D}}(\mathbf{x},\omega) = 0, \tag{10}$$

$$\nabla \cdot \hat{\mathbf{B}}(\mathbf{x},\omega) = 0. \tag{11}$$

The auxiliary field equations (5) and (6) after the Fourier transform (7) are expressed as follows:

$$\hat{\mathbf{D}}(\mathbf{x},\omega) = \varepsilon_0\boldsymbol{\varepsilon}(\mathbf{x},\omega)\cdot\hat{\mathbf{E}}(\mathbf{x},\omega), \tag{12}$$

$$\hat{\mathbf{B}}(\mathbf{x},\omega) = \mu_0\boldsymbol{\mu}(\mathbf{x},\omega)\cdot\hat{\mathbf{H}}(\mathbf{x},\omega), \tag{13}$$

where

$$\boldsymbol{\varepsilon}(\mathbf{x},\omega) = 1 + \hat{\boldsymbol{\chi}}_e(\mathbf{x},\omega),$$

$$\boldsymbol{\mu}(\mathbf{x},\omega) = 1 + \hat{\boldsymbol{\chi}}_m(\mathbf{x},\omega).$$

Substituting expressions for $\hat{\mathbf{D}}(\mathbf{x},\omega)$ and $\hat{\mathbf{B}}(\mathbf{x},\omega)$ from equations (12) and (13) into equations (8), (9), (10), and (11), we obtain the following relations:

$$i\omega\varepsilon_0\boldsymbol{\varepsilon}(\mathbf{x},\omega)\hat{\mathbf{E}}(\mathbf{x},\omega) = \nabla\times\hat{\mathbf{H}}(\mathbf{x},\omega), \tag{14}$$

$$i\omega\mu_0\boldsymbol{\mu}(\mathbf{x},\omega)\hat{\mathbf{H}}(\mathbf{x},\omega) = -\nabla\times\hat{\mathbf{E}}(\mathbf{x},\omega), \tag{15}$$

$$\nabla\cdot\hat{\mathbf{E}}(\mathbf{x},\omega) = 0,$$

$$\nabla\cdot\hat{\mathbf{H}}(\mathbf{x},\omega) = 0.$$

We examine the system composed of infinite count of parallel layers. $\mathbf{e}_1$, $\mathbf{e}_2$ unit vectors set the plane of the layer's surfaces. $\mathbf{e}_3$ unit vector set the x axis. We assume a translation invariance along the plane of layer's surfaces. There are two types of layers. The first one is Δ_1 in width and filled with a metamaterial. The second one is Δ_2 in width and filled with a vacuum. Layers alternate with each other. Then, $\Delta_1 + \Delta_2$ is the period of the system. Thus, the system is a 1DPC, and it is enough to consider only two layers, e.g., the metamaterial layer located between $x = 0$ and $x = \Delta_1$ coordinates (let its index be $j = 1$) and the vacuum layer located between $x = \Delta_1$ and $x = \Delta_1 + \Delta_2$ coordinates (let its index be $j = 2$).

We assume that the metamaterial layers are isotropic and homogeneous media. Therefore, the permittivity and permeability in all metamaterial layera are scalar functions only of the one ω frequency variable, i.e., $\boldsymbol{\varepsilon}(\mathbf{x},\omega) = \varepsilon(\omega)\mathbf{U}$ and $\boldsymbol{\mu}(\mathbf{x},\omega) = \mu(\omega)\mathbf{U}$. Also, we assume the metamaterial layers are dispersive and non-absorptive media. In that case, the susceptibilities consist of a sum of Lorentz contributions [22]. We deal with a single dispersive Lorentz contribution [23]. We assume that the permittivity and permeability of the metamaterial stand equal and

$$\varepsilon(\omega) = \mu(\omega) = 1 - \frac{\Omega^2}{\omega^2 - \omega_0^2}, \tag{16}$$

where Ω and ω_0 are constants, and $\varepsilon(\omega) = \mu(\omega) = 1$ in vacuum. From equation (16) it follows that for different ω frequencies the metamaterial behaves like a PIM or NIM (and we have the PIM or NIM system). For every ω inside the (ω_0, ω_2) interval (NIM interval) the $\varepsilon(\omega)$ and $\mu(\omega)$ values are negative and the metamaterial is the NIM, where $\omega_2 = \sqrt{\omega_0^2 + \Omega^2}$, $\varepsilon(\omega_2) = \mu(\omega_2) = 0$, and $\varepsilon(\omega_0 + 0) = \mu(\omega_0 + 0) = -\infty$. For every ω inside the $(0, \omega_0)$ or $(\omega_2, +\infty)$ intervals (first and second PIM interval, correspondingly) the $\varepsilon(\omega)$ and $\mu(\omega)$ values are positive and the metamaterial is the PIM, where $\varepsilon(\omega_0 - 0) = \mu(\omega_0 - 0) = +\infty$. For $\omega_1 = \sqrt{\omega_0^2 + \Omega^2/2}$ in the metamaterial $\varepsilon(\omega_1) = \mu(\omega_1) = -1$, where ω_1 is so-called NIM frequency [23].

Expressing the $\hat{\mathbf{H}}(\mathbf{x},\omega)$ value from equation (15), substituting it into equation (14) and recalling $\varepsilon_0\mu_0 = 1/c^2$, we obtain the Helmholtz equation for j-th layer ($j = 1, 2$) as follows:

$$\nabla \times \nabla \times \hat{\mathbf{E}}_j(\mathbf{x},\omega) = (\omega/c)^2\varepsilon_j(\omega)\mu_j(\omega)\hat{\mathbf{E}}_j(\mathbf{x},\omega). \tag{17}$$

Let $\mathbf{k} = \{k_1, k_2, k_3\}$ be a three-dimensional wave vector with k length, where $k = k(\omega) = (\omega/c)^2\varepsilon(\omega)\mu(\omega)$, $\boldsymbol{\kappa} = \{k_1, k_2, 0\} = \kappa\mathbf{e}_{\boldsymbol{\kappa}}$ be a two-dimensional wave vector with κ coordinate along the $\mathbf{e}_{\boldsymbol{\kappa}}$ unit vector, which is parallel to the plane of layer's surfaces, $\boldsymbol{\zeta} = \{0, 0, k_3\} = \zeta\mathbf{e}_3$ is an one-dimensional wave vector parallel to the x axis with the ζ coordinate, where $\zeta^2 = \zeta^2(\omega,\kappa) = k^2(\omega) - \kappa^2 = (\omega/c)^2\varepsilon(\omega)\mu(\omega) - \kappa^2$. Therefore, $\mathbf{e}_3 \times \mathbf{e}_{\boldsymbol{\kappa}}$ is a parallel to the plane of layer's surfaces unit vector. The set of $\mathbf{e}_{\boldsymbol{\kappa}}$, $\mathbf{e}_3 \times \mathbf{e}_{\boldsymbol{\kappa}}$, $\mathbf{e}_3$ unit vectors forms the Cartesian basis.

The considered system is the 1DPC. Then, to obtain the following one-dimensional expression of the Helmholtz equation (17), we use the Fourier transform with x_1 and x_2 coordinates of $\mathbf{x}^\perp = \{x_1, x_2, 0\}$ vector:

$$g_{\boldsymbol{\kappa}}(x) = \int_{-\infty}^{+\infty}\int_{-\infty}^{+\infty} e^{i(k_1x_1+k_2x_2)}g(\mathbf{x})dx_1dx_2 = \int_{\mathrm{R}^2} e^{i\boldsymbol{\kappa}\cdot\mathbf{x}^\perp}g(\mathbf{x})d\mathbf{x}^\perp, \tag{18}$$

$$g(\mathbf{x}) = \frac{1}{(2\pi)^2}\int_{-\infty}^{+\infty}\int_{-\infty}^{+\infty} e^{-i(k_1x_1+k_2x_2)}g_{\boldsymbol{\kappa}}(x)dk_1dk_2 = \frac{1}{(2\pi)^2}\int_{\mathrm{R}^2} e^{-i\boldsymbol{\kappa}\cdot\mathbf{x}^\perp}g_{\boldsymbol{\kappa}}(x)d\boldsymbol{\kappa}.$$

The Fourier transformed (18) Hamilton operator is

$$\nabla_{\boldsymbol{\kappa}} = \left(i\boldsymbol{\kappa} + \frac{\partial}{\partial x_3}\mathbf{e}_3\right).$$

Then,

$$\left[\nabla \times \nabla \times \hat{\mathbf{E}}_j(\mathbf{x},\omega)\right]_{\boldsymbol{\kappa}} = \left(i\boldsymbol{\kappa} + \frac{\partial}{\partial x_3}\mathbf{e}_3\right) \times \left[\left(i\boldsymbol{\kappa} + \frac{\partial}{\partial x_3}\mathbf{e}_3\right) \times \hat{\mathbf{E}}_{\boldsymbol{\kappa},j}(x,\omega)\right],$$

and the Fourier transformed Helmholtz equation (17) is expressed as follows:

$$\left(i\boldsymbol{\kappa} + \frac{\partial}{\partial x_3}\mathbf{e}_3\right) \times \left[\left(i\boldsymbol{\kappa} + \frac{\partial}{\partial x_3}\mathbf{e}_3\right) \times \hat{\mathbf{E}}_{\boldsymbol{\kappa},j}(x,\omega)\right] = (\omega/c)^2\varepsilon_j(\omega)\mu_j(\omega)\hat{\mathbf{E}}_{\boldsymbol{\kappa},j}(x,\omega),$$

or in a matrix form:

$$\mathbf{M}_{\boldsymbol{\kappa},j}(\omega,\kappa)\cdot\hat{\mathbf{E}}_{\boldsymbol{\kappa},j}(x,\omega) = 0, \tag{19}$$

where

$$\mathbf{M}_{\boldsymbol{\kappa},j}(\omega,\kappa) = \begin{pmatrix} \frac{\partial^2}{\partial x^2} + (\omega/c)^2\varepsilon_j(\omega)\mu_j(\omega) & 0 & -i\kappa\frac{\partial}{\partial x} \\ 0 & \frac{\partial^2}{\partial x^2} + \zeta_j^2(\omega,\kappa) & 0 \\ -i\kappa\frac{\partial}{\partial x} & 0 & \zeta_j^2(\omega,\kappa) \end{pmatrix}$$

is presented in $\{\mathbf{e}_{\boldsymbol{\kappa}}, \mathbf{e}_3 \times \mathbf{e}_{\boldsymbol{\kappa}}, \mathbf{e}_3\}$ basis. Equation (19) has the following TE part:

$$\left(\frac{\partial^2}{\partial x^2} + \zeta_j^2(\omega,\kappa)\right)\hat{\mathbf{E}}_{\boldsymbol{\kappa},j}(x,\omega)\Big|_{\mathbf{e}_3\times\mathbf{e}_{\boldsymbol{\kappa}}} = 0, \tag{20}$$

and the following TM part:

$$\left(\frac{\partial^2}{\partial x^2} + (\omega/c)^2\varepsilon_j(\omega)\mu_j(\omega)\right)\hat{\mathbf{E}}_{\boldsymbol{\kappa},j}(x,\omega)\Big|_{\mathbf{e}_{\boldsymbol{\kappa}}} = i\kappa\frac{\partial}{\partial x}\,\hat{\mathbf{E}}_{\boldsymbol{\kappa},j}(x,\omega)\Big|_{\mathbf{e}_3}, \tag{21}$$

$$i\kappa\frac{\partial}{\partial x}\,\hat{\mathbf{E}}_{\boldsymbol{\kappa},j}(x,\omega)\Big|_{\mathbf{e}_{\boldsymbol{\kappa}}} = \zeta_j^2\,\hat{\mathbf{E}}_{\boldsymbol{\kappa},j}(x,\omega)\Big|_{\mathbf{e}_3}, \tag{22}$$

where for a certain $\mathbf{A}$ vector, $\mathbf{A}\big|_{\mathbf{e}}$ notation means its projection on the $\mathbf{e}$ unit vector. Equations (21) and (22) are expressed as follows:

$$\left(\frac{\partial^2}{\partial x^2} + \zeta_j^2(\omega,\kappa)\right) \hat{\mathbf{E}}_{\boldsymbol{\kappa},j}(x,\omega)\Big|_{\mathbf{e}_{\boldsymbol{\kappa}}} = 0, \tag{23}$$

$$\hat{\mathbf{E}}_{\boldsymbol{\kappa},j}(x,\omega)\Big|_{\mathbf{e}_3} = i\kappa \frac{1}{\zeta_j^2(\omega,\kappa)} \frac{\partial}{\partial x} \hat{\mathbf{E}}_{\boldsymbol{\kappa},j}(x,\omega)\Big|_{\mathbf{e}_{\boldsymbol{\kappa}}}. \tag{24}$$

To obtain the $\hat{\mathbf{E}}_{\boldsymbol{\kappa},j}(x,\omega)$ value, it is enough to solve equations (20) and (23) and use equation (24). Equations (20) and (23) have the same structure and can be written as follows:

$$\left(\frac{\partial^2}{\partial x^2} + \zeta_j^2(\omega,\kappa)\right) E_j(x,\omega) = 0, \tag{25}$$

where $E_j(x,\omega) = \hat{\mathbf{E}}_{\boldsymbol{\kappa},j}(x,\omega)\Big|_{\mathbf{e}_3\times\mathbf{e}_{\boldsymbol{\kappa}}}$ for TE mode or $E_j(x,\omega) = \hat{\mathbf{E}}_{\boldsymbol{\kappa},j}(x,\omega)\Big|_{\mathbf{e}_{\boldsymbol{\kappa}}}$ for TM mode.

2.2. Boundary conditions

Layers in the system are divided by plane unbounded surfaces. The general form of standard boundary conditions for the surface located between considered layers at the $x = \Delta_1$ coordinate, is presented as follows:

$$(\mathbf{E}_1 - \mathbf{E}_2) \times \mathbf{e}_3 = \mathbf{0}, \tag{26}$$

$$(\mathbf{H}_1 - \mathbf{H}_2) \times \mathbf{e}_3 = \mathbf{0}, \tag{27}$$

$$(\mathbf{D}_1 - \mathbf{D}_2) \cdot \mathbf{e}_3 = 0, \tag{28}$$

$$(\mathbf{B}_1 - \mathbf{B}_2) \cdot \mathbf{e}_3 = 0, \tag{29}$$

where $\mathbf{E}_j = \mathbf{E}_j(\tilde{\mathbf{x}},t)$, $\mathbf{H}_j = \mathbf{H}_j(\tilde{\mathbf{x}},t)$, $\mathbf{D}_j = \mathbf{D}_j(\tilde{\mathbf{x}},t)$, and $\mathbf{B}_j = \mathbf{B}_j(\tilde{\mathbf{x}},t)$ stand for the one-sided limits with $x \to \Delta_1$, $\mathbf{x} = \mathbf{x}^{\perp} + x\mathbf{e}_3$, and $\tilde{\mathbf{x}} = \mathbf{x}^{\perp} + \Delta_1\mathbf{e}_3$ (left-sided ones are for $j = 1$ and right-sided ones are for $j = 2$). After the Fourier transform (7), equations (26)–(29) are expressed as follows: $x = \Delta_1$

$$\left(\hat{\mathbf{E}}_1(\tilde{\mathbf{x}},\omega) - \hat{\mathbf{E}}_2(\tilde{\mathbf{x}},\omega)\right) \times \mathbf{e}_3 = \mathbf{0}, \tag{30}$$

$$\left(\hat{\mathbf{H}}_1(\tilde{\mathbf{x}},\omega) - \hat{\mathbf{H}}_2(\tilde{\mathbf{x}},\omega)\right) \times \mathbf{e}_3 = \mathbf{0}, \tag{31}$$

$$\left(\varepsilon_1(\omega)\hat{\mathbf{E}}_1(\tilde{\mathbf{x}},\omega) - \varepsilon_2(\omega)\hat{\mathbf{E}}_2(\tilde{\mathbf{x}},\omega)\right) \cdot \mathbf{e}_3 = 0, \tag{32}$$

$$\left(\mu_1(\omega)\hat{\mathbf{H}}_1(\tilde{\mathbf{x}},\omega) - \mu_2(\omega)\hat{\mathbf{H}}_2(\tilde{\mathbf{x}},\omega)\right) \cdot \mathbf{e}_3 = 0.$$

Let us consider the case of TM mode. It is enough to use the following coordinate representation of equations (30) and (32):

$$\left(\hat{\mathbf{E}}_1(\tilde{\mathbf{x}},\omega) - \hat{\mathbf{E}}_2(\tilde{\mathbf{x}},\omega)\right)\Big|_{\mathbf{e}_\kappa} = 0, \tag{33}$$

$$\left(\varepsilon_1(\omega)\hat{\mathbf{E}}_1(\tilde{\mathbf{x}},\omega) - \varepsilon_2(\omega)\hat{\mathbf{E}}_2(\tilde{\mathbf{x}},\omega)\right)\Big|_{\mathbf{e}_3} = 0. \tag{34}$$

After the Fourier transform (18), equations (33) and (34) are expressed as follows:

$$\left(\hat{\mathbf{E}}_{1,\kappa}(\tilde{x},\omega) - \hat{\mathbf{E}}_{2,\kappa}(\tilde{x},\omega)\right)\Big|_{\mathbf{e}_\kappa} = 0,$$

$$\left(\varepsilon_1(\omega)\hat{\mathbf{E}}_{1,\kappa}(\tilde{x},\omega) - \varepsilon_2(\omega)\hat{\mathbf{E}}_{2,\kappa}(\tilde{x},\omega)\right)\Big|_{\mathbf{e}_3} = 0.$$

Recalling $E_j(x,\omega) = \hat{\mathbf{E}}_{\boldsymbol{\kappa},j}(x,\omega)\Big|_{\mathbf{e}_{\boldsymbol{\kappa}}}$ for TM mode and using equation (24), we obtain:

$$E_1(\Delta_1,\omega) = E_2(\Delta_1,\omega), \tag{35}$$

$$\frac{\partial E_1}{\partial x}(\Delta_1,\omega) = \frac{\varepsilon_2(\omega)}{\varepsilon_1(\omega)}\frac{\zeta_1^2(\omega,\kappa)}{\zeta_2^2(\omega,\kappa)}\frac{\partial E_2}{\partial x}(\Delta_1,\omega). \tag{36}$$

Now we consider the case of TE mode. It is enough to use the following coordinate representation of equations (30) and (31):

$$\left(\hat{\mathbf{E}}_1(\tilde{\mathbf{x}},\omega) - \hat{\mathbf{E}}_2(\tilde{\mathbf{x}},\omega)\right)\Big|_{\mathbf{e}_3\times\mathbf{e}_\kappa} = 0, \tag{37}$$

$$\left(\hat{\mathbf{H}}_1(\tilde{\mathbf{x}},\omega) - \hat{\mathbf{H}}_2(\tilde{\mathbf{x}},\omega)\right)\Big|_{\mathbf{e}_\kappa} = 0. \tag{38}$$

From equation (15) we have

$$\hat{\mathbf{H}}_j(\mathbf{x},\omega) = -\frac{1}{i\omega\mu_0\mu_j(\omega)}\nabla\times\hat{\mathbf{E}}_j(\mathbf{x},\omega).$$

Then, equation (38) is expressed as follows:

$$\left(\nabla\times\hat{\mathbf{E}}_1(\mathbf{x},\omega) - \frac{\mu_1(\omega)}{\mu_2(\omega)}\nabla\times\hat{\mathbf{E}}_2(\mathbf{x},\omega)\right)\Big|_{\mathbf{e}_\kappa}^{\mathbf{x}=\tilde{\mathbf{x}}} = 0.$$

Projecting on the $\mathbf{e}_{\boldsymbol{\kappa}}$ unit vector and using the fact that $\hat{\mathbf{E}}_j(\mathbf{x},\omega)\Big|_{\mathbf{e}_3} = 0$ for TE mode, we obtain

$$\frac{\partial}{\partial x}\left(\hat{\mathbf{E}}_1(\mathbf{x},\omega) - \frac{\mu_1(\omega)}{\mu_2(\omega)}\hat{\mathbf{E}}_2(\mathbf{x},\omega)\right)\Big|_{\mathbf{e}_3\times\mathbf{e}_\kappa}^{\mathbf{x}=\tilde{\mathbf{x}}}. \tag{39}$$

After Fourier transform (18), equations (37) and (39) are expressed as follows:

$$\left(\hat{\mathbf{E}}_{1,\kappa}(\tilde{x},\omega) - \hat{\mathbf{E}}_{2,\kappa}(\tilde{x},\omega)\right)\Big|_{\mathbf{e}_3\times\mathbf{e}_\kappa} = 0,$$

$$\frac{\partial}{\partial x}\left(\hat{\mathbf{E}}_{1,\kappa}(x,\omega) - \frac{\mu_1(\omega)}{\mu_2(\omega)}\hat{\mathbf{E}}_{2,\kappa}(x,\omega)\right)\Big|_{\mathbf{e}_3\times\mathbf{e}_\kappa}^{x=\tilde{x}} = 0,$$

Recalling $E_j(x,\omega) = \hat{\mathbf{E}}_{\kappa,j}(x,\omega)\Big|_{\mathbf{e}_3\times\mathbf{e}_\kappa}$, we obtain:

$$E_1(\Delta_1,\omega) = E_2(\Delta_1,\omega), \tag{40}$$

$$\frac{\partial E_1}{\partial x}(\Delta_1,\omega) = \frac{\mu_1(\omega)}{\mu_2(\omega)}\frac{\partial E_2}{\partial x}(\Delta_1,\omega). \tag{41}$$

Now let us consider the surface located at the $x = \Delta_1 + \Delta_2$ coordinate between the considered vacuum layer ($j = 2$) and the next metamaterial layer (we denote it with the $j = 3$ index). The standard boundary conditions for this surface are presented by equations (26)–(29), where $j = 1$ should be replaced with $j = 3$, $x \to \Delta_1 + \Delta_2$, and the field functions are calculated as left-handed limits for $j = 2$ and right-handed limits for $j = 3$. Analogously to the way we expressed equations (35), (36), (40), and (41) for the surface at the $x = \Delta_1$ coordinate, we obtain the following relations for the surface at the $x = \Delta_1 + \Delta_2$ coordinate for the TM mode:

$$E_3(\Delta_1+\Delta_2,\omega) = E_2(\Delta_1+\Delta_2,\omega), \tag{42}$$

$$\frac{\partial E_3}{\partial x}(\Delta_1+\Delta_2,\omega) = \frac{\varepsilon_2(\omega)}{\varepsilon_3(\omega)}\frac{\zeta_3^2(\omega,\kappa)}{\zeta_2^2(\omega,\kappa)}\frac{\partial E_2}{\partial x}(\Delta_1+\Delta_2,\omega). \tag{43}$$

and for the TE mode:

$$E_3(\Delta_1+\Delta_2,\omega) = E_2(\Delta_1+\Delta_2,\omega), \tag{44}$$

$$\frac{\partial E_3}{\partial x}(\Delta_1+\Delta_2,\omega) = \frac{\mu_3(\omega)}{\mu_2(\omega)}\frac{\partial E_2}{\partial x}(\Delta_1+\Delta_2,\omega). \tag{45}$$

The considered system is periodic. Therefore, $\varepsilon_3(\omega) = \varepsilon_1(\omega)$, $\mu_3(\omega) = \mu_1(\omega)$, $\zeta_3(\omega,\kappa) = \zeta_1(\omega,\kappa)$, and we can use the Floquet-Bloch theorem [24, 25, 26]. This theorem states that if E is a field in a periodic medium with periodicity Δ, then it has to satisfy

$$E(x+\Delta) = e^{i\theta\,\Delta}E(x),$$

where θ is a yet undefined wave vector, called the Bloch wave vector. Application of the Floquet-Bloch theorem with $\Delta = \Delta_1 + \Delta_2$ leads to the following equations:

$$E_3(\Delta_1+\Delta_2,\omega) = E_1(0,\omega)e^{i\theta\,(\Delta_1+\Delta_2)},$$

$$\frac{\partial E_3}{\partial x}(\Delta_1+\Delta_2,\omega) = \frac{\partial E_1}{\partial x}(0,\omega)e^{i\theta\,(\Delta_1+\Delta_2)},$$

where functions with $j=3$ and $j=1$ indices denote left- and right-sided limits respectively. Thus, equations (42) and (43), which correspond to the TM mode, are expressed as follows:

$$E_1(0,\omega) = E_2(\Delta_1+\Delta_2,\omega)e^{-i\theta\,(\Delta_1+\Delta_2)}, \tag{46}$$

$$\frac{\partial E_1}{\partial x}(0,\omega) = \frac{\varepsilon_2(\omega)}{\varepsilon_1(\omega)}\frac{\zeta_1^2(\omega,\kappa)}{\zeta_2^2(\omega,\kappa)}\frac{\partial E_2}{\partial x}(\Delta_1+\Delta_2,\omega)e^{-i\theta\,(\Delta_1+\Delta_2)}. \tag{47}$$

Equations (44) and (45), which correspond to the TE mode, are obtained as follows:

$$E_1(0,\omega) = E_2(\Delta_1+\Delta_2,\omega)e^{-i\theta\,(\Delta_1+\Delta_2)}, \tag{48}$$

$$\frac{\partial E_1}{\partial x}(0,\omega) = \frac{\mu_1(\omega)}{\mu_2(\omega)}\frac{\partial E_2}{\partial x}(\Delta_1+\Delta_2,\omega)e^{-i\theta\,(\Delta_1+\Delta_2)}. \tag{49}$$

Thus, we have two sets of equations: (35), (36), (46), and (47) for the TM mode and (40), (41), (48), and (49) for the TE mode.

2.3. Solutions

Solutions of equation (25) are obtained through the fundamental solution system as follows:

$$E_1(x,\omega) = Ae^{i\zeta_1 x} + Be^{-i\zeta_1 x}, \tag{50}$$

$$E_2(x,\omega) = Ce^{i\zeta_2 x} + De^{-i\zeta_2 x}, \tag{51}$$

where A, B, C, and D are unknown coefficients, $\zeta_j = \zeta_j(\omega,\kappa)$ for $j=1,2$. Using the solutions (50) and (51), we obtain two algebraic systems of equations for the unknown coefficients A, B, C, and D. The first one is composed of equations (35), (36), (46), and (47). The second one composed of equations (40), (41), (48), and (49). To solve the first system, we the denote corresponding matrix of the system coefficients in the following manner:

$$K_1(\omega,\kappa) = \begin{pmatrix} e^{i\zeta_1\Delta_1} & e^{-i\zeta_1\Delta_1} & -e^{i\zeta_2\Delta_1} & -e^{-i\zeta_2\Delta_1} \\ e^{i\zeta_1\Delta_1} & -e^{-i\zeta_1\Delta_1} & -\frac{\varepsilon_2}{\varepsilon_1}\frac{\zeta_1}{\zeta_2}e^{i\zeta_2\Delta_1} & \frac{\varepsilon_2}{\varepsilon_1}\frac{\zeta_1}{\zeta_2}e^{-i\zeta_2\Delta_1} \\ 1 & 1 & -e^{i\zeta_2(\Delta_1+\Delta_2)}e^{-i\theta(\Delta_1+\Delta_2)} & -e^{-i\zeta_2(\Delta_1+\Delta_2)}e^{-i\theta(\Delta_1+\Delta_2)} \\ 1 & -1 & -\frac{\varepsilon_2}{\varepsilon_1}\frac{\zeta_1}{\zeta_2}e^{i\zeta_2(\Delta_1+\Delta_2)}e^{-i\theta(\Delta_1+\Delta_2)} & \frac{\varepsilon_2}{\varepsilon_1}\frac{\zeta_1}{\zeta_2}e^{-i\zeta_2(\Delta_1+\Delta_2)}e^{-i\theta(\Delta_1+\Delta_2)} \end{pmatrix},$$

where $\varepsilon_j = \varepsilon_j(\omega)$ and $\zeta_j = \zeta_j(\omega, \kappa)$ for $j = 1, 2$, and compare the $\det K_1(\omega, \kappa)$ determinant to zero. Then, we obtain the following relation:

$$\left(e^{-i\theta(\Delta_1+\Delta_2)}\right)^2 - \left[\frac{\sigma^+_{1,2}\sigma^+_{2,1}}{4}\left(1 + e^{i2\zeta_1\Delta_1}e^{i2\zeta_2\Delta_2}\right) + \frac{\sigma^-_{1,2}\sigma^-_{2,1}}{4}\left(e^{i2\zeta_1\Delta_1} + e^{i2\zeta_2\Delta_2}\right)\right] \times \\ \times e^{-i\zeta_1\Delta_1}e^{-i\zeta_2\Delta_2}e^{-i\theta(\Delta_1+\Delta_2)} + 1 = 0, \tag{52}$$

where $\sigma^{\pm}_{k,l} = \frac{\varepsilon_k\zeta_l \pm \varepsilon_l\zeta_k}{\varepsilon_k\zeta_l}$ with $k = 1$ and $l = 2$, or $k = 2$ and $l = 1$, $\varepsilon_j = \varepsilon_j(\omega)$ and $\zeta_j = \zeta_j(\omega, \kappa)$ for $j = 1, 2$.

To solve the second system, we also denote the corresponding matrix of the system coefficients in the following manner:

$$K_2(\omega, \kappa) = \begin{pmatrix} e^{i\zeta_1\Delta_1} & e^{-i\zeta_1\Delta_1} & -e^{i\zeta_2\Delta_1} & -e^{-i\zeta_2\Delta_1} \\ e^{i\zeta_1\Delta_1} & -e^{-i\zeta_1\Delta_1} & -\frac{\mu_1}{\mu_2}\frac{\zeta_2}{\zeta_1}e^{i\zeta_2\Delta_1} & \frac{\mu_1}{\mu_2}\frac{\zeta_2}{\zeta_1}e^{-i\zeta_2\Delta_1} \\ 1 & 1 & -e^{i\zeta_2(\Delta_1+\Delta_2)}e^{-i\theta(\Delta_1+\Delta_2)} & -e^{-i\zeta_2(\Delta_1+\Delta_2)}e^{-i\theta(\Delta_1+\Delta_2)} \\ 1 & -1 & -\frac{\mu_1}{\mu_2}\frac{\zeta_2}{\zeta_1}e^{i\zeta_2(\Delta_1+\Delta_2)}e^{-i\theta(\Delta_1+\Delta_2)} & \frac{\mu_1}{\mu_2}\frac{\zeta_2}{\zeta_1}e^{-i\zeta_2(\Delta_1+\Delta_2)}e^{-i\theta(\Delta_1+\Delta_2)} \end{pmatrix},$$

where $\mu_j = \mu_j(\omega)$ and $\zeta_j = \zeta_j(\omega, \kappa)$ for $j = 1, 2$, and compare the $\det K_2(\omega, \kappa)$ determinant to zero. Then, recalling $\varepsilon_1(\omega) = \mu_1(\omega)$ and $\varepsilon_2(\omega) = \mu_2(\omega)$, we obtain the relation, which is identical to equation (52). This means that we have the identical PBG structure for the TE and TM modes.

3. Numerical results and discussion

3.1. PBG structure

We use a numerical approach to study the PBG structure of the considered 1DPC. We search for ω and κ values where the equality (52) holds true with any θ value that belongs to the $(0,\ 2\pi/\Delta)$ interval. In the first part of our numerical investigation, we fix the constants $\Delta_1 = \Delta_2 = 10 \quad \eta\mathrm{m}^{-1}$, $\omega_0 = 30$ THz, $\Omega = 90$ THz, and intervals for ω values from 0-240 THz (then the ω/cnormalized frequency has values from 0-0.8$\times 10^6$ m^{-1}) and for κ values from 0-0.8 ηm^{-1} (i.e., to 0.8$\times 10^6$ m^{-1}).

In accordance with the investigation [23], the $\zeta_j(\omega, \kappa)$ value in equation (52) can be real or distinctly imaginary. If $\zeta_j(\omega, \kappa)$ is real then in the j-th layer the radiative regime is observed else the evanescent regime. Thus, we have four different areas for (ω, κ) values (Fig. 1).

The PBG structure is presented in Fig. 2 and Fig. 3. In areas with numbers 1 and 3 for $\omega < \omega_2$, where $\omega_2 = 94.86$ THz (Fig. 1) and the radiative regime for the metamaterial is observed (see Fig. 2 and (a)-(d) in Fig. 3), there are a set of permitted bands, which ones comprise one continuous band for $\kappa = 0$ and become narrower and converge to a linear bands with ncreased κ values. Also, the permitted become narrower and more thickly located when ω approaches ω_0. For the NIM and first PIM intervals we observe different PBG structures. Namely, with increased κ values, the linear permitted bands are bent in the left side for the NIM interval and in the right side for the PIM interval (see (a)-(d) in Fig. 3 and Fig. 2, respectively).

In both areas marked number 4 (Fig. 1), there are no permitted bands, except the one band with ω values beside the $\omega_1 = 70.35$ THz NIM frequency (see (d) in Fig. 3). With increased κ values, the permitted band becomes narrower and converges to the ω_1 value, i.e., for the NIM frequency, there is no reflection effect for all κ values. This fact was discussed for the finite periodic system, similar to that considered in [27], for the NIM single layer in

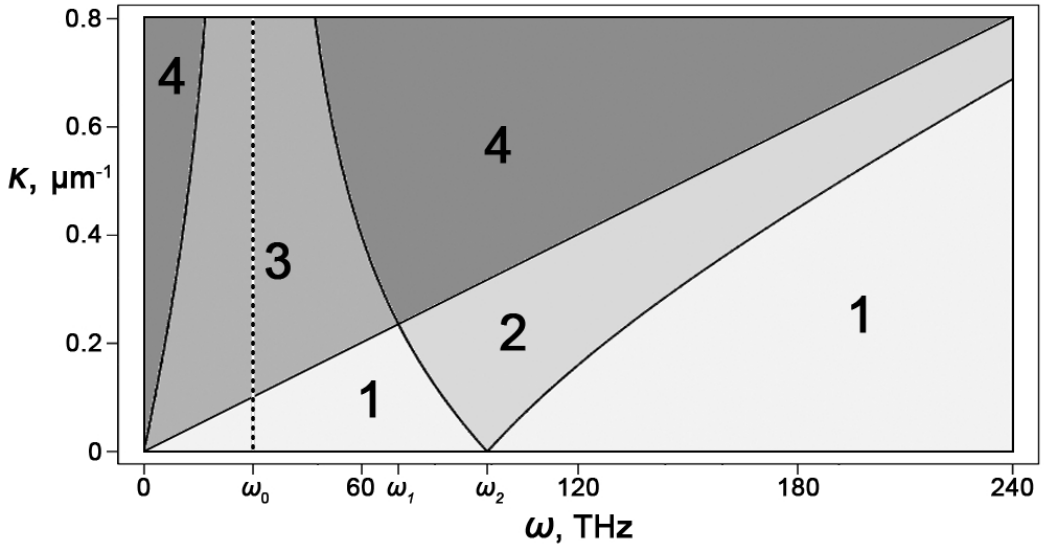

FIG. 1. Areas of the radiative and evanescent regimes. Black unbroken lines divide the (ω, κ) space into areas. Areas with number 1 correspond to cases when the radiative regime is observed in the metamaterial and vacuum simultaneously. Area number 2 corresponds to the case when the evanescent regime is observed in the metamaterial and the radiative regime is observed in the vacuum. Area number 3 corresponds to the case when the radiative regime is observed in the metamaterial and the evanescent regime is observed in the vacuum. Areas with number 4 correspond to the cases when the evanescent regime is observed in the metamaterial and vacuum simultaneously. The vertical dotted line corresponds to the $\omega_0 = 30$ THz frequency. $\omega_1 = 70.35$ THz is the NIM frequency, i.e., $\varepsilon_1(\omega_1) = \mu_1(\omega_1) = -1$. For the $\omega_2 = 94.86$ THz frequency $\varepsilon_1(\omega_2) = \mu_1(\omega_2) = 0$

vacuum [28], and for the system, composed of two half spaces filled with NIM and vacuum [23].

In the area with the number 1 for $\omega > \omega_2$ (see Fig. 1 and (e) in Fig. 3), there are no forbidden bands, except the narrow band that follows the boundary divided areas with numbers 1 and 2. The PBG structure of the second PIM interval is different from the ones for the first PIM and the NIM intervals (see (e) and (a)-(d) in Fig. 3 and Fig. 2, respectively).

The area with the number 2 (Fig. 1) has only two permitted bands. The first one arises at ω_2 and follows the boundary divided areas with numbers 2 and 4 (see (e) in Fig. 3). The second permitted band is located near the ω_1 NIM frequency (see (d) in Fig. 3).

3.2. Modification of Lorentz contribution parameters

Now, we examine the band gap structure of the considered system for the different values of ω_0 and Ω. We consider the following cases:

A) $\omega_0 = 30$ THz and $\Omega = 30$ THz
B) $\omega_0 = 30$ THz and $\Omega = 60$ THz
C) $\omega_0 = 60$ THz and $\Omega = 30$ THz
D) $\omega_0 = 30$ THz and $\Omega = 75$ THz
E) $\omega_0 = 75$ THz and $\Omega = 30$ THz

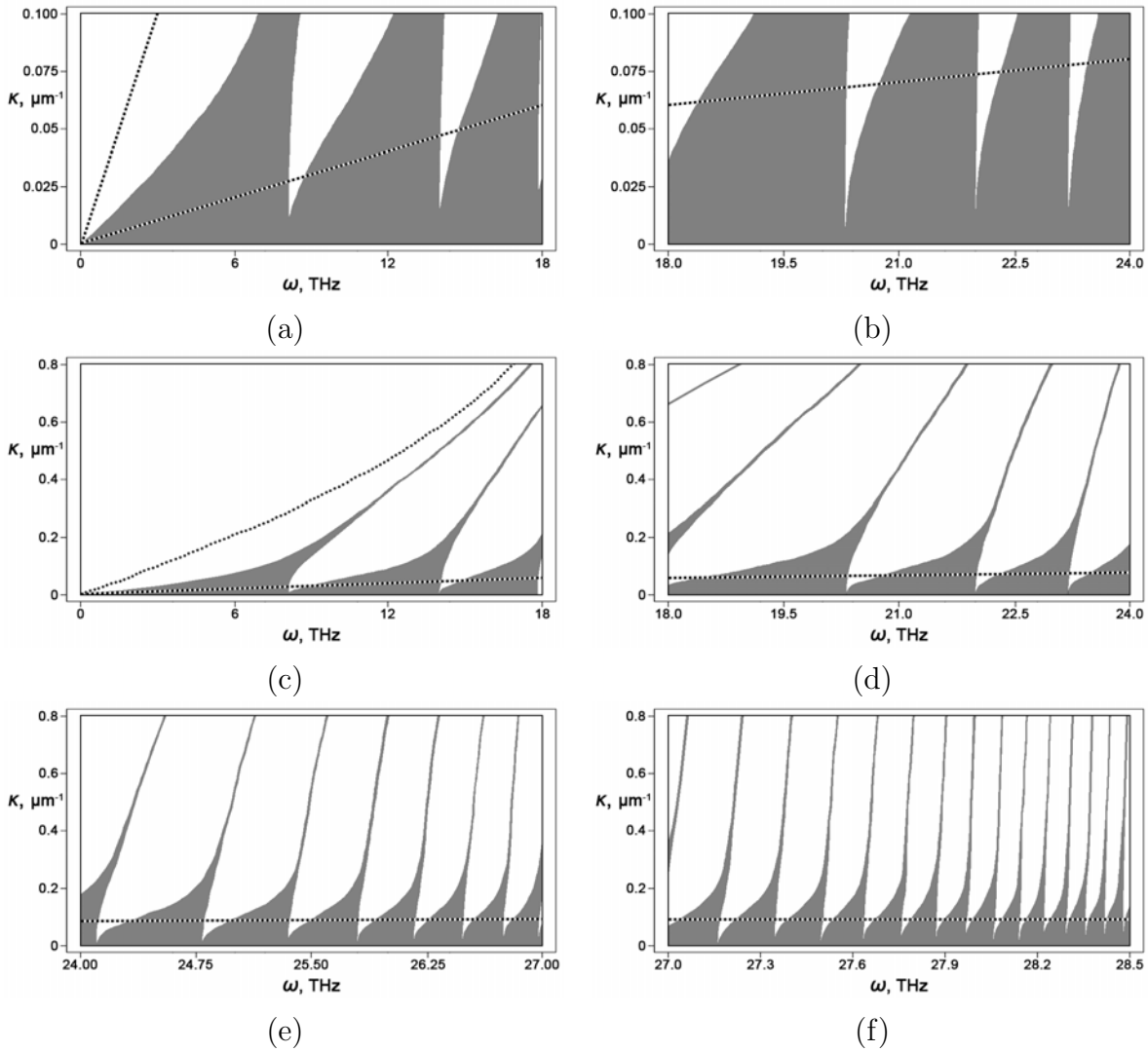

FIG. 2. Dependences of PBG structure on the ω frequency and κ values for TE and TM mode simultaneously. Permitted bands are gray, forbidden bands are white. Dotted lines divide the (ω, κ) space into four different areas (see Fig. 1). The metamaterial behaves like PIM

The D and E cases are as additional ones. We fix the constants $\Delta_1 = \Delta_2 = 10 \quad \eta\mathrm{m}^{-1}$ and the intervals for ω values from 0-90 THz (then the ω/cnormalized frequency has values from 0-0.3$\times 10^6$ m^{-1}) and for κ values from 0-0.3 ηm^{-1} (i.e., to 0.3$\times 10^6$ m^{-1}). As we noted above, (ω, κ) values comprise four different areas (Fig. 4).

Let us consider the doubling of the Ω constant, i.e., the A and B cases. It brings to a broadening of the radiative regime area for the metamaterial layers. The ω_2 value increases from 42.42 to 67.08 THz and the NIM interval of the ω frequency becomes wider but the first PIM interval of the ω frequency remains unchanged (see (a) and (b) in Fig. 4). The permitted bands become narrower and more thickly located (see (a) and (b) in Fig. 5). The permitted band, which contains the NIM frequency, redoubles along the ω axis (see (d) and (e) in Fig. 5). For the A, B and D cases we consider the ω frequency intervals of the same 24 THz length with the beginning in ω_2 (see (a), (b), and (c) in Fig. 6). With increasing of the Ω constant, the permitted band in the 2 area (Fig. 4) becomes narrower and the adjacent

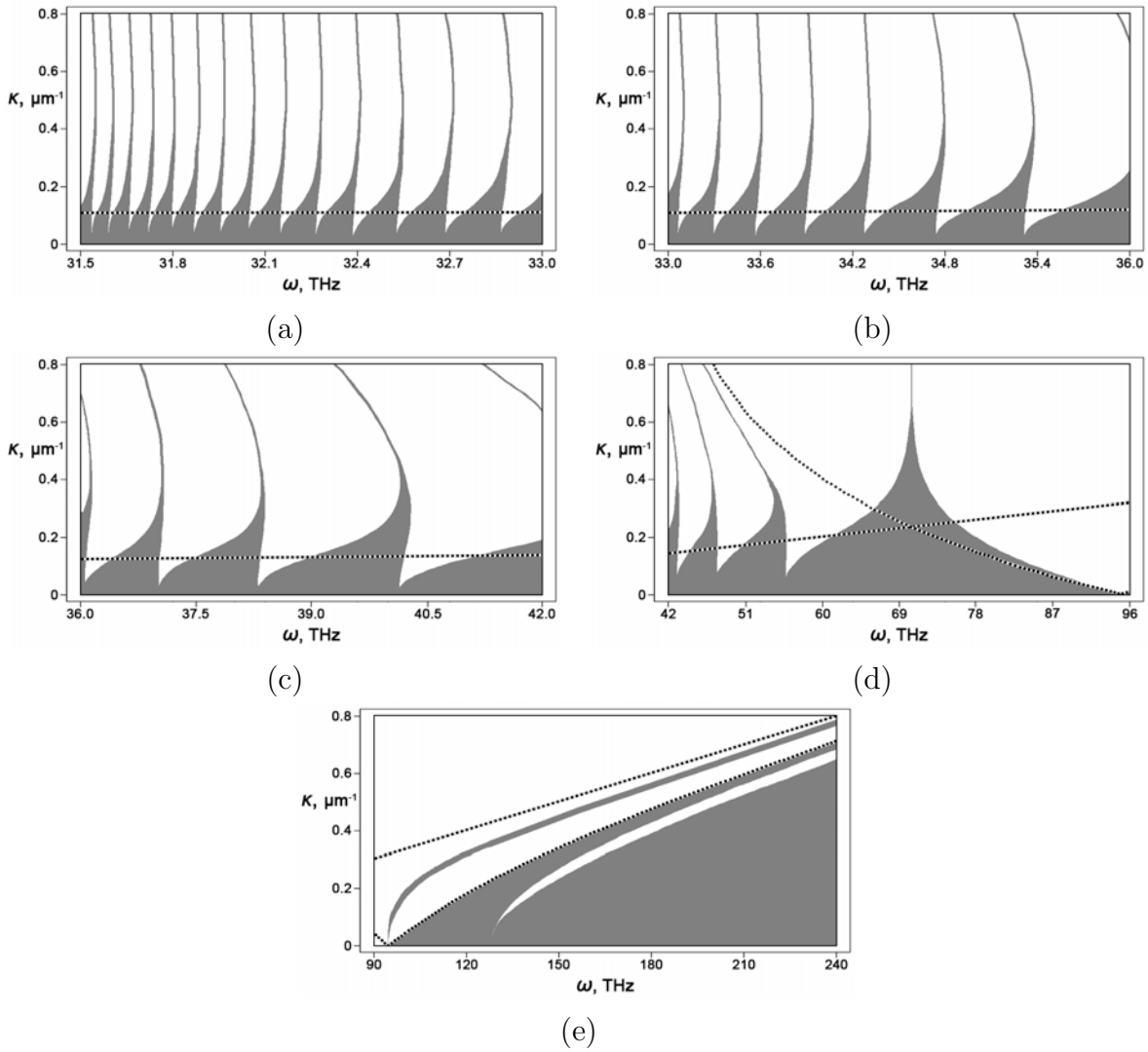

FIG. 3. Dependences of PBG structure on the ω frequency and κ values for TE and TM mode simultaneously. Permitted bands are grey, forbidden bands are white. Dotted lines divide the (ω, κ) space into four different areas (see Fig. 1). The metamaterial behaves like NIM (a)-(d), and PIM (e)

permitted band grows to the whole second part of the 1 area (Fig. 4). The forbidden band between these permitted bands becomes wider along the κ axis.

Now, we consider the doubling of the ω_0 constant, i.e., the A and C cases. As for the A and B cases, it elicits a broadening of radiative regime area for the metamaterial layers. The ω_2 value also increases from 42.42 to 67.08 THz, but the NIM interval of the ω frequency becomes narrower and the PIM interval of the ω frequency becomes wider (see (a) and (c) in Fig. 4). With increased κ values, the permitted bands become narrower but not as quickly as in the A case. The permitted band, which contains the NIM frequency, have lost about half of its width along the ω axis (see (d) and (f) in Fig. 5). Analogously, with the A, B and D cases, for the A, C and E cases we consider the ω frequency intervals of the same 24 THz length with the beginning in ω_2 (see (a), (d), and (e) in Fig. 6). With increasing of the ω_0 constant, the permitted band in the 2 area (Fig. 4) becomes narrower. It seems that

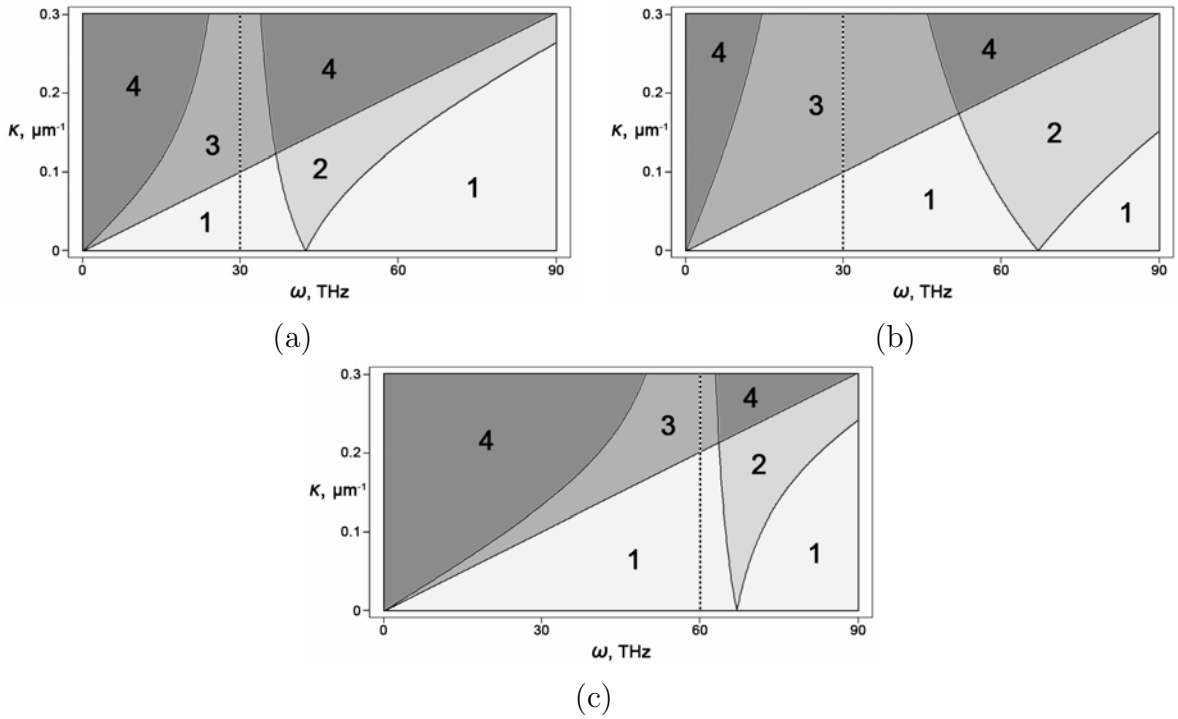

FIG. 4. Areas of the radiative and evanescent regimes. Black unbroken lines divide the (ω, κ) space into areas. Areas with number 1 correspond to the cases when the radiative regime is observed in the metamaterial and vacuum simultaneously. Area number 2 corresponds to the case when the evanescent regime is observed in the metamaterial and the radiative regime is observed in the vacuum. Area number 3 corresponds to the case when the radiative regime is observed in the metamaterial and the evanescent regime is observed in the vacuum. Areas with number 4 correspond to the cases when the evanescent regime is observed in the metamaterial and vacuum simultaneously. The vertical dotted line corresponds to the ω_0 frequency. The A, B, and C cases are presented in (a), (b), and (c), respectively

the forbidden band located between that permitted and the next band remains unchanged in width along the κ axis.

3.3. Modification of layer's width

The third our numerical investigation consists in changing of the Δ_1 and Δ_2 parameters. We fix $\omega_0 = 30$ THz, $\Omega = 90$ THz and use the four following combinations:

a) $\Delta_1 = \Delta_2 = 10 \quad \eta$m (see (a) in Fig. 7-10)

b) $\Delta_1 = 20 \quad \eta$m and $\Delta_2 = 10 \quad \eta$m (see (b) in Fig. 7-10)

c) $\Delta_1 = 10 \quad \eta$m and $\Delta_2 = 20 \quad \eta$m (see (c) in Fig. 7-10)

d) $\Delta_1 = 10 \quad \eta$m and $\Delta_2 = 100 \quad \eta$m (see (d) in Fig. 7-10 and (e) in Fig. 8)

With the each combination, we obtain the PBG structure of the considered system for different ω frequencies:

1) from 0 till 18 THz (Fig. 7)
2) from 36 till 42 THz (Fig. 8)
3) from 42 till 96 THz (Fig. 9)
4) from 90 till 120 THz (Fig. 10)

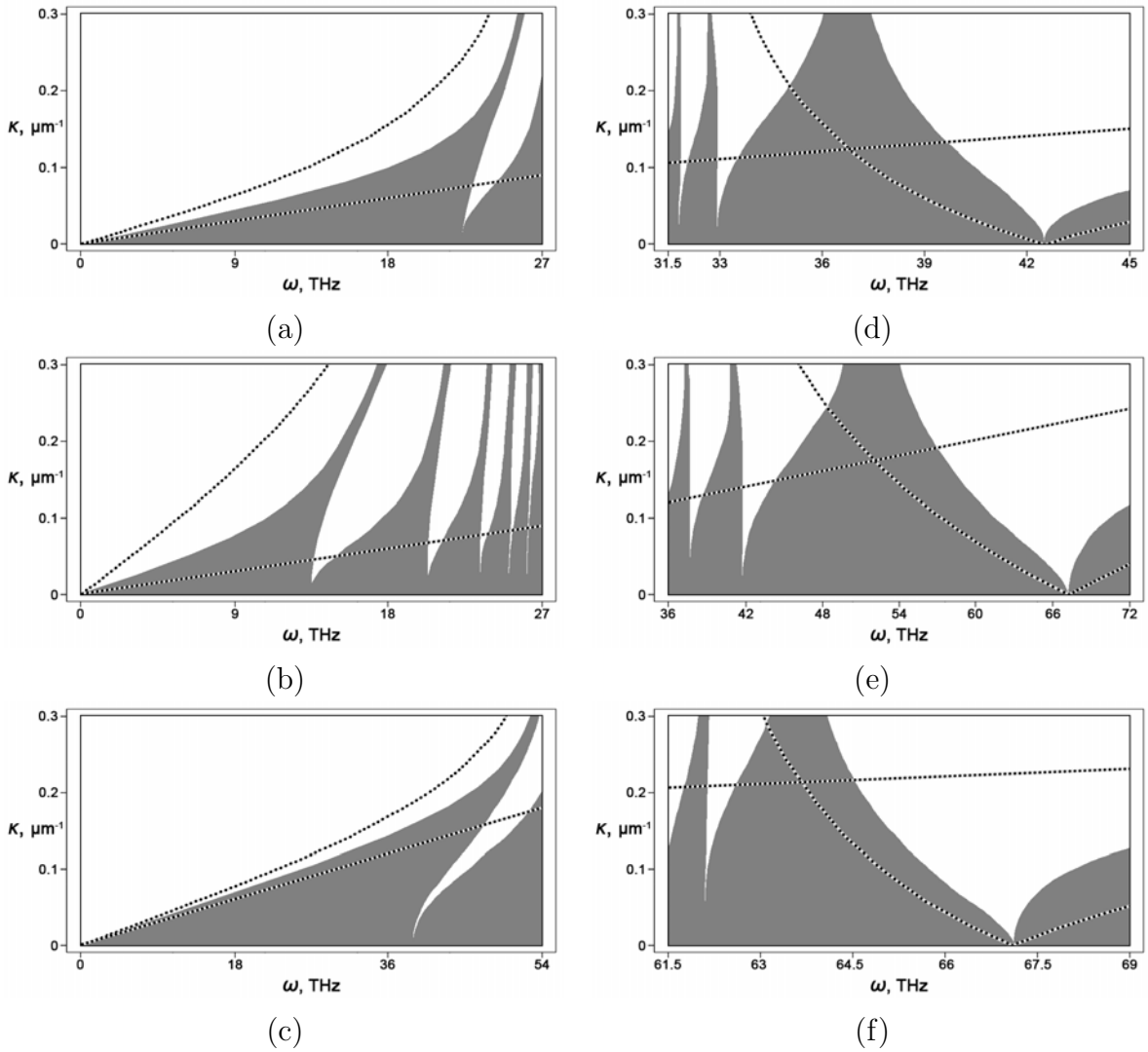

FIG. 5. Dependences of PBG structure on the ω frequency and κ values for TE and TM mode simultaneously. Permitted bands are grey, forbidden bands are white. Dot lines divide the (ω, κ) space on four different areas (see Fig. 4). The A case is presented in (a) and (d). The B case is presented in (b) and (e). The C case is presented in (c) and (f)

We obtain that doubling of the Δ_1 parameter (the a and b combinations) results in the approximately two-fold narrowing of the permitted and forbidden bands simultaneously (see (a) and (b) in Fig. 7-10). The permitted band, which contains the NIM frequency, is split into two bands (see and (b) in Fig. 9). There is no more absence of reflection for the NIM frequency, which is observed with the a combination (see (a) in Fig. 9).

Increasing of the Δ_2 parameter (a, c, and d combinations) results in a faster narrowing of the permitted bands with increased κ values (see (c) and (d) in Fig. 7-10), than is observed for the a combination (see (a) in Fig. 7-10). It seems that the permitted bands for small κ values become narrower and shift to the zero ω value. Also, for the d combination we observe conglutination of adjacent permitted bands (see (d) in Fig. 7 and (d) and (e) in Fig. 8). The right 1 area and the 2 area (Fig. 1) are filled with narrow linear permitted bands, which ones are bent approximately parallel to the bound between areas 1 and 2 (see (d) in Fig. 10).

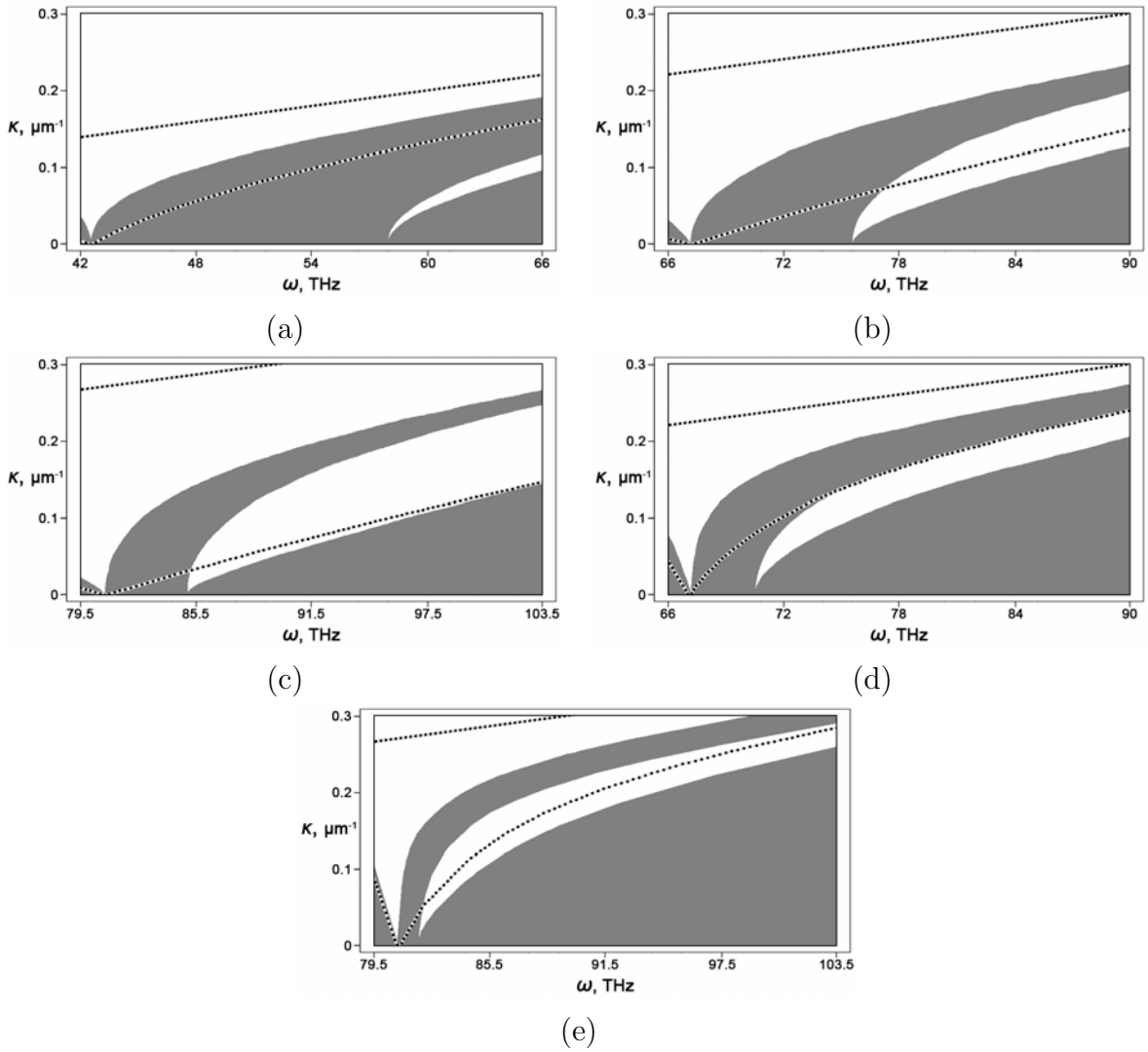

FIG. 6. Dependences of PBG structure on the ω frequency and κ values for TE and TM mode simultaneously. Permitted bands are gray, forbidden bands are white. Dotted lines divide the (ω, κ) space into four different areas (see Fig. 4). The A, B, C, D, and E cases are presented in (a), (b), (c), (d), and (e), respectively

The permitted band, which contains the NIM frequency, is split into two bands (see (c) and (d) in Fig. 9). As with the b combination, there is no more absence of reflection for the NIM frequency, which is observed with the a combination (see (a) in Fig. 9).

4. Conclusions

In this paper, we solved the problem of obtaining the PBG structure for a system composed of an infinite number of alternating parallel layers filled with a metamaterial and vacuum, i.e., for the 1DPC. We assumed the Fourier transformed permittivity and permeability stood equal and were expressed through a singly dispersive Lorentz term (16). This produced identical PBG structures for TE and TM modes. We considered combinations for the radiative and evanescent regimes in metamaterial and vacuum layers.

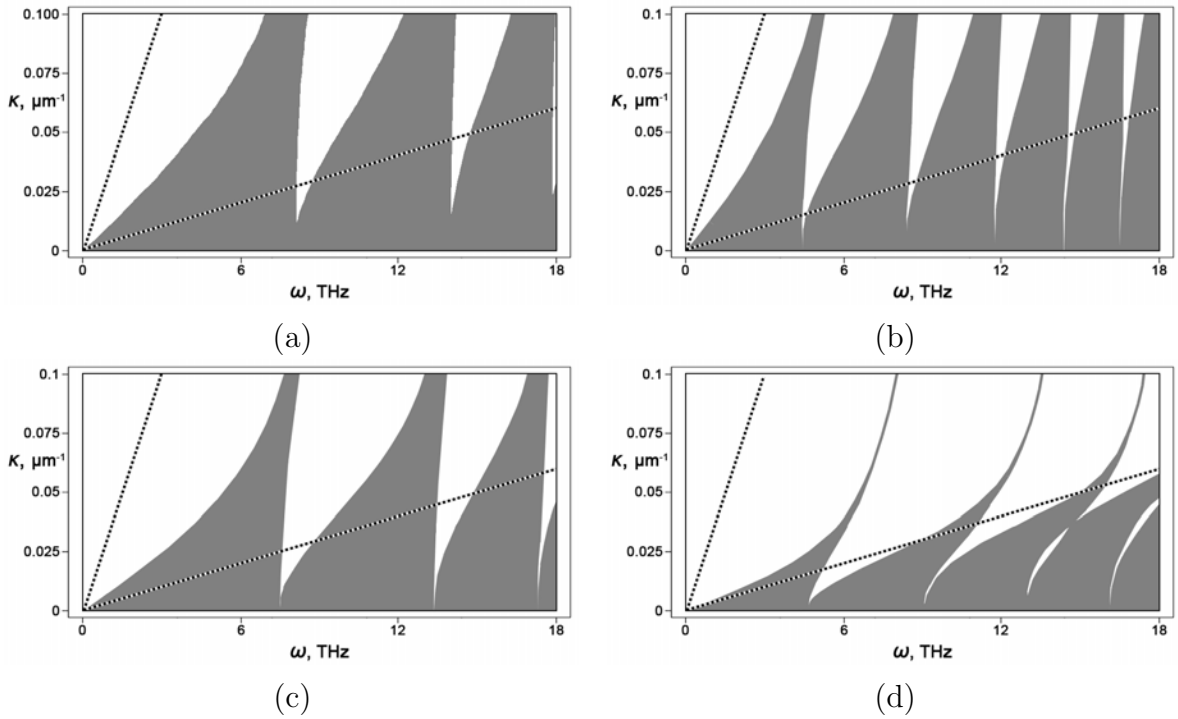

FIG. 7. Dependences of PBG structure on the ω frequency and κ values for TE and TM mode simultaneously. Permitted bands are gray, forbidden bands are white. Dotted lines divide the (ω, κ) space into four different areas (Fig. 1). The *a*, *b*, *c*, and *d* combinations are presented in (a), (b), (c), and (d), respectively

We obtained that for the radiative regime in metamaterial layers and both regimes in vacuum layers, there is a set of forbidden and permitted bands, ones which become narrower with the tending of the ω frequency to approach the ω_0 constant of the single Lorentz term expression (16). For the ω frequency intervals, where the metamaterial behaves like the NIM or PIM, we observe the different PBG structures. For the NIM frequency we observe the no reflection effect for any directions. This fact was discussed earlier for finite layered systems [23, 27, 28].

With an increase in the Ω parameter, we observed the increasing of the ω frequency interval, where the metamaterial behaves like NIM. The PBG structure became wider. With an increase in the ω_0 parameter, we observed a widening of the ω frequency interval, where the metamaterial behaves like a PIM, but for decreasing values, the metamaterial behaves like a NIM. The PBG structure became more extended along the κ axis.

With increased Δ_1 metamaterial layer width, the PBG structure became wider. With increased Δ_2 vacuum layer width, the permitted bands were accumulated in the (ω, κ) area, where the radiative regime for the metamaterial and vacuum is observed simultaneously. For other (ω, κ) areas, the permitted bands converged to the lines. In both cases (grow of Δ_1 or Δ_2) the permitted band contained the NIM frequency was split into two bands, i.e., there is no more absence of reflection for the NIM frequency, which was observed earlier. This fact disagrees with results for finite layered systems [23, 27, 28] and thus, is cause for increased interest.

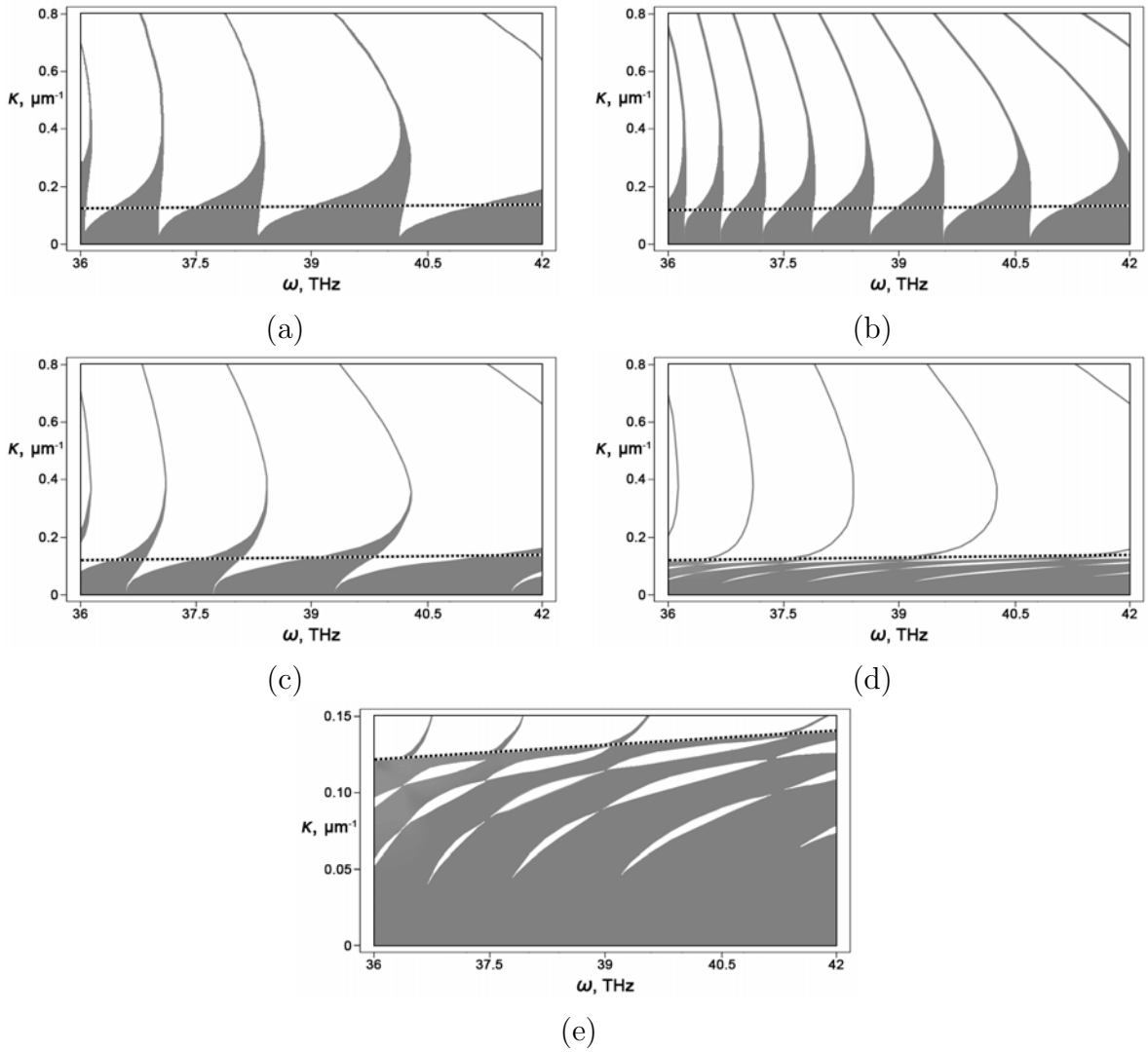

FIG. 8. Dependences of PBG structure on the ω frequency and κ values for TE and TM mode simultaneously. Permitted bands are gray, forbidden bands are white. Dotted lines divide the (ω, κ) space into four different areas (Fig. 1). The a, b, c, and d combinations are presented in (a), (b), (c), and (d), respectively

Acknowledgments

The work was partially financially supported by the Government of the Russian Federation (Grant 074-U01), by State contract of the Russian Ministry of Education and Science and grants of the President of Russia (state contract 14.124.13.2045-MK and grant MK-1493.2013.1).

References

[1] P. Vukusic, J.R. Sambles. Photonic structures in biology. *Nature*, **424**, P. 852–855 (2003).
[2] E. Yablonovitch. Inhibited Spontaneous Emission in Solid-State Physics and Electronics. *Phys. Rev. Lett.*, **58**, P. 2059–2062 (1987).
[3] S. John. Strong localization of photons in certain disordered dielectric superlattices. *Phys. Rev. Lett.* **58**, P. 2486–2489 (1987).

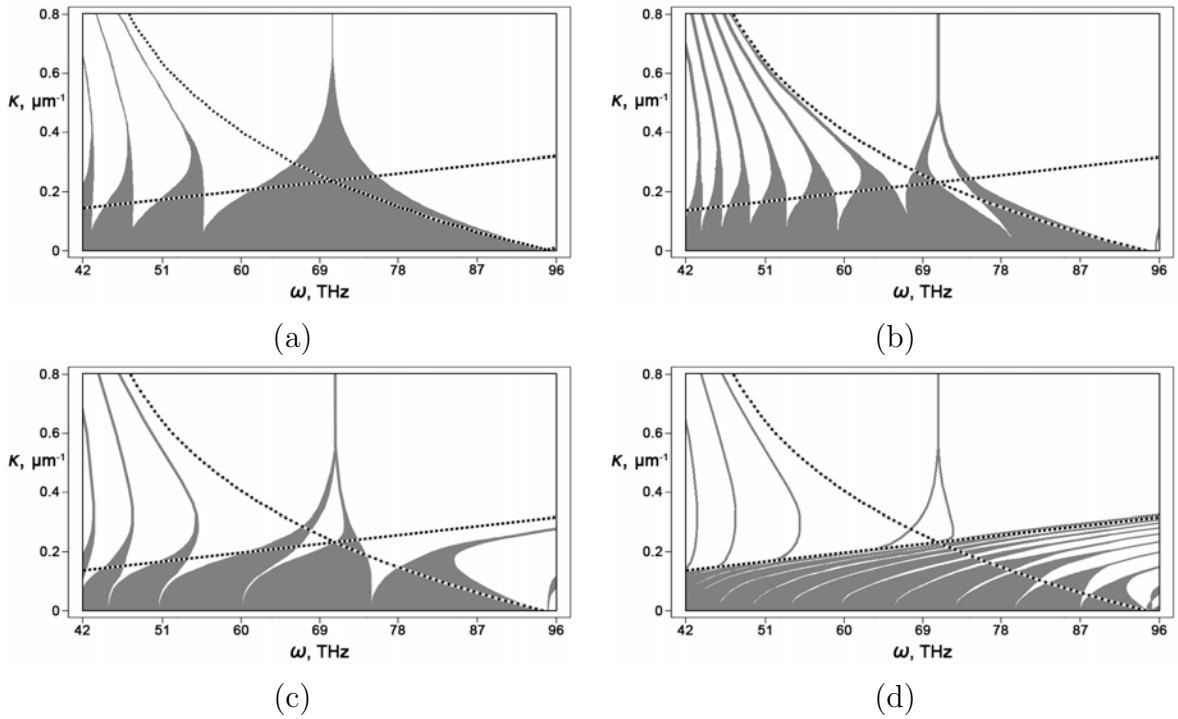

FIG. 9. Dependences of PBG structure on the ω frequency and κ values for TE and TM mode simultaneously. Permitted bands are gray, forbidden bands are white. Dotted lines divide the (ω, κ) space into four different areas (Fig. 1). The a, b, c, and d combinations are presented in (a), (b), (c), and (d), respectively

[4] J.D. Joannopoulos, S.G. Johnson, J.N. Winn, R.D. Meade. *Photonic Crystals: Molding the Flow of Light*. Princeton University Press, Princeton, second edition, 286 p. (2008).
[5] K. Sakuda. *Optical Properties of Photonic Crystals*. Springer-Verlag, Berlin, second edition, 253 p. (2005).
[6] Y. Fink, J.N. Winn, S. Fan, J. Michel, C. Chen, J.D. Joannopoulos, E.L. Thomas. A dielectric omnidirectional reflector. *Science*, **282**, P. 1679–1682 (1998).
[7] J.M. Dudley, J.R. Taylor. Ten years of nonlinear optics in photonic crystal fibre. *Nat. Phot.*, **3**, P. 85–90 (2009).
[8] J. Rosenberg, R.V. Shenoi, S. Krishna, O. Painter. Design of plasmonic photonic crystal resonant cavities for polarization sensitive infrared photodetectors. *Opt. Exp.*, **18**, P. 3672–3686 (2010).
[9] A.M.R. Pinto, M. Lopez-Amo. Photonic Crystal Fibers for Sensing Applications. *Journal of Sensors*, **2012**, P. 598178-21 (2012).
[10] A.C. Liapis, Z. Shi, R.W. Boyd. Optimizing photonic crystal waveguides for on-chip spectroscopic applications. *Opt. Exp.*, **21**, P. 10160–10165 (2013).
[11] H. Altug. *PhD Dissertation*, Stanford University, Stanford, 120 p. (2006).
[12] V.G. Veselago. The electrodynamics of substances with simultaneously negative values of ε and μ. *Sov. Phys. Usp.*, **10**, P. 509–514 (1968).
[13] J.B. Pendry. Negative Refraction Makes a Perfect Lens. *Phys. Rev. Lett.*, **85**, P. 3966–3969 (2000).
[14] L. Wu, S. He, L. Shen. Band structure for a one-dimensional photonic crystal containing left handed materials. *Phys. Rev. B*, **67**, P. 235103–10 (2003).
[15] H. Jiang, H. Chen, H. Li, Y. Zhang, J. Zi, S. Zhu. Properties of one dimensional photonic crystals containing single-negative materials. *Phys. Rev. E*, **69**, P. 066607-10 (2004).
[16] D. Bria, B. Djafari-Rouhani, A. Akjouj, L. Dobrzynski, J.P. Vigneron, E.H. El Boudouti, A. Nougaoui. Band structure and omni directional photonic band gaps in lamellar structure with left handed materials. *Phys. Rev. E*, **69**, P. 066613-12 (2005).

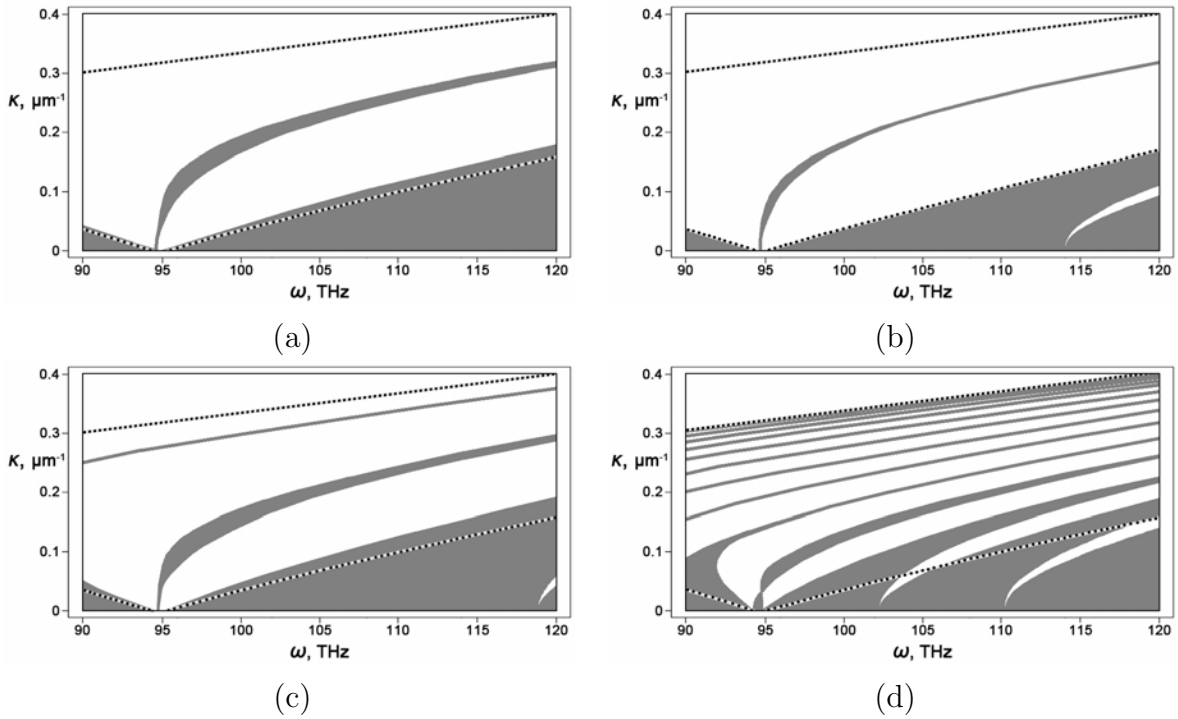

FIG. 10. Dependences of PBG structure on the ω frequency and κ values for TE and TM mode simultaneously. Permitted bands are gray, forbidden bands are white. Dotted lines divide the (ω, κ) space into four different areas (Fig. 1). The a, b, c, and d combinations are presented in (a), (b), (c), and (d), respectively

[17] S. K. Singh, J.P. Pandey, K.B. Thapa, S.P. Ojha. Structural parameters in the formation of omnidirectional high reflectors. *PIER*, **70**, P. 53–78 (2007).

[18] C. Nicolae, R.M. Osgood, Jr.S. Zhang, S.R.T. Brueck. Zero-n bandgap in photonic crystal superlattices. *J. Opt. Soc. Am. B*, **23**, P. 506–512 (2006).

[19] H. Jiang, H. Chen, S. Zhu. Localized gap-edge fields of one-dimensional photonic crystals with an ε-negative and a μ-negative defect. *Phys. Rev. E*, **79**, P. 0466601-8 (2006).

[20] G.N. Pandey, K.B. Thapa, S.K. Srivastava, S.P. Ojha. Band structures and abnormal behavior of one dimensional photonic crystal containing negative index materials. *PIER M*, **2**, P. 15–36 (2008).

[21] X. Feng, H. Li. Enlargement of the omnidirectional reflectance gap in one-dimensional photonic crystal heterostructure containing double negative index material. *Eur. Phys. J. D*, **67**, P. 40157-7 (2013).

[22] A. Tip. Linear dispersive dielectrics as limits of Drude-Lorentz systems. *Phys. Rev. E*, **69**, P. 016610-5 (2004).

[23] B. Gralak, A. Tip. Macroscopic Maxwell's equations and negative index materials. *J. Math. Phys.*, **51**, P. 052902-28 (2010).

[24] G. Floquet. Sur les équations différentielles linéaires á coefficients périodiques. *Ann. Ecole Norm. Sup.*, **12**, P. 47–88 (1883).

[25] F. Bloch. Über die Quantenmechanik der Elektronen in Kristallgittern. *Z. Phys.*, **52**, P. 555–600 (1929).

[26] L. Novotny, B. Hecht. *Principles of Nano-Optics*. Cambridge University Press, New York, 539 p. (2006).

[27] K. Pravdin, I. Popov. Point source in the layered medium with metamaterials: method of recurrent relations. *Sc. Tech. J. Inf. Tech. Mech. Opt.*, **91**, P. 11–17 (2014).

[28] K.V. Pravdin, I.Yu. Popov. Model of the interaction of point source electromagnetic fields with metamaterials. *Nanosystems: Phys. Chem. Math.*, **4**, P. 570–576 (2013).

NANOSYSTEMS: PHYSICS, CHEMISTRY, MATHEMATICS, 2014, 5 (5), P. 644–649

FEW CYCLE PULSES IN THE BRAGG MEDIUM CONTAINING CARBON NANOTUBES

M. B. Belonenko[1,2], Ju. V. Nevzorova[1], E. N. Galkina[2]

[1]Volgograd State University, Volgograd, Russia
[2]Volgograd Institute of Business, Volgograd, Russia

mbelonenko@yandex.ru, nevzorkina@yandex.ru

PACS 72.20.Ht, 42.65.Re

The effective equation for few cycle optical pulse dynamics was obtained by virtue of the Boltzmann collision-less equation solution for conduction band electrons of semiconductor carbon nanotubes in the case when medium with carbon nanotubes has spatially-modulated refractive index. The pulse retardation effect, in comparison to an unmodulated medium, was derived. The evaluation was carried out depending on task options.

Keywords: cycle optical pulse, carbon nanotubes, Bragg medium, Boltzmann equation.

Received: 24 September 2014
Revised: 29 September 2014

1. Introduction

One of the basic problems of modern optics is medium creation, thanks to which, we can process and control a signal. Among such media, the Bragg media (in which the refractive index is periodically spatially-modulated) is of great interest [1–3]. As much as the medium has a periodically variable refractive index, the light pulse propagates more slowly in it, than in a medium with any fixed refractive index. This makes it possible to construct optical delay lines based on such media, which are useful for femtosecond spectroscopy for example. Such behavior can be understood in essence, providing that the light pulse is reflected and then interferes at the interface of media with different refractive indices. Additional introduction of nonlinearity into that sort of media leads to qualitatively new effects [4–6]. Particularly, Bragg solitons can be formed in such systems. They are revealed as a specified counter assembly of waves, banded in such a manner to move collectively with reduced speed. At the same time, rising interest in carbon nanotube (CNT) physics and particularly heightened attention to the study of CNT nonlinear properties leads to the conclusion that carbon nanotubes, with their characteristic nonlinear optical properties, can be non-conventional material for the nonlinear Bragg media formation [7–9]. Note that carbon nanotube usage perspectives in nonlinear optics in particular for optical bullet formation have been mentioned in some research accounts. All the above-mentioned facts gave impetus for this investigation.

2. Basic equations

Research of carbon nanotube electronic structure is done using the tight-binding approximation within the framework of p electron dynamics. Dispersion expression for zigzag carbon nanotubes $(m, 0)$ has the form [10]:

$$E(\mathbf{p}) = \pm\gamma\sqrt{1 + 4\cos(ap_z)\cos(\pi s/m) + 4\cos^2(\pi s/m)}, \quad (1)$$

where $\gamma = 2.7$ eV, $a = 3b/2\hbar$, $b = 0.152$ nm is a distance between carbon neighbor atoms and quasimomentum $\mathbf{p}$ is defined by (p_z, s), $s = 1, 2 \ldots m$.

We will describe the pulse electromagnetic field by virtue of Maxwell equations in Coulomb calibration [11] $\mathbf{E} = -1\partial\mathbf{A}/c\partial t$ while constructing the model of few-cycle optical pulse propagation in the Bragg media with allowance for nanotube system in the case of geometry presented in the Fig. 1. The vector-potential has the form $\mathbf{A} = (0, 0, A_z(x, t))$:

$$\frac{\partial^2 \mathbf{A}}{\partial x^2} - \frac{n^2(x)}{c^2}\frac{\partial^2 \mathbf{A}}{\partial t^2} + \frac{4\pi}{c}\mathbf{j} = 0, \tag{2}$$

where $n(x)$ defines a spatial variation of a refraction index, i.e. the Bragg grating, $\mathbf{j}$ is the current resulting from the electric pulse field exposure on conduction band electrons of carbon nanotubes. Here, we neglect the diffractive blooming of laser beam in directions orthogonal to the distribution axis. The electric field of a template is also disregarded. Within the framework of our model interband transitions are neglected, this fact limits the laser pulse frequency, which belongs to the near-infrared region. Note that since typical CNT dimension and distance between nanotubes much less than the size of typical spatial domain wherein a few cycle pulse is localized, we can use the continuous medium approximation and suppose a current apportioned by volume.

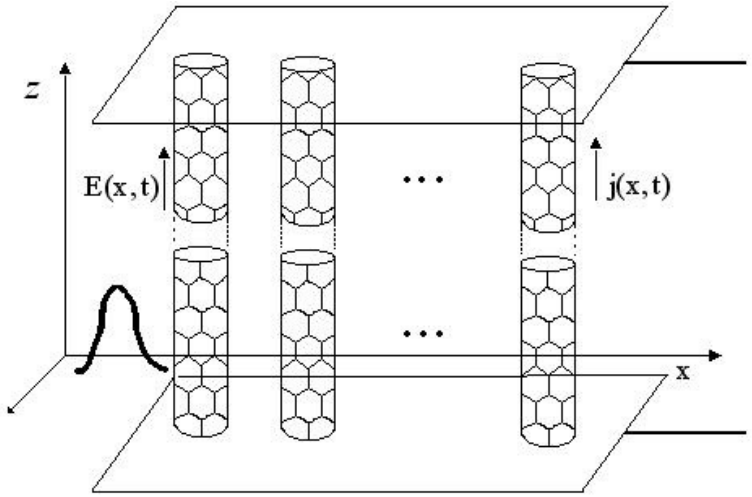

FIG. 1. Theproblem geometry. $j(x, t)$ is the current along the CNT axis, $E(x, t)$ is the pulse electric field

A typical length when the Bragg medium refractive index changes essentially turned out to be greater and dispenses additional constraints.

Since the typical relaxation time for CNT electrons can be estimated by $3 \cdot 10^{-13} A$ [12], then the electron ensemble at a time peculiar to few cycle optical pulse dynamics problems (around 10^{-14} c) can be described by collision less kinetic Boltzmann equation [13]:

$$\frac{\partial f}{\partial t} - \frac{q}{c}\frac{\partial A_z}{\partial t}\frac{\partial f}{\partial p} = 0, \tag{3}$$

where $f = f\,(p_s, s, t)$ is a distribution function, implicitly dependent on coordinate. Moreover, the distribution function f at the initial moment aligns with the equilibrium distribution Fermi function F_0 as follows:

$$F_0 = \frac{1}{1 + \exp\left\{E\left(p\right)/k_b T\right\}},$$

where T is a temperature, k_b is the Boltzmann constant.

For the current density $\mathbf{j} = (0, 0, j_z)$:

$$j_z = \frac{q}{\pi\hbar} \sum_s \int dp_z v_z f, \tag{4}$$

where $v_z = \partial E(\mathbf{p})/\partial p_z$ is the group velocity. By characteristics method [14] from the equation (3), we can obtain the following:

$$j_z = \frac{q}{\pi\hbar} \sum_s \int_{-q_0}^{q_0} dp_z v_z \left[p - \frac{q}{c} A_z\left(t\right)\right] F_0\left(\mathbf{p}\right). \tag{5}$$

Integration in (5) is over the first Brillouin zone and $q_0 = 2\pi\hbar/3b$. The group velocity can be expanded to Fourier series, the dispersion law taken into account:

$$v_z\left(s, x\right) = \sum_m a_{ms} \sin(mx),$$

where

$$a_{ms} = \frac{1}{\pi} \int_{-\pi}^{\pi} v_z(s, x) \sin(mx) dx$$

are expansion coefficients decreasing with increase in m.

Finally the effective equation can be represented in the form [15]:

$$\frac{\partial^2 A_z}{\partial x^2} - \frac{n^2(x)}{c^2} \frac{\partial^2 A_z}{\partial t^2} + \frac{q}{\pi\hbar} \sum_m c_m \sin\left(\frac{maq}{c} A_z\left(t\right)\right) = 0,$$

$$c_m = \sum_m a_{ms} b_{ms}, \quad b_{ms} = \int_{-q_0}^{q_0} dp_z \cos\left(map_z\right) F_0\left(\mathbf{p}\right). \tag{6}$$

Since the coefficients c_m decrease with increase in m, then in the sum (6) for estimation it is possible to confine to the first two summands and obtain the double equations sin-Gordon [16]. Study of this equation gives us the fact that the character of single pulse break-up depends heavily on its velocity. With an increase in velocity the pulses interact more elastically and minority of their energy goes to vibrational modes [17].

3. Results of numerical modelling

Equation (6) was solved numerically by applying the explicit finite-difference leap-frog scheme [18].The time and coordinate steps are chosen according to standard stability criterion, and then were reduced until the solution changed in the eighth significant character. The initial conditions for vector potential were chosen in the form:

$$A_{t=0} = A_0 \exp\left\{-\frac{x^2}{\gamma^2}\right\}, \quad \left.\frac{dA}{dt}\right|_{t=0} = \frac{2vx}{\gamma^2} A_0 \exp\left\{-\frac{\left(x - vt\right)^2}{\gamma^2}\right\}. \tag{7}$$

The refractive index of medium in process was simulated as

$$n\left(x\right) = n_0\left(1 + \alpha\cos\left(2\pi x/\chi\right)\right).$$

The first outcome, depicted in Fig. 2, relates to the fact that in presence of the Bragg grating few cycle pulse propagates steadily and, as it follows from the linear analysis, more slowly than in the case of no grating.

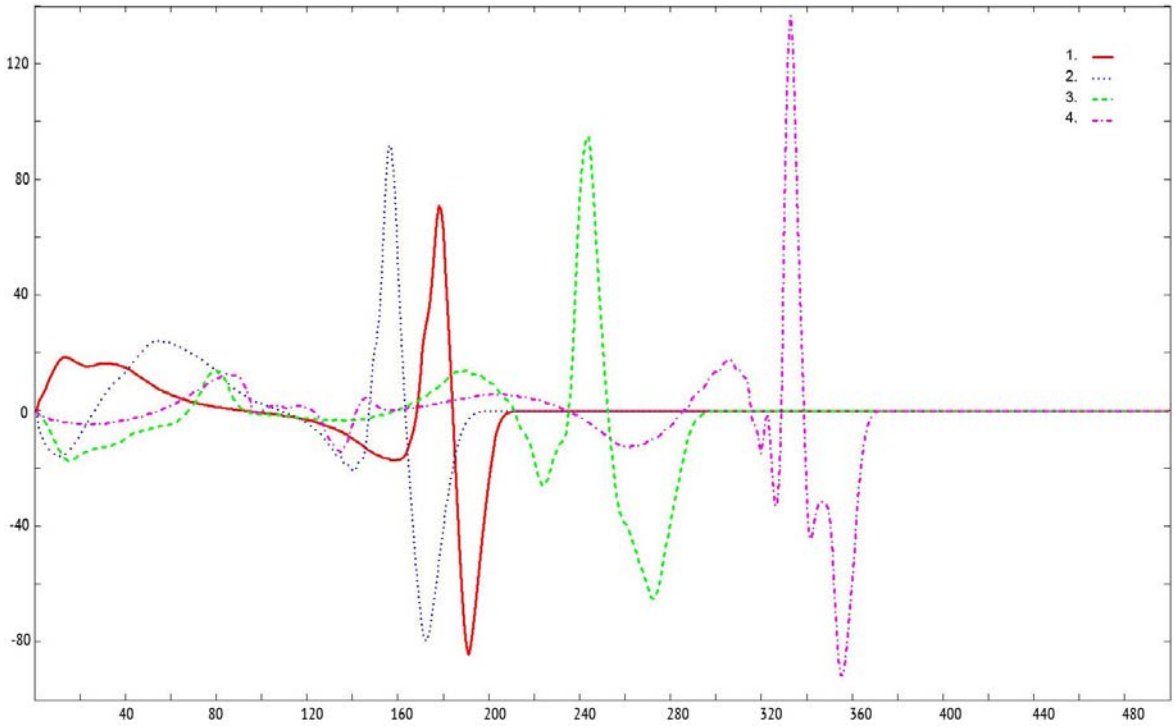

FIG. 2. Few cycle optical pulse evolution at the fixed moment of time T without Bragg grating (3); with Bragg grating present (2); and at the moment of time $2T$ (1) and $3T$ (4) with Bragg grating present. The dimensionless time is along the x-axis, the dimensionless amplitude is along the y-axis

Note that the presence of a lattice predictably leads to pulse shape deformation due to the interference of waves which have a partial reflection. The running pulse delay is correlated with the same interference.

Numerical modeling results, in terms of the lattice constant χ, are represented in Fig. 3. As expected, a few cycle pulse propagates faster with an increase in the lattice constant. It is evident that the pulse will propagate at full throttle under the infinite lattice constant, due to lack of interference processes. This was confirmed as a consequence of numeric computation. Note also that the pulse shape has significant disturbance.

The following result relates to dependence of both form and few cycle pulse velocity on modulation depth of the refraction index α, which is depicted in Fig. 4

Conspicuously, an increase in the modulation depth α leads to both a pulse delay (by the reasons mentioned above) and a change in its shape due to strong interference. Particularly, the most significant change is at the pulse front and its asymptotic form, in our opinion, this is due to reflection at lattice process and further interference. The obtained results may be also useful for predictions of pulse spread value under pulse delay by means of the Bragg grating in a carbon nanotube medium.

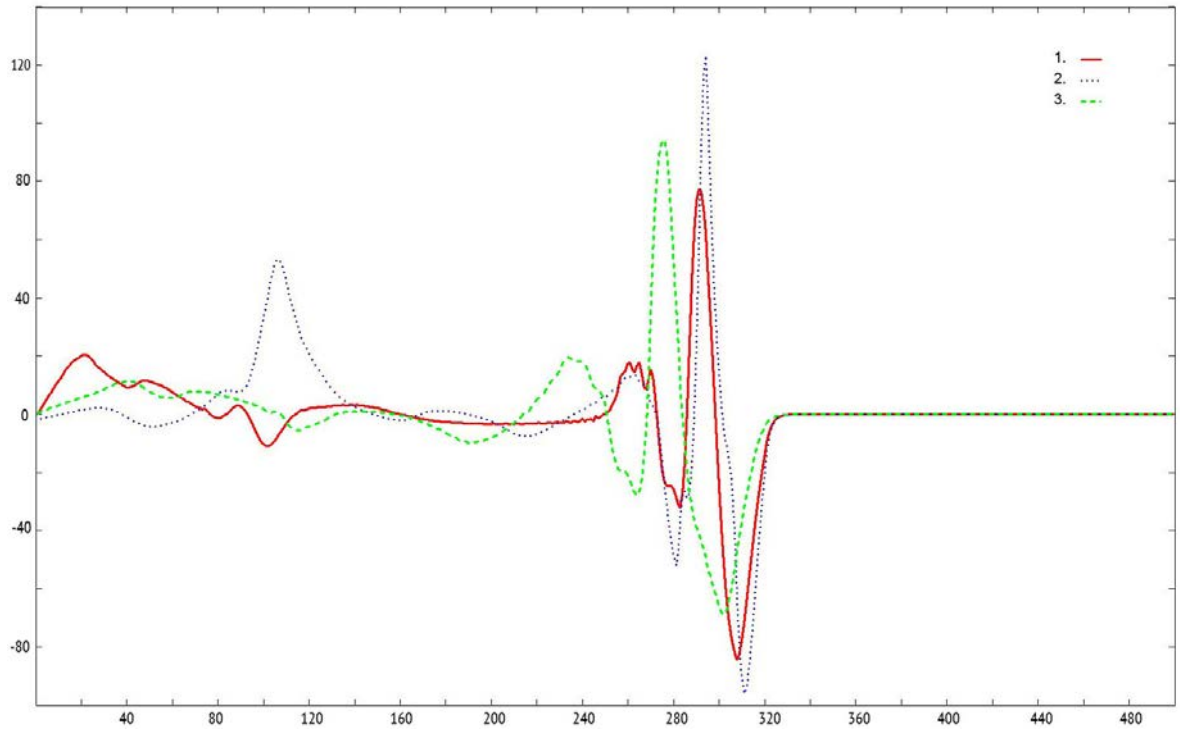

FIG. 3. The pulse shape evolution with various period χ (1), 2χ (2), 3χ (3) at the fixed moment of time under propagation in CNT system. The dimensionless time is along the x-axis, the dimensionless amplitude is along the y-axis

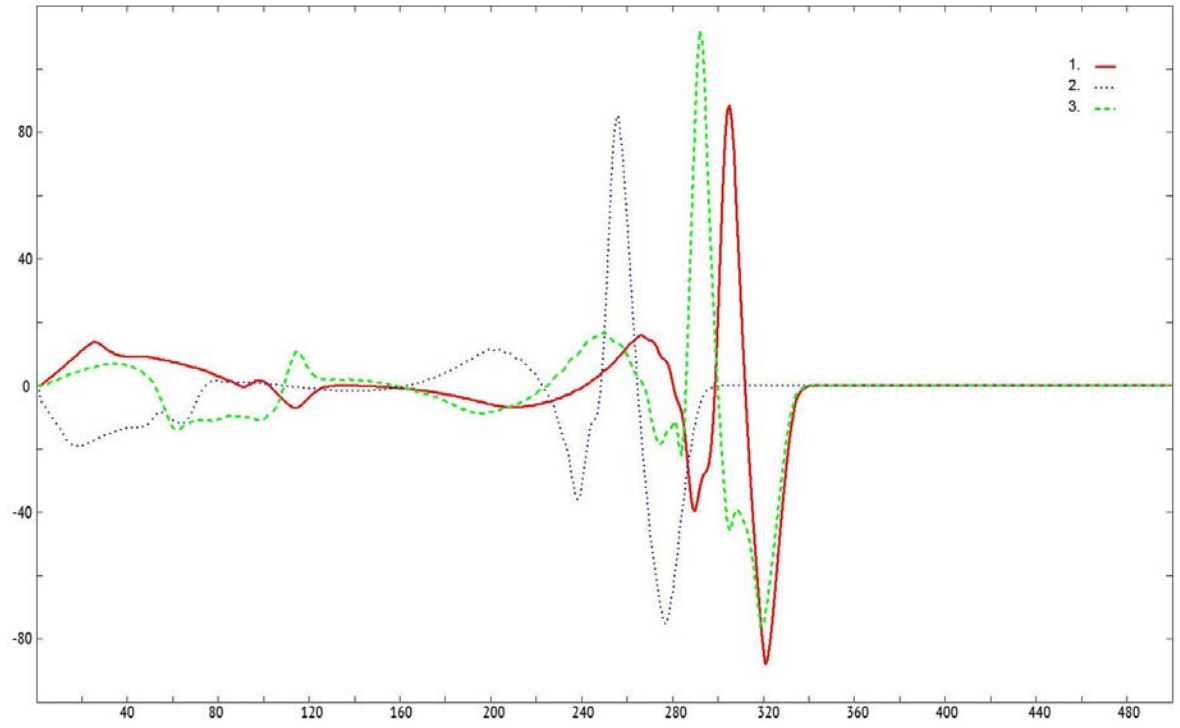

FIG. 4. The pulse shape evolution with various modulation depth α (1), 3α (2), 5α (3) under the propagation in CNT system. The dimensionless time is along the x-axis, the dimensionless amplitude is along the y-axis

4. Summary

This study allows to make the following observations:

1. Few cycle optical pulse propagation in the Bragg medium with carbon nanotubes is steady. As expected, the presence of Bragg grating deforms pulse shape, and also delays its propagation by virtue of counter wave interference.
2. It is stated that the lattice constant affects the velocity of few cycle pulse propagation. The increase in the lattice constant causes the pulse to less reflect from the lattice sites whereupon its velocity increases. Thus, we can manage the pulse propagation velocity by varying the lattice constant, which is important for solution of applied optics problems.
3. Both the pulse delay and its shape change come with the refractive index modulation enhancement by virtue of strong interference. Particularly strong changes in shape can be seen at the front of few cycle optical pulse.

References

[1] Hill K.O., Fujii Y., Johnson D.C., Kawasaki B.S. Photosensitivity in optical fiber waveguides: Application to reflection filter fabrication. *Appl. Phys. Lett.*, **32**, P. 647–649 (1978).
[2] Eggleton B.J., Slusher R.R., de Sterke CM. et al. Bragg grating solitons. *Phys. Rev. Lett.*, **76**, P. 1627–1630 (1996).
[3] deSterke ., Broderick N.G.R., Eggleton B.J., Steel M.J. Nonlinear optics in fiber gratings. *Opt. Fiber Technol.*, **2**, P. 253 (1996).
[4] Kozhekin A.E., Kurizki G., Malomed B. Standing and moving gap solitons in resonantly absorbing gratins. *Phys. Rev. Lett.*, **81**, P. 3647–3650 (1998).
[5] Conti C, Asanto G., Trillo S. Parametric gap solitons in quadratic media. *Opt. Exp.*, **3**, P. 389–404 (1998).
[6] Logvin Y.A., Volkov V.M. Complex regimes of soliton-like light pulse propagation in birefringent fibers. *J. Opt. Soc. Am. B*, **16**, P. 774–780 (1999).
[7] Champneys A.R., Malomed B.A., Friedman M.J. Thirring solitons in the presence of dispersion. *Phys. Rev. Lett.*, **80**, P. 4169–4174 (1998).
[8] Radic S., George N., Agrawal G.P. Analysis of nonuniform nonlinear distributed feedback structures: Generalized transfer matrix method. *IEEE J. Quantum Electron.*, **31**, P. 1326–1336 (1995).
[9] Radic S., George N., Agrawal G.P. Optical switching in $\lambda/4$-shifted nonlinear periodic structures. *Opt. Lett.*, **19**, P. 1789–1791 (1994).
[10] Harris P. *Carbon nanotubes and related structures. Advanced materials of the XXI century*. Tehnosfera., M., 336 p. (2003).
[11] Landau L.D., Lifshitz E.M. *Field theory*. FizMatLit., M., 536 p. (1988).
[12] Tans S.J., Devoret M.H., Dai H. et al. Individual single-wall carbon nanotubes as quantum wires. *Nature*, **386**, P. 474–477 (1997).
[13] Landau L.D., Lifshitz E.M. *Physical kinetics*. FizMatLit., M., 275 p. (1979).
[14] Krjuchkov S.V. *Semiconducting superlatticein strong fields*. Peremena, Volgograd (1992).
[15] Belonenko M.B., Demushkina E.V., Lebedev N.G. Electromagnetic solitons in bundles of zig-zag carbon nanotubes, *FTT*, **50** (2), P. 367–373 (2008).
[16] Bullaf R., Kodri F. *Solitons*. Mir, M., 408 p. (1983).
[17] Kitchenside P.W., Caudrey P.J., Bullough R.K. Solitons in laser physics. *Phys. Scr.*, **20**, P. 364–381 (1979).
[18] Bahvalov N.S. *Numerical methods (analysis, algebra, ordinary differential equations)*. Nauka, M. (1975).

NANOSYSTEMS: PHYSICS, CHEMISTRY, MATHEMATICS, 2014, 5 (5), P. 650–658

OPTICAL MICRO-STRUCTURING OF METAL FILMS ON THE SURFACE OF DIELECTRIC MATERIALS: PROSPECTS OF SHAPING BY NON-DIFFRACTING OPTICAL BEAMS

R. Drampyan[1,2], T. Vartanyan[3]

[1]Institute for Physical Research, National Academy of Sciences of Armenia, 0203, Ashtarak-2, Armenia

[2]Armenian - Russian (Slavonic) University, H. Emin str. 123, 0051, Yerevan, Armenia

[3]National Research University of Information Technologies, Mechanics and Optics, St. Petersburg, Russia

rafael.drampyan@gmail.com, Tigran.Vartanyan@mail.ru

PACS 32.80.Lg, 34.50.Dy, 81.16.Mk

The technique of optical micro-structuring of metal films based on processes of metal atoms adsorption on the surface of crystalline substrate and simultaneous controllable photo-stimulated desorption of atoms by non-uniform laser beam illumination is presented. The experiments were performed for sodium atom deposition on a sapphire substrate. The sapphire substrate was illuminated through a commercial linear mire with a pitch of 10 μm by a 440 nm laser beam with 1W/cm^2 intensity. This provides the nonuniform spatial distribution of the illumination intensity over the sapphire surface and optical control of sodium atom deposition on the sapphire substrate, preventing the nucleation and growth of the granular film in the illuminated areas. Experiments showed that the mire pattern was well reproduced in the sodium deposits, thus creating the microstructured metallic film with few tens nm thickness. The novel suggestion to use nondiffracting optical beams for high contrast microstructuring of surface metal film is presented.

Keywords: metal nanoparticle, adsorption, desorption, laser controlled growth, non-diffracting optical beams.

Received: 19 August 2014

1. Introduction

Planar micro- and nanophotonic devices are the subject of burgeoning area of research because of the wide usage of applications in optoelectronics and photonics. These uses include display devices, sensors, optical communication systems, nano-photonic devices, metamaterials etc.

Among the different technologies to manufacture metallic, semiconductor or organic nanostructures, *top-down* technologies are the most prevalent [1,2]. They include molecular beam epitaxy, mask and interference photolithography, as well as electron beam lithography.

Planar technologies for producing device structures for research in the domain of metamaterials, photonic crystals and nano-photonics were reviewed in [3-5]. Electron beam lithography (EBL) remains the most powerful method for the generation of lithographic patterns in the mentioned domain due to the combination of high precision, better than 50 nm, and programmability. EBL is relevant also as a pattern generator for the masks used in

deep ultra-violet lithography. In spite of many advantages the EBL technique requires very expensive equipment and long processing times.

In this respect, *bottom-up* technologies also have merit. These technologies are based on self-organized and photoinduced formation of nanostructures [6,7]. However, the resulting topology is rather irregular.

An attractive possibility for producing metal nanoparticles is light-induced atomic desorption as a tool for controlling the surface atom density of the adsorbed atoms during the physical vapor deposition process. Such experiments were started in the 1990's from pioneering work [8]. The physics of the process is based on the fact that strong enough nonuniform illumination diminishes the density of the adsorbed atoms in illuminated areas below a threshold value necessary for initiation of the nucleation process. Thus, the deposition pattern reproduces the spatial distribution of the illumination intensity over the surface. The adsorbtion-desorption experiments were performed with the use of alkali metal (Na, Rb, Cs) atoms in different works (see [8-13], and references therein) and Zn and Sn in [14]. The deposition of silver on a silver chloride single crystal and silver adatom absorption spectrum has been studied in [15]. Analogous experiment with deposition of gold atoms on the amorphous silica was performed in [16].

The nonuniform light beam can be obtained by mask or interference techniques. In [11] the nonuniform light beam was obtained by illumination of the substrate through the cooper wire greed with a pitch of 100 μm. In [13], in order to create a metallic grating, the spatial profile of a laser beam was modulated with reflection from a Fresnel mirror. The feasibility of the interference technique to produce surface structures with a pitch of 260 nm was substantiated in [10].

In this paper we present the results of adsorption and deposition of sodium atoms on the sapphire substrate and optical control of film deposition with the use of a mire with a pitch of 10 μm.

We suggest also the use of the non-diffracting beams, particularly Bessel beams for the formation of micrometer-scale spatially modulated beams. Exposing of the atomic deposits on the substrate surface with periodically or quasiperiodically spatially modulated non-diffracting beams is advantageous, since the light intensity distribution is stable in the course of beam propagation, providing high contrast of the metallic micro- and nanostructured patterns. The experimental formation of zeroth order Bessel beam by an axicon is presented.

2. Spectroscopy of the adsorbed atoms

The schematic for atom adsorption on the surface of the dielectric material is shown in Fig.1. Such atoms are commonly called adatoms. In some cases, the structure of the electronic levels changes dramatically, such that the adatom looses its similarity to the free atom at all.

The experimental realization of adsorption was performed with the use of a specially designed spectroscopic cell. To enhance the adatom absorption, 17 polished sapphire plates were introduced in the cell that was evacuated and filled with sodium. The cell design allows independent control of the sapphire plates' temperature and the sodium vapor density. The latter was achieved through the variation of the temperature of the metal drop placed in an appendix attached to the cell. The standard experiment run consists of absorption spectra registration at the fixed cell temperature and variable temperature of the appendix. Absorption due to the free sodium vapor was measured in a separate cell with the same optical length and subtracted. The spectra were obtained with the use of standard "Perkin-Elmer" spectrometers and are shown in Fig.2.

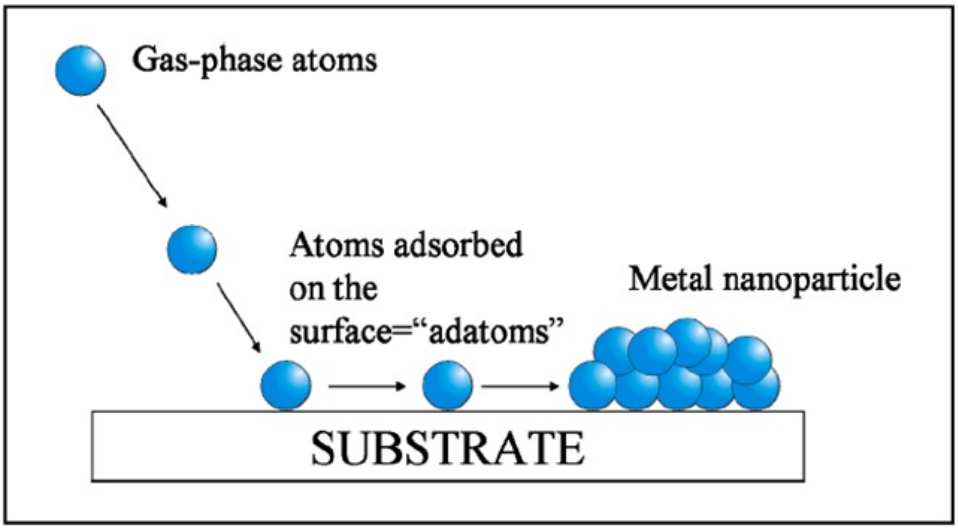

FIG. 1. Schematic of adsorbtion of atoms and nanoparticle formation on a dielectric surface

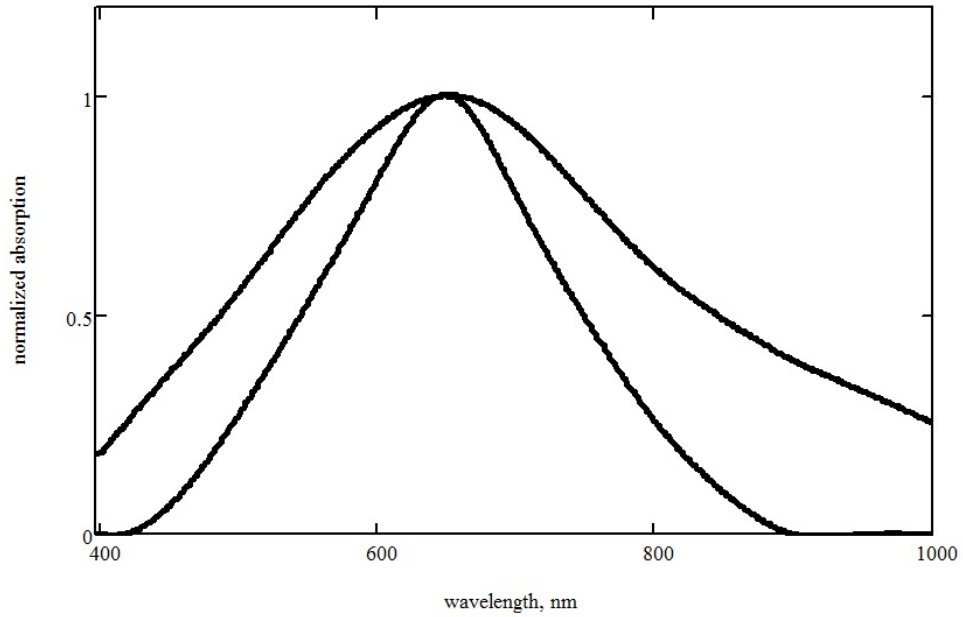

FIG. 2. Absorption spectra of sodium adatoms on the surface of sapphire kept at 470 K (narrow curve) and 670 K (broader curve). The spectra were normalized to facilitate the comparison of the broadening due to the temperature rise

Optical absorption of this system is dominated by a broad structureless band (Fig.2), somewhat shifted to the red from the position of the characteristic yellow doublet of free sodium at 589 nm. The absorption cross section of the atom at the maximum σ was found to be equal to 3×10^{-16} cm^2 while the integral of the absorption cross section over the wavelength corresponds nicely to the oscillator strength of the corresponding transition in the free atom.

These measurements proved that sodium atoms are adsorbed on the sapphire surface in atomic form and preserve their identity.

3. Photodesorption process

The photodesorption process is a very promising tool for direct laser writing of complicated patterns on surfaces. Although an ordinary heating of the substrate by absorbed radiation can cause thermal desorption of adsorbed species from the illuminated area, nonthermal mechanisms of desorption attracts much more attention. The reasons for that are higher spatial resolution, higher selectivity as well as lower inertia of nonthermal process as compared to thermal ones.

The illumination of the adsorbed atoms on the surface of the substrate can lead to photon absorption either by the substrate or by the adsorbed species. In the latter case, electronic excitation of an adatom is transformed into its motion away from the surface.

One particular example of such a process is photodesorption of sodium atoms from sapphire. Sapphire is transparent to visible light, while the adsorbed sodium atoms, as was detailed in the previous section, possess a broad absorption band in this spectral range. The nonthermal nature of sodium photodesorption from sapphire was proved in [14]. More details of the process were reported in [8]. Fig.3 shows the concept for the desorption experiment and the registration scheme. Optical methods provide high sensitivity, which allows for sure registration of the atoms desorbed with different velocities in one laser shot of 10 ns duration.

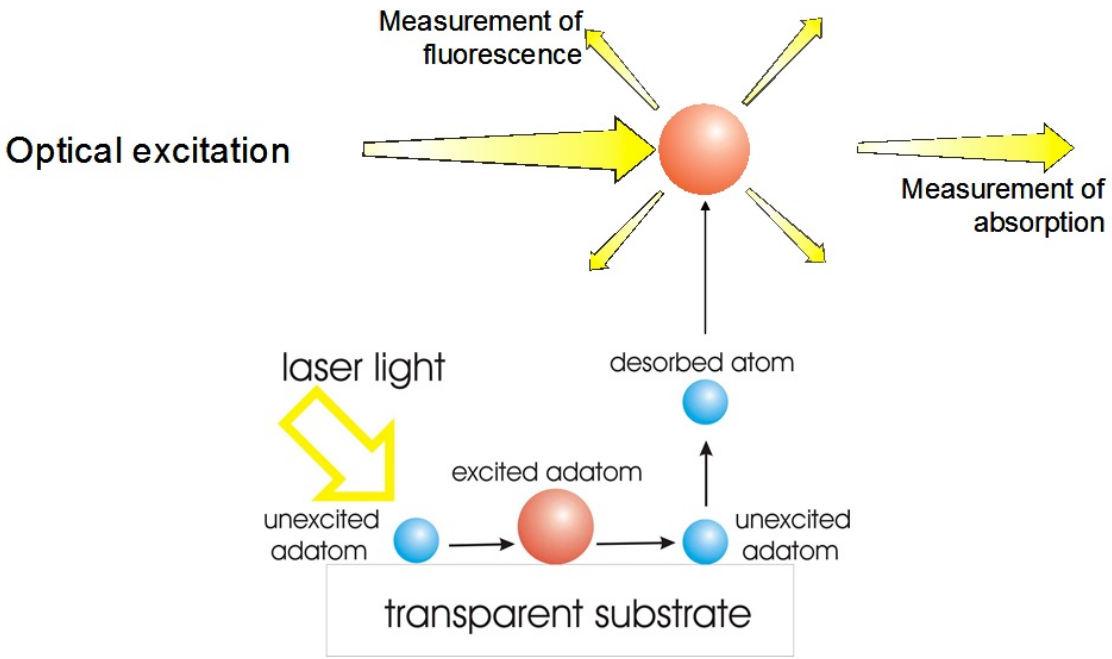

FIG. 3. Registration of photodesorption via absorption or fluorescence measurements

Fig.4 plots the photodesorption spectrum and contrasts it with the absorption spectrum already given in Fig.2. Although the maxima of the two spectra almost coincide, quantum efficiency of desorption diminishes for larger wavelengths and drops to zero at 800 nm. This threshold corresponds to the photon energy of 1.55 eV. It is in excess of the binding energy of adatoms E_{ad}=0.7 eV, which was deduced from the temperature dependence of absorption spectrum.

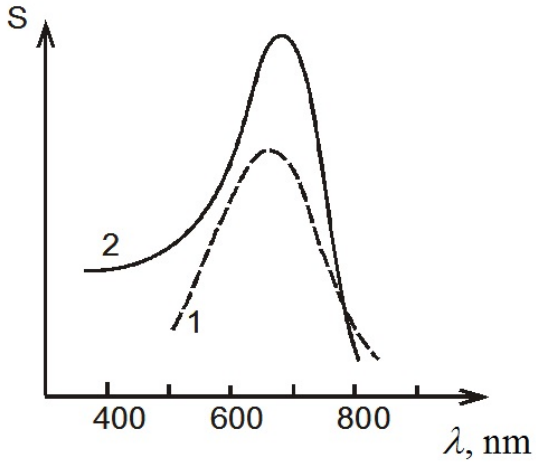

FIG. 4. Absorption (1) and photodesorption (2) spectra of individual sodium atoms adsorbed on the sapphire surface. The ordinate scale is given in arbitrary units

4. Estimation of light intensity for controllable film deposition

As was mentioned before, strong enough nonuniform illumination diminishes the number density of the adsorbed atoms in the illuminated areas below the threshold value necessary for the initiation of the nucleation process.

Estimations of light beam critical intensity, I required for the elimination of formation of metallic layer in illuminated area can be performed with the use of the following formula:

$$I = \alpha \frac{\hbar\omega}{\tau\sigma w f} \tag{1}$$

derived in [17] based on the balance equitation for surface density n of atoms for the adsorption-desorption process under illumination by nonuniform light at photon energy $\hbar\omega$. The other notations in formula (1) are as follows: α is the adhesion coefficient of a metal atom to the clean substrate admitted to be of the order of 0.01, $\tau = 1$ s is the characteristic time required to form a metal monolayer in the dark spaces, w is the photodesorption quantum yield measured in [8] to be equal to 0.001 provided the light wavelength is within absorption band of adsorbed atoms, and f is the critical surface concentration of adsorbed atoms that gives rise to the nucleation of metallic phase taken to be 0.01 of atomic monolayer. Substituting these values and the energy of photon $\hbar\omega$=2 eV in formula (1) one can obtain the value of critical intensity 3 W/cm^2.

5. Laser control for sodium metallic film deposition

In many cases, it is desirable to pattern granular metal films. Photodesorption of metal atoms from the surface of transparent dielectric materials may be used to obtain regular arrays of metal nanoparticles [10]. Illumination of the substrate during physical vapor deposition reduces the density of the atoms adsorbed on the surface, thus precluding nucleation and growth of the granular film in the illuminated areas [8,14].

We report here on the results of experiments performed with sodium deposition on sapphire. The threshold intensity of a cw diode laser operated at the wavelength of 440 nm was found to be 1 W/cm^2 for a deposition rate of 0.02 nm/s. The substrate was illuminated through the mire with a pitch of 10 μm. The microscopic images of the sodium deposits as

well as the image of the mire are presented in Fig.5. The deposition takes place at the dark sites on the cell window. The mire pattern was shown to be well reproduced in the sodium deposits.

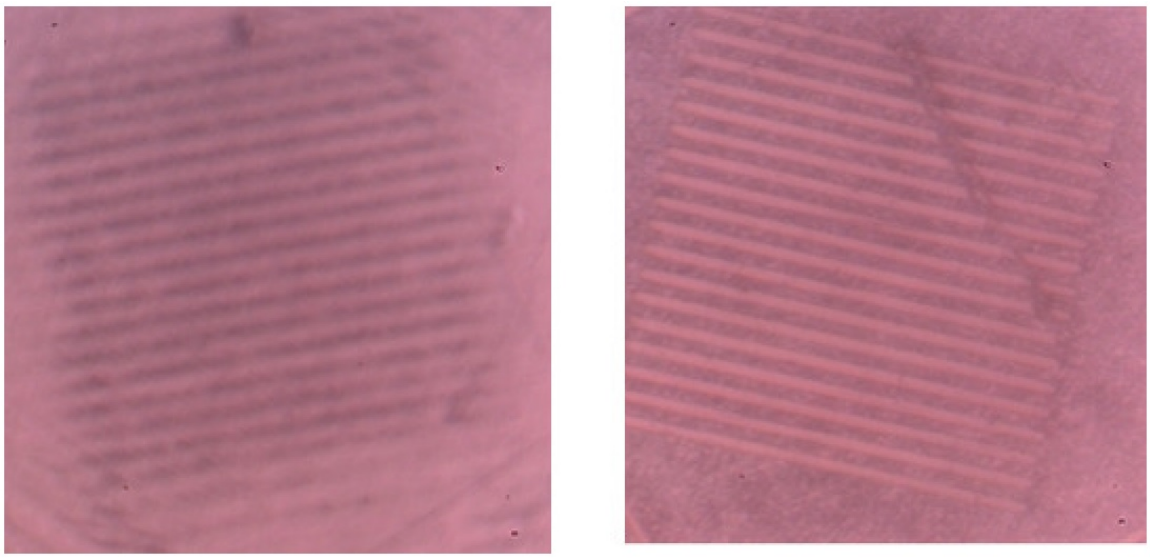

FIG. 5. (a) microscopic image of the sodium deposits on sapphire substrate obtained via physical vapor deposition under simultaneous laser illumination through the mire with 10 μm periodicity shown in (b)

Further reduction of the pitch can be achieved with an interference technique [10]. More promising is the use of non-diffracting beams providing high contrast of the metallic micro- and nanostructured patterns.

6. Prospects of the use of non-diffracting beams

Non-diffracting optics is a very active area of research in the field of optical beams and their applications. The diffraction-free beams have a feature of conserving their transverse intensity distribution during propagation in free space [18,19]. The simplest diffraction free beams can be formed by superposition of plane waves, whose wave vectors lie on the cone. The zeroth order Bessel beam is a particular case of diffraction-free beams. The profile of the Bessel beam is a set of concentric rings. The envelope of intensity profile of Bessel beam decreases inversely proportional to the radial distance [18]. A number of practical ways to generate Bessel beams have been suggested, including the use of ring apertures [18], Fabry-Perot interferometers [20], programmable phase modulators based on the phase-imprinting technique [21], holographic diffractive elements [22] and nonlinear generation of conical emission [23]. One of the ways to form Bessel beams is the use of optical element – axicon [24]. Bessel beams have numerous applications, for example, for optical manipulation of micro-sized objects, optical tweezers (see [25] and references therein), formation of Bessel like photonic lattices in photorefractive materials [26] etc.

6.1. Formation of Bessel beam by an axicon

Bessel beam formation by an axicon used in our experiments is shown schematically in Fig.6. The laser source was the Thorlabs HRP-170 single mode He-Ne laser at 633 nm operation wavelength, with 17 mW power and beam diameter of 0.7 mm. The linearly polarized Gaussian beam was expanded by confocal lenses (Fig.6a). The Gaussian beam

after passing through the axicon (Del Mar Photonics AX-BK-7-175) with aperture cone angle 175°, was transformed to the Bessel beam (Fig.6b). The convergence angle of the beams behind the axicon was adjusted by moving the output lens of the beam expander back or forth, thus varying the convergence angle within ∼4–2°, which in turn changes the spacing between the concentric rings in the range of 10–20 μm. The distance along Z axis where the converging beams are overlapped and form the Bessel beam (Fig.1a,c) was measured Z_{max} ∼10 cm. The spacing between the concentric rings, measured by beam profiler, shows their equidistant disposition, except for a few central rings. The period of annular structure shown in the Fig.6b was measured by beam profiler Thorlabs BP109-VIS and was 10 μm for certain position of output lens of beam expander. The beams become divergent behind the overlapping zone Z_{max}, forming a ring pattern (Fig.6c).

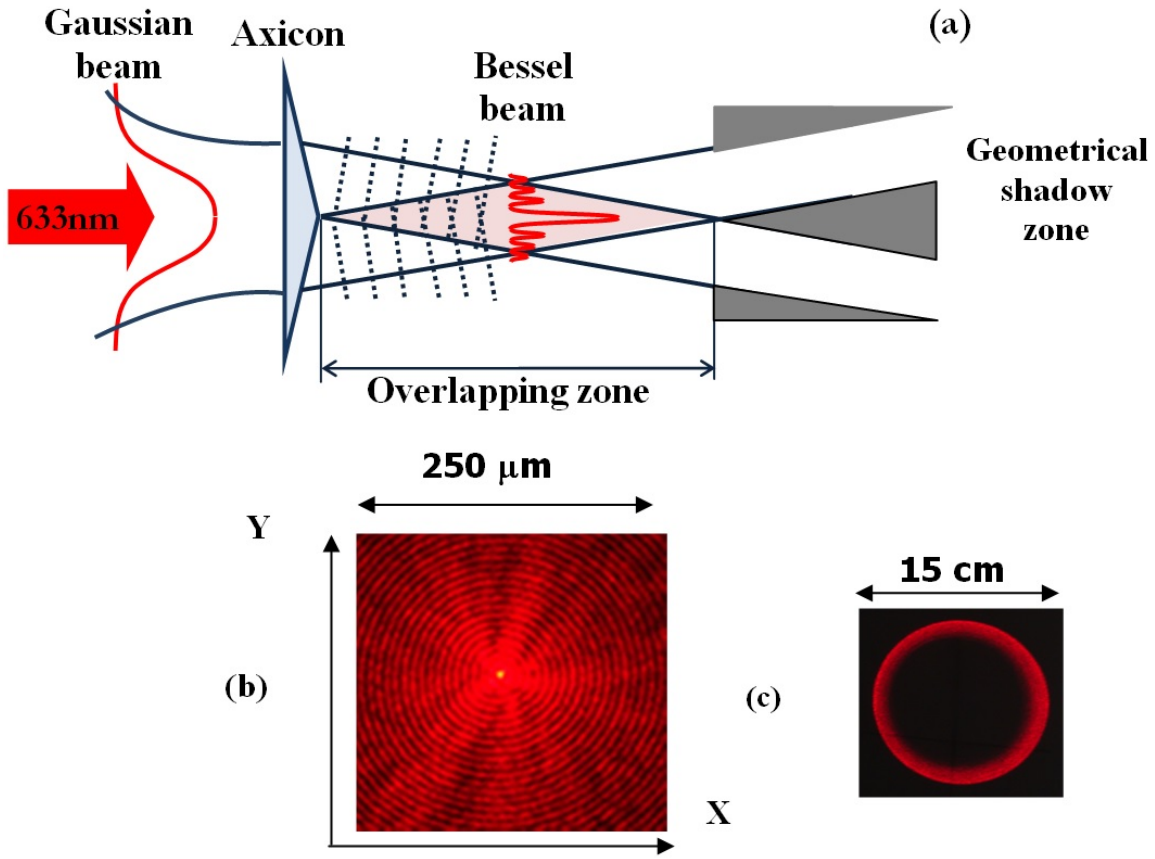

FIG. 6. (a) Experimental scheme illustrating the formation of Bessel beam by an axicon. (b) Fragment of transverse intensity distribution of Bessel beam formed by an axicon with aperture cone angle 175° in the overlapping zone of the beams. The number of rings reaches up to 500. (c) Ring pattern at the distance of 2 m behind the overlapping zone, where the beams become divergent

A Bessel beam can be formed similarly for a 100 mW cw 532 nm laser beam, which is suitable for deposition control in Na and Rb atomic vapor cells.

Exposing of the atomic deposits on the substrate surface with periodically or quasiperiodically modulated non-diffracting beams is advantageous, since the light intensity distribution is stable in the course of beam propagation [18], providing high contrast of the metallic

micro- and nanostructured pattern. These experiments are in progress and will be published elsewhere.

The technique developed for exposing of the atomic deposits by Bessel beams can be extended to other types of nondiffracting beams such as Airy [27], first order Bessel [28] and Mathieu and Weber [29] beams.

7. Conclusion

The technique of optical shaping of surface metallic micro- and nanostructures based on metal atom adsorption processes on the surface of crystalline substrate and simultaneous controllable photostimulated desorption of atoms by nonuniform laser beam illumination is presented. The experiments were performed for sodium atom deposition on a sapphire substrate. The absorption spectra of adatoms, as well as desorbed atoms are measured. The manufacturing of a micrometer-scale metal grid was performed with the use of a mire with 10 μm pitch. The novel suggestion to use nondiffracting Bessel optical beams for high contrast microstructuring of surface metal film and the formation of zeroth order Bessel beam by an axicon are presented.

The suggested techniques open new possibilities for the laser structuring of the metal films with micrometric resolution. The structured metal films have a number of applications in fast and sensitive photo-detection [30], high performance photovoltaics [31], subwavelength metal gratings and polarizers [32], surface enhanced Raman scattering [33], surface second harmonic generation [34-37] etc.

Acknowledgments

The financial support from EU project LIMACONA (IRSES-GA-2013-6126000) and from Government of Russian Federation (Grant 074-U01) is gratefully acknowledged.

References

[1] S.Y.Lin, J.G.Flemming, D.C. Hetherington et al. *Nature*, **394**, P. 251 (1998).
[2] Y.W.Su, C.S.Wu, C.C.Chen, C.D.Chen. *Advanced Materials*, **15** P. 49 (2003).
[3] N.P. Jonson, R.M. De La Rue, S.A.De La Rue, "Metamaterials at Optical Frequencies: Fabrication and Measurements" in Applications of Metamaterials, CRC Press. Ed. F. Capolino, Chapter 30 (2009).
[4] S.Linden, "Fabrication and Optical Characterization of Photonic Metamaterials" in Applications of Metamaterials, CRC Press. Ed. F. Capolino, Chapter 29 (2009).
[5] Richard De La Rue et al, "Planar nanophotonic devices in integration technologies" in Photonics and Micro- and Nano-structured materials, Ed. Rafael Drampyan, Proc. of SPIE, Vol. **8414**, P. 841402 (2012).
[6] A. Arsenault, et al, *J. Mater. Chem.* **14**, P. 781 (2004).
[7] X.Wang et al. *Adv. Mater.*, **17**, P. 2103 (2005).
[8] A.M. Bonch-Bruevich, T.A. Vartanyan, A.V.Gorlanov, Yu.N. Maksimov, S.G. Przhibrlskii, V.V.Khromov. Photodesorption of sodium from the surface of sapphire. *Sov. Phys. JETP*, **70**, P. 604–608 (1990).
[9] T.A.Vartanyan et al. "Photoexitation and photoregistration of atomic motion on the surfaces of solid materials", in New Trends in Quantum Coherence and Nonlinear Optics", Editor, R.Drampyan, Nova Science Publishers, NY, P. 245–263 (2009).
[10] T.A.Vartanyan, V.V. Khromov, N.B. Leonov, S.G. Przhibelskii, "Shaping of surface nanostructures via non-termal light-induced process", in Fundamentals of Laser-Assisted Micro- and Nanotechnologies 2010, Edited by P.Veiko , T.A. Vartanyan, Proc. SPIE, Vol.**7996**, P. 7996OH 1-7 (2011).
[11] T.A. Vartanyan et al, "Granular metal films on the surfaces of transparent dielectric materials studied and modified via optical means", in Photonics and Micro- and Nano-structured Materials 2011, Edited by Rafael Drampyan, Proc. SPIE, Vol. **8414**, P. 841404 1-7 (2012).

[12] C. Marinelly, A.Burchianti, A.Bogi, F. Della Valle, G.Bevilacqua, E.Mariotti, S.Veronesi, L.Moi. Desorption of Rb and Cs from PDMS induced by nonresonant light scattering, *Eur. Phys. D*, **37**, P. 319–325 (2006).
[13] A.E.Afanasyev, P.N. Melentyev, V.I. Balykin. Quantum adsorbtion of atoms on the surface induced by laser light, *Pis'ma Zh. Eks.Teor Fiz.*, **86**, P. 198–203 (2007).
[14] I.N.Abramova, E.B.Aleksandrov, A.M.Bonch-Bruevich, V.V.Khromov. Photostimulated desorption of metal atoms from surface of transparent insulator, *JETP Letters*, **39**, P. 203–205 (1984).
[15] A.N.Latishev, O.V.Ovchinnikov, S.S. Okhotnikov. *J.Appl.Spectr.*, **70**, P. 817–820 (2003).
[16] J.-M. Antonietti, M.Michalski, U.Heiz, H.Jones, K.H.Lim, N. Roesch, A.D.Vitto, G. Pacchioni, *Phys. Rev Lett.*, **94**, P. 213402 (2005).
[17] T.A. Vartanyan, V.V.Khromov, N.B.Leonov, S.G. Przhibelskii. Optical methods for formation of metallic nanostructures on the surface of dielectric materials, *Opticheskii Zhournal*, **78**(8), P. 47–50 (2011).
[18] J. Durnin, J.J. Mikely Jr, J.H. Eberly. Diffraction-free beams. *Phys. Rev. Lett.*, **58**, P. 1499–1501 (1987).
[19] V. Bagini, F. Frezza, M. Santarsiero, G. Schettini, G. Spagnolo. Generalized Bessel-Gauss beams, *J. Mod. Optics*, **43**, P. 1155–1166 (1996).
[20] A.J. Cox and D.C. Dibble. Nondiffracting beams from a spatially filtered Fabry–Perot resonator, *J. Opt. Soc. Am. A*, **9** P. 282–286 (1992).
[21] N. Chattrapiban, E.A. Rogers, D. Cofield, W.T. Hill, III, and R. Roy. Generation of nondiffracting Bessel beams by use of a spatial light modulator. *Opt. Lett.*, **28**, P. 2183–2185 (2003).
[22] J. Turunen, A. Vasara, and A. T. Friberg. Holographic generation of diffraction-free beams. *Appl. Opt.*, **27** P. 3959–3962 (1988).
[23] R.Drampyan. Formation of diffraction-free beams by laser generation of conical emission in a Kerr medium. *Appl. Phys.B*, **68**, P. 77–79 (1999).
[24] Shafer F. P. On some properties of axicons. *Appl. Phys. B*, **39**, P. 1-8 (1986).
[25] J. Arlt, V. Garces-Chavez, W. Sibett, K.Dholakia. Optical micromanipulation using a Bessel light beam. *Opt Commun.*, **197**, P. 239 (2001).
[26] A. Badalyan, R. Hovsepyan, P. Mantashyan, V. Mekhitaryan, R. Drampyan. Bessel standing wave technique for optical induction of complex refractive lattice structures in photorefractive materials. *J. Modern Optics*, **60**, P. 617–628 (2013).
[27] P.Rose, F. Diebel, M. Boguslawski, C. Denz. Airy beam induced optical routing. arXiv:1202.5724.v1 [physics. optics] 26 Feb 2012.
[28] J. Arlt, K. Dholakia. Generation of high-order Bessel beams by use of an axicon. *Optics Commun.*, **177**, P. 297–301 (2000).
[29] P. Rose, M. Boguslawski, C. Denz. Nonlinear lattice structures based on families of complex nondiffracting beams. *New J. Phys.*, **14**, P. 033018. (2012).
[30] D. M. Schaadt, A. B. Feng, and E. T. Yub. Enhanced semiconductor optical absorption via surface plasmon excitation in metal nanoparticles. *Appl. Phys. Lett.*, **86**, P. 063106 (2005).
[31] D. Derkacs, W. V. Chen, P. M. Matheu, S. H. Lim, P. K. L. Yu, and E. T. Yu. Nanoparticle-induced light scattering for improved performance of quantum-well solar cells. *Appl. Phys. Lett.*, **93**, P. 091107 (2008).
[32] Seh-Won Ahn, Ki-Dong Lee, Jin-Sung Kim, Sang Ho. Fabrication of a 50 nm half-pitch wire grid polarizer using nanoimprint lithography. *Nanotechnology*, **16**, P. 1874–1877 (2005).
[33] Paul L. Stiles, Jon A. Dieringer, Nilam C. Shah, Richard P. Van Duyne. Surface-enhanced Raman spectroscopy. *Annual Review of Analytical Chemistry*, **1**, P. 601–626 (2008).
[34] M. Ishifuji, M. Mitsuishi, T. Miyashita. Bottom-up design of hybrid polymer nanoassemblies elucidated plasmon-enhanced second harmonic generation from nonlinear optical dyes. *J.Am.Chem, Soc.*, **131**, P. 4418–4424 (2009).
[35] Yu. Zhang, N. K. Grady, C. Ayala-Orozco, N. K. Halas. Three-dimensional nanostructures as high efficient generator of second harmonic light. *Nano Lett.*, **11**, P. 5519–5523 (2011).
[36] J. Fuitowski et al. Mapping of gold nanostructure-enhanced near fields via laser scanning second harmonic generation and ablation. *Journal of Nanophotonics*, **6**, P. 063515 (2012).
[37] M.Centini, A.Benedetti. Second harmonic generation in plasmonic nanoresonators. *Journal of Nanophotonics*, **7**, P. 078501 (2013).

NANOSYSTEMS: PHYSICS, CHEMISTRY, MATHEMATICS, 2014, 5 (5), P. 659–676

NANOSCALE REDUCED-GRAPHENE-OXIDE ORIGIN OF SHUNGITE IN LIGHT OF NEUTRON SCATTERING

E. F. Sheka[1], N. N. Rozhkova[2], K. Hołderna-Natkaniec[3], I Natkaniec[3,4]

[1]Faculty of Physics, Mathematics and Natural Sciences,
Peoples' Friendship University of Russia, Moscow, Russia

[2]Institute of Geology, Karelian Research Centre RAS, Petrozavodsk, Russia

[3]Faculty of Physics, Adam Mickiewicz University, Poznan, Poland

[4]Frank Laboratory of Neutron Physics, Joint Institute for Nuclear Research, Dubna, Russia

sheka@icp.ac.ru, rozhkova@krc.karelia.ru, inat@jinr.ru

PACS 61.05.fg, 61.46.+w, 63.22. ±m, 81.05.Uw

New concept of shungite carbon exhibits this raw material as a multi-level fractal structure of nanosize fragments of reduced graphene oxide (rGO) (Int. J. Smart Nano Mat. 1, 1, 2014). The natural rGO deposits turn out to be quite challenging for the current graphene technology. Once consistent with all the block of the available geological and physicochemical data obtained during the last few decades, the concept nonetheless needs a direct confirmation in terms of the current graphene science. The first such acknowledgement has been received just recently when studying photoluminescence (PL) of shungite dispersions (JETP 118, 735, 2014). A close similarity of PL spectra of aqueous dispersion of shungite and those of synthetic graphene quantum dots of the rGO origin has been established. The current paper presents the next direct confirmation provided with neutron scattering. Elastic neutron diffraction and inelastic neutron scattering have left no doubts concerning both graphene-like configuration and chemical composition of basic structural elements of shungite attributing the latter to rGO nanosize sheets with an average ∼6:0.1:2 (C:O:H) atomic content ratio per one benzenoid unit. The experimental data are supplemented with quantum-chemical calculations that allowed suggesting a clear vision of the shungite structure at its first fractal levels.

Keywords: shungite; natural nanoscale reduced graphene oxide; multi-stage reduction of graphene oxide; retained water; elastic and inelastic neutron scattering; quantum chemical calculations.

Received: 13 October 2014
Revised: 21 October 2014

1. Introduction

High-yield production of few-layer graphene flakes from graphite is important for the scalable synthesis and industrial application of graphene. Graphene-based sheets show promise for a variety of potential applications, and researchers in many scientific disciplines are interested in these materials. Although many ways of generating single atomic layer carbon sheets have been developed, chemical exfoliation of graphite powders to graphene oxide (GO) sheets followed by deoxygenation to form chemically modified reduced graphene oxide (rGO) has been so far the only promising route for bulk scale production. However, available technologies face a lot of problems among which there are low yield, the potential fire risk of GO and rGO when alkaline salt byproducts are not completely removed, a great tendency to aggregation, a large variety of chemical composition, and so forth (see the latest exhaustive reviews [1, 2] and references therein). In light of this, the existence of natural

rGO is of utmost importance. As if anticipating the future need for the substance, the Nature has taken care of a particular carbon allotrope in the form of well-known shungite mineralloid from deposits of carbon-rich rocks of Karelia (Russia) that strongly kept secret of its origin and rGO-based structure. Just recently has been suggested that shungite carbon has a multilevel fractal structure based on nanoscale rGO sheets [3] that are easy dispersible in water and other polar solvents [4, 5]. Two direct justifications of the suggestion have been obtained. The first one is related to the study of photoluminescence of shungite aqueous and organic dispersions [6, 7] that exhibits properties similar to those of synthetic graphene quantum dots of the rGO origin [8]. The second was obtained in the course of the neutron scattering study that was partially presented in [9] but profoundly discussed in the current paper. The study was initiated by two reasons. The first follows from the leading concept of the suggestion [3] that shungite was born in aqueous environment. Once porous due to its fractal structure, it provides favorable conditions for the water confining. Actually, thermal analysis and mass spectroscopy pointed the water presence up to a few wt% [10]. As known, the confined water can say much about the space in which it is kept. The other reason concerns a serious problem of detecting chemical composition of rGO, in general, and in shungite, particularly. Usually, the main attention is given to the determination of the C/O ratio focusing primarily of the content of remaining oxygen and leaving the hydrogen content behind brackets [2]. The inelastic neutron scattering (INS) spectroscopy, which is the most hydrogen-sensitive technique, has allowed for the first time not only to detect the small-mass-content hydrogen component of the shungite carbon body but to suggest a general chemical formula for shungite rGO.

2. Experimental details

Neutron experiment. Neutron scattering study was performed at the high flux pulsed IBR-2 reactor of the Frank Laboratory of Neutron Physics of JINR by using the NERA spectrometer [11]. The investigated samples are illuminated by white neutron beam analyzed by time-of-flight method on the 110 m flight path from the IBR-2 moderator. The inverted-geometry spectrometer NERA allows simultaneous recording of both Neutron Powder Diffraction (NPD) and INS spectra. The latter are registered at final energy of scattered neutrons fixed by beryllium filters and crystal analyzers at $E_f = 4.65$ meV.

Samples. Three powdered shungite samples were subjected to the study. The first pristine shungite Sh1 presents the natural raw material with C $\geqslant$ 95 wt.% from Shun'ga's deposits [4]. Shungite Sh2 was obtained when drying Sh1 at 110°C under soft vacuum at temperature ∼100°C for a week until the constant weight of the solid is reached. The weight loss, which was attributed to the evaporated water, constitutes 4g per 100g of the solid. The third shungite Sh3 presents a solid condensate of colloids of the shungite Sh1 aqueous dispersions and is produced in the course of the dispersion lengthy drying until the constant weight is reached. Similarly to Sh1, additional heating of Sh3, sustained under ambient conditions for a long time, at soft vacuum and temperature above 100°C results in its releasing from the retained water constituting ∼4% of the total mass. Raman scattering [3], high-resolution solid state ^{13} NMR [10], and Auger spectroscopy [5] show a deep similarity of shungites Sh1 and Sh3. Powdered spectral graphite was used to register both the reference NPD and INS spectrum from pure carbon material.

3. Neutron powder diffraction

A set of NPD plottings for the three shungite samples at 20 K is presented in Fig. 1. The data are related to samples in aluminum sample holder and cryostat due to which the

plottings are overloaded with Al(hkl) reflections. Exempted from the Al reflections and corrected for background inelastic scattering, NDP plottings of Sh1 and Sh2 are presented in Fig. 2. Similarly to the reference graphite spectrum, given at the bottom, the main features of the shungite diffractograms concern peaks related to Gr(002), Gr(100) and Gr(110) reflections all of which are broadened and upshifted. Figure 3 presents a detailed view on Gr(002) peaks. As seen in the figure, the narrow peak of graphite, the shape and width of which correspond to the resolution function of spectrometer and whose position determines d_{002} interfacial distance between the neighboring graphite layers, is substituted with broad peaks whose characteristics are given in Table 1. To fix the positions $A_{002}$of the peaks maxima and to obtain the relevant FWHMs, B_{002}, the Gauss fitting procedure was applied. According to the fitting, A_{002} andB_{002} values of all shungite samples are identical within the limits of standard errors.

TABLE 1. Characteristics of Gr(002) peaks

Samples	Peak position, A_{002}, Å	FWHM, B_{002}, Å
Graphite	3.3501±0.0002	0.0341±0.0006
Sh1 Sh2 Sh3	3.4513±0.0015	0.5408±0.0063

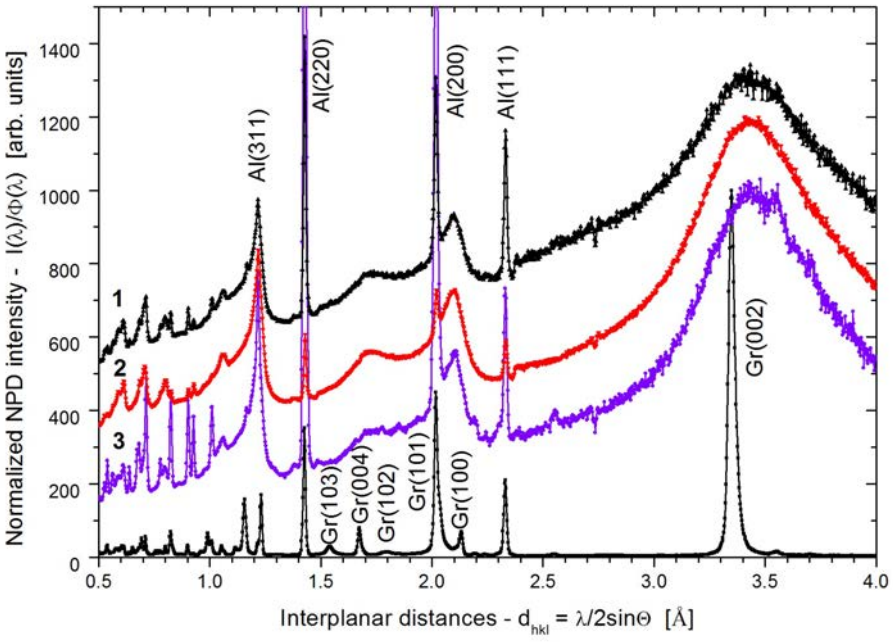

FIG. 1. NPD of spectral graphite (Gr) and shungites Sh1 (1), Sh2 (2), and Sh3 (3) recorded at T=20 K. Scattering angle $2\Theta = 117.4°$. The data are normalized per neutron flux intensity $\Phi(\lambda)$ at each neutron wave length λ; Gr(hkl) and Al(hkl) denote characteristic diffraction peaks of spectral graphite and cryostat aluminum at different Miller indexes, respectively

Slight upshift of the shungite peaks convincingly evidences a conservation of the graphite-like structure of all the samples, while the peak wide broadening tells about a

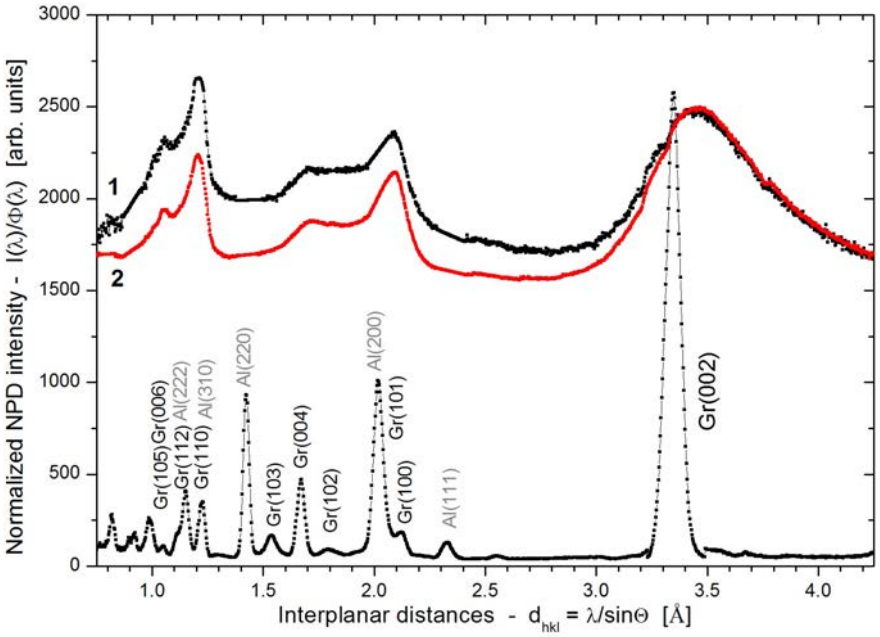

FIG. 2. NPD of shungites Sh1 (1) and Sh2 (2) recorded at T=20 K after extraction of Al(hkl) reflections. Scattering angle $2\Theta = 44.7°$. The data are normalized per neutron flux intensity $\Phi(\lambda)$ at each neutron wave length λ; Gr(hkl) (black) and Al(hkl) (gray) denote characteristic diffraction peaks of spectral graphite and cryostat (alongside with sample holder) aluminum at different Miller indexes, respectively

considerable space restriction. The latter is usually attributed to the narrowing of the coherent scattering region (CSR) of scatterers. According to widely used Scherrer's equation, the FWHM of a diffraction peak B and the CSR length L_{CSR} are inversely connected: $B = k\lambda/L_{CSR}\sin\Theta$, where k is a fitting factor, λ and Θ are the neutron wave length and scattering angle. When the diffraction study is performed for a set of samples under the same conditions, it is possible to take one of the samples as the reference and to determine L_{CSR} of the remaining samples addressing to that of the reference. In our study, L^{ref}_{CSR} is attributed to crystalline graphite and constitutes ~20 *nm* along *c* direction [12]. Therefore, L^{c}_{CSR} of the studied shungites can be determined as

$$L^{c}_{CSR} = (B_{002ref}/B_{002})\,(\lambda/\lambda_{ref})\,L^{c\ ref}_{\ CSR}. \tag{1}$$

Substituting λ/λ_{ref} by the ratio of the Gr(002) peak positions A_{002}/A_{002ref} and using B_{002} values given in Table 1, we obtain $L^{c}_{CSR} = 1.3$ *nm*. The data correlates well with those of 2.18 *nm* and 2.30 *nm* for Sh1 and Sh3, respectively, obtained by X-Ray diffraction [13]. Summarizing NPD and X-Ray data, L^{c}_{CSR} of ~1.5–2 *nm* can be suggested. The obtained L^{c}_{CSR} corresponds to the coherency along the direction normal to graphene layers and points to ~5–6 layer structure of the relevant stacks. It should be noted that a multi-layer graphene-like packing is characteristic for rGO of any origin [1].

As early pointed [14], L^{a}_{CSR}, which determines the layer lateral dimension, is characterized by the width of Gr(110) peak. On the basis of the Scherrer equation and using

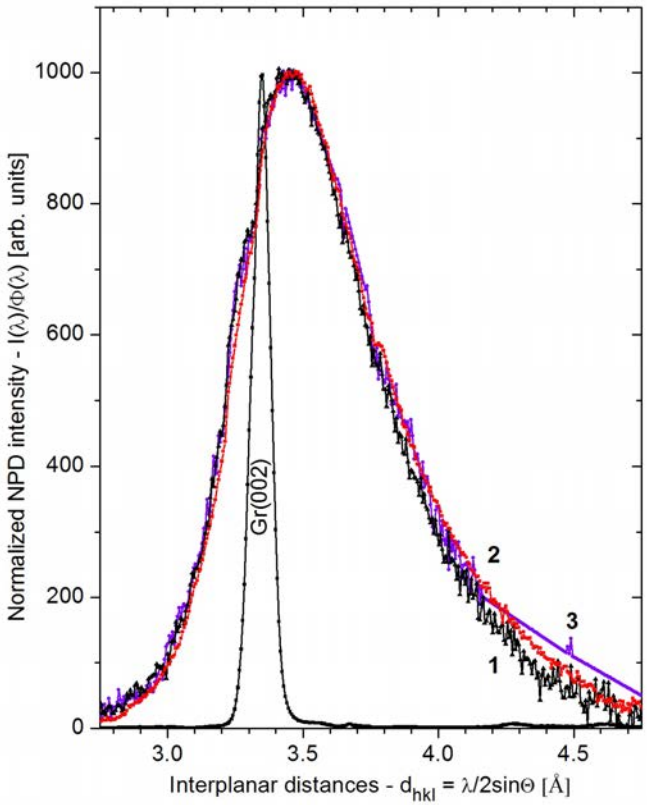

FIG. 3. NDP fragments of spectral graphite (Gr) and shungites Sh1 (1), Sh2 (2), and Sh3 (3) in the region of Gr(002) diffraction peaks; T=20 K; scattering angle $2\Theta = 44.7°$. The data are normalized per neutron flux intensity $\Phi(\lambda)$ at each wave length of incident neutrons λ; after a linear background subtraction, the intensity maxima of all the peaks are normalized to 1000 arbitrary units

results presented in Fig.2, the corresponding value can be evaluated following the ratio

$$L^a_{CSR} = L^c_{CSR}\frac{A_{110}\cdot B_{002}}{A_{002}\cdot B_{110}} \tag{2}$$

B_{110} values of the Gr(110) peak of both shungites are quite similar and constitute ∼0.0723 $\mathring{A}$ so that the relevant$L^a_{CSR} \approx 1.93L^c_{CSR}$. As known, {hk0} reflections are influenced by not only the lateral extent of the graphene layers but the presence of both translational and rotational disorder (turbostratic structure) of the stacks [14]. Therefore, the obtained L^a_{CSR} ∼3–4 nm can be considered as the upper limit of the lateral size of graphene sheets while the size of individual rGO sheets might be significantly less.

4. Inelastic neutron scattering

Figure 4 presents time-of-flight (TOF) INS spectra of the studied samples at T=20K. The spectra are summarized over 15 scattering angles, normalized per 10 hours exposition time. As seen in the figure, the INS intensity from graphite is at the level of the instrumental background and can be taken as the background to be extracted from the shungite spectra for both experimental background and INS from carbon atoms to be excluded. The spectra clearly exhibit strong scattering from all the samples in contrast with that from graphite

thus indicating that all of them are evidently hydrogen-enriched. At the same time, the spectra differ by both intensity and shape. Thus, if the spectra of Sh1 and Sh3 differ only in intensity, the spectra of Sh1 and Sh2 differ in shape as well. The first finding points that the hydrogen atom dynamics in Sh1 and Sh3 is rather identical while in Sh2 the later is quite different. As shown in [9], the difference TOF spectrum 1–2 between spectra 1 and 2 evidently presents the spectrum of the released water since Sh2 was produced from Sh1 by lengthy heating, which was followed by removing water previously retained in Sh1. At the same time, the spectrum of Sh2 is quite intense, which undoubtedly points to the presence of hydrogen atoms incorporated in the carbon structure of shungite. Therefore, the observed INS spectra of shungites are provided with incoherent inelastic neutron scattering (IINS) from hydrogens incorporated in the shungites structure and contained in the retained water.

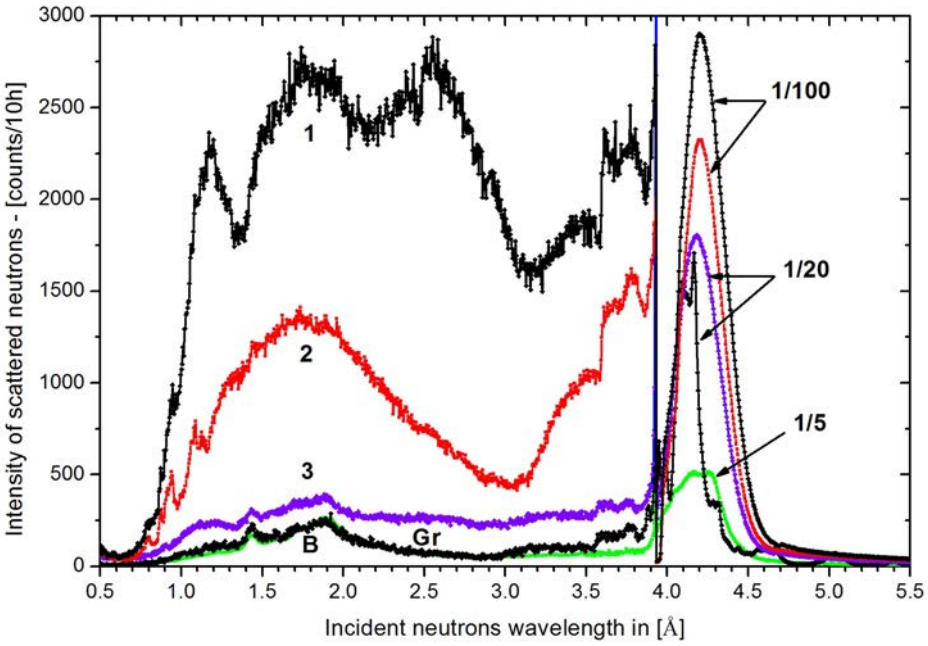

FIG. 4. Time-of-flight INS spectra from shungites Sh1 (1=100g), Sh2 (2=96g), Sh3 (3=10g) and spectral graphite (Gr=10g). Curve B presents background from Al cryostat and sample holder material. T=20K. The intensity of elastic peaks is 100-fold, 20-fold, and 5-fold reduced for Sh1 and Sh2, Sh3 and graphite, and background, respectively. Spectra are normalized per 10 hours exposition time at constant power of the IBR-2 equal 1.9 MW

Within the confines of commonly used incoherent inelastic one-phonon scattering approximation, the IINS spectra intensity is determined by the scattering cross-section (see for example Ref. 15) as

$$\sigma_1^{inc}\left(E_i, E_f, \varphi, T\right) \approx \sqrt{\frac{E_f}{E_i}} \frac{\hbar \left|Q\left(E_i, E_f, \varphi\right)\right|^2}{\omega} \sum\nolimits_n \frac{\left(b_n^{inc}\right)^2}{M_n} \frac{\exp\left(-2W_n\right)}{1-\exp\left(-\frac{\hbar\omega}{k_B T}\right)} G_n\left(\omega\right) \quad . \qquad (3)$$

Here, $Q\left(E_i, E_f, \varphi\right)$ is the neutron momentum transfer; $\omega = \left(E_i - E_f\right)$ is the neutron energy transfer; b_n^{inc} and M_n are the incoherent scattering length and mass of the $n-th$ atom; $\exp\left(-2W_n\right)$ is the Debye-Waller factor; $G_n\left(\omega\right)$ presents the n-th atom contribution into the

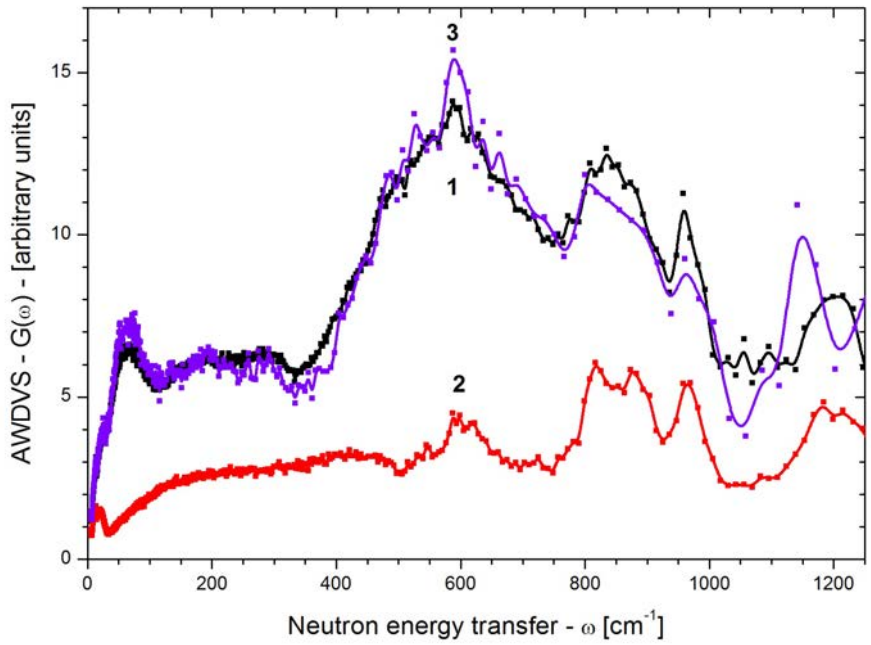

FIG. 5. One-phonon AWDVS spectra of shungites Sh1 (1), Sh2 (2), and Sh3 (3) at 20K

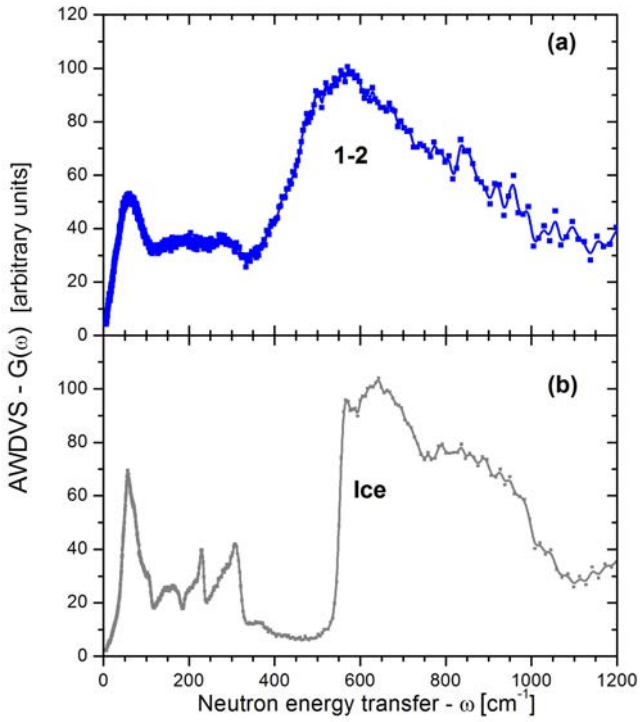

FIG. 6. (a) The difference spectrum 1–2 attributed to retained water; (b) $G(\omega)$ spectrum of I_h ice. T = 20K

amplitude-weighted density of vibrational states (AWDVS) expressed as

$$G(\omega) = \sum\nolimits_n G_n(\omega) = \sum\nolimits_n \sum\nolimits_j \left[A_j^n(\omega)\right]^2 \delta(\omega - \omega_j). \quad (4)$$

Here, $A_j^n(\omega)$ is the n-th atom contribution into the eigenvector of the j-th phonon mode thus presenting the amplitude of the $n-th$ atom displacement at the vibrational frequencyω_j.

Figure 5 presents one-phonon AWDVS $G(\omega)$ spectra obtained in the course of a standard treatment procedure [15] and related to the TOF spectra shown in Fig. 4 after extraction of the INS spectrum of graphite taken as background and normalization of the TOF spectra per 10^6 monitor counts of incident neutrons. When obtaining $G(\omega)$ spectra, Debye-Waller factors were taken as unity due to low temperature and rather narrow frequency region. The spectra were not corrected on multi-phonon contribution that is quite small at low temperature. All the spectra are normalized per 10 g of mass. As seen in the figure, $G(\omega)$ spectra of Sh1 and Sh3 are practically identical. Changing in the fine structure of spectrum 3 above 500 cm^{-1} may be connected with either poor statistic of experimental data due to small mass of shungite Sh3 or reconstruction of its structure in the course of transformation of the pristine shungite Sh1 to Sh3 first through dispersion in water and then consolidation of a solid phase after the water evaporation. $G(\omega)$ spectrum of Sh2 differs from the above two spectra quite significantly. The difference between $G(\omega)$ spectra 1 and 2 is presented in Fig. 6a as spectrum 1–2.

Analyzing the spectra obtained, three features can be noted. The first concerns spectrum 1–2 in Fig. 6a that can be evidently considered as the spectrum $G^{wat}(\omega)$of retained water. Actually, the spectrum has much in common with that of bulk water presented in Fig. 6b and presents the contribution of 4wt% water in the spectrum of the pristine shungite Sh1. It is pretty similar to those well known for retained water in silica gels [16, 17], Gelsil glasses [18], nanosized graphite oxide [19], and various zeolites [20]. The second feature is related to spectrum 2 in Fig. 5 that evidently exhibits hydrogen atoms in the shungite core not connected with water. The relevant $G^{core}(\omega)$ differs drastically from the water one and has much in common with that one of a synthetic rGO [21] thus confirming the rGO nature of shungite. The spectrum is characterized by a considerable flattening up to 500 cm^{-1} and reveals a pronounced structure in the region of 600–1200 cm^{-1}. The third feature concerns the evident absence of the retained water crystallization so that the $G^{wat}(\omega)$ spectrum represents bound water [19]. As shown in [22], this water may be supercooled without crystallization up to very low temperature.

As known, water molecules can be retained either on the surface of solid nanoparticles (see adsorbed water on aerosil [17]) and in the interfacial region of layered nanostructures [19] or in pores formed by the bodies [18, 20]. The multi-layer stack structure of shungites with interfacial spacing of ∼3.5Å leaves no possibility of introducing 1.75Å-thick water molecules between the layers. The latter can be accommodated either on the outer surface of ∼1.5–2 nm shungite stacks or in pores made of the latter and their aggregates. Small angle neutron scattering (SANS) from shungite [23] exhibited pores of 2–10 nm and >20 nm in size thus pointing the place of the water accommodation. This explains a very deep similarity that is observed between the AWDVS spectra of the water retained in pores of silica gels [16, 17], Gelsil glass [16] and $G^{wat}(\omega)$ spectrum of shungite.

5. rGO sheet modeling

The hydrogen-enriched rGO core is the main intrigue of the current study. According to [24], the remaining chemical addends are concentrated in the circumference of graphene

sheets and are mainly presented by carbonyl units complemented by a small portion of hydroxyls. However, in the case of shungite [3], the relevant oxygen contribution is too high which contradicts with real data indicating a small amount of oxygen at the level of 3–2 wt% as shown by the latest point microanalysis that accompanies extensive HRTEM study [25]. Moreover, as follows from the $G^{core}(\omega)$ spectrum in Fig. 5, there is no indication of the presence of bands, which could be attributed to hydroxyls (either in the region of 90–100 cm^{-1}, which is characteristic for hydroxyls attached to silica [17], or at 400–500 cm^{-1}, which is typical for hydroxyls on carbon substrate [21, 26]). In contrast, clearly vivid maxima at $\sim$ 610 cm^{-1}, 820 cm^{-1}, 880 cm^{-1}, 960 cm^{-1}, and 1200 cm^{-1}, which fall in the region of the most characteristic non-planar deformational vibrations of the alkene C–H bonds [21, 26], are observed. The hydrogen presence is supported by the hydrophobicity of rGOs that is often noted by chemists. The finding convincingly points to the presence of C–H bonds in the circumference of rGO nanosheets thus exhibiting a *post factum* hydrogenation of the pristine rGO that is produced in the course of deoxygenating the pristine GO [3].

TABLE 2. Chemical composition and mass content of differently reduced (5, 5) rGOs in vacuum

Atomic composition	Mass content, wt %			Remarks
	C	O	H	
$C_{66}O_{22}H_2$	69,13	30,70	0,17	calc., Fig. 7b
$C_{66}O_9H_{13}$	83,46	15,17	1,37	calc., Fig. 7d
$C_{66}O_6H_{16}$	87,61	10,62	1,77	calc.
$C_{66}O_5H_{17}$	89,09	9,00	1,91	calc.
$C_{66}O_4H_{18}$	90,62	7,32	2,06	calc.
$C_{66}O_3H_{19}$	92,20	5,59	2,21	calc., Fig. 7e
$C_{66}O_2H_{20}$	93,84	3,79	2,37	calc.
$C_{66}O_1H_{21}$	95,54	1,93	2,53	calc.Fig. 9a
$C_{66}H_{22}$	97,30	-	2,70	calc.
Product 1 $C_{66}O_6H^*_{16}$ $(\boldsymbol{C}_6\boldsymbol{O}_{0.54}\boldsymbol{H}_{1.45})^{**}$	85.7±1.0	9.59±0.5	1.06±0.5	Exp. [30]
Product 2 $C_{66}O_3H^*_{19}$ $(\boldsymbol{C}_6\boldsymbol{O}_{0.27}\boldsymbol{H}_{1.73})^{**}$	92.0±1.0	5.5±0.5	1.5±0.5	Exp. [29]
Shungite $C_{66}O_2H^*_{20}$ $(\boldsymbol{C}_6\boldsymbol{O}_{0.18}\boldsymbol{H}_{1.82})^{**}$	95,3-92,4***	3.3-2.5***	unknown	Exp. [25]

*Proposed (5, 5) rGO compositions that best fit experimental data.

**Averaged atomic composition per one benzenoid unit.

***The scatter in the data obtained from measurements in four points of one sample.

Usually, rGO structural models are tightly connected with those of GO ones thus relating to the latter when removing all oxygen containing units from the sheet basal plane. There is a large variety of GO models, mainly just 'drawn' basing on a chemical intuition.

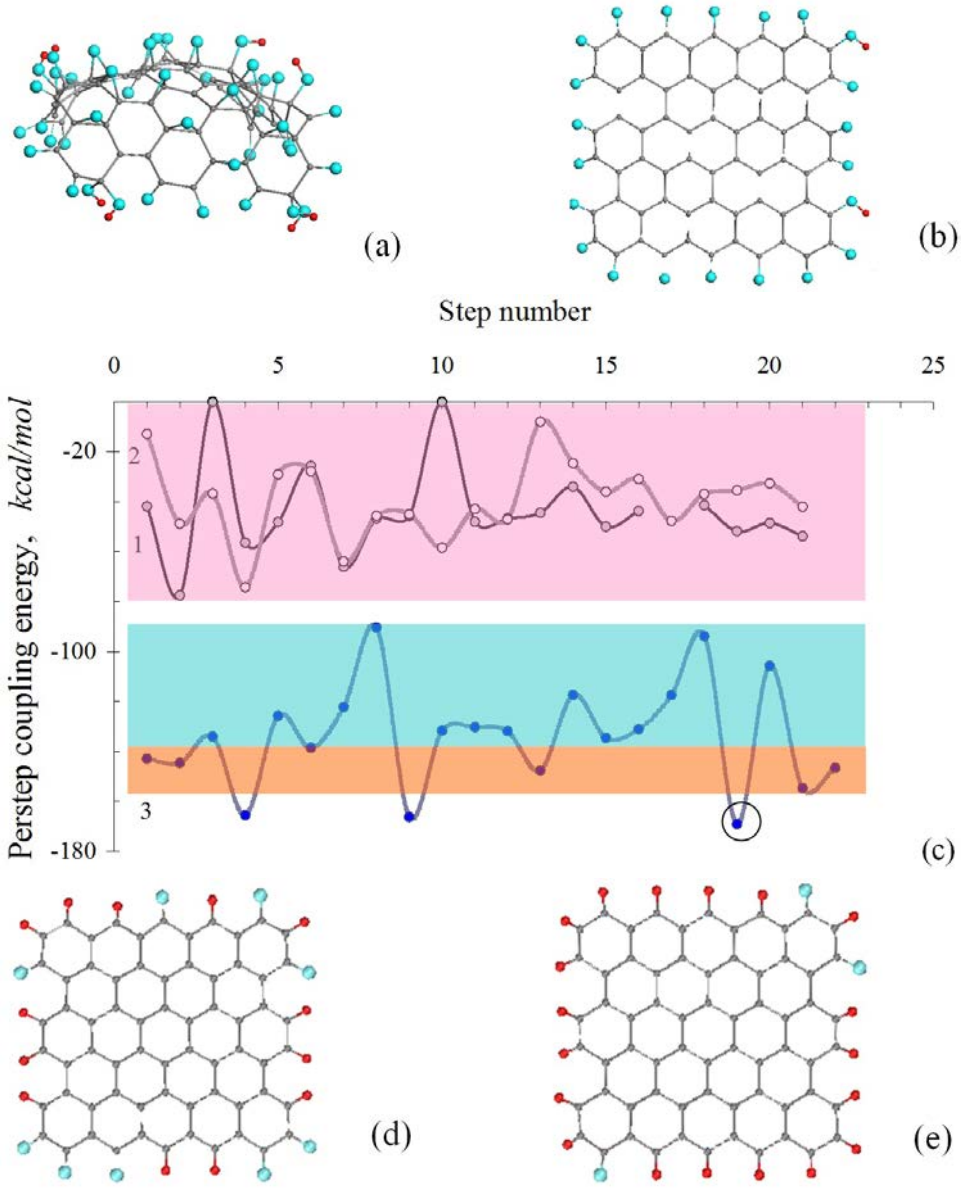

FIG. 7. (a). Equilibrium structure of ∼1 *nm* (5, 5) GO sheet corresponding to one-side oxidation of the pristine (5, 5) NGr molecule [24]. (b). Model rGO sheet corresponding to the first stage of the (5, 5) GO deoxygenating that affects the atoms in the basal plane of the GO sheet only (soft reduction) [24]. (c). *per step* coupling energies related to the one-side oxygenation of the (5, 5) NGr molecule: O- and OH-attachments to the basal plane (curves 1 and 2, respectively) and the combination of O and OH attachments in the circumference (curve 3) [24]; the circled point corresponds to the formation of carbonyl unit on the rGO circumference with the largest coupling energy. (d) and (e) Model (5, 5) rGO sheets corresponding to a medium and hard reduction of the (5, 5) GO in the framework of the blue and blue-and-cream shaded zones in (c), respectively. Gray, blue and red balls present carbon, oxygen, and hydrogen atoms

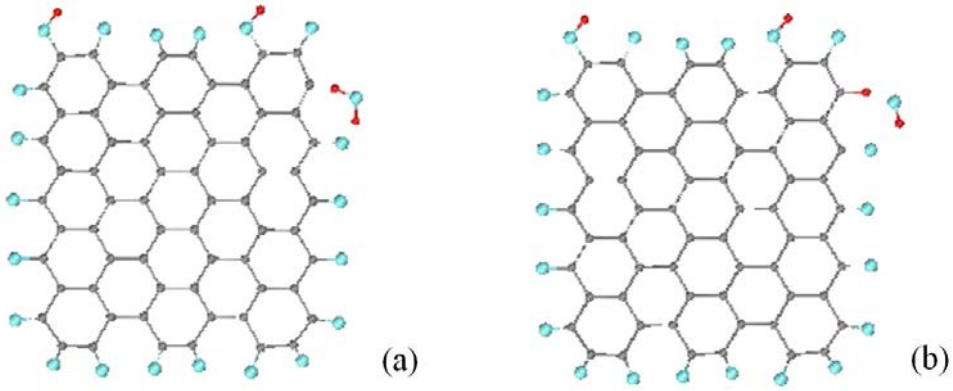

FIG. 8. a. Starting configuration of the complex of one water molecule and the soft-reduced (5, 5) rGO molecule after removing one oxygen atom in the circumference. (b). Equilibrium structure of the (5, 5) rGO + water complex (UHF calculations). The atom colorings see in the caption to Fig.7

On this background, there is a definite preference of that one produced in due course of a sequential polyderivatization of a graphene flake [24] in the framework of the computational experiment subordinated to a particular algorithm [27]. Thus constructed (5, 5) GO molecule is shown in Fig. 7a. The latter was computationally synthesized in the course of the stepwise oxidation of the pristine (5, 5) nanographene (NGr) molecule (a rectangular graphene fragment containing n_a=5 and n_z=5 benzenoid units along armchair and zigzag edges, respectively) in the presence of three oxidants, such as O, OH, and COOH [24].

The GO reduction concerns removing oxygen containing units. As evidences by the *per step* coupling energies, which accompany the attachment of the oxidants to either basal plane atoms (curves 1 and 2 in Fig. 7c) or edge atoms in the circumference area (curve 3), the reduction is obviously multistage or multimode one. Actually, the oxygen atoms located at the basal plane of the pristine (5, 5) GO molecule (within the rose shading) should be removed first. The corresponding (5, 5) rGO molecule is shown in Fig. 7b. This apparently happens at the first stage of the real reduction and may present the final state of the reduction procedure when the latter is either short-time or not very efficient; the relevant reduction might be attributed to a soft one. The corresponding mass content of the obtained rGO molecule is given in Table 2. These and other calculated data in the table are related to the relevant rGO molecules in vacuum.

However, when the reduction occurs during long time or under action of strong reducing agents, it may concern oxidants located at the rGO molecules circumference. Such two-step reduction of a pristine GO has been actually fixed [28]. However, due to a waving character of the *per step* coupling energy dependence with a large amplitude from −90 kcal/mol to −170 kcal/mol, the second step reduction could be highly variable. Thus, limiting the energy interval to 30 kcal/mol (removing oxidants covered by blue shading) results in remaining only 9 oxygen atoms (see Fig. 7d) instead of 22 in the pristine (5, 5) rGO sheet shown in Fig.7b. As seen in Table 2, such a reduction halves the oxygen content and causes the appearance of a remarkable quantity of hydrogen. Further strengthening of the reduction, counted by lowering the number of remaining oxygen atoms, gradually decreases the oxygen content while increasing the hydrogen contribution. Consequently, the structures presented in Figs. 7b, 7d, and 7e might be attributed to rGOs obtained in the course of soft, medium, and hard reduction, respectively.

Coming back to the rGO hydrogenation, we face the problem, whence comes the hydrogen. As discussed in [3], the hydrogenation of the pristine graphene lamellae loses to oxidation on all parameters in the course of the first stage of the graphenization of carbon rich sediments. Therefore, GO sheets similar to that shown in Fig. 7a do not contain either mono-atomic or diatomic hydrogen among its framing atoms. However, the abundance of hot water around GO and rGO sheets, which accompanies the shungite derivation, suggests that water can provide not only the GO reduction (see the corresponding discussion in [3]), but the hydrogenation of the formed rGO as well. Actually, the release of one of the edge carbon atoms of the rGO within the blue zone shown in Fig. 7c from oxygen makes the atom highly chemically active [27] and promotes the dissociation of a water molecule in the vicinity of this atom and neighboring oxygen. A possibility of such reaction in demonstrated in Fig. 8. The water molecule, initially located at 1.10 Å apart from both the carbon and oxygen atoms in Fig. 8a, willingly dissociates (see Fig. 8b) while the formed hydroxyl remains in the vicinity of the newly formed C-H bond, once connected with both the bond hydrogen atom and neighboring oxygen via hydrogen bonds. The energy gain of the reaction constitutes 25.94 *kcal/mol* which points to a high efficacy of the reaction. Evidently, the considered mechanism of the rGO hydrogenation, parallel or alongside with the simultaneous GO reduction, might not be the only one and will strongly depend on the reducing agents such as, for example, alcohols under critical regime [29]. Actually, hydrophobic character of produced rGOs, oppositely to high hydrophilicity of the pristine GO, which is noted by many chemists, strongly evidences the reality of the hydrogenation of pristine rGOs.

When supposing that in due course of the *post factum* hydrogenation of the rGO molecule each of the remaining oxygen atoms is substituted by one hydrogen, the limiting case, presented by $C_{66}H_{22}$polyhydride in Table 2, corresponds to the one-atom-hydrogen termination of the edge atoms of the (5, 5) NGr sheet. However, as shown in [31], in this case, the edge atoms remain yet still chemically active and are able to accept one more hydrogen atom each. The addition of the second hydrogen atom in response to removing one oxygen atom can occur at any stage of the hydrogenation of the circumference area. However, this action influences the oxygen content only slightly due to which the data presented in Table 2 may be used for estimation of the C/O ratio. In contrast, the hydrogen content may considerably increase thus greatly lifting, for example, the IINS intensity, which should be taken into account when analyzing IINS spectra.

6. Chemical composition of rGOs: Comparison with experiment

The dependence of the chemical composition of final products of the GO reduction on the efficacy of the *post factum* hydrogenation results in the formation of a large class of oxyhydrides of graphene that all are covered under the term rGO. This explains the C/O variation characteristic for rGOs of different origin, a large scale of which is observed in practice depending on which namely chemicals and how long the latter are involved in the reduction procedure [2]. A common situation is presented in Table 2 by two extended accounts related to synthetic rGO [29, 30]. As seen from the table, the mass content of the two products is well consistent with that of $C_{66}O_6H_{16}$ and $C_{66}O_3H_{19}$ atomic compositions, the former of which tells about uncompleted (medium) reduction of the rGO circumference area of product 1 while the latter evidences quite hard reduction in the case of product 2. The relevant (5, 5) rGO molecule is shown in Fig. 7e. As for shungite, its formation during a long period of time allows for suggesting a hard type of the reduction, which explains low oxygen content in the carbon-most-reach shungite deposits [25] and simultaneously provides a high stability of the chemical composition of the rGO basic elements. The relevant C/O

mass content given in Table 2 was determined by point microanalysis in different areas of shungite samples when performing an extensive HRTEM study. According to the data, the chemical composition of shungite is in between $C_{66}O_2H_{20}$ and $C_{66}O_1H_{21}$ compositions, closer to the former.

TABLE 3. Chemical composition and mass content of reduced (5, 5) rGO of the $C_{66}O_1H_{21}$ chemical composition in the presence of retained water

Atomic composition	Mass content, wt %			Remarks
	C	O	H	
$C_{66}O_1H_{21}$ $(\boldsymbol{C}_6\boldsymbol{O}_{0.09}\boldsymbol{H}_{1.91})^*$	95.54	1.93	2.53	calc.
$C_{66}O_1H_{21} + 2H_2O$	91.56	5.55	2.89	calc.
Shungite	96.52–92.52	4.22–2.43	unknown	Exp. [25]

*Averaged atomic composition per one benzenoid unit.

The above analysis concerned rGO models in vacuum while the current study has revealed 4wt% water in shungite sustained under ambient conditions. The water content corresponds to 34 a.u. and 35 a.u. with respect to the total mass of the above two compositions, respectively, which points to the presence of two water molecule per each (5, 5) rGO sheet resulting in replacing the previous compositions by $C_{66}O_4H_{24}$ and $C_{66}O_3H_{25}$. Assuming that the composition mass content must be consistent with empirical data for shungite and basing on the C/O regulation presented in Table 2, the preference should be given to the latter one in contrast to the former that provides too high oxygen content. Table 3 presents the mass content redistribution caused by retained water. As seen in the table, new data are quite consistent with experimental thus allowing to lay the $C_{66}O_1H_{21}$ composition of the (5, 5) rGO sheet into the ground of a reliable model for shungite structure.

7. Basic elements of shungite fractal structure

Taking $\sim$1 *nm* (5, 5) rGO sheet of $C_{66}O_1H_{21}$ atomic composition as the model basic element of shungite as well as four-six-layer stacks of the element (see the top part of Fig. 9), is possible to suggest a microscopic vision of the shungite at the third level of its fractal structure concerning individual globules. Irregular structures of the stacks in Fig.9 reflect a possible presence of both translational and rotational disorder (turbostratic structure) of the latter [14]. Presented in Fig. 10 is a planar projection of a globe structure voluntary packed with differently projected stacks of different size. The interglobe pores are compatible with linear dimensions of rGO stacks and are quite suitable for retaining water. As for retained water, it is well known that in the low-frequency region (0–1000 cm^{-1}), the IINS spectrum of bulk water $G^{ice}(\omega)$ shows a hindered translational spectrum (I and II in Fig. 6b) alongside with the low-frequency Debye phonon-like acoustical contribution and a librational spectrum (III). Both the hindered translational and rotational (librations) modes are present in water because of intermolecular hydrogen bonds (HB) that are formed by each water molecule surrounded by other four ones. The configuration changes when water molecules can not move freely in space due to which it is quite natural to expect a strong spectral modification when passing from the bulk to retained water, which is clearly seen in Fig. 6a. Actually, the only ice mode positioned at $\sim$56 cm^{-1} (HB bending) is retained in the $G^{wat}(\omega)$ spectrum while $\sim$150 cm^{-1} (HB bending) as well as $\sim$224 and $\sim$296 cm^{-1} (HB stretchings)

ice modes reveal clearly seen flattening and downshift. Analogous spectral modification takes place with respect to the ice librational modes forming a broad band in the region of 600–1200 cm^{-1}. The band is provided with water molecule rotations around three symmetry axes whose partial contribution determines the band shape. As shown by detail studies [18, 20], the modes conserve their dominant role in the IINS spectra of retained water, albeit are downshifted, when water molecules are coupled with the pore inner surface via hydrogen bonds. This very behavior is characteristic for the $G^{wat}(\omega)$ spectrum in Fig. 6a. The three-ax partial contribution is sensitive to both chemical composition of the pore walls and the pore size [20]. Thus, the downshift of the red edge of the band from 550 cm^{-1} to 320 cm^{-1} when going from the $G^{ice}(\omega)$ spectrum to the $G^{wat}(\omega)$ one highlights the shungite pore size of a few nm, which is well consistent with SANS data [23].

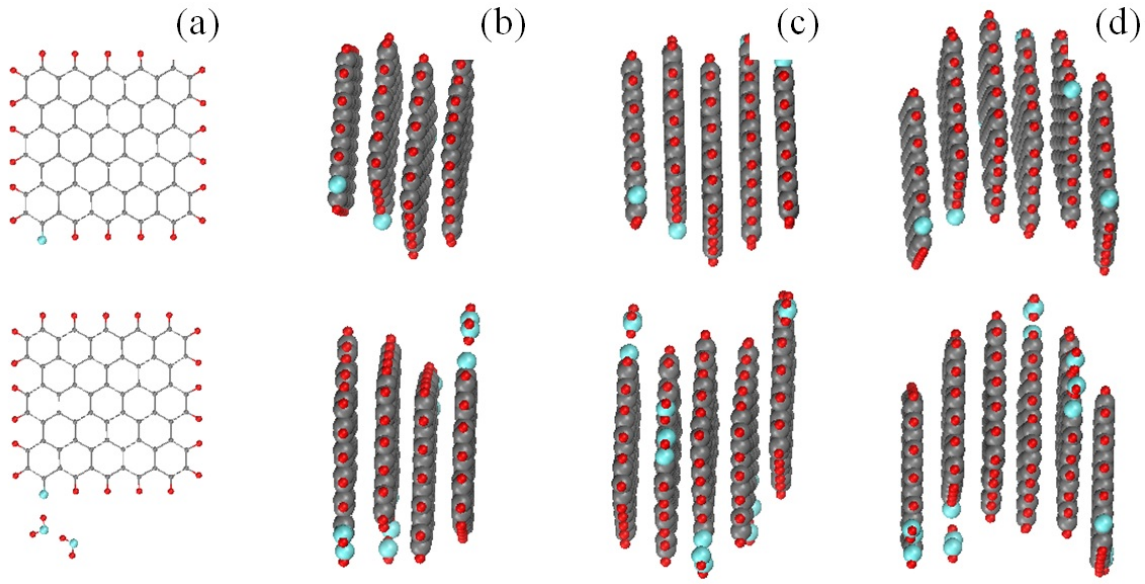

FIG. 9. (a). Equilibrium structure of ∼1 nm (5, 5) rGO sheets of the $C_{66}O_1H_{21}$ chemical composition, 'dry' (top) and 'wet' (bottom), respectively. (b)–(d). Arbitrary models of four-, five-, and six-layer stacks of the relevant rGO sheets with 3.Å interlayer distance. The atom colorings see in the caption to Fig.7

As was mentioned earlier, 4 wt% water in Sh1 implies two water molecules per one rGO sheet of the $C_{66}O_1H_{21}$ chemical composition. The two molecules are evidently located in the vicinity of the only oxygen atom in the sheet circumference, once connected with both the atom and between each other by hydrogen bonds (see the bottom of Fig. 9). Analogously to 'dry' sheets, the 'wet' ones are grouped in graphite-like stacks that form globules when aggregating. A possible model of such a globe is shown in Fig. 11. As seen in the figure, the stacks with water molecules can be comfortably packed forming pores of a comparable size. The stacks surface forms the inner surface of the pores that are carpeted with hydrogens while the only oxygen atom is shaded by two water molecules. The amount of oxygen atoms determines the quantity of water which is bound with the pore surface thus considerably limiting the monolayer coverage of the pores at much lower level than that revealed by the IINS study of graphene oxide [19].

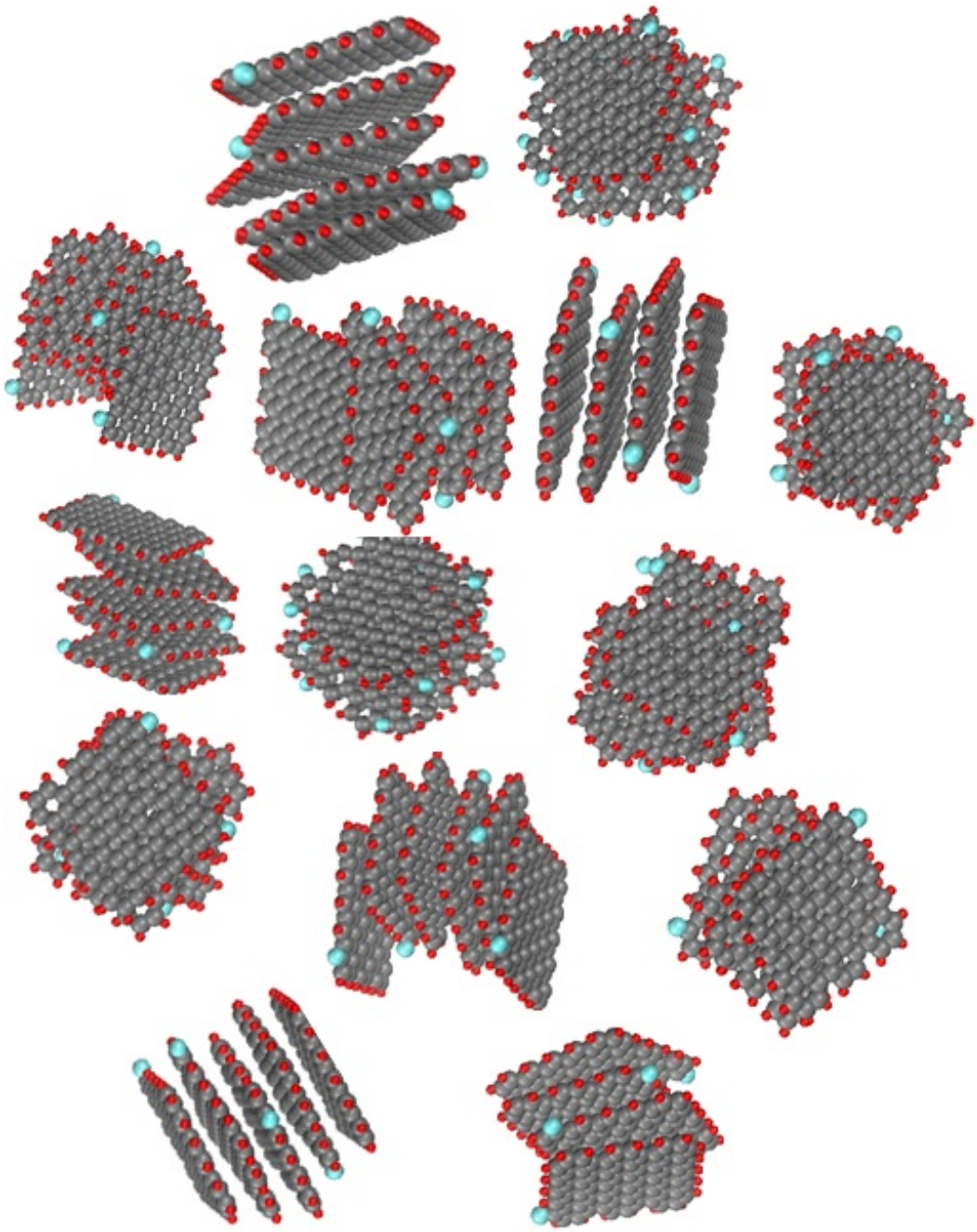

FIG. 10. Planar presentation of a model of 'dry' shungite globule consisting of a set of four-, five- and six-layer stacks of 'dry' (5, 5) rGO sheets of the $C_{66}O_1H_{21}$ chemical composition voluntary located and oriented in space. Linear dimensions along the vertical and horizontal are of $\sim$6 *nm*. The atom colorings see in the caption to Fig.7

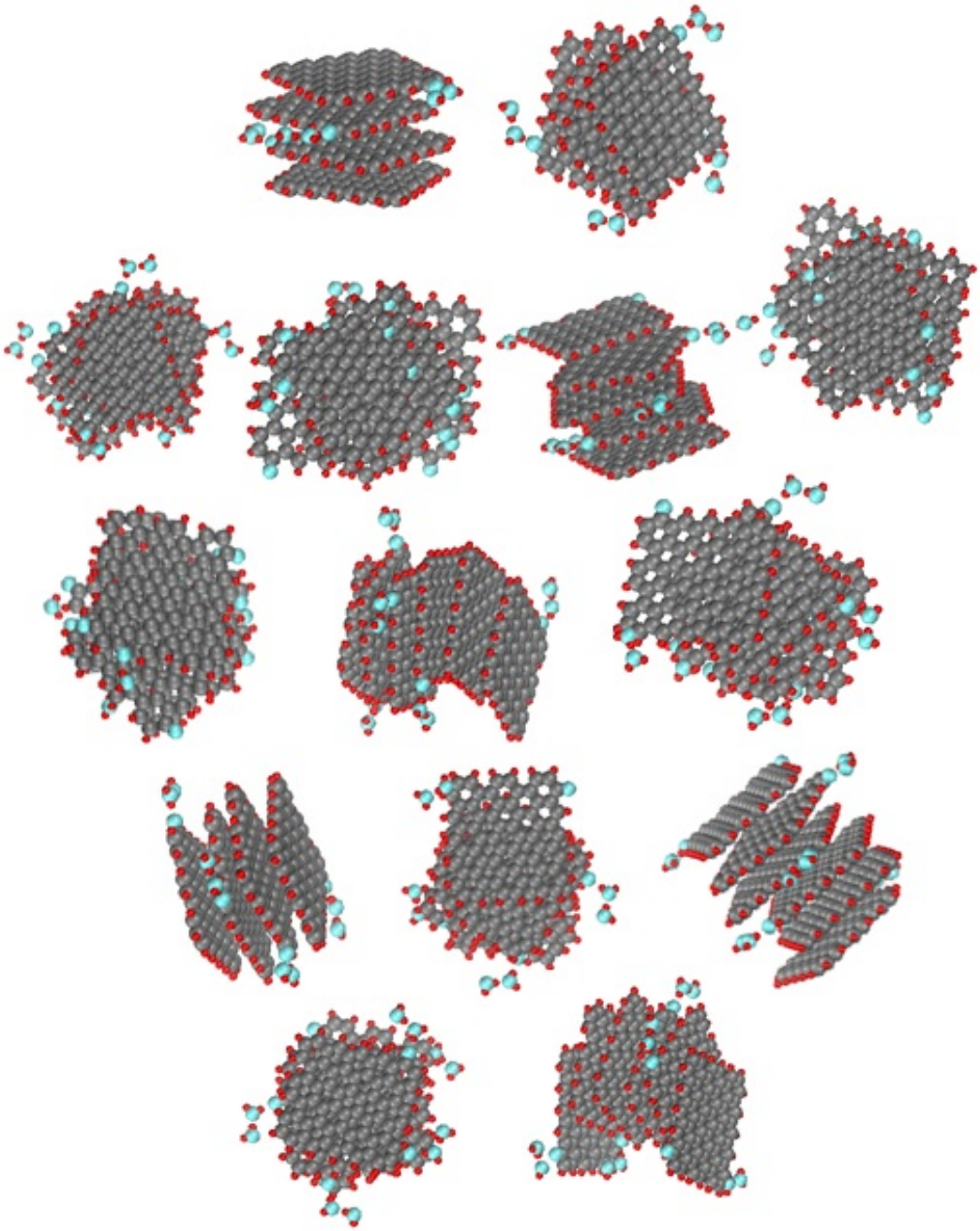

FIG. 11. Planar presentation of a model of 'wet' shungite globule consisting of a set of four-, five- and six-layer stacks of 'wet' (5, 5) rGO sheets of the $C_{66}O_1H_{21}$ chemical composition voluntary located and oriented in space. Linear dimensions along the vertical and horizontal are of ∼6 *nm*. The atom colorings see in the caption to Fig.7

8. Conclusion

The performed neutron scattering study allows putting certain ends in the study of the structure and chemical composition of shungite. The rGO nature of the basic structural element, its size and chemical composition as well as five-six-layer stacking have received an experimental confirmation fully supporting the general concept on the shungite structure suggested earlier [3]. Both the linear size of individual rGO sheets and the sheet stacks are responsible for the obtained L_{CSR} values of 2–3 *nm* and 1.5–2 *nm*, respectively. The former characterizes not only the lateral dimension of the rGO sheets but the presence of both translational and rotational disorder (turbostratic structure) of the stack layers, the latter concerns stacks' thickness. The stacks of such dimension form globules of ∼6–8 *nm* in size (the third level of structure) while the latter produce agglomerates of 20 *nm* and more (the forth level of structure) completing the fractal packing of shungite. The basic rGO fragments are hard reduced products, actually, only slightly oxygenated graphene hydrides, of an averaged stable chemical composition described by ∼6:0.1:2 (C:O:H) atom content ratio. The sheet planarity, drastically distorted for the pristine GOs (see Fig. 7a), is fully restored thus allowing to speak about 'flat graphene' that is a highly important raw material for the modern graphene technologies and the natural pantry of which is presented by shungite deposits of Karelia.

Acknowledgement

The authors greatly appreciates financial support of RSF grants 14-08-91376 (E. Sh.) and 13-03-00422 (N.R.) as well as the Basic Research Program, RAS, Earth Sciences Section-5. The grants of the Polish Plenipotentiary in JINR for the modernization project of the NERA spectrometer in 2007–2012 are gratefully acknowledged.

References

[1] Luo J., Kim J., Huang J. Material processing of chemically modified graphene: Some challenges and solutions. *J. Acc Chem. Res.*, **46**, P. 2225–2234 (2013).
[2] Chua C.K., Pumera M. Chemical reduction of graphene oxide: a synthetic chemistry viewpoint. *Chem. Soc. Rev.*, **43**, P. 291–312 (2014).
[3] Sheka E.F., Rozhkova N.N. Shungite as the natural pantry of nanoscale reduced graphene oxide *Int. J. Smart Nano Mat.*, **5**, P. 1–16 (2014).
[4] Rozhkova N.N. Shungite Nanocarbon (in Russ). Karelian Research Centre of RAS, Petrozavodsk (2011).
[5] Rozhkova N.N. Aggregation and stabilization of shungite carbon nanoparticles. *Russ J Gen Chem*, **83**, P. 2676–2685 (2013).
[6] Razbirin B.S., Rozhkova N.N., Sheka E.F., et. al. Fractals of graphene quantum dots in photoluminescence of shungite. *J. Exp.Theor. Phys.*, **118**, P. 735–746 (2014).
[7] Razbirin B.S., Rozhkova N.N., Sheka E.F. Photonics of shungite quantum dots arXiv:1406.1703v1 [cond-mat.mtrl-sci] (2014).
[8] Li L., Wu G., Yang G., Peng J., Zhao, Zhu J.J. Focusing on luminescent graphene quantum dots: current status and future perspectives. *Nanoscale*, **5**, P. 4015–4039 (2013).
[9] Sheka E.F., Natkaniec I., Rozhkova N.N., HoldernaNatkaniec K. Neutron scattering study of reduced graphene oxide of natural origin. *JETP Lett.*, **118**, P. 735–746 (2014).
[10] Rozhkova N.N., Gribanov A.V., Khodorkovskii M.A. Water mediated modification of structure and physical chemical properties of nanocarbons. *Diam. Rel. Mat.*, **16**, P. 2104–2108 (2007).
[11] Natkaniec I., Bragin S.I., Brankowski J., Mayer J. NERA spectrometer at IBR2 in Proc ICANS XII Meeting, Abington 1993, RAL Report 94-025 I: 89–85 (1994).
[12] Opalev S.V., Belenkov E.A. Experimental study of changing graphite structure under milling. (in Russ.) *Izvestiya Chelyabinskogo Nauchnogo Centra*, **3**, P. 27–30 (2004).

[13] Emel'yanova G.I., Gorlenko L.E., Rozhkova N.N. et. al. Effect of the conditions of structure formation on the physicochemical properties of ozonated shungites. *Russ. J. Phys. Chem. A*, **84**, P. 1376–1381 (2010).
[14] Kovalevski V.V., Buseck P.R., Cowley J.M. Comparison of carbon in shungite rocks to other natural carbons: An X-ray and TEM study Carbon, **39**, P. 243–256 (2001).
[15] Bokhenkov E.L., Natkaniec I., Sheka E.F. Determination of the density of phonon states of naphthalene crystal from inelastic incoherent neutron scattering. *J. Exp. Theor. Phys.*, **43**, P. 536–545 (1976).
[16] Hall P.G., Pidduck A., Wright C.J. Inelastic neutron scattering by water adsorbed on silica. *J. Colloid. Interface Sci.*, **79**, P. 339–344 (1981).
[17] Sheka E.F., Khavryutchenko V.D., Markichev I.V. Technological polymorphism of disperse amorphous silicas: inelastic neutron scattering and computer modeling Russ. *Chem. Rev.*, **64**, P. 389–414 (1995).
[18] Crupi V., Majolino D., Migliardo P., Venuti V. Neutron scattering study and dynamic properties of hydrogen-bonded liquids in mesoscopic confinement. 1. The water case. *J. Phys. Chem. B*, **106**, P. 10884–10894 (2002).
[19] Buchsteiner A., Lerf A., Pieper J. Water dynamics in graphite oxide investigated with neutron scattering. *J. Phys. Chem. B*, **110**, P. 22328–22338 (2006).
[20] Corsaro C., Crupi V., Majolino D. et. al. Inelastic neutron scattering study of water in hydrated LTA-type zeolites. *J. Phys. Chem. A*, **110**, P. 1190–1195 (2006).
[21] Natkaniec I., Sheka E.F., Drubicki K. et. al. arXiv:1411.xxxx [cond-mat.mtrl-sci] (2014).
[22] Bertrand C.E., Zhang Y., Chen S.H. Deeply-cooled water under strong confinement: neutron scattering investigations and the liquid–liquid critical point hypothesis. *Phys. Chem. Chem. Phys.*, **15**, P. 721–745 (2013).
[23] Avdeev M.V., Tropin T.V., Aksenov V.L. et. al. Pore structures in shungites as revealed by small-angle neutron scattering Carbon. **44**, P. 954–961 (2006).
[24] Sheka E.F., Popova N.A. Molecular theory of graphene oxide. *Phys. Chem. Chem. Phys.*, **15**, P. 13304–13322 (2013).
[25] Golubev E.A., Suvorova T., Sheka E.F. HRTEM structure and microanalysis of shungite. arXiv:1411.xxxx [cond-mat.mtrl-sci] (2014).
[26] Druzbicki K., Natkaniec I. Vibrational properties of water retained in graphene oxide. *Chem. Phys. Lett.*, **600**, P. 106–111 (2014).
[27] Sheka E.F. Computational strategy for graphene: Insight from odd electrons correlation Int. *J. Quant. Chem.*, **112**, P. 3076–3090 (2012).
[28] Xu Z., Bando Y., Liu L. et. al. Electrical conductivity, chemistry, and bonding alternations under graphene oxide to graphene transition as revealed by *in situ TEM. ACS Nano*, **5**, P. 4401–4406 (2011).
[29] Tkachev S.V., Buslaeva E.Yu., Naumkin A.V. et. al. Reduced graphene oxide *Inorg. Mater.*, **48**, P. 796–802 (2011).
[30] Stobinski L. www.nanomaterials.pl (2014).
[31] Sheka E.F., Popova N.A. Odd-electron molecular theory of the graphene hydrogenation. *J. Mol. Mod.*, **18**, P. 3751–3768 (2012).

NANOSYSTEMS: PHYSICS, CHEMISTRY, MATHEMATICS, 2014, 5 (5), P. 677–684

ELECTRIC FIELD ENHANCEMENT OF GOLD TIP OPTICAL ANTENNA WITH SPECIAL GEOMETRY

M. Zohrabi

Department of Optics and Nanophotonics, Institute of Physics, Kazan Federal University, Kazan, Russia

zh_als@yahoo.com

PACS 78.67.-n

This paper provides a new design for a gold tip optical antenna based on a specific geometry, and then, the change of electric field enhancement for plane wave laser excitation with 400 to 700 nm in the vicinity of optical antenna are simulated. Progressions of geometry incorporate the change of period of circular grating from 200–300 nm, on the shaft of antenna. In addition, the distribution of enhancement of the electric field in a plane perpendicular to the shaft has been acquired. Finally, the optimal value for the maximum enhancement at the period of 208.843 nm is calculated.

Keywords: optical antenna, tapered gold tip, field enhancement, surface plasmon.

Received: 10 July 2014
Revised: 11 August 2014

1. Introduction

An optical antenna is a device which is designed to efficiently convert free-propagating optical radiation to localized energy, and vice versa [1]. They can enhance the coupling between free-space propagating light and the localized excitation of nanoscopic light emitters or receivers, thus forming the basis for many nanophotonic applications. Additionally, they can enhance the interaction between light and matter by several orders of magnitude and localize the energy of electromagnetic radiation in the subwavelength region. With the assistance of optical antennas, the diffraction Abbe limit can be overcome, leading to new opportunities in advanced optical spectroscopy and microscopy in the subwavelength range. Because of these properties, a subwavelength optical antenna would allow the detection of high frequency spatial features and the analysis of the electronic and vibrational structure for nanoscale objects. Properties of localized plasmons critically depend on the shape of the nanoparticles, which allows selective "tuning" of the system resonances to an effective interaction between light and matter.

This has potential for an extensive range of novel photonic applications, including chemical [2,3] and thermal sensors [4], near-field microscopy [5,6], nanoscale photodetectors [7], and plasmonic devices [8,9]. By utilizing optical antenna, it is possible to concentrate the energy of the laser in a little scale zone such as nanometer. The gold tip is one of the most popular optical antennas in the recent years. One advantage of this antenna, is the breaking of the diffraction limit. The enhancement in the electrical field around the gold tip as a result of the plasmon resonance, which is dependent on the antenna geometry and the impact of lightning rod effect [10]. Direct irradiation of the tip apex, in the near-field optical scanning microscope (NSOM) prompted the creation of a foundation signal and suppression of the efficiency of the antenna and thus, numerous explorations have been carried out to reduce this issue. Adiabatic nanofocusing along conical metal tapers describes a coherent

transport of optical excitations in the form of surface plasmon polariton (SPP) waves over several tens of μm and the concentration of this energy into a nanometric volume at the taper apex. In the adiabatic limit, i.e., if the waveguide cross section variation is slow and relative changes of the SPP wave vector are small, on the scale of the SPP wavelength, radiative and reflective losses are minimized and energy transport to the apex is expected to be particularly efficient [3]. From an application perspective, adiabatic nanofocusing results in the creation of a single, dipole-like emitter, spatially localized to a few nm and with an intense optical near field. Such an emitter holds a high potential for, e.g., ultrahigh resolution optical microscopy, tip-enhanced Raman spectroscopy, or extreme ultraviolet (EUV) generation.

Raschke Et al [11] proposed the concept of adiabatic nanofocusing, in this method by reducing the size of the region in which enhancement of electric field occurs, the background might be greatly diminished. In the adiabatic nanofocusing method, first, the surface plasmon of the shaft is energized, then the surface plasmon travels to the apex of tip and is finally converted to the localized plasmon in the apex. In this paper, the geometry of the ordinary gold tip has been changed. Moreover, circular gratings with a period of 200, 250 and 300 nm have been included. Maxwell equations with FDTD simulation numerical software have been utilized to obtain the results. Using this geometry, a different peak, resulting from grating surface plasmon excitation, was obtained.

2. Methodology

The finite-difference time-domain (FDTD) approach is a reliable method for solving Maxwell's equations with complex geometries [14]. FDTD provides time domain information, offering insight into the electrodynamics of a system [15]. In FDTD, the electromagnetic field and structural materials of interest are described on a discrete mesh composed of so-called Yee cells.

Maxwell's equations are solved discretely in time, where the time step used is related to the mesh size through the stability criterion. This technique is an exact representation of Maxwell's equations in the limit that the mesh spacing goes to zero. All the calculated and reported intensities are normalized with respect to the intensity of the incident light. In side illumination, the light is linearly polarized along the tip axis. The software lumerical, based on the FDTD method, is utilized. The FDTD approach has rapidly become to one of the most important computational methods in Electromagnetics since Yee proposed it in 1966 [16]. The FDTD method involves the discretization of Maxwell's equations in both the time and the space domain in order to find the E and H fields at different positions and at different time-steps. The FDTD method can conveniently be applied to simulating the electromagnetic scattering and radiation from a target of complex shape as well as non-uniform dielectric objects by simply adjusting the number, size and material properties of the Yee cell [17].

Only the electric field component is chosen to evaluate the enhancement. The light intensity is presented by the square of the electric field intensity, which has the same tendency with the light intensity.

To generate a strong field enhancement at the tip, the electric field of the exciting laser beam needs to be polarized along the tip axis. The influence of tip shape and material on the field enhancement has been discussed in a series of publications with the aim of discovering the optimum tip [18, 19].

The electric field around the optical antenna is calculated and simulated based on Maxwell's equations:

$$E(r) = E_0 + i\omega\mu\mu_0 \int_v \bar{G}(r, r')j(r')dV', \tag{1}$$

and

$$H(r) = H_0 + \int_v [\nabla \times \bar{G}(r, r')]j(r')dV', \tag{2}$$

where $\bar{G}$ is the dyadic Green's function and E_0 represents the initial electric field for the plane wave laser.

3. Simulation results

In this work, we investigated the influence of tip shape on the field enhancement. We assumed a golden tip, a 10 – nm radius of apex and a 30°. Cone angle and three proposed period of grating which are 200, 250 and 300 nm. The laser beam is considered as a plane wave with the wavelength of 400–700 nm. The considered model and the simulation results for the considering grating period are shown in following figures.

Figure 1 illustrates the shape of proposed optical antenna with 200 nm period grating.

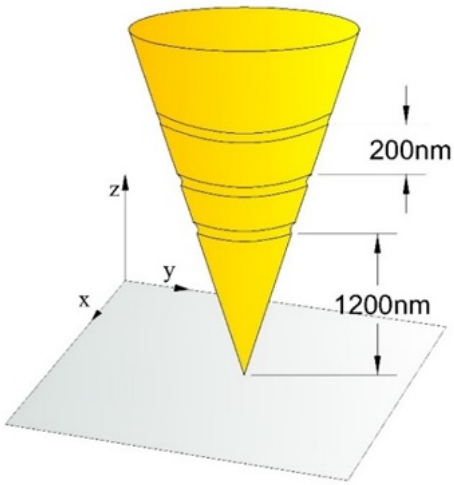

FIG. 1. Considered shape for optical antenna

Figures 2 show the intensity distribution for three proposed period of grating with 90 degree laser incident angle in X and Y axis.

These figures confirm that there are no significant changes in the intensity distribution in the plane of X–Y where Z = 0 nm.

Figures 3 to 5 represent the distribution intensity in X and Y directions for three proposed grating periods. Moreover, the curves of enhancement for the X and Y component of electric field versus their wavelength are depicted.

According to the simulation results, it can be concluded that by changing the grating period on the shaft, the resonance can be shifted, which results in changing the distribution of the electric field enhancement.

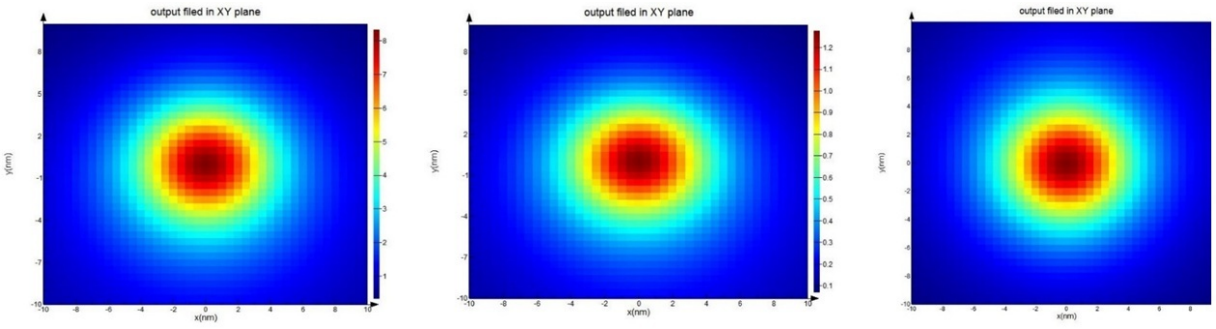

(a) (b) (c)

FIG. 2. (a) Intensity distribution with 200 nm period grating. (b) Intensity distribution with 250 nm period grating. (c) Intensity distribution with 300 nm period grating

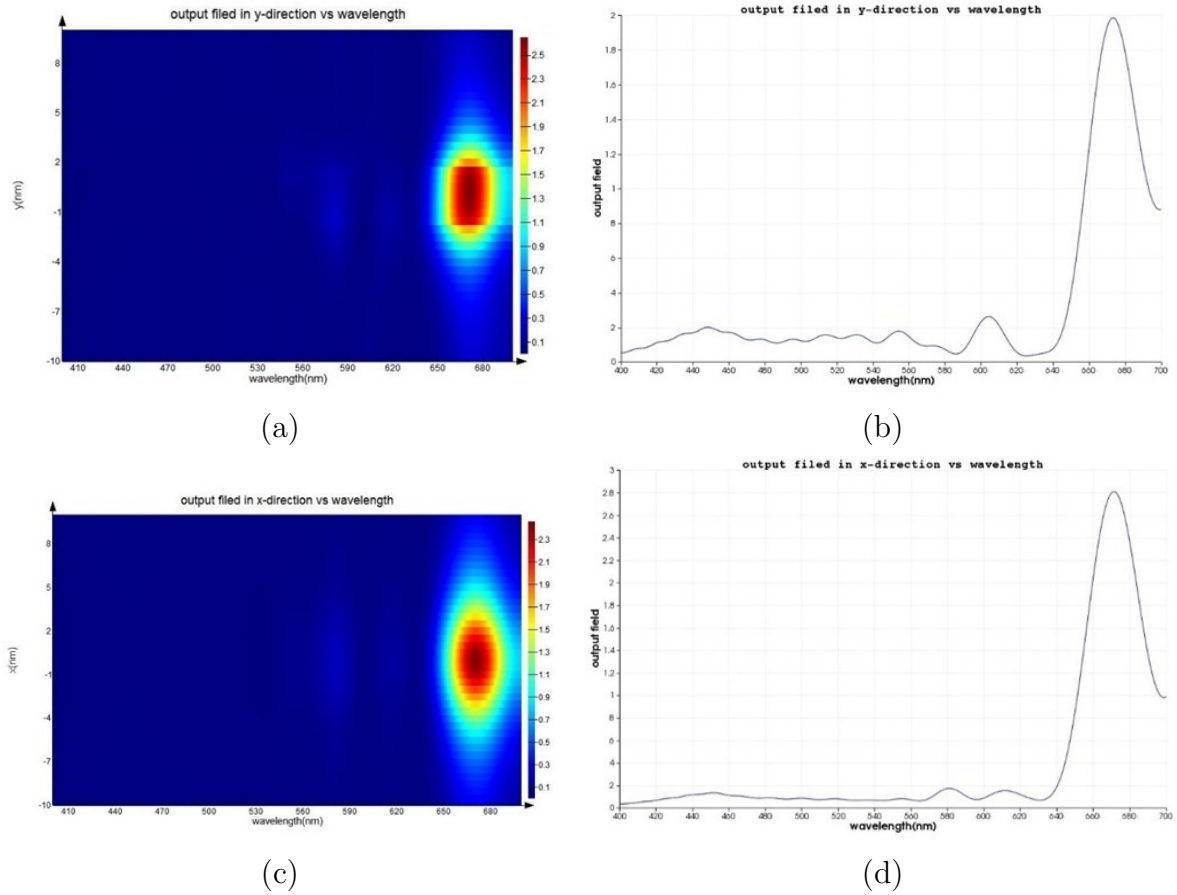

(a) (b)

(c) (d)

FIG. 3. Results with 200 nm period grating: (a) the distribution intensity with y on the line of x=0, z=0 (b) the curve of enhancement of y component of electric field in y=0 versus wavelength (c) the intensity distribution intensity with an x on the line of y=0, z=0 (d) the curve of enhancement of the x component of electric field in x=0 versus wavelength

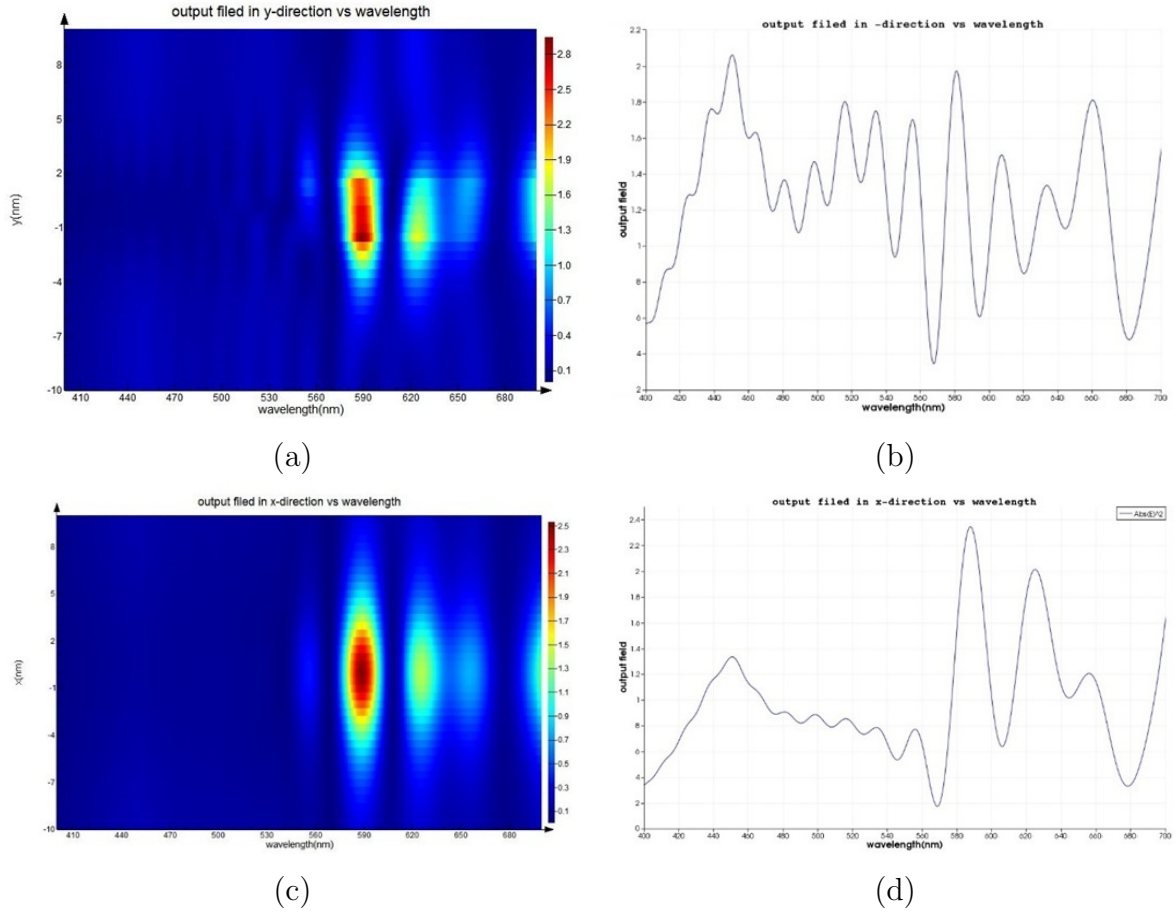

FIG. 4. Results with 250 nm period grating: (a) the distribution intensity with y on the line of x=0, z=0 (b) the curve of enhancement of y component of electric field in y=0 versus wavelength (c) the intensity distribution intensity with an x on the line of y=0, z=0 (d) the curve of enhancement of the x component of electric field in x=0 versus wavelength

4. Maximize the electric field enhancement

Obtaining the maximum enhancement in an electric field is an important fact and can be utilized for the optimum design of an antenna. The optimized value for the grating period, based on the maximum electric field enhancement, is 208.843 nm.

The results of the optimization and maximum enhancement of the electric field for the new period of grating are illustrated in figure 6.

5. Conclusion

In this work, to calculate the enhancement of electric field intensity in the near – field area, the FDTD algorithm was applied. To summarize, the enhancement of the near-field using an apertureless probe system has been verified. The proposed gold tip optical antenna has a special geometry, a series of concentric circular gratings added to the shaft. The simulated model shows that by changing the grating period on the shaft, the resonance can be shifted, leading to a change in the distribution of the electric field enhancement. Changes of geometry include a change in the circular grating period from 200–300 nm, on the shaft of

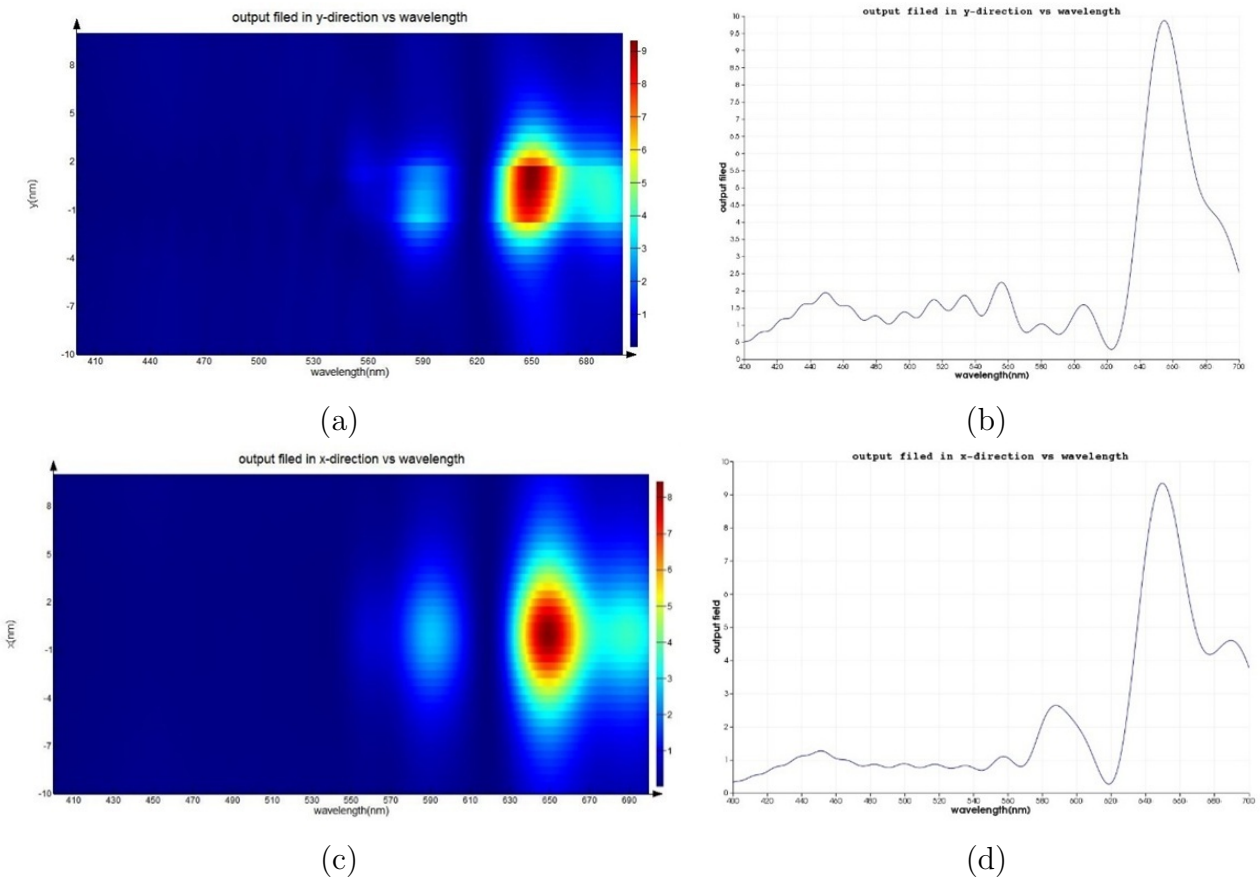

FIG. 5. Results with 300 nm period of the grating: (a) the distribution intensity with y on the line of x=0, z=0 (b) the curve of enhancement of y component of electric field in y=0 versus wavelength (c) the intensity distribution intensity with an x on the line of y=0, z=0 (d) the curve of enhancement of the x component of electric field in x=0 versus wavelength

the antenna. The distribution of the electric field enhancement in a plane perpendicular to the shaft for the three samples has been analyzed. In addition, investigation revealed that the maximum electric field enhancement occurs at a period of 208.843 nm.

Acknowledgments

The authors wish to thank prof. R. H. Gajnutdinov, for helpful discussions. We are also grateful to Department of Optics and Nanophotonics, Kazan Federal University for giving us access to their equipment.

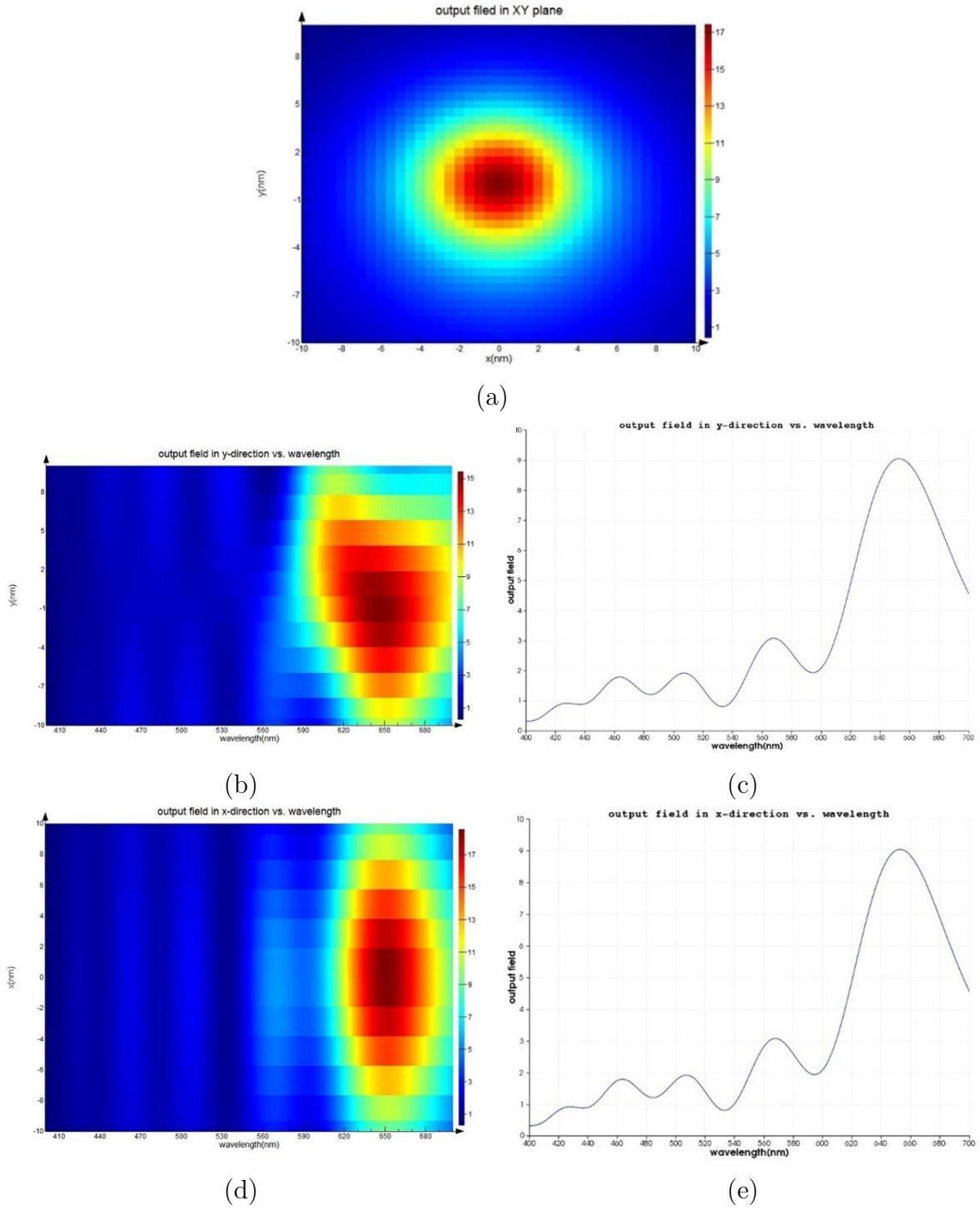

FIG. 6. Intensity distribution in simulation result when the grating period is 208.843 nm (optimized) with 90 degree laser incident angle. (a) the intensity distribution in the plane of x-y (z = 0 nm), (b) the distribution intensity with y on the line of x=0, z=0 (c) the curve of enhancement of y component of electric field in y=0 versus wavelength (d) the intensity distribution intensity with an x on the line of y=0, z=0 (e) the curve of enhancement of the x component of electric field in x=0 versus wavelength

References

[1] Lukas Novotny, Palash Bharadwaj, Bradley Deutsch. Optical Antennas. *Advances in Optics and Photonics*, **1**(3), P. 438–483 (2009).

[2] T. H. Taminiau, F. D. Stefani, F. B. Segerink, and N. F. van Hulst. Optical antennas direct single-molecule emission. *Nat. Photonics*, **2**, P. 234–237 (2008).

[3] V. Giannini and J. A. Sanchez-Gil. Excitation and emission enhancement of single molecule fluorescence through multiple surface-plasmon resonances on metal trimer nanoantennas. *Opt. Lett.*, **33**, P. 899–901 (2008).

[4] P. Krenz, J. Alda, and G. Boreman. Orthogonal infrared dipole antenna. *Infrared Phys. Technol.*, **51**, P. 340–343 (2008).

[5] N. Yu, E. Cubukcu, L. Diehl, M. A. Belkin, K. B. Crozier, F. Capasso, D. Bour, S. Corzine, and G. Höfler. Plasmonic quantum cascade laser antenna. *Appl. Phys. Lett.*, **91**, P. 173113–3 (2007).

[6] A. Cvitkovic, N. Ocelic, J. Aizpurua, R. Guckenberger, and R. Hillenbrand. Infrared imaging of single nanoparticles via strong field enhancement in a scanning nanogap. *Phys. Rev. Lett.*, **97**, P. 060801 (2006).

[7] L. Tang, S. E. Kocabas, S. Latif, A. K. Okyay, D.-S. Ly-Gagnon, K. C. Saraswat, and D. A. B. Miller. Nanometre-scale germanium photodetector enhanced by a near-infrared dipole antenna. *Nat. Photonics*, **2**, P. 226–229 (2008).

[8] M. Pelton, J. Aizpurua, and G. Bryant. Metal-nanoparticle plasmonics. *Laser Photon. Rev.*, **2**, P. 136–159 (2008).

[9] J. N. Farahani, D.W. Pohl, H.-J. Eisler, and B. Hecht. Single quantum dot coupled to a scanning optical antenna: A tunable superemitter. *Phys. Rev. Lett.*, **95**, P. 017402–4 (2005).

[10] Liao, P. F., and A. Wokaun. Lightning rod effect in surface enhanced Raman scattering. *The Journal of Chemical Physics*, **76.1**, P. 751–752 (1982).

[11] S. Berweger, J. M. Atkin, R. L. Olmon, and M. B. Raschke. Adiabatic tip-plasmon focusing for nano-Raman spectroscopy. *The Journal of Physical Chemistry Letters*, **1.24**, P. 3427–3432 (2010).

[12] Höppener, Christiane, Ryan Beams, and Lukas Novotny. Background suppression in near-field optical imaging. *Nano letters*, **9.2**, P. 903–908 (2009).

[13] C. Ropers, C. C. Neacsu, M. B. Raschke, M. Albrecht, C. Lienau, and T. Elsaesser. Light confinement at ultrasharp metallic tips. *Japanese Journal of Applied Physics*, **47.7S2**, P. 6051–6054 (2008).

[14] A. Taflove and S. C. Hagness. *in Computational Electrodynamics: the Finite - Difference Time – Domain Method*. Artech House (2000).

[15] B. C. Galarreta, I. Rupar, A. Young, and F. Lagugné-Labarthet. Mapping hot-spots in hexagonal arrays of metallic nanotriangles with azobenzene polymer thin films. *J. Phys. Chem. C*, **115**(31), P. 15318–15323 (2011).

[16] L. Novotny. Optical antennas tuned to pitch. *Nature*, **455**, P. 879 (2008).

[17] Frey HG, Witt S, Felderer K, Guckenberger R, High-resolution imaging of single fluorescent molecules with the optical near-field of a metal tip. *Physical review letters*, **93.20**, P. 200801 (2004).

[18] Gerton J.M., Wade L.A., Lessard G.A., Ma Z., Quake S.R. Tip-enhanced fluorescence microscopy at 10 nanometer resolution *Physical review letters*, **93.18** (2004).

[19] Martin, Y. C., Hamann, H. F., Wickramasinghe, H. K. Strength of the electric field in apertureless near-field optical microscopy. *J. Appl. Phys.*, **89**, P. 5774–5778 (2001).

NANOSYSTEMS: PHYSICS, CHEMISTRY, MATHEMATICS, 2014, 5 (5), P. 685–691

REGULARITIES OF LIGHT DIFFUSION IN THE COMPOSITE MATERIAL PENTAERYTHRIOL TETRANITRATE – NICKEL

A. A. Zvekov[1], M. V. Ananyeva[2], A. V. Kalenskii[2], A. P. Nikitin[1]

[1] Institute of Coal Chemistry and Material Science SB RAS, Kemerovo, Russia,
[2]Kemerovo State University, Kemerovo, Russia

kriger@kemsu.ru, zvekovaa@gmail.com

PACS 52.25.Tx, 82.40.Fp

The solution of the radiative transfer equation in the layer of a diffusing medium with Frenel fronts was observed by the example of light transfer in a dielectric medium containing nickel nanoparticles. The method of spherical harmonics was used. A scattering indicatrix was calculated for 532 nm light for 140 nm nickel nanoparticles in a pentaerythriol tetranitrate matrix. The angular distribution of illumination on the sample's fronts was calculated for reflected and transmitted light. The maximum of the scattering indicatrix is observed for the diffusion in the opposite direction. The minimum of the illumination on the front in direction of the sample's bulk is a result of using the Frenel's boundary conditions and the asymmetric property of the scattering indicatrix of the nickel nanoparticles. The possibility of using of the composites explosives – nickel nanoparticles as a cap of the optical detonator is considered.

Keywords: metal nanoparticles, simulation, diffusion of light.

Received: 15 September 2014

1. Introduction

Nanosystems based on transparent dielectrics containing light-absorbing and light- diffusing metal particles have wide practical application [1–7]. That is why the optical properties of metal nanoparticles in transparent media were studied in many experimental and theoretical works [8–12]. The applied side of the problem deals with the potential practical use light absorption and diffusion by nanoparticles in the semi-conductor solar battery [1]; in process of atmospheric sounding [2]; in analysis of biological [3] and alimentary [4] products; in the caps of optical detonators [5–7]. The complexity of the problem is caused by simultaneous absorption [8–13] and diffusion [8]. Using typical conditions for the experimental samples width and nanoparticle concentration [14], the multiple diffusion of light becomes more significant. This effect is described by the radiative transfer equation. To solve this type of problem, the diffusion approximation [15], Kubelka-Munk theory [9] and solution using Monte Carlo method [10] are typically applied. The reason for their popularity is the relative simplicity (diffusion approximation and Kubelka-Munk theory), and the availability of the ready code for process simulation (Monte Carlo method). At the same time, diffusion approximation and Kubelka-Munk theory might be used only in the extreme case of the very strong light diffusion [9] and for them, only approximate boundary conditions might be done. As a result, the application of these methods can cause some significant errors [9]. In most works on the radiative transfer, Marshal's boundary conditions are used [16]. Marshal's boundary conditions might be used as approximate conditions for the fronts on which the refractive index does not change. In case

of the systems where the refractive index does change on the fronts (for example, pressed nanocomposites dielectric-metal), it is necessary to use the Frenel's conditions [8]. In work [8], the adopted method of the spherical harmonics was proposed for use in cases of homogeneous layer radiative transfer. The aim of this work is the simulation of the diffusion of light by metal nanoparticle in transparent media in terms of radiative transfer theory by the example of pentaerythriol tetranitrate (PETN) containing nickel nanoparticles with defined sizes (average radius 140 nm).

2. Model

PETN samples containing nickel nanoparticles were chosen as a model system. The wavelength was 532 nm, which corresponds to the second harmonic of Nd:Yag laser. The model was chosen because of several advantages – this composite might be used as a cup of the optical detonators [7, 11, 12, 17, 18]; matrix material (PETN) might be pressed in order to get dense and optically transparent sample without visible imperfections; methods of synthesis of spherical nickel nanoparticles with necessary sizes are well known [19].

In terms of the radiative transfer theory, the matrix is characterized by the linear extinction coefficient k, the absorptivity k_{abs} and the scattering coefficient k_{sca}, the albedo of single interaction of the light quantum with the scattering media $\Lambda = k_{sca}/k$ and the scattering indicatrix. Equations for the absorptivity, scattering coefficient, and extinction coefficient are the following [19]:

$$k_{abs} = \pi r_{eff}^2 Q_{abs} C, \quad k_{sca} = \pi r_{eff}^2 Q_{sca} C, \quad k = \pi r_{eff}^2 C \cdot (Q_{sca} + Q_{abs}), \tag{1}$$

where r_{eff} – inclusion's effective radius, C – inclusion's concentration (cm^{-3}), Q_{abs} and Q_{sca} – the average values of the absorptivity and scattering coefficient of the nanoparticles. Effective radius was taken as 140 nm. Concentration was calculated using mass fraction. To solve the radiative transfer equation, a sort of spherical harmonics method was used, which divides the total illumination into the incident (nonscattered I_0) and the scattered (I_s), both giving ($I = I_0 + I_s$). The nonscattered part decreases according to Bouguer's law taking into account back edge reflection. The differential equation system for the expansion coefficients of the reflected part of the illumination on the spherical harmonics (C_m) is:

$$\begin{gathered} \frac{1}{2m+1} \cdot \left[(m+1) \frac{dC_{m+1}}{d\tau} + m \frac{dC_{m-1}}{d\tau} \right] + \left(1 - \frac{\Lambda x_m}{2} \right) C_m = \\ = \frac{J \Lambda x_l}{2} \left[\exp(-\tau) + R_f \exp(\tau - 2L) \right] \end{gathered} \tag{2}$$

where x_l – expansion coefficients of the scattering indicatrix on the spherical harmonics. Boundary conditions for (2) correspond to the Frenel's reflection:

$$I_s(0, \mu) = R(\mu) I_s(0, -\mu), \quad 0 \le \mu \le 1, \tag{3}$$

$$I_s(L, -\mu) = R(\mu) I_s(L, \mu), \quad -1 \le \mu \le 0, \tag{4}$$

where $R(\mu)$ – angle dependence of the Frenel's reflection coefficient, $\mu = \cos\theta$ – cosine of a spherical angle. Equations (3) – (4) define the boundary conditions on the top face and the back edge correspondingly. Expansion of $R(\mu)$ in terms of Legendre polynomial gives the boundary condition for the harmonics' contributions:

$$\sum_{m=0}^{N} \left(N_{lm} - R'_{lm}\right) C_m\left(0\right) = 0, \tag{5}$$

where the matrix elements are the following:

$$R'_{lm} = \left(-1\right)^m \frac{2m+1}{2} \int_0^1 P_m\left(\mu\right) R\left(\mu\right) P_l\left(\mu\right) d\mu,$$
$$N_{lm} = \frac{2m+1}{2} \int_0^1 P_m\left(\mu\right) P_l\left(\mu\right) d\mu. \tag{6}$$

Similar boundary conditions were made for the top face and the back edge of the sample. According to Frenel's equations, the angle dependence of the reflection coefficient while $\mu \geq \sqrt{1-n^{-2}}$ is the following:

$$R\left(\mu\right) = \frac{1}{2}\left(\frac{\sqrt{n^{-2}-1+\mu^2}-\mu}{\sqrt{n^{-2}-1+\mu^2}+\mu}\right)^2 \left[1+\left(\frac{\mu\sqrt{n^{-2}-1+\mu^2}+\mu^2-1}{\mu\sqrt{n^{-2}-1+\mu^2}-\mu^2+1}\right)^2\right]. \tag{7}$$

When $\mu < \sqrt{1-n^{-2}}$, total reflection take place and $R\left(\mu\right)$=1.

For simulation, the first 20 harmonics ($N = 19$) were used, because the further increase of their quantity does not change the calculation results. At the same time, using fewer components is not desirable because of the strong instability of the angle distribution.

Solution of (2) might be expressed as:

$$C_m\left(\tau\right) = \sum_{l=0}^{N} a_{ml}\tilde{C}_l \exp\left(\gamma_l\tau\right) + C_p^1 \exp\left(-\tau\right) + C_p^2 \exp\left(\tau\right). \tag{8}$$

The last two components are the particular solution for the heterogeneous equation. Coefficients C_p^1 and C_p^2 are equal to each other:

$$C_p^1 = -J\Lambda \cdot \sum_{m=0}^{N} \left[\delta_{pm} + A_{pm}\right]^{-1} B_m,$$
$$C_p^2 = J\Lambda R_f \exp\left(-2L\right) \cdot \sum_{m=0}^{N} \left[\delta_{pm} - A_{pm}\right]^{-1} B_m, \tag{9}$$

where

$$A_{pm} = -\left[\frac{p+1}{2p+1}\delta_{p,p'+1} + \frac{p}{2p+1}\delta_{p,p'-1}\right]^{-1} \left[\left(1-\frac{\Lambda x_m}{2}\right)\delta_{p'm}\right],$$
$$B_m = \left[\frac{m+1}{2m+1}\delta_{m,m'+1} + \frac{m}{2m+1}\delta_{m,m'-1}\right]^{-1} \left[\frac{x_{m'}}{2}\right].$$

Two multipliers in square brackets are multiplied as matrixes. The first component in (8) corresponds to the expansion of the solution on the eigenvector of A_{pm} (matrix a_{ml}) according to the corresponding eigenvalue γ_l. Expansion coefficients $\tilde{C}_l$ must be defined in the form of the boundary conditions (3) – (4). These boundary conditions make system of $2N+2$ equations, $2N$ of which are linearly dependent. Number of coefficients which might be defined is $N+1$, so that the problem is overspecified. So it was decided to use the minimizing of sum of deviation squares of the values in the left parts (3) – (4) from zero. As a result, the following equation (in matrix form) for the coefficients was obtained:

$$\tilde{C} = -\left[(Z\tilde{a})^T (Z\tilde{a})\right]^{-1} (Z\tilde{a})^T (ZC_p)\,, \tag{10}$$

where

$$Z = \begin{pmatrix} N - R' \\ \tilde{N} - \tilde{R}' \end{pmatrix}, \quad \tilde{a} = \begin{pmatrix} a \\ a \cdot \exp(-\gamma L) \end{pmatrix}, \quad C_p = \begin{pmatrix} C_p^1 \\ C_p^2 \end{pmatrix}.$$

3. Results and discussion

In figure 1, the scattering indicatrix, calculated in terms of Mie theory, of the 140 nm nickel nanoparticles in PETN matrix for the second harmonic of Nd:Yag laser is presented. The maximum of the scattering indicatrix corresponds to the point $\mu = -1$. This means that the light mainly reflects in the opposite direction of the incident light. The indicatrix shape is defined by the relatively large particles' radii when the modulus of the nickel's complex refractive index is significant ($1.87 - 3.49i$). The anisotropy factor (the average value of the scattering angle cosine) is -0.833. As it stands, the calculated values for the scattering coefficient Q_{sca} and absorptivity Q_{abs} for the nickel nanoparticles are 2.109 and 1.199 respectively. The efficiencies of both these processes are high because the irradiation wavelength in the medium is comparable to the nanoparticles' diameters.

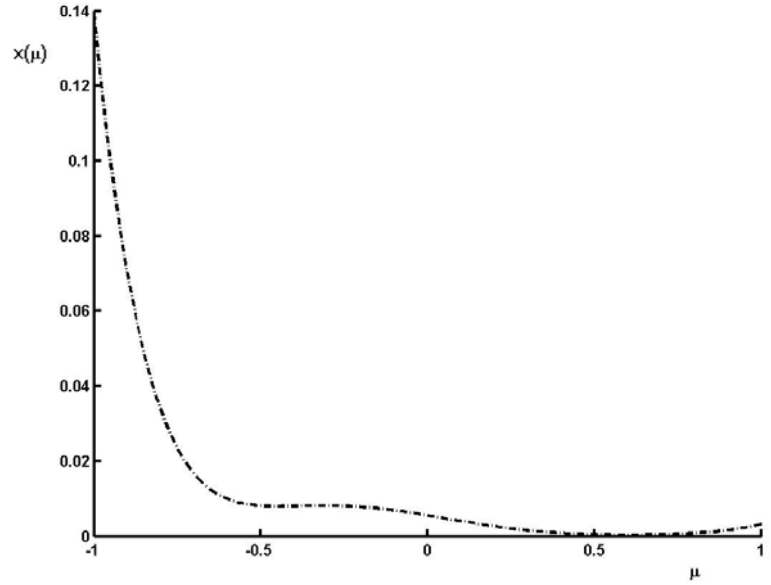

FIG. 1. Scattering indicatrix of the nickel nanoparticles in PETN matrix for 532 nm wavelength

Figure 2 shows distribution of the absorbed energy along the sample (1). Contributions of the nonscattered (2) and scattered part (3) are separately matched. The nonscattered part refers to the irradiation which is absorbed directly by the sample at first interaction. This part decreases according to the Bouguer low with the coefficient which is equal to the ratio of extinction. Scattered part includes all the radiation, which was at least once scattered. This part was calculated using equation (2). The scattered part decreases more slowly in the sample bulk and near to the top face, having a slanting maximum, concerning the partial permittivity of the border to the irradiation. Total dependence (1) is close to the exponential dependence with some deviations in the vicinity of the sample's borders. At some distance away from the border the dependence is close to the exponential with absorptivity equal to $\kappa = 26.74$ cm^{-1}.

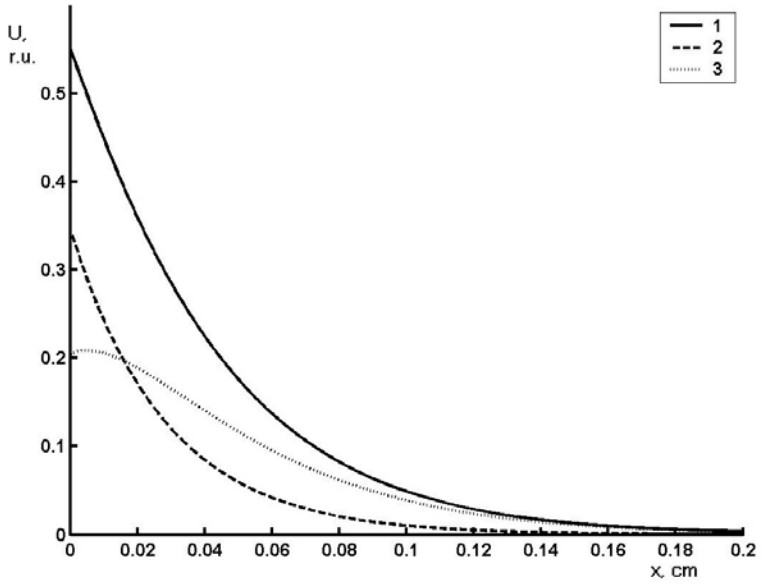

FIG. 2. Distribution of absorbed energy of irradiation (1) along the composite PETN – nickel with the nickel's mass fraction 0.1%, contributions of the non-scattered (2) and scattered part (3)

Figure 3 shows the results of simulation of the angle dependence the scattered and transmitted irradiation (relative units) for the samples where the nickel's mass fraction equal to 0.1% (nanoparticle's radius is 140 nm). The sample width is 0.1 cm, which is almost four times the extinction length. For wider samples, the transmission coefficient becomes a negligible quantity. Values of the transmission and reflection coefficients are 0.060 and 0.169 correspondingly. Let us now discuss the main particularities of the obtained angle dependences. In the case of reflected light, the distribution of intensity has two local minima in the vicinity of $\mu \approx 0.9$ (moving into the sample, perpendicularly to the top face) and two slanting maxima in the vicinity of $\mu \approx -0.5$ and $\mu \approx 0.5$. At the point $\mu = -1$, there is a maximum for the reflected light intensity, so the reflected light is mostly reflected in the opposite direction. In case of transmitted light, there is the opposite situation – the maximum of light intensity is in the area of the reflected light minimum, i.e. near $\mu = 1$. The minimum of the calculated dependences in the area of the normal direction of light into the sample is explained by the use of Frenel's boundary conditions (3) – (4). The maxima appear because the scattering indicatrix of the nickel nanoparticles is very dissymmetric (Fig. 1).

Let us estimate the extension factor of absorption in the conditions of multiple scattering. The extension factor might be determined as ratio of the absorption cross-section, calculated using the absorptivity, and the nanoparticle's geometric cross-section – $K = \kappa / \left(\pi r_{eff}^2 C\right)$. Substitution gives the following value K = 2.51. It is necessary to mention that this value is greater than 1 not only because of the large absorptivity ($Q_{abs} = 1.199$), but mainly because of multiple scattering.

The results are very important in order to determine the cap composition for optical detonators. Nickel nanoparticles with an average size of 140 nm might be a very promising additive in the transparent explosives (particularly in PETN, initiated by the second harmonic of the Nd:Yag laser), i.e. because of the multiple scattering and large absorptivity value, light absorption is considerably amplified. This must cause corresponding decrease of the critical energy density of the laser initiation.

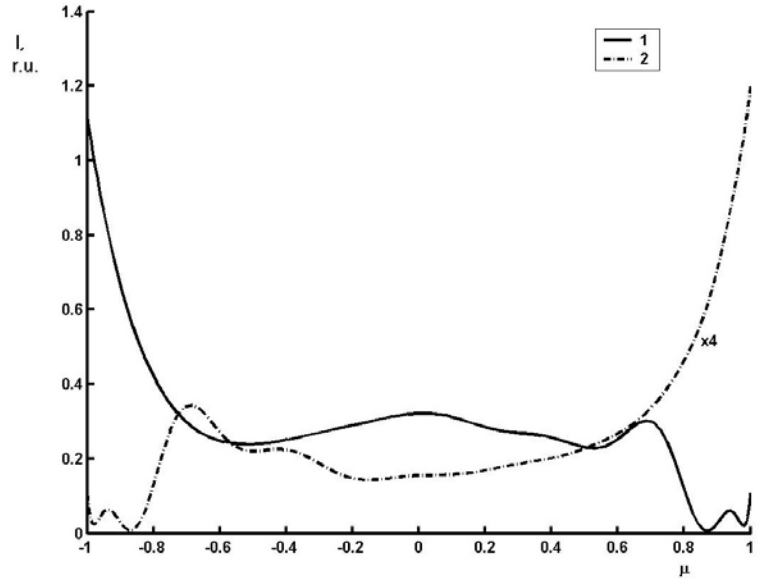

FIG. 3. Angle distribution of the scattering part of illumination on the sample's borders by the reflected (1) and transmitted (2) light

Acknowledgments

This work was supported by Ministry of Education and Science of the Russian Federation (governmental project No. 2014/64) and Russian Foundation for Basic Research for the financial support (grant No. 14-03-00534 A).

References

[1] Moulin E., Sukmanowski J., et al. Improved light absorption in thin-film silicon solar cells by integration of silver nanoparticles. *Journal of Non-Crystalline Solids*, **354**, P. 2488–2491 (2008).

[2] Kochikov I.V., Morozov A.N., Fufurin I.L. Numerical procedures for substances identification and concentration calculation in the open atmosphere by processing a single FTIR measurement. *Computer Optics*, **36** (4), P. 554–561 (2012).

[3] Lisenko S.A., Kugeiko M.M., Firago V.A., Sobchuk A.N. Noninvasive express analysis of hemoglobin derivates in blood by reflectance spectroscopy. *Journal of Applied Spectroscopy*, **81** (1), P. 120–128 (2014).

[4] Rey J.M., Kottman J., Sirgist M.W. Photothermal diffuse reflectance: a new tool for spectroscopic investigation in scattering solids. *Applied Physics B*, **112** (4), P. 547–551 (2013).

[5] Kriger V.G., Kalenskii A.V., et al. Heat transfer processes during laser heating included in an inert matrix. *Teplofizika and aeromekhanika*, **20** (3), P. 375–382 (2013).

[6] Chumakov Yu.A., Knyazeva A.G. Initiation of reaction in the vicinity of a single particle heated by microwave radiation. *Fizika goreniya i vzryva*, **48** (2), P. 24–30 (2012).

[7] Ananyeva M.V., Zvekov A.A., et al. Promising compounds for the cap of optical detonator. *Perspektivnye materialy*, **7**, P. 5–12 (2014).

[8] Aduev B.P., Nurmukhametov D.R., et al. Integrating Sphere Study of the Optical Properties of Aluminum Nanoparticles in Tetranitropentaerytrite. *Zhurnal Tekhnicheskoi Fiziki*, **84** (9), P. 126–131 (2014).

[9] Sandoval C., Kim A.D. Deriving Kubelka-Munk theory from radiative transport. *Journal of Optical Society of America A*, **31** (3), P. 628–636 (2014).

[10] Hayakawa C.K., Spanier J., Venugopalan V. Comparative analysis of discrete and continuous absorption weighting estimators used in Monte Carlo simulations of radiative transport in turbid media. *Journal of Optical Society of America A*, **31** (2), P. 301–311 (2014).

[11] Kriger V.G., Kalenskii A.V., et al. Influence the efficiency of absorption of the laser radiation on the temperature of the heating inclusion in transparent glass. *Fizika goreniya i vzryva*, **48** (6), P. 54–58 (2012).

[12] Zykov I.Y. Accounting of the absorbance of nano-inclusions heated by laser impulse. *Mezhdunarodnoe nauchnoe izdanie* '*Sovremennyie fundamentalnyie i prikladnyie issledovaniya*', **3** (6), P. 42–48 (2012).

[13] Aduev B.P., Nurmukhametov D.R., et al. Explosive decomposition of TEN with nanoadditives aluminum under the action of pulsed laser radiation of different wavelengths. *Khimicheskaya fizika*, **32** (8), P. 39–42 (2013).
[14] Kalenskii A.V., Zvekov A.A., et al. Influence of the laser irradiation wavelength on the energetic materials' initiation critical energy. *Fizika goreniya i vzryva*, **50** (3), P. 98–104 (2014).
[15] Gao M., Huang X., Yang P., Kattawar G.W. Angular distribution of diffuse reflectance from incoherent multiple scattering in turbid media. *Applied Optics*, **52** (24), P. 5869–5879 (2013).
[16] Budak V.P. *Methods of solution the radiative transfer equation*. Publishing house MEI, Moscow, 52 p. (2007).
[17] Ananyeva M.V., Kalenskii A.V., et al. Kinetic regularities of the explosive decomposition of PETN containing nanosized inclusions of aluminium, cobalt, and nickel. *Bulletin of Kemerovo State University*, **1-1** (57), P. 194–200 (2014).
[18] Kalenskii A.V., Ananyeva M.V., Zvekov A.A., Zykov I.Yu. Spectrum dependence of the critical energy density of composites based on pentaerythritol tetranitrate with nikel nanoparticles. *Fundamental'nye problemy sovremennogo materialovedenia*, **11** (3), P. 340–345 (2014).
[19] Zakharov Y.A., Pugachev V.M., et al. Structure of nanosize bimetals Fe–Co and Fe–Ni. *Bulletin of the Russian Academy of Sciences: Physics*, **77** (2), P. 142–145 (2013).

NANOSYSTEMS: PHYSICS, CHEMISTRY, MATHEMATICS, 2014, 5 (5), P. 692–702

SYNTHESIS AND THE STUDY OF MAGNETIC CHARACTERISTICS OF NANO $La_{1-x}Sr_xFeO_3$ BY CO-PRECIPITATION METHOD

A. T. Nguyen[1], M. V. Knurova[2], T. M. Nguyen[3], V. O. Mittova[4], I. Ya. Mittova[5]

[1]Ho Chi Minh City Pedagogical University, Ho Chi Minh City, Viet Nam

[2]Voronezh State University, Voronezh, Russia

[3]Ha Noi National University of Education, Ha Noi, Viet Nam

[4]Voronezh State Medical Academy, Voronezh, Russia

[5]Voronezh State University, Voronezh, Russia

anhtien0601@rambler.ru, cnurova2010@yandex.ru, montvn@gmail.com, vmittova@mail.ru, imittova@mail.ru

PACS 75.50.Cc, 81.07.Wx

The goal of this study was the sol-gel synthesis of nanocrystals $La_{1-x}Sr_xFeO_3$ (x=0.0, 0.1, 0.2, 0.3) and an examination of their magnetic properties. An aqueous solution of ammonia and 5% ammonium carbonate solution were used as precipitating agents. It was established that the crystallization of $LaFeO_3$ is completed at 750°C (annealing for 1 h). The average diameter of the synthesized particles was 80–100 nm. Investigation of the magnetic properties showed non-monotonic changes of saturation magnetic moment and increase of coercive force with increased Sr content in the sample.

Keywords: sol-gel synthesis; nanopowders; lanthanum ferrite; magnetic properties; high-coercivity materials.

Received: 28 August 2014
Revised: 13 October 2014

1. Introduction

In the late 1980's, nanotechnology began to develop and achieved many great improvements not only in research but also in many applications. Nanomaterials and nanotools exhibit new physical and chemical effects and properties that do not exist in bulk materials with the same chemical composition [1].

Materials widely used in practice are magnetic materials and other functional materials, which are applied to various electronic devices such as transformers, generators, electric motors, digital detectors, voice recorder, video recorder, etc. These materials, having ABO_3-typed perovskite-like structure (where A is a such as Y, La, Ln (rare earth metals), Bi and B is transition metal such as Mn, Fe, Co , Ni, Cr), are studied intensively due to their outstanding properties and difficult synthesis [5-11]. These materials are also studied as catalysts [12].

Modified ABO_3 compounds are materials where A or B or both A and B ions are partially replaced by other metal ions (such as Ca, Sr, Cd, Ln (rare earth metals), Mn, Fe, Ni, Al, etc.) [13-17]. This modification produces mixed-valence state of metals and structural defects, which create more interesting effects such as thermal effects, thermomagnetic effects, and large magnetoresistance for material substrate. That has opened up new application of

perovskite materials in a number of modern industrial areas such as electronics, information, petro-chemical processing technologies.

Currently, in order to prepare ABO_3-typed perovskite materials with small particle size, various basic methods are commonly used, such as co-precipitation at room temperature, sol-gel method, co-complexing method, etc. The advantage of these methods is that the crystallization process occurs at lower temperatures than that of traditional ceramic synthesis and the obtained composite materials have more uniform compositions with higher purity. However, to synthesize nanosized ABO_3 materials via these methods, it is required to investigate many factors affecting the formation of the single-crystalline phase such as temperature, calcination time, pH, gelling substance/metal molar ratio, gelling temperature, etc. This investigation requires much time and effort.

Currently, much attention is being devoted to the investigation of the particle size, structure and properties of substituted ferrite. In particular, [15] it was shown that the doping of yttrium ferrite by calcium leads to a reduction of particle size from 50 nm to 27.5 nm, an increase of magnetization (J) from 0.070 to 0.148 Am^2/kg and a decrease in the coercive force (H_c) from 3.58 to 2.78 kA/m in a field of 640 kA/m. The fact that the doping of cobalt ferrite with zinc leads to increased magnetization from 71.297 Am^2/kg for $CoFe_2O_4$ up to 152.531 Am^2/kg for $Co_{0.5}Zn_{0.5}Fe_2O_4$ was demonstrated [18].

However, the synthesis of nano $La_{1-x}Sr_xFeO_3$-typed perovskite materials by hydrolysis of metal cations in boiling water and the addition of a solution containing a precipitating agent and the study of magnetic characteristics of the synthesized material have not been reported.

In this study, nano $La_{1-x}Sr_xFeO_3$-typed perovskite materials (x = 0.0, 0.1, 0.2 and 0.3) were synthesized using the co-precipitation method in boiling water and studied their magnetic properties.

2. Materials and methods

The chemicals used in the research were analytically pure: $Fe(NO_3)_3{\cdot}9H_2O$, $La(NO_3)_3{\cdot}6H_2O$, $Sr(NO_3)_2$, 25% NH_3, $(NH_4)_2CO_3$. The salts were dissolved in water with the concentration of 0.15M. Precipitating agents used in the experiments were aqueous ammonia and ammonium carbonate in 15% excess as compared to the amount in stoichiometry equation to ensure the complete precipitation of metal ions in the solution.

Many studies demonstrate that sols of iron and lanthanum oxides, and a mixture of sols of iron (III) and lanthanum oxides can be obtained by co-precipitation of Fe^{3+} and La^{3+} in boiling water [11, 19, 20]. The results of a previous study [11] demonstrated that use of the co-precipitation is the optimal method.

Nano $La_{1-x}Sr_xFeO_3$ materials were synthesized by adding an aqueous solution containing $La(NO_3)_3$, $Sr(NO_3)_2$ and $Fe(NO_3)_3$ drop wise into boiling water with the molar ratio La : Sr : Fe = (1- x) : x : 1 and x = 0.0, 0.1, 0.2, 0.3 with magnetic stirring. The solution was boiled for 5 minutes and then cooled down to room temperature. Then, 5% ammonia solution (for x = 0.0) and 5% ammonium carbonate (x = 0.1, 0.2, 0.3) were slowly added into the obtained solution with concurrent vigorous stirring for about 30 minutes. The obtained precipitate was separated using vacuum filter, washed with distilled water before being dried naturally at room temperature. The obtained powder was finely ground then calcined in air at different temperatures: 750, 850 and 950°C to examine the completion of crystallization process and the formation of homogeneous phase.

The physicochemical processes, occurring when heating the samples, were studied by DTA/TGA method performed on a TGA Q500 V20.13 Build 39, with a maximum temperature of 1100°C and heating rate of 10°C/min.

The phase composition of obtained powder was examined by X-ray diffraction method on a D8-ADVANCE.

Elemental composition of the samples was tested by the method of energy-dispersive X-ray spectroscopy (EDXS, INCA Energy-250) and atomic absorption spectroscopy according to the reference of Ref. AOAC 965.09 (ICE-3500).

The size and shape of particles were determined by scanning electron microscope (SEM, JE-1400).

The magnetic characteristics (saturation magnetization, remanent magnetization, coercive force) of the material were determined on vibrating sample magnetometers Microsene EV11, performed at room temperature.

3. Results and discussion

3.1. $LaFeO_3$ nano-materials synthesis results

Fig. 1 shows TGA diagram of powder sample (with x = 0.0) dried naturally at room temperature.

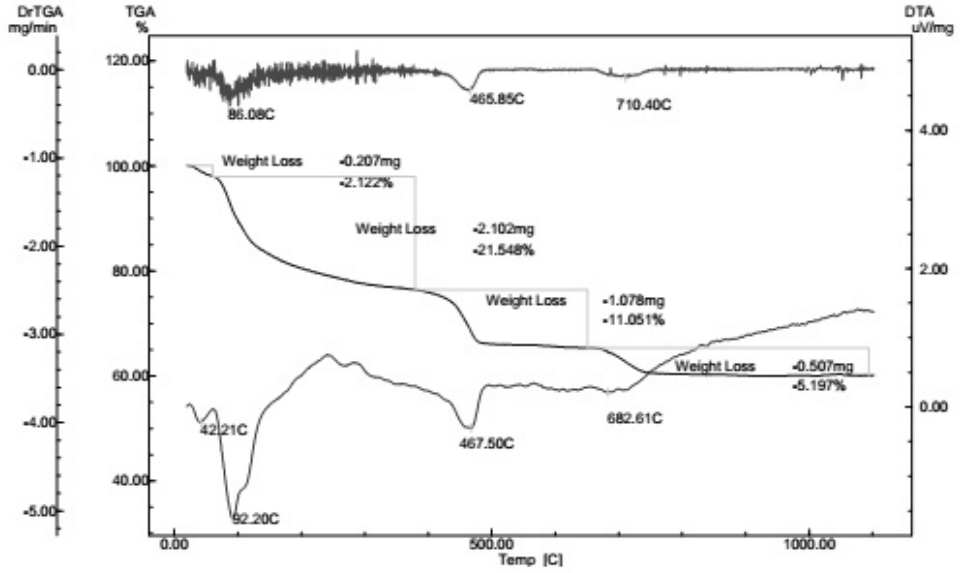

Fig. 1. TGA/DTA diagram of powder sample

It can be seen from Fig. 1 that the TGA curve exhibited 3 weight loss effects with a total weight loss of about 40%. The first weight loss period occurred from room temperature to 370°C with the weight loss of 23.67% corresponding to an endothermic peak at 92.20°C and a small peak at 42.21°C, which was attributed to the loss of surface water, desorption, and the dehydration of iron(III) hydroxide to from FeOOH [11]. The second weight loss period occurred from 370°C to 650°C, the third period started at 650°C and finished at 750°C corresponding to the weight loss of 11.051% and 5.197%, respectively. This was due to the heat absorption of complete decomposition of FeOOH and $La(OH)_3$ to form corresponding oxides. From about 750°C, it could be observed that the weight of sample was unchanged with respect to the formation of single $LaFeO_3$ phase. It is notable that the exothermic

effect for the phase transformation of $LaFeO_3$, which forms the corresponding oxides, was not observed. This can be explained by the thermal compensation occurring when $LaFeO_3$ transformed from amorphous to crystalline nano-phase. A similar phenomenon was described in [17, 19].

From the results of TGA analysis, the calcination temperatures of 750, 850 and 950°C were chosen to study the formation of single phase $LaFeO_3$. Fig. 2 shows the XRD $LaFeO_3$ pattern of samples after calcination at 750, 850 and 950°C for 1 h.

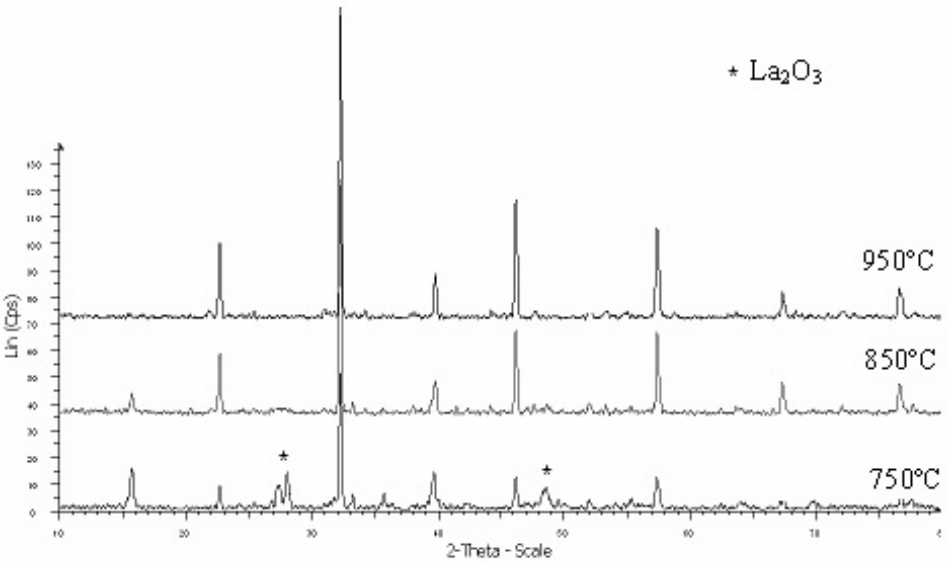

FIG. 2. XRD pattern of $LaFeO_3$ sample heated for 1 h

In the XRD pattern, the typical peaks of single phase of crystalline perovskite $LaFeO_3$ were observed. It can be inferred that the crystallization is almost completed at 750°C, there were only 2 peaks with low intensity at 750°C. At 850°C and 950°C peaks of impurity were not observed.

The result of scanning electron microscope (SEM) of the samples after calcination at 850°C (t = 1 h) shows that the particles exhibit spherical or oval shapes (Fig. 3) with two ranges of size: small particles with a size from 50 to 70 nm, and large particles with a size of about 100 nm or larger. Additionally, it is also demonstrated in the SEM images that the particles bound together to form bulks of particles. This is the limitation of synthesized metal oxides, and particularly $LaFeO_3$, using the co-precipitation method.

As a result, the $LaFeO_3$ material with a particle size of 100 nm was synthesized via the co-precipitation of metal cations Fe^{3+} and La^{3+} in boiling water with aqueous ammonia as co-precipitating agent and calcination temperature of 850°C.

3.2. $La_{1-x}Sr_xFeO_3$ nano-materials synthesis results (x=0.1; 0.2; 0.3)

Because of the high solubility product of $Sr(OH)_2$ (Ts = $3.2x10^{-4}$ at 20°C) [20], and the small solubility product of $Fe(OH)_3$ and $La(OH)_3$ at the same temperature ($3.8x10^{-38}$ and $1.05x10^{-21}$ respectively) [20], it was not possible to co-precipitate La^{3+}, Sr^{2+} and Fe^{3+} cations by aqueous ammonia. Therefore, co-precipitating agent was replaced by ammonium carbonate. The results obtained from experiments of $La_{1-x}Sr_xFeO_3$ (x = 0.1, 0.2, 0.3) synthesis are presented in the section 2.

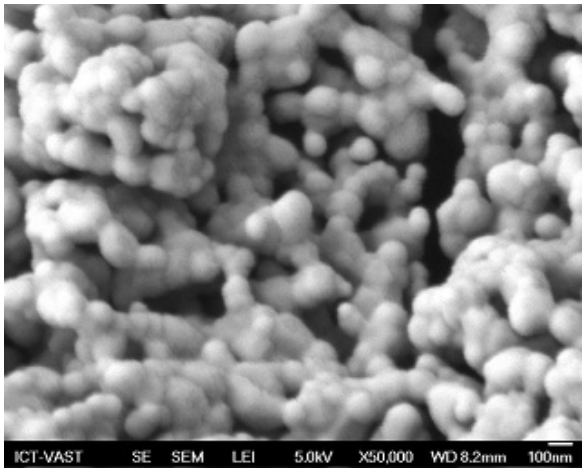

FIG. 3. SEM picture of $LaFeO_3$ sample heated at 850°C (t=1 h)

From the TGA results of synthesized $LaFeO_3$ powders (see Fig. 1), we chose samples with calcination temperatures at 750°C, 850°C and 950°C for 1 h to investigate the formation of single $La_{1-x}Sr_xFeO_3$ phase.

Figure 4, 5, 6 present the XRD patterns of $La_{1-x}Sr_xFeO_3$ materials (x = 0.1, 0.2, 0.3) after calcination at temperatures of 750°C, 850°C and 950°C for 1 h. Figures 4, 5, 6 shows that the obtained products had composition of orthorhombic $LaFeO_3$ phase.

However, the lattice spacing (d) of synthesized crystalline samples decreased with increasing x values (table 1). This could be explained by the replacement of La^{3+} ions by Sr^{2+} ions that led to the lattice shrinkage, therefore the lattice spacing (d) decreased when the Sr^{2+} concentration increased. Indeed, the ionic radius of Sr^{2+} (0.126 nm) is much larger than that of La^{3+} (0.104 nm) [21]. Hence, when La^{3+} ions were replaced by Sr^{2+} ions, charge compensation occurred in the crystalline lattice; consequently, Fe^{3+} ions with a radius of 0.0645 nm were oxidized to Fe^{4+} with a smaller radius (0.0585 nm) [20], thus the lattice spacing (d) decreased. Additionally, the characteristic peaks of lanthanum or strontium phases ($La(OH)_3$, La_2O_3, $La_2(CO_3)_3$, SrO, or $SrCO_3$) were not observed on the XRD pattern. The absence of diffraction peaks for lanthanum and strontium suggested the alloying of strontium in the crystalline lattice of $LaFeO_3$.

Elemental composition of the samples was determined by energy-dispersive X-ray spectroscopy and atomic absorption spectroscopy, indicating that atomic weight percentage of elements in the samples was equal to their stoichiometric percentages. The calculated errors were from 0.7% to 3.5% for samples synthesized by both methods. This could be attributed to the insufficiency of oxygen when replacing La^{3+} by Sr^{2+} in the crystalline lattice.

A study of $La_{0.8}Sr_{0.2}FeO_3$ and $La_{0.7}Sr_{0.3}FeO_3$ materials by scanning electron microscopy (SEM) showed that the formed crystals had an average particle size of about 80–100 nm but it was demonstrated that the differentiation of particles shapes was more obvious as compared to the pure $LaFeO_3$. This once again confirmed that Sr^{2+} doping can affect the structure of the $LaFeO_3$ crystalline lattice.

As a result, Sr doping in the $LaFeO_3$ crystal can lead to a change in the lattice structure, particularly in decreased lattice spacing (d) and the alteration of the crystal shape with increased Sr concentration. This can provide a change in magnetic characteristics of doping $La_{1-x}Sr_xFeO_3$ as compared to pure $LaFeO_3$.

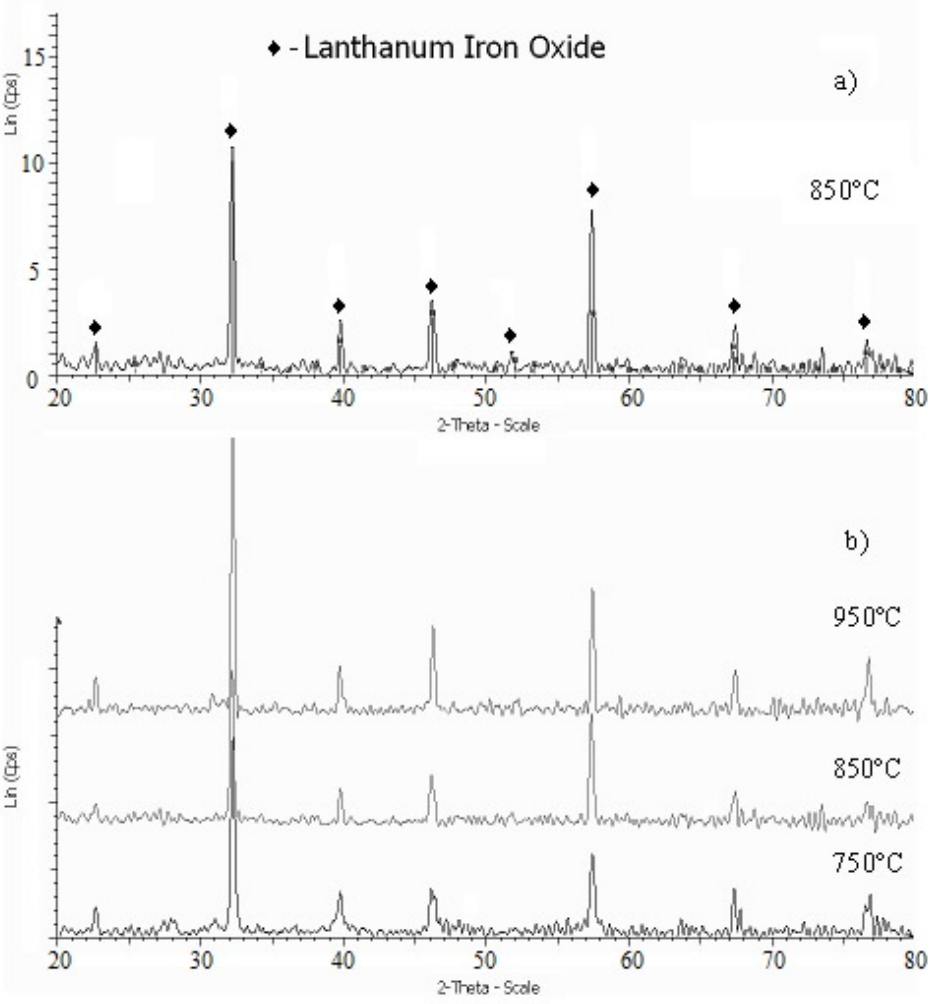

FIG. 4. XRD pattern of $La_{0.9}Sr_{0.1}FeO_3$ sample heated at 850°C (a) and stack XRD diagram of $La_{0.9}Sr_{0.1}FeO_3$ heated at 750°C, 850°C and 950°C (b) (t=1 h)

TABLE 1. The comparison of lattice spacing (d) of $La_{1-x}Sr_xFeO_3$ (x=0.1; 0.2; 0.3) samples heated at 850°C (t=1 h) (from XRD results, Fig. 5, 6, 7)

No	Lattice spacing d; $\AA$		
	$La_{0.9}Sr_{0.1}FeO_3$	$La_{0.8}Sr_{0.2}FeO_3$	$La_{0.7}Sr_{0.3}FeO_3$
1	3.93402	3.91905	3.91813
2	2.78176	2.77718	2.76904
3	2.26766	2.26596	2.26330
4	1.96576	1.96266	1.95876
5	1.76393	1.75545	1.75545
6	1.60434	1.60262	1.60062
7	1.38814	1.38427	1.38427
8	1.24208	1.24057	1.24020

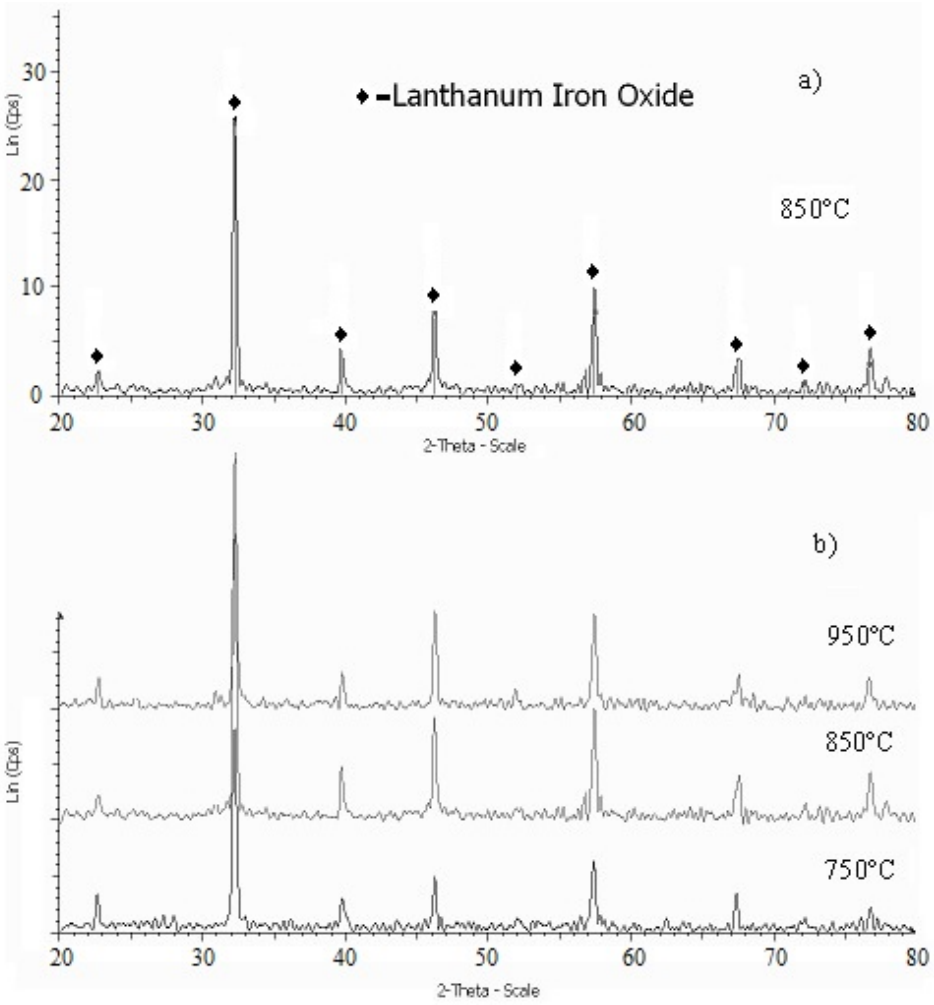

FIG. 5. XRD pattern of $La_{0.8}Sr_{0.2}FeO_3$ sample heated at 850°C (a) stack XRD diagram of $La_{0.8}Sr_{0.2}FeO_3$ heated at 750°C, 850°C and 950°C (b) (t=1 h)

3.3. Magnetic characteristics of $La_{1-x}Sr_xFeO_3$ nanomaterial (x=0.0; 0.1; 0.2; 0.3)

Study of the magnetic properties of nano $La_{1-x}Sr_xFeO_3$ materials (x = 0.0, 0.1, 0.2, 0.3) calcined at 850°C (t=1 hour) on vibrating sample magnetometers at room temperature indicated that the Sr^{2+} doping in the $LaFeO_3$ lattice influenced their magnetic properties (Fig. 8 and table 2). Indeed, in a magnetic field of 1273.6 kA/m the magnetic characteristics of the material, such as saturation magnetization (M_s), remanent magnetization (M_r), decreased with x from 0.0 to 0.1, then increased with x from 0.1 to 0.2, then decreased again with x form 0.2 to 0.3. Meanwhile, the value of coercive force (H_c) of all samples was greater than 15.92 kA/m and increased in the order $LaFeO_3 < La_{0.9}Sr_{0.1}FeO_3 < La_{0.8}Sr_{0.2}FeO_3 < La_{0.7}Sr_{0.3}FeO_3$ (where, H_c of $La_{0.7}Sr_{0.3}FeO_3$ was 20 times greater than H_c of pure $LaFeO_3$). This can be explained in that the alloying of Sr^{2+} in the crystal of pure $LaFeO_3$ increased the non-directionality in shape and crystal lattice of the synthesized materials. Therefore, the synthesized $La_{1-x}Sr_xFeO_3$ samples are hard magnetic materials ($H_c > 7.96$ kA/m).

The regular change in $M_s$and M_r values calculated for $La_{1-x}Sr_xFeO_3$ material with the increasing of Sr^{2+} concentration in the $LaFeO_3$ crystal lattice was due to structure disordering when replacing La^{3+} by Sr^{2+} in the $LaFeO_3$ lattice, which caused the poor orientation of

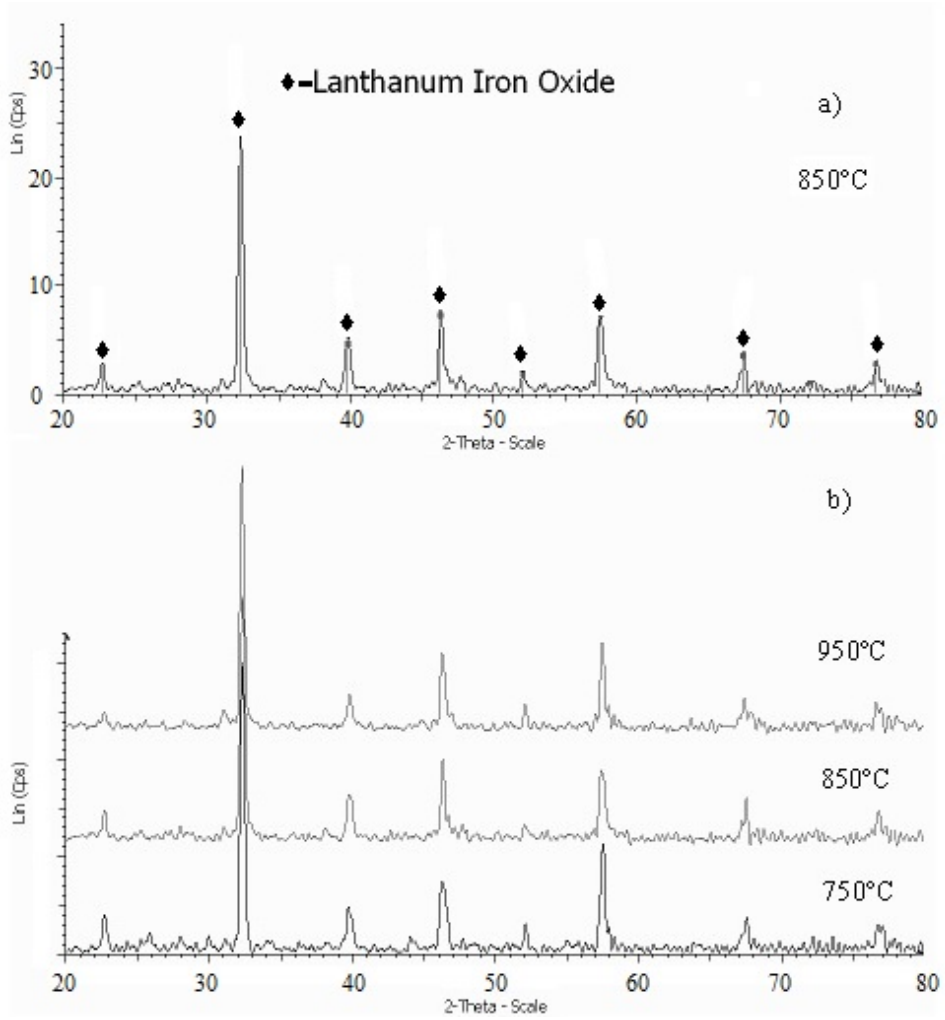

FIG. 6. XRD pattern of $La_{0.7}Sr_{0.3}FeO_3$ sample heated at 850°C (a) and stack XRD diagram of $La_{0.7}Sr_{0.3}FeO_3$ heated 750°C, 850°C and 950°C (b) (t=1 h)

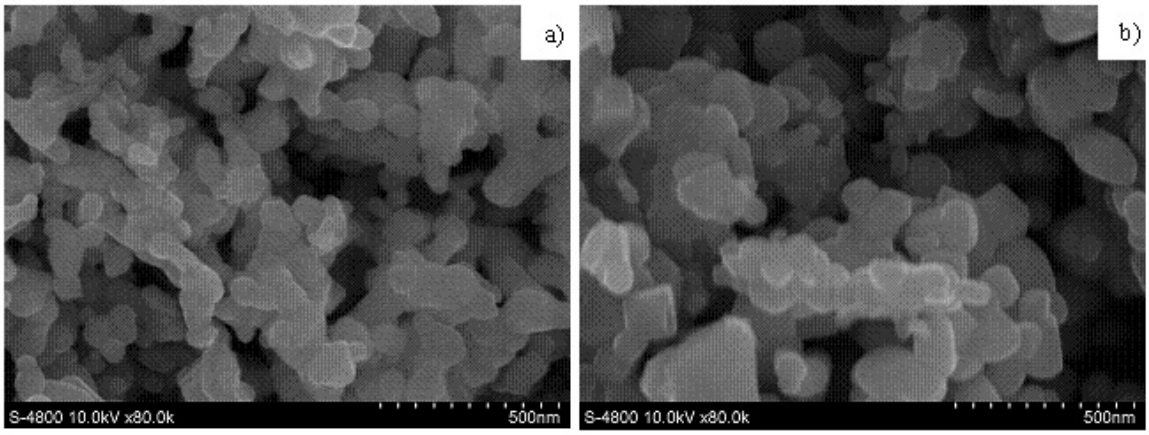

FIG. 7. SEM images of $La_{0.8}Sr_{0.2}FeO_3$ sample (a) and $La_{0.7}Sr_{0.3}FeO_3$ (b) heated at 850°C (t=1 h)

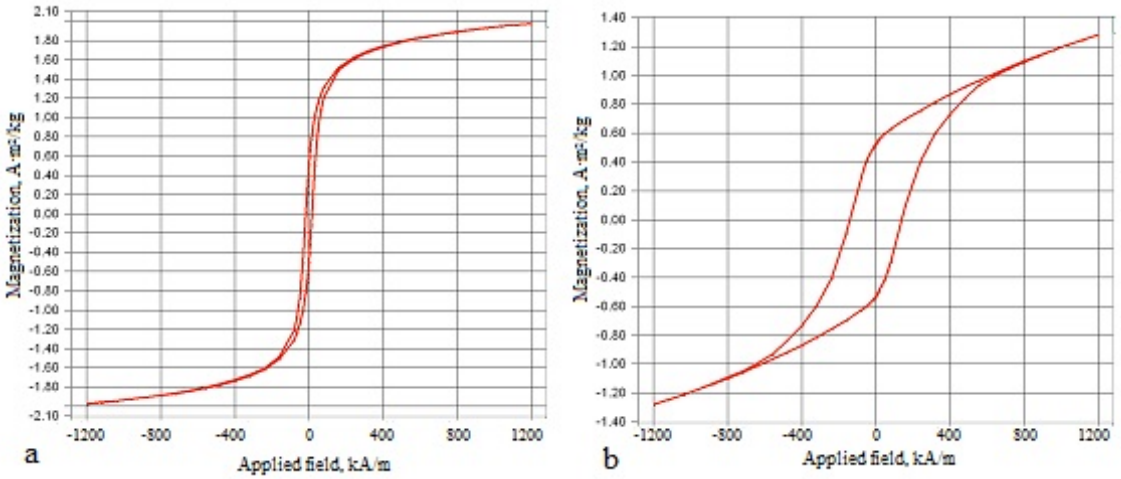

FIG. 8. Magnetic hysteresis loop of $LaFeO_3$ (a) and $La_{0.8}Sr_{0.2}FeO_3$ (b) materials heated at 850°C (t=1 h)

magnetic iron, because of the change in the Fe–O–Fe angle with x from 0.0 to 0.1. With the addition of Sr^{2+} to the crystal lattice to concentration of 20%, the crystalline structure became stabilized and therefore, the M_s and M_r values increased. However, the further addition of Sr^{2+} to the x value of 0.3 could lead to the over-replacement of La^{3+} (trivalent) by Sr^{2+} (divalent). With respect to the charge compensation, some Fe^{3+} ions were oxidized to Fe^{4+} ions (the similar phenomenon was observed in the $Bi_{1-x}Sr_xFeO_3$ [16]). This resulted in the appearance of the magnetic exchange interaction between Fe^{3+} and Fe^{4+} ions through O^{2-} (Fe^{3+}–O^{2-}–Fe^{4+}), leading to a change in the magnetic properties of the synthesized materials.

TABLE 2. Magnetic characteristics of $La_{1-x}Sr_xFeO_3$ nanomaterial (x=0.0; 0.1; 0.2; 0.3) heated at 850°C (t=1h)

Charateristics		$LaFeO_3$	$La_{0.9}Sr_{0.1}FeO_3$	$La_{0.8}Sr_{0.2}FeO_3$	$La_{0.7}Sr_{0.3}FeO_3$
M_r, Am^2/kg	Remanent Magnetization: M at H=0	0.510	0.085	0.527	0.104
M_s, Am^2/kg	Saturation Magnetization: maximum M measured	1.974	0.220	1.278	0.572
H_c, kA/m	Coercive Field: Field at which M/H changes sign	16.183	28.490	138.928	336.952

4. Conclusions

Powders of $La_{1-x}Sr_xFeO_3$ (x = 0.0, 0.1, 0.2, 0.3) with a particle size of about 100 nm was synthesized from La^{3+}, Sr^{2+} and Fe^{3+} cations in heated water by co-precipitation method with ammonia and ammonium carbonate as precipitating agents and a calcination temperature of 750°C (t=1 h). The increase of Sr^{2+} concentration provided to the increase of coercive force of synthesized $La_{1-x}Sr_xFeO_3$ material. The obtained $La_{1-x}Sr_xFeO_3$ nanomaterial showed high coercive force ($H_c > 15.92$ kA/m), hence it was related to the hard magnetic materials and could be used to produce permanent magnets for motors.

Acknowledgments

This work was supported by the Ministry of Education and Science of the Russian Federation in line with government order for Higher Education Institutions in the field of science for 2014-2016 years (project N 225).

References

[1] Rusanov A.I. Striking world of nanostructures. *Russian Journal of General Chemistry*, **72**(4), P. 495–511 (2002).

[2] Popkov V.I., Almjasheva O.V. Yttrium orthoferrite $YFeO_3$ nanopowders formation under glycine-nitrate combustion conditions. *Russian Journal of Applied Chemistry*, **87**(2), P. 167–171 (2014).

[3] Khetre S.M., Jadhav H.V., Jagadale P.N., Kulal S.R., Bamane S.R. Studies on electrical and dielectric properties of $LaFeO_3$. *Journal of Applied Sciences Research*, **2**(4), P. 503–511 (2011).

[4] Wang J., Dong X., Qu Z., Liu G., Yu W. Electrospinning preparation of $LaFeO_3$ nanofibers. *Modern Applied Science*, **3**(9), P. 65–71 (2009).

[5] Cao X., Kim Ch.-S., Yoo H.-I. Effect of substitution of manganese for iron on the structure and electrical properties of yttrium ferrite. *Journal of the American Ceramic Society*, **84**(6), P. 1265–1272 (2001).

[6] Nguyen A.T., Almjasheva O.V., Mittova I.Ya., Stognei O.V., Soldatenko S.A. Synthesis and magnetic properties of $YFeO_3$ nanocrystals. *Russian Journal of Inorganic Materials*, **45**(11), P. 1304–1308 (2009).

[7] Nguyen A.T., Mittova I.Ya., Al'myasheva O.V. Influence of the synthesis conditions on the particle size and morphology of yttrium orthoferrite obtained from aqueous solutions. *Russian Journal of Applied Chemistry*, **82**(11), P. 1915–1918 (2009).

[8] Morozov M.I., Lomanova N.A., Gusarov V.V. Specific features of $BiFeO_3$ formation in a mixture of bismuth(III) and iron(III) oxides. *Russian Journal of General Chemistry*, **73**(11), P. 1772–1776 (2003).

[9] Lomanova N.A., Gusarov V.V. Effect of surface melting on the formation and growth of nanocrystals in the Bi_2O_3-Fe_2O_3 system. *Russian Journal of General Chemistry*, **83**(12), P. 2251–2253 (2013).

[10] Lomanova N.A., Gusarov V.V. Influence of synthesis temperature on $BiFeO_3$ nanoparticles formation. *Nanosystems: Physics, Chemistry, Mathematics*, **4**(5), P. 696–705 (2013).

[11] Nguyen A.T., Mittova I.Ya., Almjasheva O.V., Kirillova S.A., Gusarov V.V. Influence of the preparation conditions on the size and morphology of nanocrystalline lanthanum orthoferrite. *Glass Physics and Chemistry*. **34**(6), P. 756–761 (2008).

[12] Peter S.D., Garbowski E., Perrichon V., Primet M. NO reduction by CO over aluminate-supported perovskites. *Catalysis Letters*, **70**(1-2), P. 27–33 (2000).

[13] Stathopoulos V.N., Belessi V.C., Ladavos A.K. Samarium based high surface area perovskite type oxides $SmFe_{1-x}AlxO_3$ (x= 0.00, 0.50, 0.95). Part II, catalytic combustion of CH_4. *Reaction Kinetics and Catalysis Letters*, **72**(1), P. 49–55 (2001).

[14] Dinh V.T., Mittova V.O., Almjasheva O.V., Mittova I.Ya. Synthesis and magnetic properties of nanocrystalline $Y_{1-x}Cd_xFeO_{3-\delta}$ ($0 \leqslant x \leqslant 0.2$). *Russian Journal of Inorganic Materials*, **47**(10), P. 1141–1146 (2011).

[15] Nguyen A.T., Mittova I.Ya., Solodukhin D.O., Al'myasheva O.V., Mittova V.O., Demidova S.Yu. Sol-Gel Formation and Properties of Nanocrystals of Solid Solutions $Y_{1-x}Ca_xFeO_3$. *Russian Journal of Inorganic Chemistry*, **59**(2), P. 40–45 (2014).

[16] Golubeva O.Yu., Gusarov V.V., Semenov V.G., Volodin V.S. Structural stabilization of Fe^{4+} ions in perovskite-like phases based on the $BiFeO_3$-$SrFeO_y$ system. *Glass Physics and Chemistry*, **35**(3), P. 313–319 (2009).

[17] Oanh P.T.H., Ngoc T.M., Tuyen T.N. Synthesis and electrical properties of materials $La_{1-x}Mn_x$xSrO_3 by the precipitation method. *Vietnam Journal of Chemistry*, **49**(3A), P. 240–245 (2011).

[18] Abdulaziz A.F., Khaleel K.I., Bakr N.A.. Magnetic and magnetostrictive properties of $Co_{1-x}Zn_xFe_2O_4$ nanoparticles produced by co-precipitation method. *Tikrit Journal of Pure Science*, **16**(4), P. 216–222 (2011).

[19] Schweitzer G.K., Pesterfield L.L. *The Aqueous Chemistry of the Elements*. Oxford: OUP, 448 p. (2010).

[20] Richens D.T. *The Chemistry of Aqua Ions*. Wiley, 604 p. (1997).

[21] Sharikov F.Yu., Almjasheva O.V., Gusarov V.V. Thermal analysis of formation of ZrO_2 nanoparticles under hydrothermal. *Russian Journal of Inorganic Chemistry*, **51**(10), P. 1538–1542 (2006).

[22] Lide R.D. *Handbook of Chemistry and Physics*, 84-th Edition. Copyright CRC Press LLC, 2475 p. (2004).

[23] Shannon R.D. Revised effective ionic radii and systematic studies of interatomic distances in halides and chalcogenides. *Acta Crystallographica. Section A*, **32**(5), P. 751–767 (1976).

NANOSYSTEMS: PHYSICS, CHEMISTRY, MATHEMATICS, 2014, 5 (5), P. 703–708

FORMATION MECHANISM OF $YFeO_3$ NANOPARTICLES UNDER THE HYDROTHERMAL CONDITIONS

V. I. Popkov[1,3], O. V. Almjasheva[2,3]

[1]Saint Petersburg State Technological Institute (Technical University), St. Petersburg, Russia
[2]Saint Petersburg Electrotechnical University 'LETI', St. Petersburg, Russia
[3]Ioffe Physical Technical Institute, St. Petersburg, Russia

vadim.i.popkov@gmail.com, almjasheva@mail.ru

PACS 61.46.+w

Yttrium orthoferrite nanocrystals with an average crystallite size of 55 – 60 nm have been obtained under hydrothermal conditions. The influence of the hydrothermal synthesis temperature on the structure and crystallite size has been investigated. Mechanism of the $YFeO_3$ formation under the hydrothermal conditions has been proposed.

Keywords: yttrium orthoferrite, $YFeO_3$, hydrothermal synthesis, phase formation, formation mechanism.

Received: 1 July 2014
Revised: 4 September 2014

1. Introduction

Nanoparticles are often synthesized by 'soft-chemical' methods because the techniques are accessible, simple, use relatively low temperatures and have a large number of varied parameters that allow one to control products' properties [1–4]. Additionally, these methods usually allow relatively rapid forming of nanoparticles [5]. One such method is hydrothermal synthesis, which permits to one to obtain relatively non-agglomerated oxide nanoparticles with a narrow size distribution [6–11].

The solid state method is conventionally used to obtain yttrium orthoferrite. In this case, mechanically mixed oxides of the corresponding metals [12] or a mixture of its hydroxides obtained by the coprecipitation process can be used as precursors [13, 14]. However, the process can be complicated by yttrium orthoferrite thermodynamic instability and yttrium-iron garnet $Y_3Fe_5O_{12}$ formation at high temperatures [15]. Additionally, the obtained nanoparticles are highly agglomerated and their size is relatively large. Therefore, investigation of $YFeO_3$ formation under hydrothermal synthesis conditions is of interest. It should be noted, that despite the potential for using this method in nanoparticle synthesis, data about its application for $YFeO_3$ synthesis is very limited. In works [18, 19], the authors use concentrated KOH solution as mineralizer to reduce the synthesis temperature. This resulted in yttrium orthoferrite formation [18] as well as in formation of the almost all rare-earth metals orthoferrites [19], but the obtained nanoparticle sizes were 10 – 30 μm. This is due to partial dissolution of the initial hydroxides under hydrothermal conditions in the presence of the concentrated KOH solution, so that rare-earth orthoferrite formation is carried out by crystallization from solution, leading to rapid nanoparticle growth.

Another variant of hydrothermal synthesis usage is described elsewhere [20]. In this case, hydrothermal processing was used only for precursor preparation – hydrolysis of yttrium and iron nitrate mixture was carried out under hydrothermal conditions at 200 °C. The obtained X-ray amorphous sample was heat treated in air from 400 – 1000 °C. The formation of yttrium

orthoferrite nanoparticles with average size of ∼100 nm was observed at 800 °C, which corresponds to temperature of the $YFeO_3$ formation from coprecipitated hydoxides under thermal treatment [14, 21].

Thus, investigation of the possibility and the mechanism by which weakly agglomerated yttrium orthoferrite nanoparticles are formed under hydrothermal conditions is of great interest.

2. Experimental

2.1. Synthesis procedure

An yttrium and iron hydroxide mixture was obtained using the reprecepitation process. An $Y(NO_3)_3$ and $Fe(NO_3)_3$ solution mixture was added in a dropwise manner to 1 M NaOH solution under vigorous stirring. The obtained precipitate was washed with distilled water and dried at 70 °C.

Hydrothermal treatment was then carried out according to the procedure described in [11] at 200 – 400 °C, at the 50 MPa over 3 hours. Distilled water was used as the solvent.

2.2. Characterization of the prepared samples

The elemental composition of the specimens were analyzed by means of scanning electron microscopy (SEM) using Hitachi S-570, coupled with Oxford Link Pentafet microprobe analyzer.

The phase composition of the specimens were controlled by powder X-ray diffraction (XRD) using a Shimadzu XRD-700 with monochromatic CuK_α radiation (λ=0.154051 nm). Qualitative X-Ray analysis was carried out with powder base of the diffraction data PDF2-2012 using, quantitative X-Ray analysis was carried out with using of the Rietveld method [22]. Average crystallite size was calculated according to Scherer's equation [23].

3. Results and discussion

According to the results of phase composition analysis obtained after coprecipitation, the material is X-ray amorphous. Results of elemental analysis showed that molar ratio of Fe:Y was 50.4:49.6 and corresponded to the stoichiometric value within the range of experimental error.

According to the results of X-ray analysis (Fig. 1), hydrothermal treatment at 200 °C leads to iron (III) oxide-hydroxide FeOOH (goethite) crystallization only. With an increase in the treatment temperature to 250 °C, a reduction in the peak intensity was observed as well as the appearance of weak peaks of iron (III) oxide Fe_2O_3 (hematite), yttrium hydroxycarbonate $Y_2(OH)_4CO_3$, and yttrium orthoferrite $YFeO_3$. Further increase of the hydrothermal synthesis temperature leads to goethite peak disappearance (at 350 °C) and to $YFeO_3$ peaks intensity growth while Fe_2O_3 and $Y_2(OH)_4CO_3$ peak intensities were practically unchanged.

The presence of yttrium hydroxycarbonate can be explained by the high reactivity of the newly-precipitated yttrium hydroxide, which leads to its quick reaction with atmospheric carbon dioxide [24, 25].

The presence of the goethite reflection at Fe_2O_3-stable temperatures [23, 24] can be explained as a result of an iron (III) oxide reverse hydration process that may be caused due to autoclave cooling inertia. So, it would seem that FeO(OH) doesn't participate in yttrium orthoferrite formation.

Quantitative X-ray analysis results are shown in Fig. 2. The content of FeO(OH) and Fe_2O_3 is represented in terms of $FeO_{1.5}$, and analogically content of $Y_2(OH)_4CO_3$ – in terms of $YO_{1.5}$.

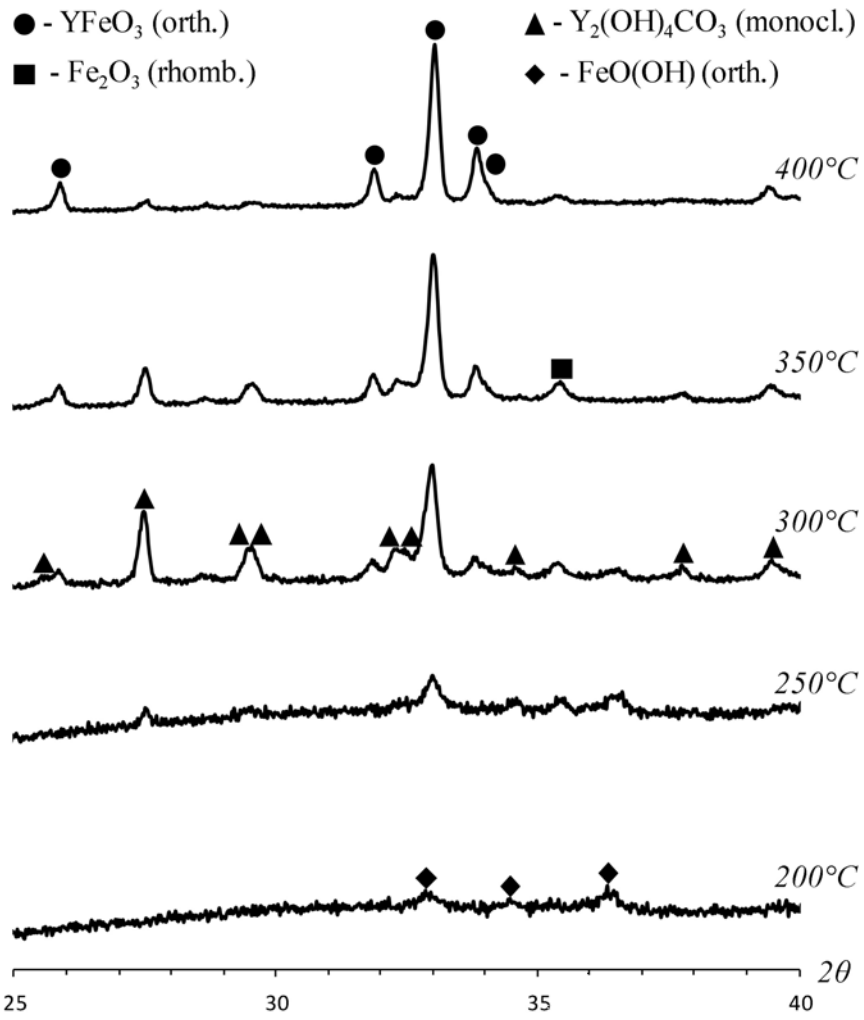

FIG. 1. X-ray difractograms of the hydrothermal synthesis products

Analysis of the data Fig. 2 indicates that initial components may exist in two essentially different states.

Hydroxycarbonate formation leads to precursor inhomogeneity and to the separated crystallization of the iron-containing and yttrium-containing components. At the same time, the homogeneous precursor portion remains X-ray amorphous during hydrothermal treatment and gradually transforms into yttrium orthoferrite without intermediate phase crystallization. This system behavior may be connected with existence of the relatively stable nanoheterogeneeous structures. One can imagine such structure like a nanoscale amorphous clusters of the iron-containing and yttrium-containing precipitate components.

Average crystallite size was calculated from X-ray line broadening for each phase. Obtained data are shown in Fig. 3. Yttrium-containing phase crystallite size is given in terms of yttrium oxide with using molar volume of the $Y_2(OH)_4CO_3$ (monoclinic) and Y_2O_3 (cubic).

Comparison of data in Fig. 2 and 3 allows one to assume that under hydrothermal conditions, nanoparticle formation occurs from amorphous clusters as described above. These clusters transform into Fe_2O_3 and Y_2O_3 crystallites, or they can aggregate in tetrahedral complexes to subsequently form $YFeO_3$ nanoparticles. The proposed mechanism for $YFeO_3$ nanoparticle formation is shown schematically in Fig. 4.

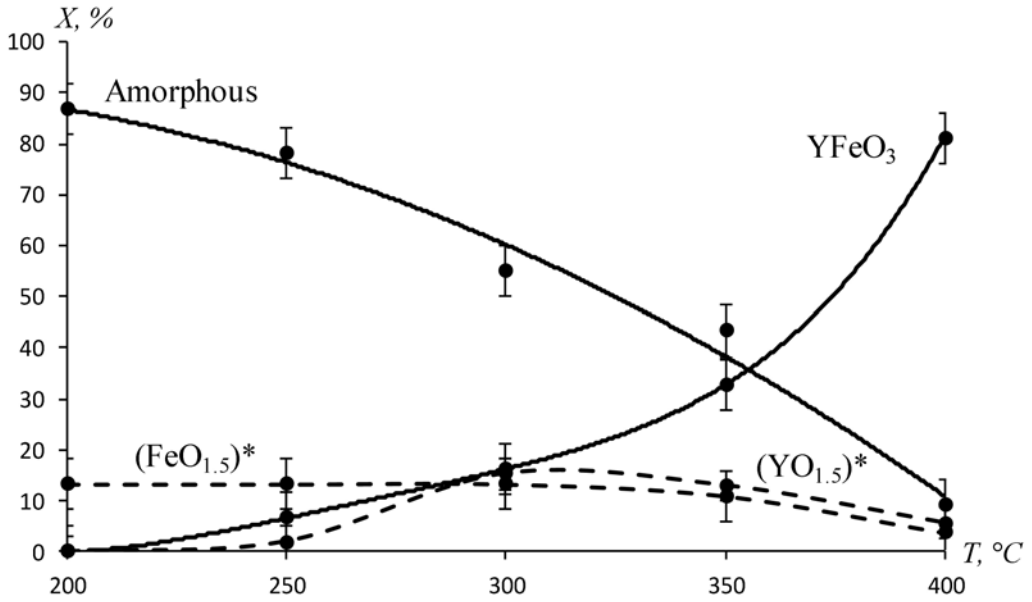

FIG. 2. Molar fraction (X, %) depending on the isothermal exposure temperature (T °C)

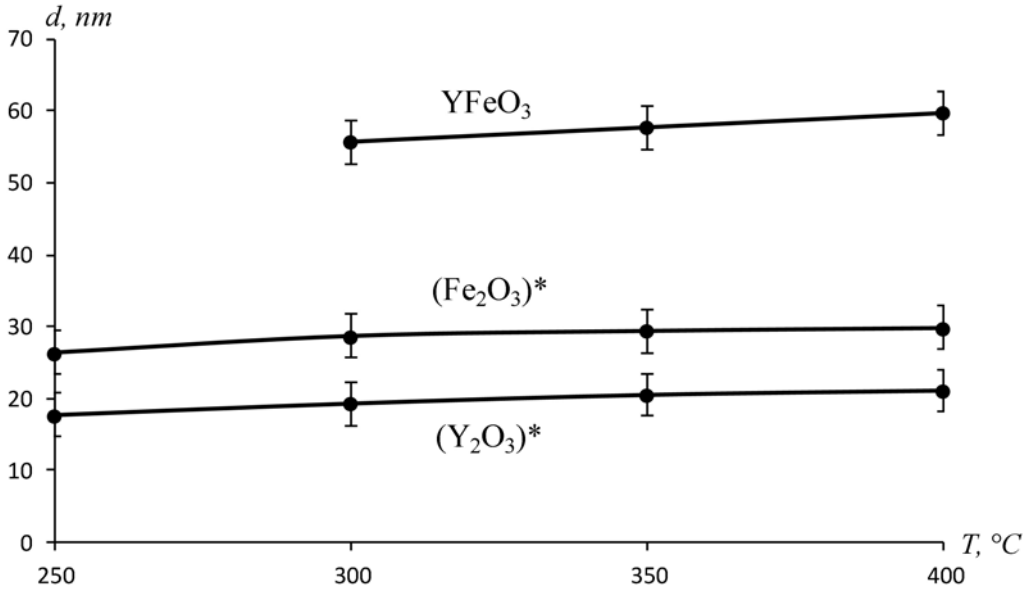

FIG. 3. Average crystallite size (d, nm) depending on the isothermal exposure temperature (T °C)

It should be noted that this assumption can be confirmed by crystallite size comparison of simple oxides and $YFeO_3$.

4. Conclusion

Orthorhombic yttrium orthoferrite with average crystallite size from 55 ± 3 nm to 60 ± 3 nm was obtained by hydrothermal treatment of the coprecipitated iron (III) and yttrium hydroxides. It was shown that $YFeO_3$ formation proceeded from four-fold complexes of the

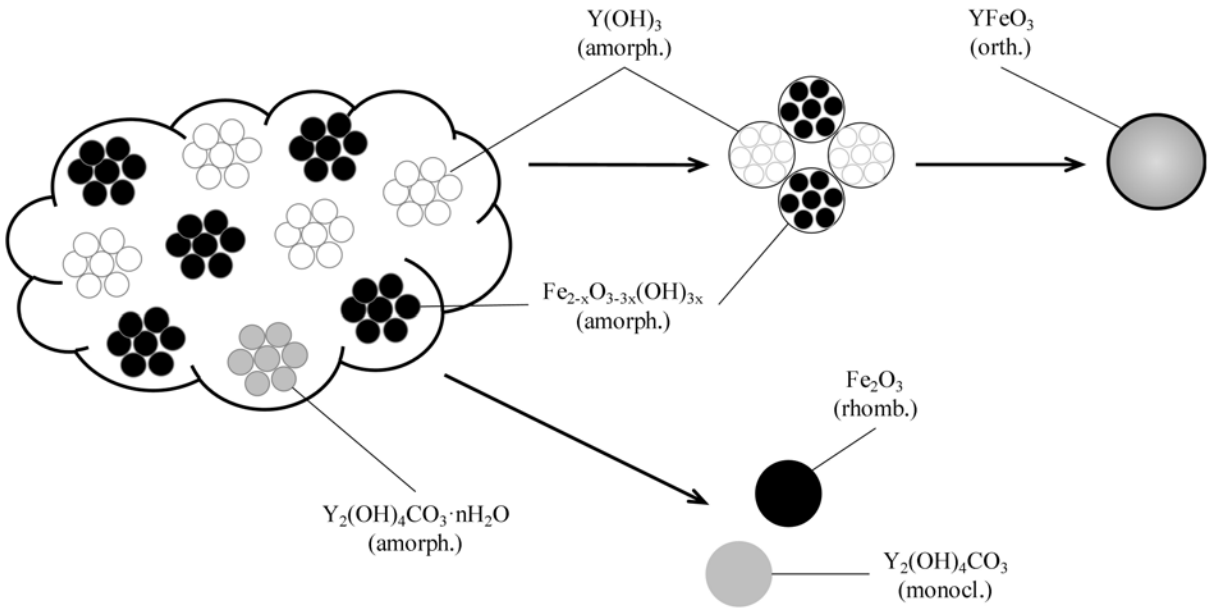

FIG. 4. Formation mechanism of $YFeO_3$ under the hydrothermal conditions

iron-containing and yttrium-containing amorphous clusters that resulted in the formation of relatively large yttrium orthoferrite nanoparticles. The presence of iron (III) oxide and yttrium hydroxycarbonate may be associated with exposure to atmospheric carbon dioxide, which occurs in the precipitation stage. Therefore, iron-containing and yttrium-containing phase crystallization occurs independently of the main $YFeO_3$ formation process.

Acknowledgments

The authors would like to thank Prof. V. V. Gusarov for interest in the work and help in the interpretation of results.

The authors wish to thank V. S. Fundamensky for help in complex X-ray analysis and interpretation of its results.

This work was financially supported by the Russian Foundation for Basic Research (project 13-03-12470).

References

[1] Livage J. Vanadium pentoxide gels. *Chemistry of Materials*, **3** (4), P. 578 (1991).

[2] Sanchez C., Rozes L., et al. "Chimie douce": A land of opportunities for the designed construction of functional inorganic and hybrid organic-inorganic nanomaterials. *Comptes Rendus Chimie*, **13** 3 (2010).

[3] Brec R., Rouxel J., Tournoux M. Soft chemistry routes to new materials: chimie douce. Proceedings of the international symposium held in Nantes, France, September 6–10, 1993, Aedermannsdorf, Switzerland: Trans Tech Pubs, (1994).

[4] Gopalakrishnan J. Chimie Douce Approaches to the Synthesis of Metastable Oxide Materials. *Chemistry of Materials*, **7** (7), P. 1265 (1995).

[5] Gusarov V.V. Fast solid phase chemical reactions. *Zhurnal Obshchei Khimii*, **67** (12), P. 1959–1964 (1997).

[6] Pozhidaeva O.V., Korytkova E.N., Drozdova I.A., Gusarov V.V. Phase state and particle size of ultradispersed zirconium dioxide as influenced by conditions of hydrothermal synthesis. *Russ. J. Gen. Chem.*, **69** (8), P. 1265–1269 (1999).

[7] Pozhidaeva O.V., Korytkova E.N., Romanov D.P., Gusarov V.V. Formation of ZrO_2 nanocrystals in hydrothermal Media of various chemical compositions. *Russ. J. Gen. Chem.*, **72** (6), P. 910–914 (2002).

[8] Al'myasheva O.V., Korytkova E.N., Maslov A.V., Gusarov V.V. Preparation of nanocrystalline alumina under hydrothermal conditions. *Inorg. Mater.*, **41** (5), P. 460–467 (2005).
[9] Komlev A.A., Gusarov V.V. Mechanism of the nanocrystals formation of the spinel structure in the MgO–Al_2O_3–H_2O system under the hydrothermal conditions. *Russ. J. Gen. Chem.*, **81** (11), P. 2222–2230 (2011).
[10] Vasilevskaya A.K., Almjasheva O.V. Features of phase formation in the ZrO_2–TiO_2 system under hydrothermal conditions. *Nanosystems: physics, chemistry, mathematics*, **3** (4), P. 75–81 (2012).
[11] Tugova E.A., Zvereva I.A. Formation mechanism of $GdFeO_3$ nanoparticles under the hydrothermal conditions. *Nanosystems: physics, chemistry, mathematics*, **4** (6), P. 851–856 (2013).
[12] Nakayama S. $LaFeO_3$ perovskite-type oxide prepared by oxide-mixing, co-precipitation and complex synthesis methods. *J. Mater. Sci.*, **6**, P. 5643–5648 (2001).
[13] Tac D.V., Mittova V.O., Almjasheva O.V., Mittova I.Ya. Synthesis, structure, and magnetic properties of nanocrystalline $Y_{3-x}La_xFe_5O_{12}$ ($0 \leq x \leq 0.6$). *Inorg. Mater.*, **48** (1), P. 74–78 (2011).
[14] Tac D.V., Mittova V.O., Almjasheva O.V., Mittova I.Ya. Synthesis and magnetic properties of nanocrystalline $Y_{1-x}Cd_xFeO_{3-\delta}$ ($0 \leq x \leq 0.2$). *Inorg. Mater.*, **47** (10), P. 1141–1146 (2011).
[15] Tang P., Chen H., Cao F., Pan G. Magnetically recoverable and visible-light-driven nanocrystalline $YFeO_3$ photocatalysts. *Catal. Sci. Technol.*, **1** (7), P. 1145–1148 (2011).
[16] Tien N.A., Mittova I.Ya., et al. lanthanum orthoferrite. *Glas. Phys. Chem.*, **34** (6), P. 756–761 (2008).
[17] Tien N.A., Mittova I.Ya., Al'myasheva O.V. Influence of the synthesis conditions on the particle size and morphology of yttrium orthoferrite obtained from aqueous solutions. *Russ. J. Appl. Chem.*, **82** (11), P. 1915–1918 (2009).
[18] Shang M., Zhang C., et al. The multiferroic perovskite $YFeO_3$. *Appl. Phys. Lett.*, **102** (6), P. 062903(3 p.) (2013).
[19] Zhou Z., Guo L., et al. Hydrothermal synthesis and magnetic properties of multiferroic rare-earth orthoferrites. *J. Alloys Compd. Elsevier B*, **583**, P. 21–31 (2014).
[20] Tang P., Sun H., Chen H., Cao F. Hydrothermal processing-assisted synthesis of nanocrystalline $YFeO_3$ and its visible-light photocatalytic activity. *Curr. Nanosci.*, **8**, P. 64–67 (2012).
[21] Tien N.A., Almjasheva O.V., et al. Synthesis and magnetic properties of $YFeO_3$ nanocrystals. *Inorg. Mater.*, **45** (11), P. 1304–1308 (2009).
[22] Rietveld H.M. A profile refinement method for nuclear and magnetic structures. *J. Appl. Crystallogr.*, **2** (2), P. 65–71 (1969).
[23] Patterson A. The Scherrer formula for X-ray particle size determination. *Phys. Rev.*, **56**, P. 978–982 (1939).
[24] Christensen A.N., Hazell R.G. Hydrothermal investigation of the systems Y_2O_3–H_2O–Na_2O, Y_2O_3–D_2O–Na_2O, Y_2O_3–H_2O, and Y_2O_3–H_2O–NH_3. The crystal structure of $Y(OH)_3$. *Acta Chem. Scand.*, **21**, P. 481–492 (1967).
[25] Christensen A.N., Hazell R.G. The crystal structure of $Ho_2(OH)_4CO_3$. *Acta Chem. Scand.*, **38** (A), P. 157–161 (1984).

NANOSYSTEMS: PHYSICS, CHEMISTRY, MATHEMATICS, 2014, 5 (5), P. 709–717

CONCENTRATION DEPENDENCE OF ELECTRIC CONDUCTIVITY AND pH FOR AQUEOUS SOLUTIONS OF WATER-SOLUBLE LIGHT FULLERENE – $C_{60}[=C(COOH)_2]_3$ TRIS-MALONATE

K. N. Semenov[1], N. A. Charykov[2,3], A. S. Kritchenkov[1], I. A. Cherepkova[2], O. S. Manyakina[2], D. P. Tyurin[2], A. A. Shestopalova[2], V. A. Keskinov[2], E. A. Kulenova[6], K. V. Ivanova[2], N. M. Ivanova[1], D. G. Letenko[4], V. A. Nikitin[5], E. L. Fokina[1]

[1]St. Petersburg State University, Saint-Petersburg, Russia
[2]St. Petersburg State Technological Institute (Technical University), Saint-Petersburg, Russia
[3]St. Petersburg State Electro-Technical University (LETI), Saint-Petersburg, Russia
[4]St. Petersburg State University Architecture Academy, Saint-Petersburg, Russia
[5]St. Petersburg State Technical University, Saint-Petersburg, Russia
[6]D. Serikbayev East-Kazakhstan state technical university, Ust-Kamenogorsk, Kazakhstan
keskinov@mail.ru

PACS 61.48.+c

Studies of the concentration dependence of electric conductivity and pH for aqueous solutions of the light fullerene – $C_{60}[=C(COOH)_2]_3$ tris-malonate were performed at 25 °C. From both data (from the equivalent electric conductivity and pH), the apparent degree of dissociation and concentration dissociation constants of $C_{60}[=C(COOH)_2]_3$ in aqueous solutions were calculated. Thermodynamic dissociation constants of $C_{60}[=C(COOH)_2]_3$ in aqueous solutions, calculated for infinitely dilute solutions by the both methods, were reasonably similar.

Keywords: tris-malonate of light fullerene, electric conductivity.

Received: 20 March 2014

1. Introduction

This article continues the investigations, which were initiated in articles [1–3], devoted to the synthetic description and identification of tris-malonate $C_{60}[=C(COOH)_2]_3$ [1] (the original synthesis of this water soluble derivative was described earlier in [4]). The investigation of volume and refraction properties of its aqueous solutions at 25 °C were discussed in [2], while poly-thermal solubility and complex thermal analysis were discussed in [3]. This article is devoted to the investigation of some transport properties – *e.g.* concentration dependence of electric conductivity and pH for light fullerene - $C_{60}[=C(COOH)_2]_3$ tris-malonate aqueous solutions. From both data, the apparent degree of dissociation, concentration and thermodynamic dissociation constants of $C_{60}[=C(COOH)_2]_3$ in aqueous solutions were calculated. These investigations will be used to determine the state of the $C_{60}[=C(COOH)_2]_3$ species in aqueous solutions.

2. Electric conductivity of water solutions of $C_{60}[=C(COOH)_2]_3$

The concentration dependence of specific electric conductivity of aqueous $C_{60}[=C(COOH)_2]_3$ solutions at 25 °C – $\varkappa$ ($S \cdot cm^{-1}$) was investigated by the measurement of the specific resistance of the solutions ρ ($\Omega \cdot cm$):

$$\varkappa = 1/\rho, \tag{1}$$

so, specific electric conductivity corresponds to the unit volume of the solution, put between two parallel planar electrodes with surfaces of 1 cm^2 and at a distance of 1 cm. The device, a HAMEG HM8118 LCR bridge (Rohde & Schwarz), temperatures $T = 25 \pm 0.1$ °C, Pt – electrodes were used. One can see that the dependence $\varkappa(W)$ (where W is mole fraction of C_{60}[=C(COOH)$_2$]$_3$) is non-monotonic and crosses through the maximum at $W = 0.005$ rel. un. The last fact is traditionally connected with electrophoresis and relaxation effects, which are characteristic to moderate electrolytes.

Equivalent electric conductivity (λ – S·cm^2/eq), i.e. conductivity for such electrolyte volume, which contains 1 equivalent of electrolyte was calculated:

$$\lambda = 1000\varkappa/C_N, \tag{2}$$

where: C_N is equivalent concentration (eq/l). Experimental data are represented in Table 1 and in Fig. 1. One can see natural monotonic growth of λ values when the concentration of the solutions' C_N decreases.

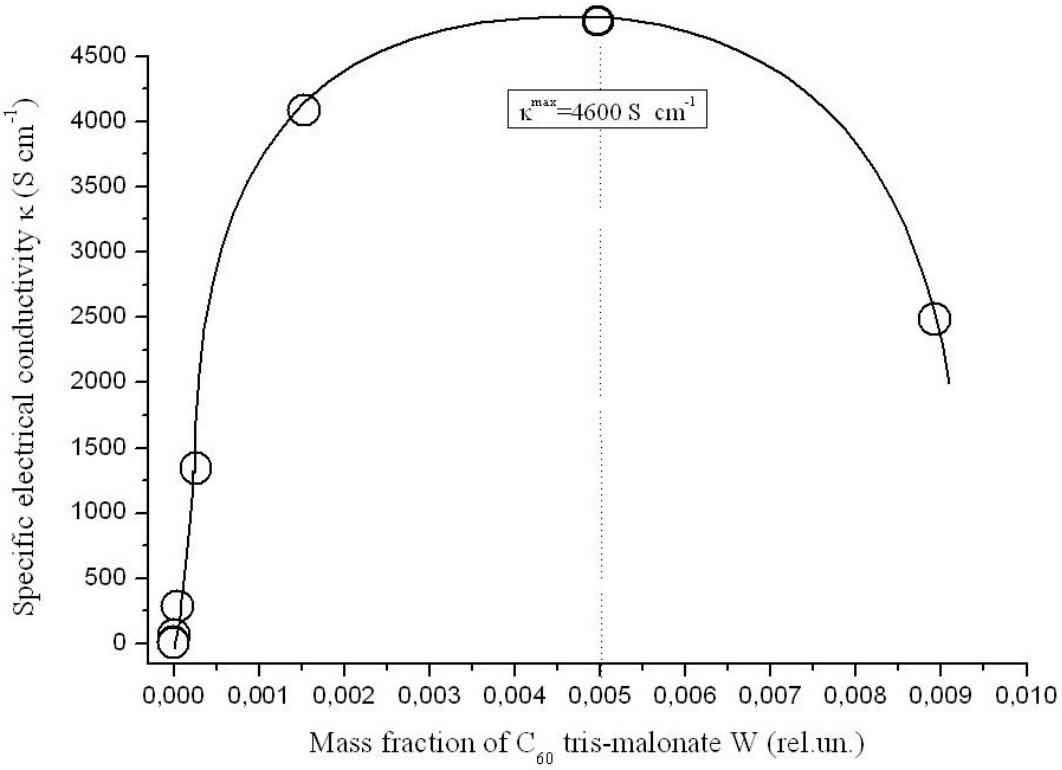

FIG. 1. Concentration dependence of specific electric conductivity of C_{60}[=C(COOH)$_2$]$_3$ aqueous solutions

In order to determine the equivalent electric conductivity value in infinitely dilute solutions – λ_0, we have extrapolated the dependence $\lambda(C_N^{1/2})$ into the value $C_N^{1/2} = 0$, according to well-known Onsager equation [6]:

$$\lambda = \lambda_0 - AC_N^{1/2}, \tag{3}$$

where A in the conditions of the experiment is constant (see Fig. 3).

TABLE 1. Experimental data, concerning electric conductivity of water solutions of C_{60}[=C(COOH)$_2$]$_3$

Solution number No.	Volume concentration C (g/l)	Mass fraction W (rel.un.)	Equivalent concentration C_N (eq/l)	Specific electric conductivity $\varkappa$ (S·cm^{-1})	Equivalent electric conductivity λ (S·cm^2/eq)
1	0.0	0.0	0.0	—	$1.33\cdot10^{10}$ (extrapolation)
2	0.0002	0.000000206	0.000000315	3.30	$1.05\cdot10^{10}$
3	0.0012	0.00000123	0.00000190	14.5	$7.61\cdot10^{9}$
4	0.0071	0.00000727	0.0000112	63.1	$5.60\cdot10^{9}$
5	0.0428	0.0000437	0.0000681	285	$4.18\cdot10^{9}$
6	0.256	0.000260	0.000409	1340	$3.27\cdot10^{9}$
7	1.534	0.00154	0.00249	4090	$1.64\cdot10^{9}$
8	9.201	0.00892	0.0154	2490	$1.61\cdot10^{8}$

Solution number No.	Apparent dissociation degree α (rel.un.)	$-\lg$ (concentration dissociation constant) pK_D (rel.un.)
1	1.0 (extrapolation)	6.15 (extrapolation)
2	0.74	—
3	0.54	5.92
4	0.40	5.53
5	0.30	5.07
6	0.23	4.54
7	0.11	4.41
8	0.011	5.69

The apparent dissociation degree α (rel.un.) was calculated, according to the equation (neglecting transmission coefficients of the ions):

$$\alpha = \lambda/\lambda_0, \tag{4}$$

and is represented in Table 1 and Fig. 4. ($\lambda_0 \approx 1.40\cdot10^{10}$ S·cm^2/eq). One can see that at more or less significant concentrations $C_N > 0.01$ eq/l C_{60}[=C(COOH)$_2$]$_3$, it is weakly electrolytic and at lower concentrations, $C_N = 10^{-7}$ – 10^{-2} eq/l, it is moderately and even strongly electrolytic.

The concentration dependence of the concentration dissociation constant – K_D was calculated according to the 'Ostwald law of the dilution' (neglecting activity coefficients of the ions and non-dissociated molecule – $\gamma_i = \gamma_\pm = 1$):

$$K_D = C_N\alpha^2/(1-\alpha), \tag{5}$$

and is also represented in Table 1 and Fig. 5. Thermodynamic dissociation constant – K_D^{therm} was calculated by the extrapolation of $K_D(C_N)$ values for an infinitely dilute solution:

$$K_D^{therm} = \lim_{C_N \to 0}(K_D), \quad pK_D = -\lg K_D. \tag{6}$$

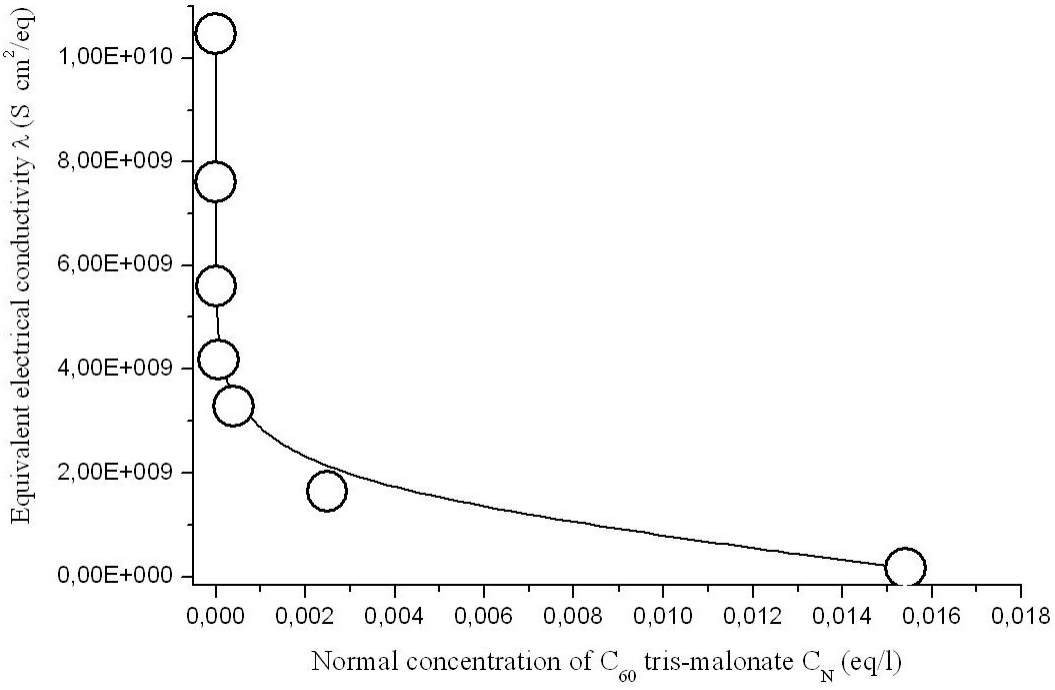

FIG. 2. Concentration dependence of equivalent electric conductivity for $C_{60}[=C(COOH)_2]_3$ aqueous solutions

According to our calculation, one obtains the value $pK_D^{therm} = 6.15 \pm 0.25$ rel.un.

3. pH of aqueous solutions of $C_{60}[=C(COOH)_2]_3$

The concentration dependence of pH for aqueous $C_{60}[=C(COOH)_2]_3$ solutions was measured with the help of pH-meter – Mill Volt-meter pH-121 and glass electrode with hydrogen function EVL 1M3 (rus.). Calibration of the electrode was performed with the help of water basic buffer solutions NH_4OH – NH_4Cl. Accuracy of measurements was $\Delta pH = \pm 0.1$ rel.un. The results are represented in the Table 2 and Fig. 6.

The concentration dependence of the apparent dissociation degree α (rel.un.) was calculated according to trivial equation:

$$\alpha = \exp\left((14 - pH) \cdot \ln 10\right)/C_N. \tag{7}$$

The concentration dependence of the concentration dissociation constant – K_D was calculated according to the 'Ostwald's law of dilution' (see earlier eq. (5), also neglecting activity coefficients of the ions and non-dissociated molecule).

The results of the calculation of α and K_D concentration dependencies are also represented in the Table 2 and Fig. 7, 8.

The thermodynamic dissociation constant – K_D^{therm} was calculated by the extrapolation of $K_D(C_N)$ values for infinitely dilute solutions. According to our calculations, one obtains a value for the pK_D^{therm} of 6.01 ± 0.30 rel.un. So, this method proves that in comparatively concentrated solutions ($5.8 \cdot 10^{-4} \leq C_N \leq 5.8 \cdot 10^{-2}$ eq/l), $C_{60}[=C(COOH)_2]_3$ is a weak

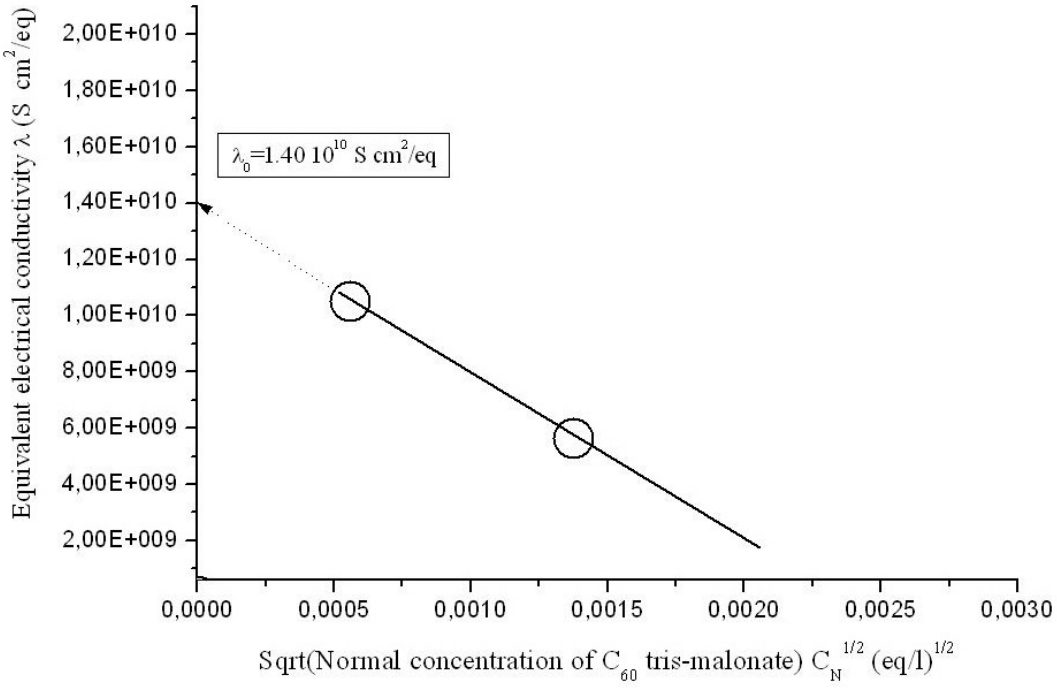

FIG. 3. Extrapolation of concentration dependence of equivalent electric conductivity for $C_{60}[=C(COOH)_2]_3$ aqueous solutions for an infinitely dilute solution in the variables $\lambda(C_N^{1/2})$

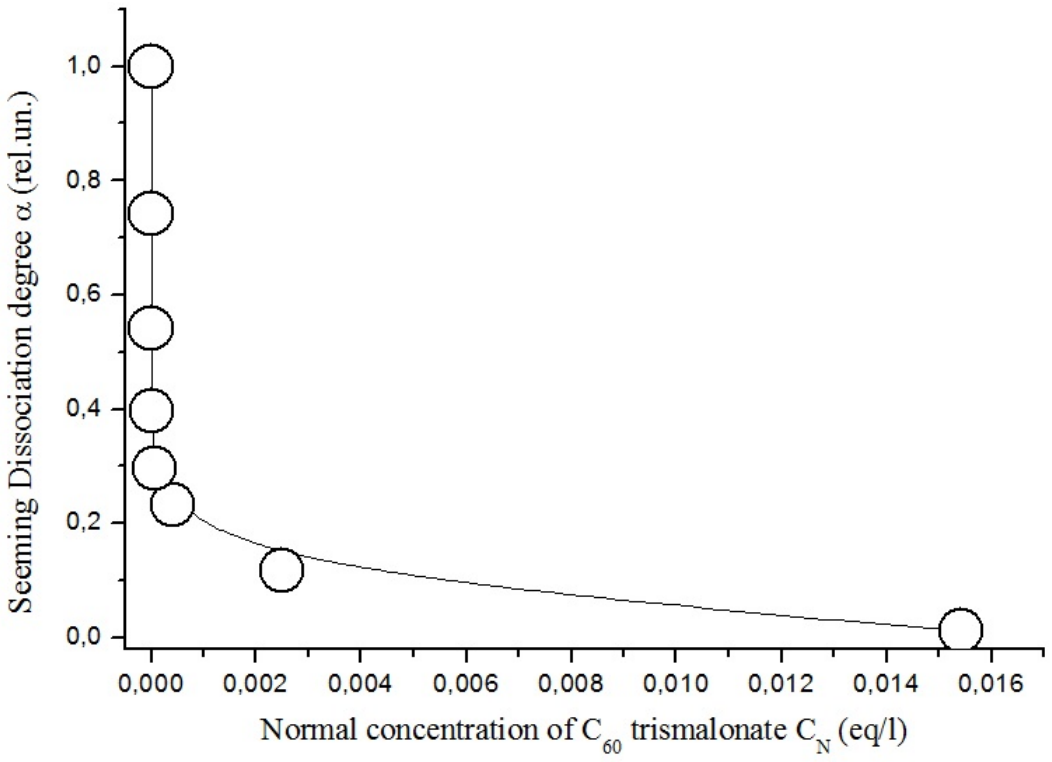

FIG. 4. Concentration dependence of apparent dissociation degree α

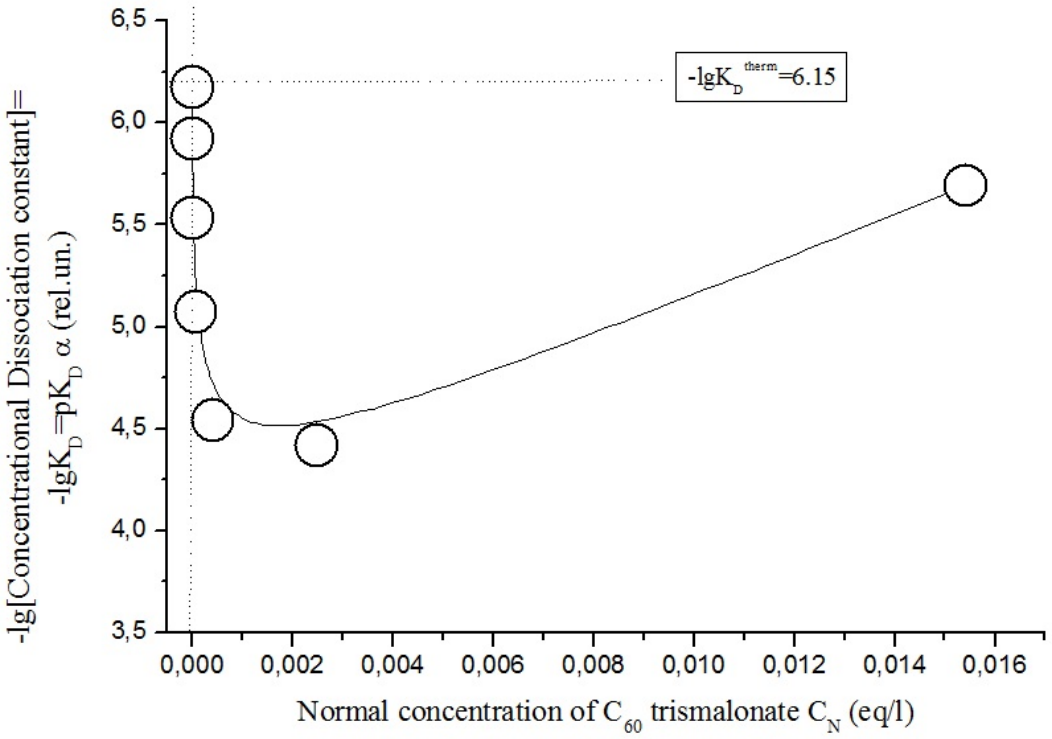

FIG. 5. Concentration dependence of the logarithm of concentration dissociation constant: $pK_D = -\lg K_D$

TABLE 2. Experimental data, concerning pH of $C_{60}[=C(COOH)_2]_3$ aqueous solutions

Solution number No.	Volume concentration C (g/l)	Equivalent concentration C_N (eq/l)	Hydrogen indicator (rel.un.)	Seeming dissociation degree α (rel.un.)	lg (concentration dissociation constant) pK_D (rel.un.)
9	0.0	0.0	—	1.00 (extrapolation)	6.01 (extrapolation)
10	0.1	0.000585	9.00	0.0171	6.76
11	1.0	0.00585	9.41	0.00439	6.92
12	2.5	0.0146	9.62	0.00272	6.97
13	5.0	0.0292	9.69	0.00171	7.07
14	10.0	0.0585	9.80	0.00108	7.17

electrolyte. Obviously in more dilute solutions the tris-malonate will be moderately electrolytic and in very dilute solutions, will be formally strong.

If one compares the thermodynamic dissociation constant – K_D^{therm} , obtained by both methods — i.e. from electric conductivity and pH, they will note fairly good agreement, $pK_D^{therm} = 6.07 \pm 0.40$ rel.un. However, if one compares the concentration dissociation constant – pK_D, they will see sufficient deviation in the concentration functions $pK_D(C_N)$. From the electric conductivity, the pK_D changes during dilution of the solution in the range ($pK_D = 5.69 > 6.15$), crossing through the minimum), and from pH, it changes in the range

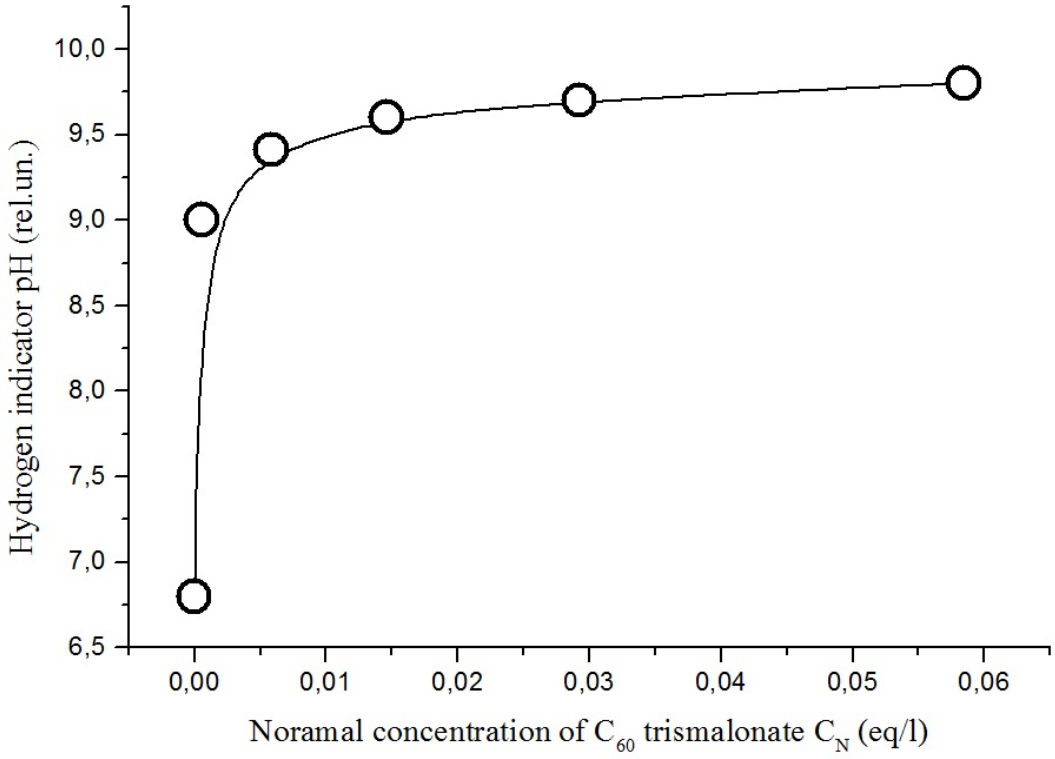

FIG. 6. Concentration dependence of pH for $C_{60}[=C(COOH)_2]_3$ aqueous solutions

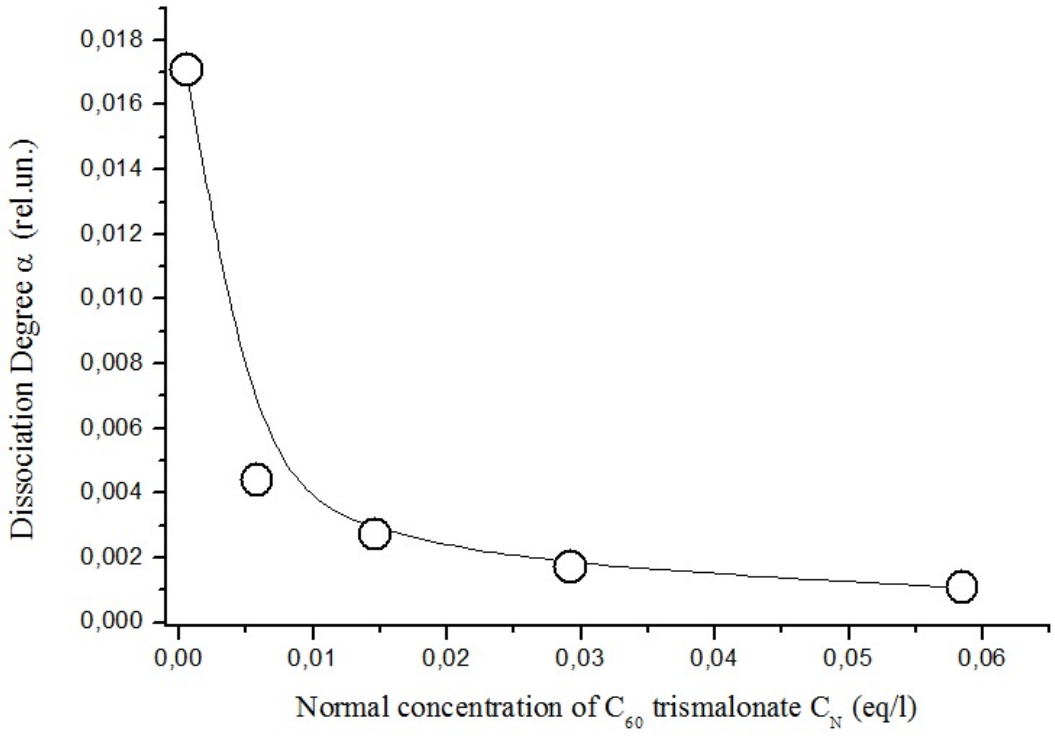

FIG. 7. Concentration dependence of apparent dissociation degree α for $C_{60}[=C(COOH)_2]_3$ aqueous solutions

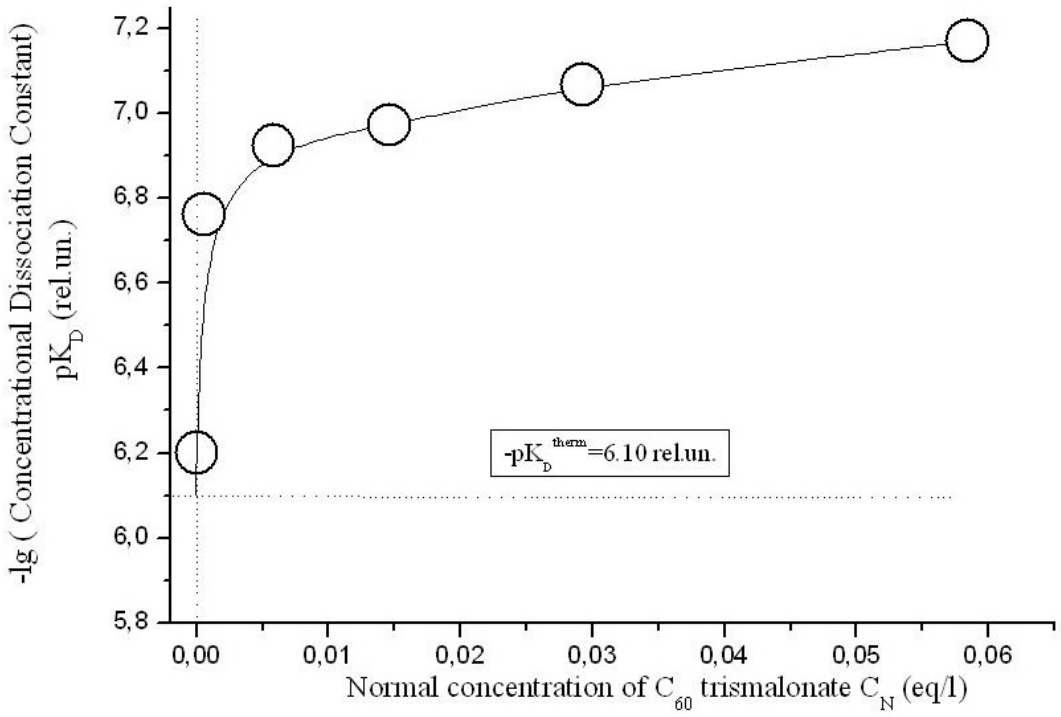

FIG. 8. Concentration dependence of lg (concentration dissociation constant) pK_D of $C_{60}[=C(COOH)_2]_3$ aqueous solutions

($pK_D = 7.17 > 6.01$), changing monotonicity. We can explain this fact, first, the concentration ranges in the investigations were different: $(3.1 \cdot 10^{-7} \leq C_N \leq 1.5 \cdot 10^{-2}$ eq/l) and $(5.8 \cdot 10^{-4} \leq C_N \leq 5.8 \cdot 10^{-2}$ eq/l), correspondingly. The second reason, in our opinion, is that we have neglected the transmission coefficients of the ions and activity coefficients of ions and non-dissociated forms, correspondingly, but the concentration dependence of these functions is sufficiently different for both types of the experiment.

Thus, the concentration dependence of electric conductivity and pH for aqueous solutions of the water soluble light fullerene – $C_{60}[=C(COOH)_2]_3$ tris-malonate were investigated. The dissociation degree and constants of the tris-malonate were calculated. The values for the thermodynamic dissociation constants, calculated using the solutions' electrical conductivity and pH data, are reasonably similar.

Acknowledgement

Research was executed with the help of the equipment of the Resource Center 'Geo-Model' of Saint Petersburg State University.

References

[1] K.N.Semenov, N.A.Charykov, A.S.Kritchenkov et al. Synthesis and identification water-soluble tris-malonate of light fullerene – $C_{60}[=C(COOH)_2]_3$. *Nanosystems: Physics, Chemistry, Mathematics*, **5** (2), P. 315–319 (2014).

[2] K.N.Semenov, N.A.Charykov, A.S.Kritchenkov et al. Volume properties of water solutions and refraction at 25 °C water soluble tris-malonate of light fullerene – $C_{60}[=C(COOH)_2]_3$. *Nanosystems: Physics, Chemistry, Mathematics*, **5** (3), P. 427–434 (2014).

[3] K.N.Semenov, N.A.Charykov, A.S.Kritchenkov et al. Poly-thermal solubility and complex thermal analysis of water soluble tris-malonate of light fullerene – $C_{60}[=C(COOH)_2]_3$. *Nanosystems: Physics, Chemistry, Mathematics*. **5** (3), P. 435–440 (2014).

[4] I. Lamparth, A. Hirsch. Water-soluble malonic acid derivatives of C_{60} with a defined three-dimensional structure. *J. Chem. Soc Chem. Commun.*, **14**, P. 1727–1728 (1994).

[5] A.L. Horvath. *Handbook of aqueous electrolyte solutions: physical properties, estimation and correlation methods*. Ellis Horwood series in physical chemistry. Chichester: Halsted Press, 631 pp. (1985).

[6] A.G. Stromberg, D.P. Semchenko. *Physical Chemistry*. Handbook for Chemical Specialists of Institutes. Moscow: High School, 527 pp. (1999).

NANOSYSTEMS: PHYSICS, CHEMISTRY, MATHEMATICS, 2014, 5 (5), P. 718–727

CONTROLLED INTERFERENCE COLOR OF THE METAL SURFACE BY COMBINATION OF THE CHEMICAL AND ELECTROCHEMICAL ALUMINUM SURFACE TREATMENT

V. V. Shelkovnikov, G. A. Lyubas, S. V. Korotaev

Novosibirsk institute of organic chemistry N. N. Vorozchtcov SB RAS,
630090, av. Lavrent'eva 9, Novosibirsk, Russia

sciencenano@yandex.ru

PACS 81.15.Pq, 82.45.Aa, 82.45.Yz, 81.07.-b

The method of the electrochemical and chemical treatment of an aluminum surface to obtain selective coloration of the anodic aluminum oxide films (AAOF) with high index of the reflection and wide range of the color tones was developed. AAOF were formed and both Ag and Au were chemically deposited. The physical and chemical properties of the obtained color AAOF were studied. It was shown that the additional chemical deposition of the noble metal leads to the enhancement of the selective reflection ability and the interference contrast. Silver nanoparticle formation on the surface of the pores after chemical deposition was shown by electron microscopy. The optical reflection spectra at different angles (10° – 85°) of metalized AAOF were measured and the effective refractive index ($n \approx 1.6$) and thickness were calculated. The spectral shift of the reflection peaks of nanoporous metalized AAOF was shown to depend on the nature of the marked solvents.

Keywords: selective coloration, nanoporous anodic aluminum oxide films, electrochemical and chemical metallization, nanoparticles.

Received: 20 August 2014
Revised: 4 September 2014

1. Introduction

When anodized in an acidic electrolyte, aluminum forms a porous oxide with uniform and parallel pores open at top end and sealed at the other. Anodic aluminum oxide film (AAOF) has been the subject of numerous studies due to its porous nature and has numerous practical application. The use of the anodic aluminum oxide on aluminum is an effective way to increase the corrosion stability of the metal. Special interest in this material is raised as a result of its use as a template medium for creating nanostructures inside the pores. Among different approaches to fill materials into the pores of anodic aluminum oxide templates, electrochemical deposition technology has received considerable attention for its simplicity and high efficiency. Different metals including Au, Ag, Cu, and Ni [1–12] and some semiconductors [13] have been deposited into AAOF by electrochemistry. This process is applied for the electrochemical interference coloration of the anodic aluminum to get the protective decorative coating [14]. Little attention has been paid to the possibilities of the double electrochemical and chemical deposition of the two metals on the anodic aluminum oxide surface for coloration. This is quite possible in the case of the chemical reduction of noble metals from their salt solutions on the first electrodeposited active metals such Zn, Bi, Cu, Ni, Co, Fe, Cd, Sn, Pb and others. The conditions and regimes of the aluminum electrochemical anodization and electrochemical and chemical metallization are not investigated from the point of view the influence of the additional

metal deposition on the effect of the interference coloration. Today, we are not aware of any articles on this topic.

The goal of this research is the development of the electrochemical and chemical treatment processes for the aluminum surface to obtain selective coloration of the aluminum anodic films with a high index of reflection and a wide range of color tones.

2. Experimental Section

Porous anodic oxide films were formed on the metal surface by anodization of Al in acidic solution. Anodization of the samples was processed in 2 % solution of sulfuric acid at 20 °C in potentiostatic mode. The oxidation time, applied voltage magnitude and current density were the following: 1.5 – 50 minutes, 12 – 20 volts and 200 A/m^2, respectively. A high purity (99.95 %) aluminum foil with 0.1 mm thickness was used for fabrication of porous anodic oxide films. The foil was cleaned in a solution of 10 % sodium hydroxide and then electrochemically polished at 60 °C in a mixture of 34 g orthophosphoric acid (specific weight 1.7), 34 g sulfuric acid (specific weight of 1.84), 4 g chromic anhydride, water (to 100 g) at a constant voltage of 12 volts for 2 min to achieve a mirror finished surface. From analysis of the oxidation time and applied voltage magnitude, parameters for the anodic oxidation were optimized. The optimal oxidation time, applied voltage magnitude and current density were the following: 3 – 5 minutes, 12 volts and 200 A/m^2, respectively. Porous alumina was prepared by electrochemical anodization [15] and metallization, into which noble metal nanoparticles were chemically or electrochemically deposited. To improve the interference properties of anodic porous alumina film, three types of processes have been produced: polishing, electrochemical deposition of metal nanoparticles (Cu, Ni) inside the pores of the aluminum oxide and additional chemical deposition of the noble metals (Ag, Au) on the aluminum surface. Electrochemical deposition of nickel particles in pores of anodic alumina was performed using alternating current (potentiostatic regime). The optimal deposition time, applied voltage magnitude, current density and frequency of alternating current were the following: 3 – 4 minutes, 12 - 15 volts, 150 A/m^2 and 50 Hz, respectively. The electrolyte consisted of nickel sulfate (40 kg/m^3), cobalt sulfate (40 kg/m^3) and boric acid (40 kg/m^3). Electrochemical deposition of copper particles in pores of anodic alumina was done using alternating current (potentiostatic mode). The optimal deposition time, applied voltage magnitude, current density and frequency of alternating current were the following: 3 – 4 mins, 12 - 14 volts, 200 - 500 A/m^2 and 50 Hz, respectively. The electrolyte consisted of copper sulfate (50 kg/m^3), magnesium sulfate (20 kg/m^3) and sulfuric acid (to pH = 1). The aim of this procedure, which was to form particles of gold or silver by the exchange reactions layers, went in the following manner. The processing of gold was conducted by a solution of the following composition: chloroauric acid ($HAuCl_4$) (1 kg/m^3), sulfuric acid (to pH = 1 – 2). Silver processing was conducted by a solution of the following composition: silver nitrate (1 kg/m^3), sulfuric acid (to pH = 2). The processing time was 3 – 4 minutes.

Reflection and absorption spectra of the studied films were recorded on a AvaSpec1024 spectrometer. Resolution of spectrometer is about 0.5 nm. The light source was a halogen lamp (AvaLightDHS). The spectra were recorded under various input angles. The range of the input angles of light varied from 10° to 85°, as is shown on the measurement scheme (fig. 1). High-resolution scanning electron microscopy was performed using Zeiss MERLIN VP Compact scanning electron microscope operating at high-resolution mode at 20 kV with 5 nm resolution.

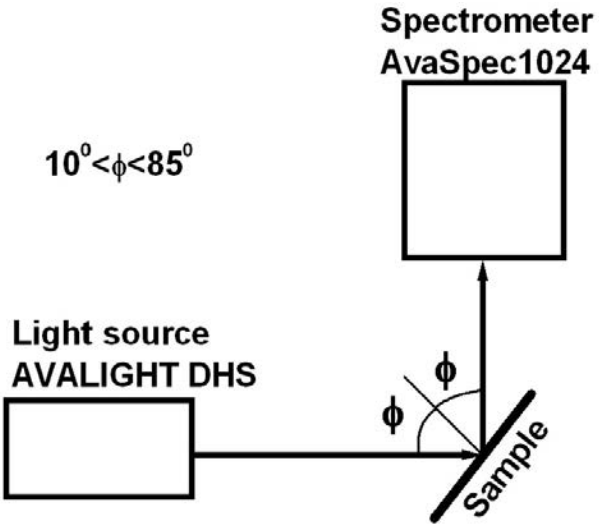

FIG. 1. Measurement scheme of reflectance spectra

3. Results and Discussion

Immediately after anodization of the poled aluminum and formation of the oxide layer the interference color is not visible. The interference is very weak (curve 4 on the fig. 2) on the thin oxide layer. In our case, the kinetics of the anodic aluminum oxide layer growth is slower than in usual sulfate electrolytes due to the lowered sulfuric acid concentration and the thin layer of anodic aluminum oxide formed. After electrodeposition of the Cu or Ni inside the pores of anodic aluminum oxide the interference color appears, depending on the thickness of the initial oxide layer or on the time of the anodic film growth. Due to the low degree of the metal deposition, the metal absorbance is weak and the interference color is bright. It was shown that the controlled interference color of the metal surface was obtained by combination of the chemical and electrochemical aluminum surface treatment. After additional metal electrodeposition, we observe the growth of the metal nanoparticles absorption and a reduction of the interference color.

The reflection spectra of the aluminum oxide films colored by Cu deposition, in reference to the Al mirror, is shown on the fig. 2. One can observe the growth of the interference minima and maxima of the reflection peaks. The metal cuprum is in the left side in the electrochemical series compared to the silver and gold and it displace the noble metals from the solution of their salts. Both Ag and Au were chemically deposited on the Cu electrodeposited nanoparticles. The additional chemical deposition changes the relationship between interference peaks and leads to a small red shift for the maximum on the left and blue shift for the maximum on the right in the visible spectral range. The chemical deposition of the noble metal on the copper nanoparticles electrodeposited in anodic aluminum oxide leads to a noticeable enhancement of the selective reflectivity of the anodized film (see fig. 2).

The blank AAOF without deposited metals has a very weak, on the noise level interference reflection. The first Cu electrodeposition on anodic aluminum oxide leads to a three-fold amplification of the reflection peaks compared to AAOF. Second chemical deposition of the noble metals leads to the formation of AAOF with Cu–Au nanoparticles. The obtained film showed an additional two-fold amplification of the reflection peaks and enhanced contrast (difference between the maximum and minimum) of the interference peaks.

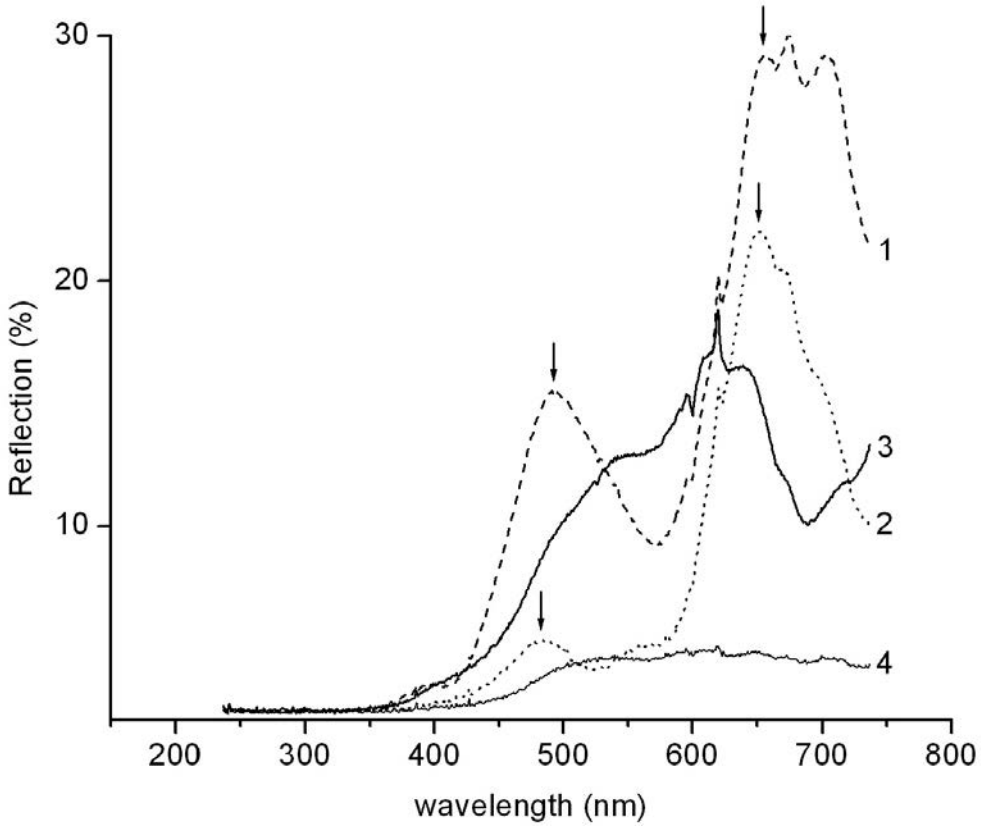

FIG. 2. Reflection spectra of the anodized films with chemical deposited gold (1) and silver (2) nanoparticles by substitution of copper in reference to Al mirror. The solid curve (3) is spectrum of the anodized film with Cu. The solid curve (4) is spectrum of the blank anodized film. It is seen that the difference between the maximum and minimum increases. The input angle of light is 75°

The reflection spectra of the obtained color AAOF were measured under different incident angles of the light and are shown in fig. 3 for AAOF with Cu-Au nanoparticles. One can see that the spectral changes are dependent on the angle, with the interference maxima in the spectra being shifted to the short-wavelength side when the angle of incident light on the sample increases. The appearance of the number of contrasted reflection peaks can be explained by interference phenomena. This is clearly seen in fig. 4, where the reflection spectra of the anodized 20 min films with electrochemical deposited silver nanoparticles are shown. The high contrast interference reflection spectra are shifted one half of phase when changing the input angle from 20° to 40°. The formation of the interference color reflection in anodic aluminum oxide metalized structure is shown schematically in fig. 5.

Both interfaces Al_2O_3/air and Al/Al_2O_3 are partly reflective, and reflectivity is enhanced by the combination of the electrochemical and chemical metal deposition on the anodic aluminum oxide surface. For films with the thickness h, the wavelengths λ of the reflection intensity maxima are given by the interference condition:

$$2h\sqrt{n^2 - \sin^2\varphi} = m\lambda, \qquad m = 1,\ 2,\ 3,\ \ldots,$$

where n is refractive index, h is film thickness, φ is incident angle corresponding to the maximum with wavelength.

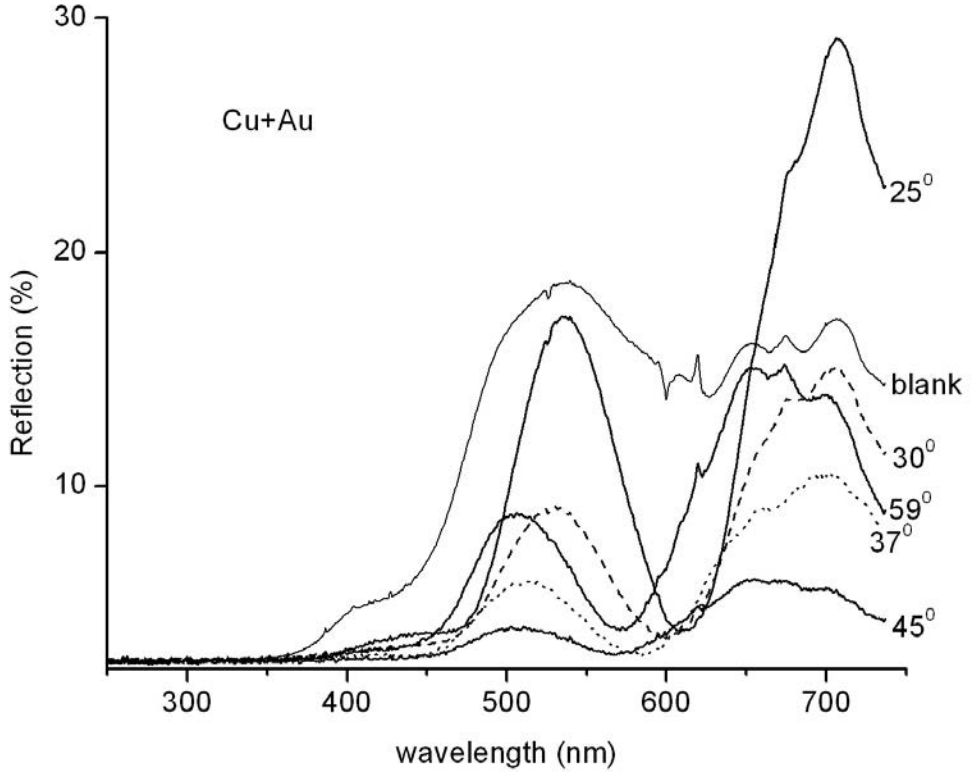

FIG. 3. The reflection spectra under different incident angles. The solid curve (blank) is reflection spectrum of the blank AAOF for the input angle of light 25°

Using the theory of interference in thin films, it is possible to calculate the refractive index (n) and thickness (h) of the film from the angle dependence the reflection peak spectral shift. For the m-th order of the reflection peak, we have next original relationships:

$$h^2 = \frac{m^2\lambda^2}{4(n^2 - \sin^2\varphi)},$$

$$n^2 = \frac{\sin^2\varphi - \dfrac{\lambda_1^2}{\lambda_2^2}\sin^2\theta}{1 - \dfrac{\lambda_1^2}{\lambda_2^2}},$$

where φ is incident angle corresponding to the maximum with wavelength λ_1, θ is incident angle corresponding to the maximum with wavelength λ_2. The angular dispersion of the reflection peak in coordinates ($\lambda^2 \div \sin^2\varphi$) is shown in fig. 6. The experimental points are in good agreement with the modeling theoretical line.

The calculated values for the effective refractive index of the measured films is approximately 1.6. This result is in good agreement with the data obtained by other authors for AAOF [14]. The calculated value of h for the measured film was found to be ~ 0.2 μm.

The obtained metalized AAOF were studied by high-resolution scanning electron microscopy. The electron microscopy image of the film is shown in fig. 7. The Cu–Ag metalized AAOF with high nanopore density and minimal baffle thickness are observed in the image. The diameter of nanopores is about 30 – 50 nm. The thickness of porous layer is ~ 0.2 μm. This value coincides well with the thickness calculated from the interference reflection angle

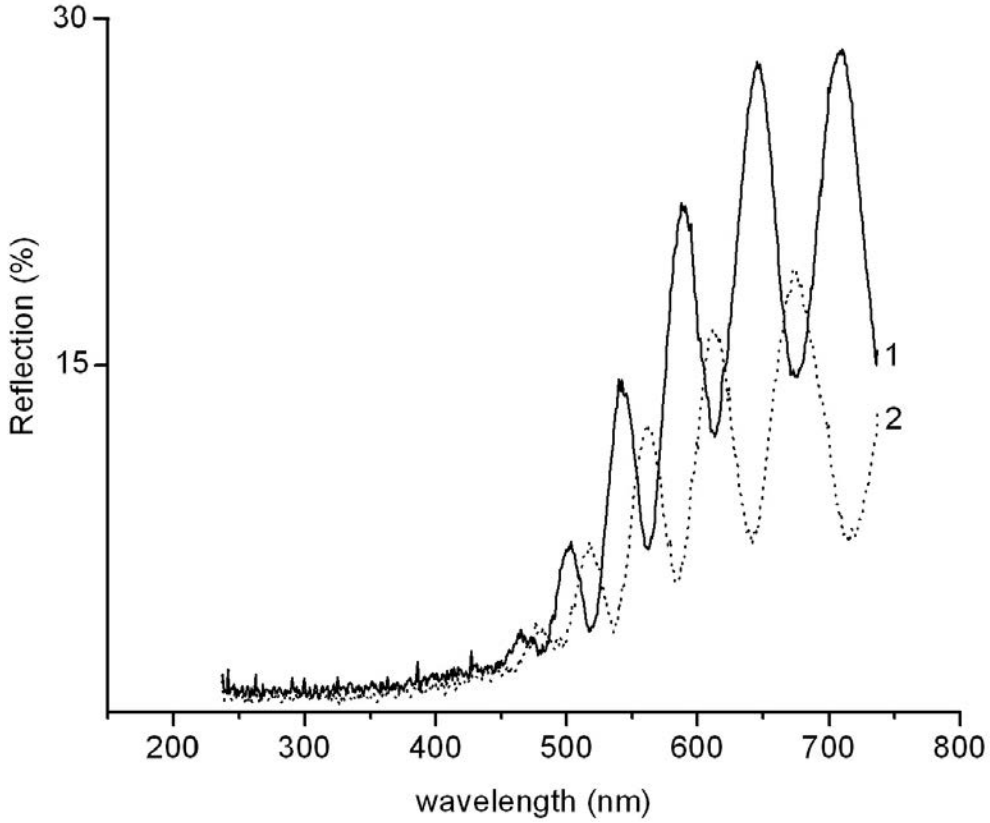

FIG. 4. Reflection spectra of the anodized 20 min films with electrochemical deposited silver nanoparticles in reference to Al mirror. The solid curve (1) is spectrum for the input angle of 20°. The dot curve (2) is spectrum for the input angle of 40°. It is seen that the high contrast interference reflection spectra are shifted one half of phase when changing the input angle from 20° to 40°

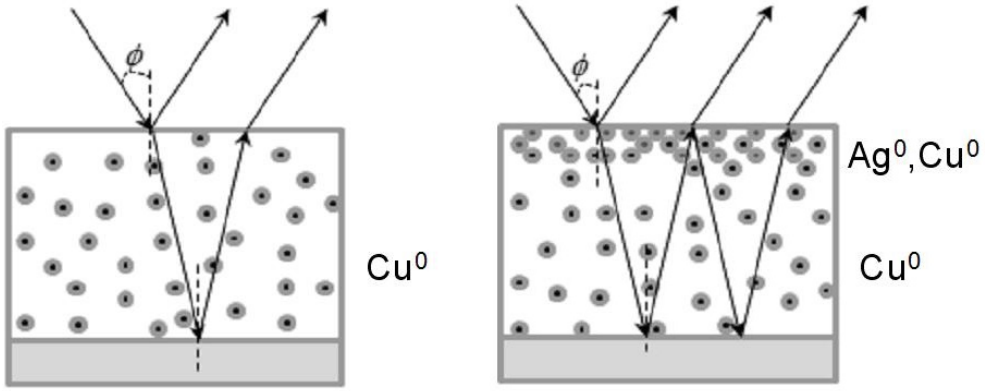

FIG. 5. Scheme of formation of the interference color

dispersion data. The bright spheroid particles on the top of porous film are 20 – 50 nm Ag nanoparticles.

We explain the enhancement of the reflection interference intensity and contrast by the specific deposition of the effective additional metal layer on the anodic aluminum oxide surface leading to the formation of the nanostructure metalized AAOF like the structure of

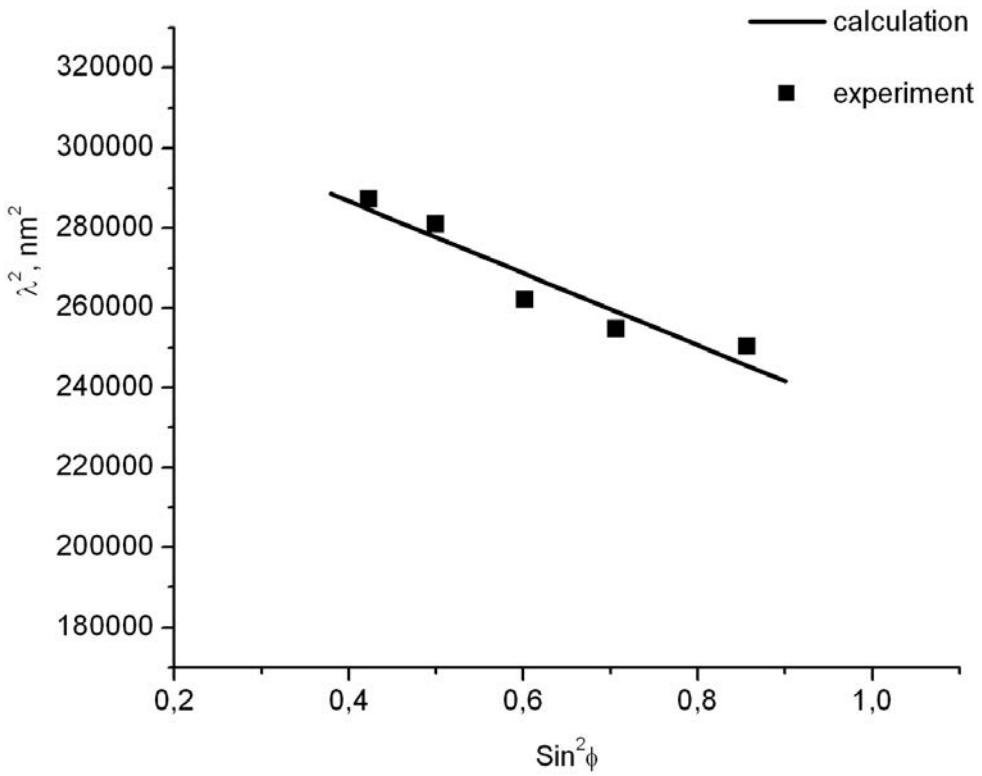

FIG. 6. Angular dispersion of the reflection peak. The dark squares are the experimental data. The solid curve is calculated using the theory of interference in thin films

Fabry–Perot interferometer (see the right part of the 5). According to common knowledge, the electrodeposition of the metal in anodic aluminum oxide occurs inside the aluminum oxide pore and is initiated near the bottom of the pore [16]. During chemical noble metal deposition, metal nanoparticles cover the open ends of the pores on the surface of the film according to the electron microscopy image (fig. 7). This is possible due to the reduction of the silver cations and oxidation of the copper nanoparticles inside the pore comes through the formation of the solvated Cu^+ intermediate cation in close contact with Ag^0 atoms. The diffusion of the solvated intermediate valence compounds (Cu^+,Ag^0) to the top of the pore leads to the formation of noble metal nanoparticles predominately on or near the surface of the AAOF. The possible reactions are shown in the scheme below.

$$Cu^0 + Ag^+ \longrightarrow \left(Cu^+,\, Ag^0\right)_{solv} \tag{1}$$

$$\left(Cu^+,\, Ag^0\right)_{solv} \overset{\text{diffusion}}{\longrightarrow} \left(Cu^+,\, Ag^0\right) n_{solv} \tag{2}$$

$$\left(Cu^+,\, Ag^0\right) n_{solv} \longrightarrow Ag^0_n + Cu^+_n \tag{3}$$

$$Cu^+_n + Ag^+_n \longrightarrow Cu^{+2}_n + Ag^0_n \tag{4}$$

$$Cu^+_n \longrightarrow Cu^0_n + Cu^{+2}_n \tag{5}$$

Reactions (3 – 5) occur on the surface of the film. The disproportionation of the Cu^+ intermediate cations regenerates the Cu^0 atoms (stage 5) that actively reduce silver cations on the top surface of the pore and then reactions (1 – 5) repeat with aggregation of the

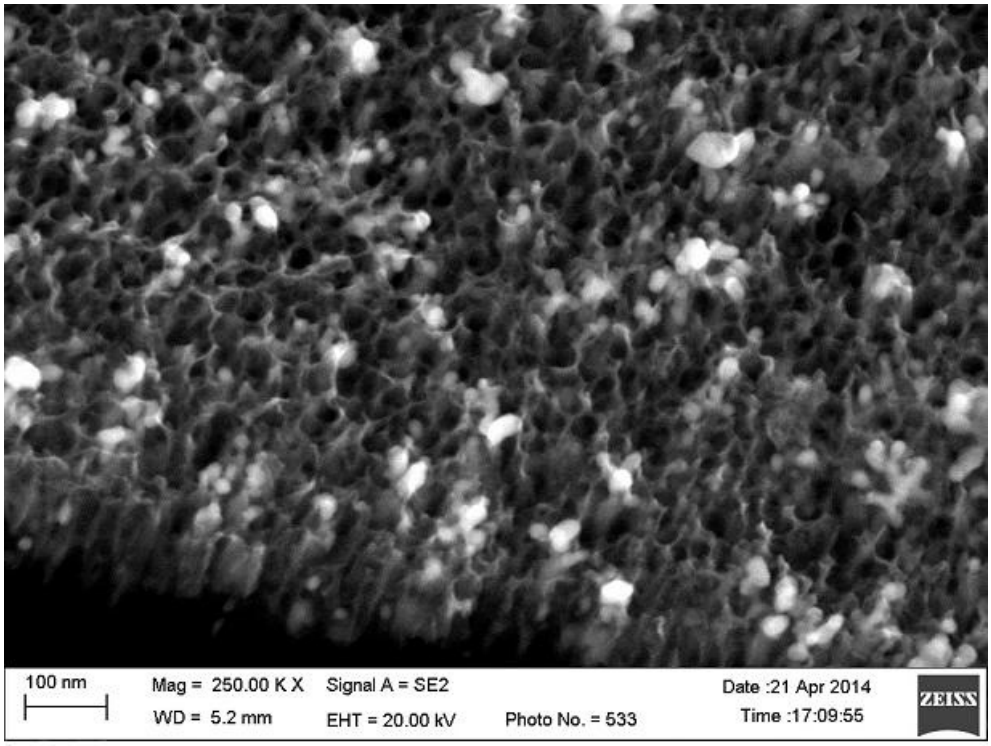

FIG. 7. The high-resolution scanning electron microscopy image of nanoporous layer of anodic aluminum oxide with sequential electrochemical (Cu) – chemical (Ag) metal deposition

silver nanoparticles on the AAOF surface. A similar reaction may occur in the case of the gold chemical deposition. By this way, the process of chemical deposition of noble metal on anodic aluminum oxide with electrochemically pre-deposited copper nanoparticles leads to the redistribution of the metal nanoparticles from the bottom and walls to the top surface of the pores. The thin surface of the Ag or Au nanoparticle-rich layer has a high contribution to the imaginary part to the complex index of the refraction due to the plasmonic nature of the nanoparticles absorption and the reflectivity of this layer became higher. Formation of the Fabrey–Perot interferometer-like nanostructure gives the effect of the mutual reflection inside the anodic aluminum oxide layer and enhances the interferometric contrast of the reflection peaks.

The porous nature of the AAOF allows it to efficiently absorb the different solvents and substances. Solvent absorption and removal reversibly changes the reflection spectra. The measured reflection spectra of the Cu–Ag metalized AAOF covered by water, ethanol and dimethylsulfoxide are shown on fig. 8. In the absence of water, the spectral maximum is located at 538 nm (see curve 1). In the presence of water, the spectral maximum is shifted to the long-wave region by 29 nm (see curve 2). A similar shift in the spectra of reflection is observed for ethanol and dimethylsulfoxide (see curve 3 and 4, respectively). The organic solvent fills porous layer and increases the refractive index of anodic aluminum oxide, so the wavelength of the reflection maximum is shifted to the long-wave spectral region. After solvent removal, the reflection maximum returns to its initial position. The observed reversible spectral shift effect gives the possibility of creating simple chemical sensors based on metalized AAOF.

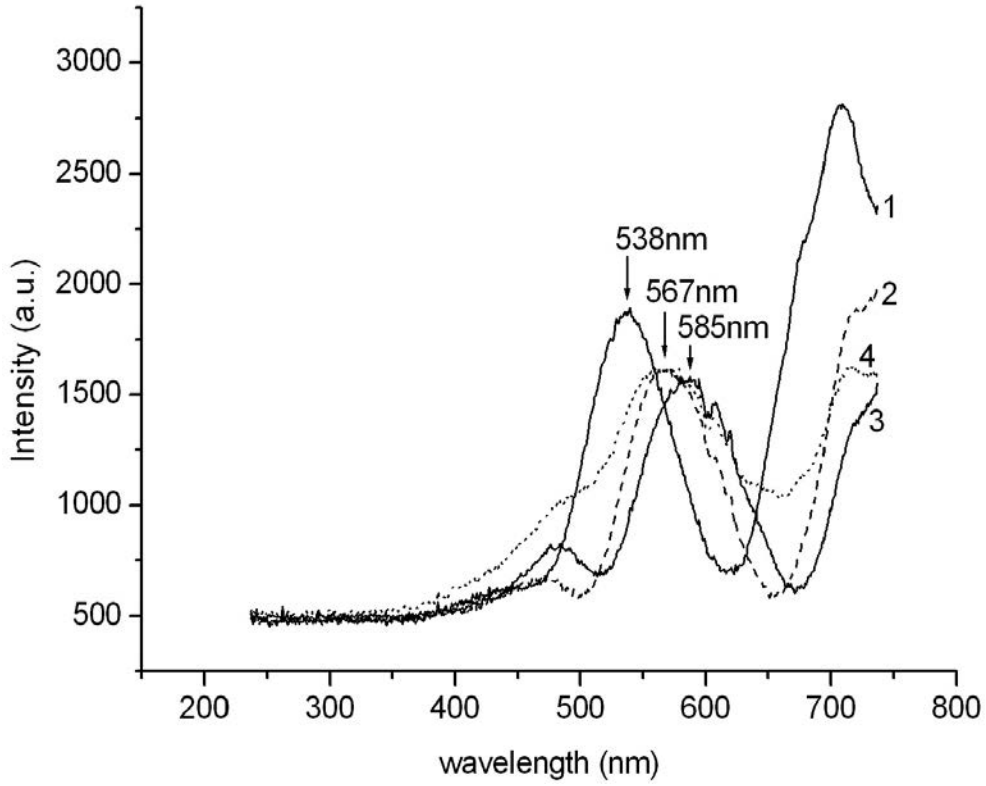

FIG. 8. Reflection spectra of Cu–Ag metalized AAOF (1) with water (2), ethanol (3) and dimethylsulfoxide (4)

4. Conclusion

The combination of the electrochemical and chemical metal deposition on the anodized aluminum film leads to the appearance of selective interference reflection colors and to the enhancement of the reflection interference contrast. Interference coloration of the anodic aluminum can be use for protective and decorative coatings. The optical reflection spectra of metalized AAOF were measured and the effective index of refraction and thickness of AAOF were calculated based on the conditions of optical wave interference. Noble metal nanoparticles were found to be redistributed to the surface of the porous layer during chemical deposition of silver and gold. The spectral shift of the reflection peaks for nanoporous metalized AAOF were shown to be dependent upon the nature of the used solvents. These phenomena are important for applications in the aerospace industry and for the manufacturing of chemical sensors.

References

[1] Moon J. M., Wei A. Uniform gold nanorod arrays from polyethylenimine-coated alumina templates. *J. Phys. Chem. B*, **109** (49), P. 23336–23341 (2005).

[2] Sauer G., Brehm G., et al. Highly ordered monociystalline silver nanowire arrays. *J. Appl. Phys.*, **91** (5), P. 3243–3247 (2002).

[3] Sauer G., Brehm G., et al. In-situ surface-enhanced Raman spectroscopy of monodisperse silver nanowire arrays. *J. Appl. Phys.*, **97**, P. 024308 (2005).

[4] Nielsch K., Muller F., Li A. P., Gosele U. Uniform nickel deposition into ordered alumina pores by pulsed electrodeposition. *Adv. Mater.*, **12** (8), P. 582–586 (2000).

[5] Belov A., Gavrilov S., Shevyakov V., Redichev E. Pulsed electrodeposition of metals into porous anodic alumina. *Applied physics A: materials science & processing*, **102**, P. 219–223 (2011).

[6] Barnakov Y. A., Kiriy N., Black P. et al. Toward curvilinear metamaterials based on silver-filled alumina templates. *Optical materials express*, **1** (6), P. 1061–1064 (2011).
[7] Ng C.K.Y. , Ngan A.H.W. Precise control of nanohoneycomb ordering over anodic aluminum oxide of square centimeter areas. *Chemistry of materials*, **23** (23), P. 5264–5268 (2011).
[8] Guo Y., Zhou L., Kameyama H. Thermal and hydrothermal stability of a metal monolithic anodic alumina support for steam reforming of methane. *Chemical engineering journal*, **168**, P. 341–345 (2011).
[9] Alam K.M., Singh A.P., Bodepudi S.C., Pramanik S. Fabrication of hexagonally ordered nanopores in anodic alumina: An alternative pretreatment. *Surface science*, **605** (3–4), P. 441–449 (2011).
[10] Atrashchenko A.V., Krasilin A.A., et al. Electrochemical methods for the synthesis of hyperbolic metamaterials. *Nanosystems: Physics, Chemistry, Mathematics*, **3** (3), P. 31–51 (2012).
[11] Chen C.Y., Huang J.H., et al. Anisotropic outputs of a nanogenerator from oblique-aligned ZnO nanowire arrays. *ACS Nano*, **5** (8), P. 6707–6713 (2011).
[12] Devan R.S., Patil R.A., Lin J.-H., Ma Y.-R. One-dimensional metal-oxide nanostructures: recent developments in synthesis, characterization, and applications. *Adv. Funct. Mater.*, **22**, P. 3326–3370 (2012).
[13] Xu D.S., Chen D.P., et al. Preparation of II-VI group semiconductor nanowire arrays by dc electrochemical deposition in porous aluminum oxide templates. *Pure and Applied Chemistry*, **72**, P. 127–135 (2000).
[14] Zhang D., Zhang H., He Y. In-situ thickness measurement of porous alumina by atomic force microscopy and the reflectance wavelength measurement from 400–1000 nm. *Microscopy Research and Technique*, **69**, P. 267–270 (2006).
[15] Masuda H., Fukuda K. Ordered metal nanohole arrays made by a two-step replication of honeycomb structures of anodic alumina. *Science*, **268** (5216), P. 1466–1468 (1995).
[16] Hwang S.K., Jeong S.H., Lee O.J., Lee K.H. Fabrication of vacuum tube arrays with a sub-micron dimension using anodic aluminum oxide nano-templates. *Microelectronic Engineering*, **77**, P. 2–7 (2005).

NANO Ф&Х&М

NANOSYSTEMS:

PHYSICS, CHEMISTRY, MATHEMATICS

INFORMATION FOR AUTHORS

The journal publishes research articles and reviews, and also short scientific papers (letters) which are unpublished and have not been accepted for publication in other magazines. Articles should be submitted in English. All articles are reviewed, then if necessary come back to the author to completion.

The journal is indexed in Chemical Abstract Service of the American Chemical Society and in Russian Scientific Citation Index.

Author should submit the following materials:

1. Article file in English, containing article title, the initials and the surname of the authors, Institute (University), postal address, the electronic address, the summary, keywords, MSC or PACS index, article text, the list of references.
2. Files with illustrations, files with tables.
3. The covering letter in English containing the article information (article name, MSC or PACS index, keywords, the summary, the literature) and about all authors (the surname, names, the full name of places of work, the mailing address with the postal code, contact phone number with a city code, the electronic address).
4. The expert judgement on possibility of publication of the article in open press (for authors from Russia).

Authors can submit a paper and the corresponding files to the following addresses: nanojournal.ifmo@gmail.com, popov1955@gmail.com.

Text requirements

Articles should be prepared with using of text editors MS Word or LaTEX (preferable). It is necessary to submit a pdf copy. In the name of files the English alphabet is used. The recommended size of short communications (letters) is 4-6 pages, research articles – 6-15 pages, reviews – 30 pages.

Recommendations for text in MS Word:

Formulas should be written using Math Type. Figures and tables with captions should be inserted in the text. Additionally, authors present separate files for all figures and Word files of tables.

Recommendations for text in LaTex:

Please, use standard LaTex without macros and additional style files. The list of references should be included in the main LaTex file. Single LaTex file of the paper with the corresponding pdf file should be submitted.

References in the article text are given in square brackets. The list of references should be prepared in accordance with the following samples:

[1] N. Surname. *Book Title*. Nauka Publishing House, Saint Petersburg, 281 pp. (2000).
[2] N. Surname, N. Surname. Paper title. *Journal Name*, **1**(5), P. 17-23 (2000).
[3] N. Surname, N. Surname. Lecture title. In: Abstracts/Proceedings of the Conference, Place and Date, P. 17-23 (2000).
[4] N. Surname, N. Surname. Paper title (2010). URL: http://books.ifmo.ru/ntv.
[5] N. Surname, N. Surname. Patent Name. Patent No. 11111, Bul. No. 33, 5 pp. (2010).
[6] N. Surname, N. Surname. Thesis Title. Thesis for full doctor degree in math. and physics, Saint Petersburg, 105 pp. (2000).

Requirements to illustrations

Illustrations should be submitted as separate black-and-white files. Formats of files – jpeg, eps, tiff.

Pure mathematics is, in its way, the poetry of logical ideas.
Albert Einstein

2nd North Countries Universities Mathematical Competition (NCUMC - 2015)

St. Petersburg, University ITMO, April 20-22, 2015

For university students of any countries!

Personal and team competition.

April 20 — Registration;

April 21 — Registration, Competition and Marking session;

April 22 — Complain session and Closing ceremony.

Keep the Mathematics alive!

Registration payment: free.

Registration deadline: April 14, 2015.

Competition language: English.

Location: Saint Petersburg National Research University of Informational Technologies, Mechanics and Optics: Kronverkskij, 49.

More information about NCUMC and registration: http://mathdep.ifmo.ru/ncumc/
or Department of High Mathematics, University ITMO,
Igor Yu. Popov: +7 (812) 232-67-65, popov1955@gmail.com.

NANOSYSTEMS:

PHYSICS, CHEMISTRY, MATHEMATICS

Журнал зарегистрирован
Федеральной службой по надзору в сфере связи, информационных технологий и массовых коммуникаций
(свидетельство ПИ № ФС 77 - 49048 от 22.03.2012 г.)
ISSN 2220-8054

Учредитель: федеральное государственное автономное образовательное учреждение высшего образования
«Санкт-Петербургский национальный исследовательский университет информационных технологий, механики и оптики»

Издатель: федеральное государственное автономное образовательное учреждение высшего образования
«Санкт-Петербургский национальный исследовательский университет информационных технологий, механики и оптики»

Отпечатано в Учреждении «Университетские телекоммуникации»
Адрес: 197101, Санкт-Петербург, Кронверкский пр., 49

Подписка на журнал НФХМ
На первое полугодие 2015 года подписка осуществляется через
ОАО Агентство «Роспечать»
Подписной индекс 57385 в каталоге «Издания органов научно-технической информации»